

ROCCO GASTEIGER

VISUAL EXPLORATION OF  
CARDIOVASCULAR HEMODYNAMICS







# VISUAL EXPLORATION OF CARDIOVASCULAR HEMODYNAMICS

DISSERTATION

zur Erlangung des akademischen Grades

**Doktoringenieur (Dr.-Ing.)**

angenommen durch die Fakultät für Informatik  
der Otto-von-Guericke-Universität Magdeburg

von **DIPL.-ING. ROCCO GASTEIGER**

geb. am 07.10.1978, in Grimma

**Gutachterinnen / Gutachter**

Prof. Dr.-Ing. Bernhard Preim

Prof. Dr.-Ing. Anna Vilanova Bartroli

Prof. Dr.-Ing. Gerik Scheuermann

Magdeburg, den 07.02.2014



## ABSTRACT

---

Cardiovascular diseases (CVD) are the most common cause of death worldwide and can lead to fatal consequences for the patient. Relevant examples of CVDs are acquired or congenital heart failures, stenosis and aneurysms. Among the various causes of such diseases, hemodynamic information plays an important role and is in focus of current clinical and biomedical research. Thereby, the term *hemodynamics* comprises quantitative and qualitative blood flow information in the heart, the vessels or corresponding vessel pathology. This includes, for example, blood flow velocity, inflow behavior, wall shear stress and vortex structures. Investigations have shown that hemodynamic information may provide hints about the initiation, existence, progression and severity of a particular CVD. An important part of these investigations is a *visual exploration* and qualitative analysis, respectively, of the complex morphological and hemodynamic datasets for which the thesis at hand achieves new contributions.

The data acquisition of the hemodynamic information relies primarily on MRI imaging and simulation, whereby the thesis describes essential data processing steps for both modalities. Existent visual exploration approaches and relevant application areas from the clinical and biomedical research domain are discussed, which are used to derive three research goals of the thesis. These goals consist of the development of a new visualization method to expressively depict vessel morphology with embedded flow information, an automatic extraction approach of qualitative hemodynamic parameters as well as a flexible focus-and-context approach to investigate multiple hemodynamic information. Although the proposed methods focus on simulated hemodynamics in cerebral aneurysms, this thesis also demonstrates their application to other vessel domains and measured flow data.

The achieved results are evaluated and discussed with clinicians as well as biomedical and simulation experts, who are involved in the data analysis of hemodynamic information. The obtained insights are incorporated into recommendations and challenges for future works in this field.



## ZUSAMMENFASSUNG

---

Kardiovaskuläre Erkrankungen zählen zu den häufigsten Todesursachen weltweit und können zu schwerwiegenden gesundheitlichen Folgen für den Patienten führen. Beispiele für relevante Gefässerkrankungen sind erworbene oder angeborene Herzfehler, Stenosen und Aneurysmen. Unter den vielschichtigen Erkrankungsursachen hat sich gezeigt, dass hämodynamische Information eine wesentliche Rolle spielen und damit verstärkt im Fokus aktueller klinischer sowie biomedizinischer Forschungen sind. Der Begriff *Hämodynamik* umfasst dabei quantitative und qualitative Blutflussinformationen im Herzen, den Gefäßen oder einer entsprechenden Gefäßpathologie. Dazu gehören beispielsweise Blutflussgeschwindigkeit, Wand-schubspannung, Einströmverhalten und Verwirbelungen. Untersuchungen haben gezeigt, dass derartige Informationen Hinweise über die Entstehung und Existenz sowie den Verlauf und den Risikograd bestimmter Gefäßerkrankung geben können. Ein wichtiger Bestandteil dieser Untersuchungen ist die *visuelle Exploration* bzw. qualitative Analyse der komplexen morphologischen und hämodynamischen Daten, wozu die vorliegende Dissertation neue Beiträge leistet.

Die Datenakquirierung der hämodynamischen Informationen erfolgt im Wesentlichen durch MRT-Messungen oder Simulationen, wobei die Dissertation die wesentlichen Datenverarbeitungsschritte beider Modalitäten beschreibt. Existierende Visualisierungsmethoden und relevante Anwendungsbeispiele aus der klinischen sowie biomedizinischen Forschung werden innerhalb der Arbeit diskutiert und dienen zur Herleitung von drei Forschungszielen. Diese Ziele bestehen aus der Entwicklung einer expressiven Visualisierungsmethode für Gefäßdarstellungen mit eingebetteten Flussinformationen, der automatischen Extraktion von qualitativen hemodynamischen Parametern sowie eine flexiblen Fokus-und-Kontext Darstellung zur Untersuchung von Multiparameterdaten der Hämodynamik. Obwohl die entwickelten Methoden sich dabei auf die Anwendung von simulierten Daten in zerebralen Aneurysmen konzentrieren, wird in der Dissertation gezeigt, dass diese sich auch auf andere Gefäßanatomien und gemessene Blutflussdaten anwenden lassen können.

Evaluiert und diskutiert wurden die Ergebnisse mit Klinikern, Biophysikern und Simulationsexperten, welche in der Analyse von hämodynamischen Daten involviert sind. Die daraus gewonnenen Erkenntnisse fließen in Empfehlungen und offenen Problemen für fortführende Arbeiten ein.



*For God so loved the world that he gave his one and only Son,  
that whoever believes in him shall not perish but have eternal life.*

— (The Bible, Gospel of John, Chapter 3, Verse 16)

## ACKNOWLEDGMENTS

---

Such a huge scientific work cannot be accomplished alone and many people contributed to its final state. Thus, the acknowledgment starts with that person who I am most grateful to: *Jesus Christ*. Thank you Jesus for all the strength and endurance you have given me to succeed this work...without you I would be lost.

The next important person I want to thank is my supervisor Prof. Bernhard Preim for his great and encouraging supervision. Bernhard, you have seen more in me than I did when you have asked me to do the PhD in your group back then. Thank you for all your support and confidence during the last years! I am also grateful for all my colleagues at the Visualization Group and the ISG for their valuable contributions and for creating an enjoyable working atmosphere. I would like to name some of them representatively. At first Mathias Neugebauer, with whom I had a supporting and successful collaboration in the field of blood flow exploration. Mathias, thank you for your inspirations, the good conversations we had and all the things I have learned from you. I am also thankful to Dr. Steffen Oeltze for all the valuable discussions and amusing events we had on some conference trips. I thank Tobias Mönch for turning around my mouse ☺ and various GPU discussions. In the same way I thank Kai Lawonn and Benjamin Köhler for their support in some mathematical issues. I am also grateful to Prof. Holger Theisel, Dr. Dirk J. Lehmann and Dr. Alexander Kuhn from the Visual Computing Group for their great collaboration and aha moments in the field of vector field analysis. It would be a shame if I forgot the two Petras from our ISG office as well as our admins Thoro and Heiko...thank you for all your organization and practical help.

I would like to thank our cooperation partners for the constructive and straightforward collaboration in the last years. In particular Prof. Dominique Thévenin, Dr. Gábor Janiga and Philipp Berg (ISUT), Prof. Oliver Speck and Daniel Stucht (BMMR), Prof. Martin Skalej and Dr. Oliver Beuing (INR, University Hospital) and Volker Diehl (MR- and PET-CT Center, Bremen). Furthermore, I thank Prof. Anna Vilanova (TU Delft), Dr. Roy van Pelt (TU/e Eindhoven) and Dr. Ralph Brecheisen for their helpful discussions and collaborations as well as nice experiences during my research stay in Eindhoven and beyond. I thank Dr. Anja Hennemuth (Fraunhofer MEVIS, Bremen) for providing the MEVISFlow tool as well as her constructive collaboration and feedback. I am also grateful to all the participants of the conducted user studies and their feedback, in particular Dr. Uta Preim (Community Hospital of Magdeburg) and Dr. Cordula Scherlach (INR, University Hospital). For the sustained proof-reading of this thesis I am very thankful to Stefanie Quade (ISG) and Catherine Winzer.

I would also like to mention Cornelia Göbel and Benjamin Roderwald with his family, who accompanied me during this work in the last year. Thank you for your support and prayers! Last but not least I am deeply grateful to my family,



who believed in me and provided support in all the years. Dad, mum, grandma Wella and Kai: we went through so much together, including this one.

Rocco Gasteiger, February 2014

*Denn also hat Gott die Welt geliebt, dass er seinen eingeborenen Sohn gab, damit alle, die an ihn glauben, nicht verloren werden, sondern das ewige Leben haben.*

— (Die Bibel, Johannes Evangelium, Kapitel 3, Vers 16)

## DANKSAGUNG

---

Eine solche wissenschaftliche Arbeit kann man nur schwer im Alleingang schaffen und viele Personen haben dazu beigetragen, dass sie zustande gekommen ist. Die Danksagung beginnt bei der Person, der ich am meisten in meinem Leben zu verdanken habe: *Jesus Christus*. Danke Jesus, dass du mir die Kraft und Ausdauer für das Gelingen der Arbeit geschenkt hast...ohne dich wäre ich verloren.

Als weitere wichtige Person möchte ich meinem Doktorvater Prof. Bernhard Preim für seine sehr gute und inspirierende Betreuung danken. Bernhard, du hast damals in der Frage, ob ich bei dir promovieren möchte, mehr in mir gesehen als ich und mich die ganzen Jahre unterstützt, dass dieses Ziel erreicht wird...danke für dein Zutrauen! Sehr dankbar bin ich auch für alle Kollegen in der AG-Visualisierung für ihre wertvolle Mitarbeit und möchte stellvertretend einige hier nennen. Da wäre zunächst Mathias Neugebauer, mit dem ich die vergangenen Jahre eine durchtragende und gewinnbringende Zusammenarbeit im Bereich Blutflussexploitation hatte. Mathias, du warst oft inspirierend für mich, wir hatten viele gute Gespräche und ich habe einiges von dir gelernt. Daneben danke ich Dr. Steffen Oeltze für die fachlichen Diskussionen und amüsanten Begebenheiten bei den Konferenzreisen. Tobias Mönch danke ich für das ständige Umdrehen meiner Maus ☺ sowie Hilfe bei verschiedenen GPU-Fragen. Ebenso bedanke ich mich bei Kai Lawonn und Benjamin Köhler für so manche mathematische Hilfestellungen. Prof. Theisel, Dr. Dirk J. Lehmann und Dr. Alexander Kuhn danke ich für die gute Zusammenarbeit und Aha-Erlebnisse im Bereich der Vektorfeldanalyse. Fehlen dürfen natürlich nicht die Petras aus dem Sekretariat und die Admins Thoro sowie Heiko...danke für eure Hilfe in vielen organisatorischen und praktischen Dingen.

Allen Koooperationspartnern möchte ich für ihre konstruktive und unkomplizierte Zusammenarbeit danken. Im speziellen Prof. Dominique Thévenin, Dr. Gábor Janiga und Philipp Berg (ISUT), Prof. Oliver Speck und Daniel Stucht (BMMR), Prof. Martin Skalej und Dr. Oliver Beuing (INR, Universitätsklinikum Magdeburg) sowie Volker Diehl (MR- und PET-CT Zentrum, Bremen). Ein besonderer Dank gilt auch Prof. Anna Vilanova (TU Delft), Dr. Roy van Pelt (TU/e Eindhoven) und Dr. Ralph Brecheisen für die gute Zusammenarbeit und schönen Erlebnisse während meines Aufenthaltes in Eindhoven sowie darüber hinaus. Dr. Anja Hennemuth (Fraunhofer MEVIS, Bremen) danke ich für die Bereitstellung von MEVISFlow sowie ihr konstruktives Feedback. Ebenso möchte ich mich bei allen Nutzerstudienteilnehmern für ihr Feedback bedanken, insbesondere Dr. Uta Preim (Städtisches Klinikum Magdeburg) und Dr. Cordula Scherlach (INR, Universitätsklinikum Magdeburg). Für das Korrekturlesen dieser Arbeit danke ich Stefanie Quade (ISG) und Catherine Winzer.

Erwähnen möchte ich auch Cornelia Göbel sowie Benjamin Roderwald und seine Familie, die mich vor und während dieser Arbeit begleitet haben. Danke für

eurer Mittragen und beten! Abschließend gilt ein großer Dank meiner Familie, die über die Jahre an mich geglaubt und unterstützt haben. Vati, Mutti, Oma Wella und Kai: Wir haben vieles gemeinsam durchgestanden, so auch dieses!

Rocco Gasteiger, Februar 2014

## CONTENTS

---

<b>i</b>	<b>BACKGROUND</b>	<b>1</b>
<b>1</b>	<b>MOTIVATION AND CONTRIBUTIONS</b>	<b>3</b>
1.1	Introduction . . . . .	3
1.2	Motivation and Leading Questions of the Thesis . . . . .	4
1.3	Contributions and Structure of the Thesis . . . . .	5
1.4	General Remarks and Notations . . . . .	6
<b>2</b>	<b>MEDICAL BACKGROUND</b>	<b>9</b>
2.1	Introduction . . . . .	9
2.2	Cardiovascular Diseases . . . . .	9
2.3	Cerebral Aneurysms . . . . .	12
2.3.1	Morphological Classification and Characterization . . . . .	14
2.3.2	Treatment Procedures . . . . .	15
2.4	Vascular Imaging . . . . .	19
2.4.1	Minimally Invasive Image Modalities . . . . .	19
2.4.2	Non-Invasive Image Modalities . . . . .	24
2.5	Flow Measurement with 4D Phase-Contrast MRI . . . . .	25
2.5.1	Data Acquisition Principles . . . . .	25
2.5.2	Accuracy and Artifacts . . . . .	28
2.5.3	Other Flow Measurement Approaches . . . . .	30
2.6	Summary and Conclusion . . . . .	32
<b>3</b>	<b>CARDIOVASCULAR HEMODYNAMICS</b>	<b>35</b>
3.1	Introduction . . . . .	35
3.2	Hemodynamic Information and Application Areas . . . . .	36
3.2.1	Quantitative Parameters . . . . .	36
3.2.2	Qualitative Parameters . . . . .	38
3.2.3	Application Areas . . . . .	39
3.2.4	Data Analysis . . . . .	43
3.3	Post-Processing of 4D PC-MRI Datasets . . . . .	47
3.3.1	Correction of Image Artifacts . . . . .	48
3.3.2	Vessel Segmentation and Surface Reconstruction . . . . .	51
3.4	Data Acquisition for Simulated Hemodynamics . . . . .	52
3.4.1	Image Acquisition . . . . .	53
3.4.2	Vessel Segmentation . . . . .	54
3.4.3	Surface Reconstruction and Geometric Processing . . . . .	58
3.4.4	Volume Grid Generation . . . . .	63
3.4.5	CFD Simulation . . . . .	64
3.5	Clinical Research Applications of 4D PC-MRI . . . . .	66
3.5.1	Heart and Great Vessels . . . . .	67
3.5.2	Carotid Arteries . . . . .	69
3.5.3	Intracranial Hemodynamics . . . . .	70
3.5.4	Hepatic and Peripheral Vessels . . . . .	71
3.6	Biomedical Research Applications of Simulated Hemodynamics . . . . .	72
3.6.1	Verification and Validation . . . . .	73

3.6.2	Hemodynamics and Vessel Wall Biomechanics . . . . .	76
3.6.3	Hemodynamics and Risk Assessment of Cerebral Aneurysms . . . . .	77
3.6.4	Virtual Treatment Planning for Cerebral Aneurysms . . . . .	80
3.7	Software Tools and Frameworks . . . . .	83
3.7.1	Data Acquisition Simulated Datasets . . . . .	84
3.7.2	Post-Processing 4D PC-MRI Datasets . . . . .	88
3.7.3	Data Analysis . . . . .	89
3.7.4	Integrated Software Tools . . . . .	90
3.8	Further Reading . . . . .	94
3.9	Summary and Implications for the Thesis . . . . .	95
4	VISUALIZATION OF FLOW AND HEMODYNAMIC DATA . . . . .	99
4.1	Introduction . . . . .	99
4.2	General Flow Visualization . . . . .	99
4.2.1	Challenges . . . . .	100
4.2.2	Categorization . . . . .	101
4.3	Visualization of Hemodynamic Data . . . . .	108
4.3.1	Challenges . . . . .	109
4.3.2	Cardiac and Aortic Flow . . . . .	110
4.3.3	Hemodynamics in Cerebral Aneurysms . . . . .	115
4.4	Discussion . . . . .	119
4.4.1	Structured vs. Unstructured Grids . . . . .	120
4.4.2	Flow Reduction and Depiction . . . . .	120
4.4.3	Seeding and Interaction . . . . .	123
4.4.4	Conclusion . . . . .	123
4.5	Further Reading . . . . .	124
ii	MAIN CONTRIBUTIONS . . . . .	127
5	VISUALIZATION OF BLOOD FLOW VESSELS WITH EMBEDDED FLOW INFORMATION . . . . .	129
5.1	Introduction . . . . .	129
5.2	Related Work . . . . .	131
5.3	Requirement Analysis and Data Input . . . . .	135
5.4	Adaptive Surface Visualization . . . . .	136
5.4.1	Ghosted View Rendering . . . . .	137
5.4.2	Silhouette Rendering . . . . .	139
5.4.3	Flow Visualization . . . . .	140
5.4.4	Shadow and Atmospheric Attenuation . . . . .	141
5.4.5	Compositing . . . . .	143
5.5	Results and Informal User Feedback . . . . .	145
5.5.1	Informal User Feedback . . . . .	147
5.5.2	Consequences and Improvements . . . . .	148
5.6	Controlled Perceptual Study . . . . .	151
5.6.1	Experimental Setup . . . . .	152
5.6.2	Shape Perception Experiment . . . . .	153
5.6.3	Smart Visibility Experiment . . . . .	154
5.6.4	Spatial Relation Experiment . . . . .	155
5.6.5	Experiment Analysis and Results . . . . .	155
5.7	Conclusion and Future Work . . . . .	158

6	DETECTION AND VISUALIZATION OF QUALITATIVE FLOW PARAMETERS	161
6.1	Introduction . . . . .	161
6.2	Related Work . . . . .	163
6.3	Requirement Analysis and Data Input . . . . .	165
6.4	Detection of the Inflow Jet and Impingement Zone . . . . .	166
6.4.1	Formalization of the Inflow Jet . . . . .	167
6.4.2	Construction of the Inflow Jet Boundary Contour . . . . .	169
6.4.3	Indication of the Impingement Zone . . . . .	170
6.5	Visualization of Hemodynamic Characteristics . . . . .	170
6.5.1	Visualization of the Inflow Jet Boundary Contour . . . . .	170
6.5.2	Visualization of the Inflow Jet as Glyph . . . . .	171
6.5.3	Visualization of the Impingement Zone . . . . .	171
6.6	Results and Evaluation . . . . .	172
6.6.1	Evaluation . . . . .	174
6.6.2	Discussion and Limitations . . . . .	180
6.7	Conclusions and Future Work . . . . .	182
7	FOCUS-AND-CONTEXT VISUALIZATION OF MULTIPLE HEMODYNAMIC PARAMETERS	185
7.1	Introduction . . . . .	185
7.2	Related Work . . . . .	187
7.3	Requirement Analysis and Data Input . . . . .	189
7.4	FLOWLENS Concept . . . . .	191
7.4.1	Identification of Hemodynamic Parameters . . . . .	191
7.4.2	Spatial Scopes and Hemodynamic Parameters . . . . .	192
7.4.3	The FLOWLENS Design . . . . .	193
7.5	FLOWLENS Visualization Templates . . . . .	196
7.5.1	Global Flow Scope . . . . .	196
7.5.2	Near-Wall Scope . . . . .	199
7.5.3	Aneurysm Scope . . . . .	200
7.5.4	Implementation . . . . .	202
7.6	Results . . . . .	203
7.7	Informal Evaluation . . . . .	206
7.8	Conclusion and Future Work . . . . .	208
8	DISCUSSION	211
8.1	Introduction . . . . .	211
8.2	Recommendations for Visual Exploration Techniques . . . . .	213
8.3	Remaining Challenges for Visual Exploration . . . . .	218
iii	APPENDIX	223
	BIBLIOGRAPHY	225
	ABBREVIATIONS	257
	PUBLICATIONS	259
	CURRICULUM VITAE	263



## Part I

### BACKGROUND

The fear of the Lord is the beginning of wisdom.  
*(The Bible, Psalm 111, Verse 10)*





## MOTIVATION AND CONTRIBUTIONS

---

### 1.1 INTRODUCTION

Cardiovascular diseases (CVD) are the most common cause of death worldwide (30% of all global deaths) and will remain the leading cause of death for the near future [83]. They affect the heart and blood flow vessels, which can lead to fatal consequences for the patient, such as heart failure and strokes. The initiation, progression and outcome of a CVD is a multi-factorial problem largely involving lifestyle, wall biomechanics, genetics, vessel morphology and hemodynamics. However, for some CVDs, such as cerebral aneurysms and atherosclerosis, the mechanisms for their initiation and evolution are not well understood. Research studies and clinical experience give rise to the assumption that hemodynamics plays an important role in the pathogenesis of vascular diseases [253]. Thus, numerous studies have been conducted investigating the influence of hemodynamic characteristics on the cellular level of the vessel wall, thrombus formation and risk of rupture. Moreover, this research domain becomes more relevant than in the past due to the advance of image modalities, computational power and modeling of blood flow behavior. *Time-resolved three-dimensional phase contrast magnetic resonance imaging* (4D PC-MRI) and *computational fluid dynamics* (CFD) simulation with appropriate blood flow models provide the potential to acquire reliable and patient-specific hemodynamic information.

Based on this information, biomedical researchers are able to investigate how the knowledge of hemodynamics can be used to support the understanding of CVD initiation and prognosis as well as to evaluate individual treatment options. For example, CFD simulations facilitate the assessment of virtual conducted endovascular procedures with certain flow diverters placed in a patient-specific vessel geometry. Although the resulting findings are not applied in clinical work yet, its embedding in clinical research becomes relevant, since 4D PC-MRI and CFD modalities are increasingly available in the clinical environment and workstations. Thus, clinicians like neuroradiologists have been involved in the analysis of hemodynamic data in recent years.

The analysis of hemodynamic information is performed quantitatively by obtaining measurements of hemodynamic quantities and qualitatively by means of visual exploration of blood flow data and the vessel morphology. A visual exploration, however, is a challenging task for several reasons. On the one hand, blood flow information is complex and enclosed by vessel morphology, which may lead to occlusions and distractions. On the other hand, standard flow visualization and exploration techniques are not adapted to the needs and habits of domain experts, like biomedical researchers and clinicians. As a consequence, the visual exploration is tedious and time-consuming, which hinders the investigation process.

## 1.2 MOTIVATION AND LEADING QUESTIONS OF THE THESIS

The aim of this thesis is to develop and validate methods that improve the visual exploration of complex hemodynamic information in cardiovascular systems. It focuses on hemodynamics in anatomical and pathological vascular structures, in particular flow in aortic vessels and in cerebral aneurysms. The considerations and developments are motivated by the aims and leading questions of the domain experts in their qualitative hemodynamic exploration. In contrast to established engineering tools, the solutions are tailored to the capabilities and habits of the domain experts as well as to the vascular anatomy. Thus, the design decisions of the proposed methods are made to support a wide range of cardiovascular applications. This generalization is motivated by the observation that, for the visual exploration of hemodynamics, common problems arise, which are not only related to particular vascular or pathological structures. Common visualization problems are visibility and spatial correlations of embedded surfaces information, dealing with multivariate flow data as well as extraction of complex flow structures. This thesis analyzes common approaches to resolve these problems and their applicability to the medical and biomedical research domain. Because of the complex data characteristic, the potential of illustrative rendering techniques is investigated. Illustrations are well known and established in medical education due to their capabilities to abstract and simplify complex information.

In particular, the thesis deals with the exploration of 3D and 4D hemodynamic information, embedded in a 3D spatial context of the vessel morphology. Due to the spatial correlation between flow and morphology, domain experts are interested in both kinds of information simultaneously. Thus, methods and techniques are proposed to convey this information appropriately by reducing occlusions and enhancing spatial and depth perception. Furthermore, the progress of hemodynamic research related to CVDs reveals more and more hemodynamic parameters consisting of different scalar and vector data. This multivariate and multidimensional information is often correlated in a focus-and-context relation. As a consequence, the thesis develops visualization and interactions schemes, which may support visual exploration tasks concerning this information. Some of the proposed hemodynamic parameters, however, are extracted manually in a time-consuming process with a low grade of reproducibility. Especially for comparison purposes like differences between follow-up studies or between individual treatment options, these procedures seem not to be appropriate. Thus, one aspect of the thesis is to develop methods to extract this kind of parameters automatically and to visualize them in an appropriate manner.

In summary, the following leading questions are investigated in this thesis:

- What is the current workflow for visual exploration of hemodynamic information in both the medical and biomedical research domain?
- Which hemodynamic parameters are relevant and what visualization techniques are employed to explore them?
- What is an effective way to depict vessel morphology with embedded flow information?

- How can complex hemodynamic characteristics be extracted and visualized in an automatic, reliable, and reproducible way?
- How can multivariate and multidimensional hemodynamic parameters be explored to minimize visual clutter and to preserve spatial correlations?
- Which recommendations can be proposed for the visual exploration of cardiovascular hemodynamics?

### 1.3 CONTRIBUTIONS AND STRUCTURE OF THE THESIS

Based on the aforementioned motivation and leading questions, the thesis provides several results and novel contributions. They comprise insights and challenges of the various research applications, the development of adaptive visual exploration methods, and recommendations for further developments. In summary, the following results and contributions are achieved:

- A detailed presentation about the medical and biomedical research application of cardiovascular hemodynamics based on measured and simulated flow information, respectively. This includes different aspects of the data acquisition and processing pipeline as well as common visualization approaches the domain experts are currently using.
- An overview and discussion about existing flow visualization techniques and visual exploration techniques for cardiovascular hemodynamics.
- The development of an adaptive vessel surface rendering with embedded flow information that ensures both maximum visibility of the enclosed information and shape perception of the vessel.
- The development of an approach for an automatic detection and visualization of qualitative hemodynamic parameters, which ensures reproducibility and comparability.
- The development of a focus-and-context approach to investigate different kind of hemodynamic information, which ensures spatial correlations and minimal visual clutter.
- Proposing of recommendations and remaining challenges for the development of visual exploration techniques and for the incorporation of cardiovascular hemodynamics in the clinical workflow.

Overall, it was possible to show that hemodynamic information with an effective and reliable qualitative analysis plays an important role in the investigation of several CVDs and treatment planning. The proposed visual exploration approaches are applicable for several CVDs or vascular structures and complement existing methods. However, the results also show how important it is to integrate these methods into the domain expert's workflow of large-scale and multicenter studies to obtain clinically relevant information.

This thesis is structured in eight chapters. After background information about the medical context and fields of hemodynamic applications is presented, current

visual exploration approaches are presented. Subsequently, the three main contributions of the thesis are proposed with a final discussion about recommendations and remaining challenges as a conclusion from the thesis.

**Chapter 2** presents relevant medical background information about cardiovascular diseases and vascular imaging. In this context flow measuring modalities are also introduced with a focus on 4D PC-MRI.

**Chapter 3** gives an overview and classification of hemodynamic information that is investigated for CVDs. This information is incorporated into the introduction of the clinical and biomedical research domain as the two main application areas. Leading research questions, relevant image and data processing steps as well as typical applications are presented and discussed. Additionally, current software tools and frameworks are introduced that are utilized by domain experts to analyze their measured and simulated hemodynamic datasets.

**Chapter 4** starts with an overview and categorization of existing flow visualization techniques. Subsequently, adaptive visual exploration methods are presented that aim for an efficient and expressive investigation of cardiac and aortic flow as well as of hemodynamics in cerebral aneurysms.

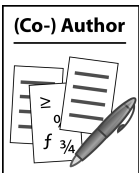
**Chapter 5** represents the first main contribution and proposes an adaptive surface visualization method that is developed for vessel structures with embedded blood flow information. It focuses on shape and depth perception of the vessel surface whilst simultaneously gaining appropriate visibility of the embedded flow depiction. The approach incorporates illustrative rendering techniques such as line rendering and ghosted view. Additionally, the increased shape and flow perception of this method in comparison to a standard semitransparent rendering is demonstrated by an experimental user study.

**Chapter 6** represents the second main contribution and proposes an automatic approach to extract and visualize two qualitative hemodynamic parameters, in particular the inflow jet and impingement zone. Both parameters have recently been identified as indicators to assess the risk of rupture for cerebral aneurysms.

**Chapter 7** represents the third main contribution and proposes a focus-and-context visualization for multiparameter datasets. It introduces the FLOWLENS as a *picture-in-picture* approach, which incorporates visualization templates to investigate correlations between focus and context parameters.

**Chapter 8** concludes the results and provides recommendations as well as remaining challenges for future developments that arise from the thesis.

#### 1.4 GENERAL REMARKS AND NOTATIONS



During the PhD the author of this thesis was involved in several projects related to the investigation of cardiovascular hemodynamics, especially for cerebral aneurysms. As a result, he was also co-author of some further published works in addition to his main contributions. These publications are incorporated in the related sections of the subsequent chapters and are indicated with the icon shown in the left margin.

Thereby, the most relevant project was **MoBeStAN**<sup>1</sup> that addressed the modeling and steering of blood flow in cerebral aneurysms. The project was funded by

<sup>1</sup> The term MoBeStAN is an abbreviation for the German phrase *Modellierung und Beeinflussung von Strömungen in Aneurysmen*.

TYPE	NOTATION	EXAMPLES
scalar	lowercase italic	$\alpha, w_i, \rho, \mu$
point	lowercase bold	$\mathbf{p}, \mathbf{q}, \mathbf{r}(\alpha)$
normalized vector	lowercase italic with hat	$\hat{v}, \hat{n}$
vector field	capital bold	$\mathbf{V}$
scalar product	dot symbol	$\cdot$
cross product	cross symbol	$\times$

**Table 1:** Summary of the mathematical notations in this thesis.

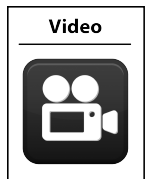
the federal state Saxony-Anhalt in Germany (grant no. 5161AD/0308M, duration October 2008 to February 2011) and consisted of following steering committee members with their heading research groups at the Otto-von-Guericke University of Magdeburg:

- Prof. Dominique Thévenin (coordinator) from the Institute of Fluid Dynamics and Thermodynamics (**IFDT**)
- Prof. Bernhard Preim from the Institute for Simulation and Computer Graphics (**ISG**)
- Prof. Georg Rose from the Institute for Information Technology and Communications (**ITC**)
- Prof. Martin Skalej from the Institute for Neuroradiology, University hospital (**IFN**)
- Prof. Klaus Tönnies from the Institute for Simulation and Computer Graphics (**ISG**)

The hard copy version of this thesis includes a DVD that contains all publications by the author and his co-authorship including video material (if available) to each publication. At the corresponding section, an associated video is indicated with the icon and its *ID* in the right margin to find it on the DVD.

At the end of some chapters a *further reading* section is integrated that contains additional information with related references. This information has been reported recently or is out of the scope of the associated chapter but is worthwhile to read.

In this thesis are also used some mathematical notations, most of which are summarized in Table 1. Vectors and normalized vectors are denoted by lowercase italic letters with an arrow and hat, respectively. Points are indicated with lowercase bold letters. The components for vectors and points are accessed with subscripts of  $x, y, z$  such as  $\mathbf{p} = (p_x, p_y, p_z)$ . For some notations it will be more convenient to use numerical indices, for example  $\mathbf{p} = (p_1, p_2, p_3)$ . If not other stated scalars are real numbers and taken from  $\mathbb{R}$  as well as vectors and points from  $\mathbb{R}^2$  or  $\mathbb{R}^3$ .



See video no. ID  
on DVD



## 2.1 INTRODUCTION

This chapter presents relevant medical information to CVDs with a focus on cerebral aneurysms. In Section 2.2 common information about several CVDs is given. A particular field of application of this thesis is cerebral aneurysms, which are discussed in Section 2.3 in more detail. Specifically, current treatment options are introduced where knowledge about the hemodynamic information can be used to support treatment decisions. For the diagnosis of CVDs, vascular imaging is necessary and relevant imaging modalities are described in Section 2.4. The acquired image data are used for reconstructing patient-specific anatomical surface models, which are utilized for visualization purposes and later as geometric boundaries for CFD simulations. In addition to simulated flow data, phase-contrast flow measuring is becoming more and more relevant for clinical and research applications. Thus, Section 2.5 gives an overview of the fundamental principles of this flow measuring modality including the inherent artifacts and the necessary post-processing steps to minimize them.

## 2.2 CARDIOVASCULAR DISEASES

Cardiovascular diseases refer to the class of diseases that affect the heart and blood flow vessels (arteries and veins). They include coronary heart diseases, cerebrovascular diseases, peripheral arterial diseases, rheumatic heart diseases, congenital heart diseases, deep vein thrombosis, and pulmonary embolism. The latest data of the World Health Organization (WHO) reveals that in 2008 about 17.3 million people died from CVDs, which represents 31% of all global deaths [232]. In 2012, CVDs caused nearly half of all deaths in Europe (47%) and in the European Union (40%), with economic costs of about €196 billion a year [100]. In the United States, CVD accounts for 33.6% of all deaths, with economic costs of about \$286 billion per year, which exceeds the costs of any other diagnostic group, e. g., cancer with \$228 billion [132]. In Figure 1a, the distribution of CVD deaths due to heart attacks, strokes and other types of cardiovascular diseases is shown.

These statistics enhance the impact of CVD on the global population and current medical research is focusing on an early diagnoses and optimized treatment. A CVD can lead to an insufficient supply, an acute blockage (so-called *ischemia*) or a leakage (so-called *hemorrhage*) of blood flow to the heart, parts of the brain and the remaining body. Heart attacks or strokes are often the outcome of these diseases. In this section, common CVDs are introduced that are also relevant for the investigation of hemodynamic information in this thesis. Since this thesis focuses on cerebral aneurysms, this CVD and treatment options are described in more detail in Section 2.3. For illustration purposes and to clarify some heart-related anatomical terms, Figure 1b shows a diagram of the human heart with inflow and outflow directions.



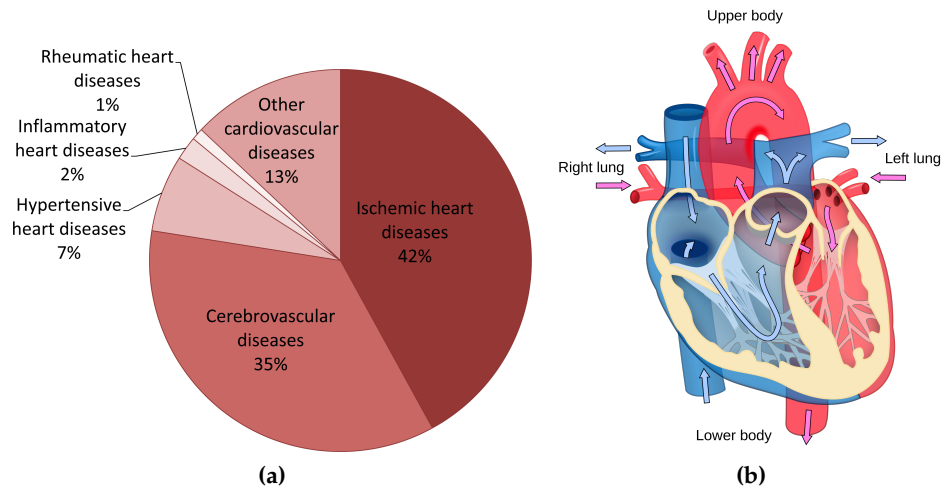


**Figure 1:** (a) Distribution of global CVD deaths due to heart attacks, strokes and other types of cardiovascular diseases according to the current WHO report. (b) Illustration of the anatomy and blood circulation of the human heart. (Data in image (a) is based on Mendis et al. [232], image (b) © User: ZooFari / Wikimedia Commons / CC-BY-SA-3.0.)

The heart is a muscle divided into two main parts, the right and left *ventricle* each with its *atrium*. In healthy subjects, these two parts are separated by the *septum*. The heart acts as a double pump that provides a continuous blood circulation of oxygenated and deoxygenated blood through the cardiac cycle. A cardiac cycle consists of two main phases, the *diastole* and *systole*. In the systole, both ventricles start to contract and the pulmonary valve as well as the aortic valve are open. During contraction the right ventricle ejects deoxygenated blood into the lung through the *pulmonary artery* and the left ventricle ejects oxygenated blood into the body through the *aorta*. The tricuspid valve and the mitral valve are closed to prevent a backward flow or *regurgitation* into both atria. Simultaneously, each atrium relaxes to collect deoxygenated blood from the body in the right atrium and oxygenated blood from the lung in the left atrium, respectively.

After the systole, the diastole follows with the relaxing of both ventricles. Thereby, the blood from each atrium flows into the corresponding ventricle through the open tricuspid valve and the mitral valve. The pulmonary and aortic valve are closed to prevent a retrograde flow from the aorta and pulmonary artery into the ventricles. In the following, some CVDs are described that impair a normal blood flow circulation [232], partly shown in Figure 2.

- **Tetralogy of Fallot:** The *tetralogy of Fallot*<sup>1</sup> is a complex congenital heart defect consisting of four components (see Fig. 2a): (1) A *ventricular septal defect* (VSD) causes a mixture of deoxygenated and oxygenated blood in the left ventricle. After VSD surgery, which closes this hole in the cardiac septum, patients have a high risk of developing an improperly shutting pulmonary valve. (2) Due to a stenosis in the pulmonary artery, the mixed blood from both ventricles is preferably pumped through the aorta. This behavior is called *right-to-left shunt*. (3) A right ventricular hypertrophy develops progressively to blood flowing through the narrowed pulmonary artery because

<sup>1</sup> Named after the French pathologist Étienne-Louis Arthur Fallot.

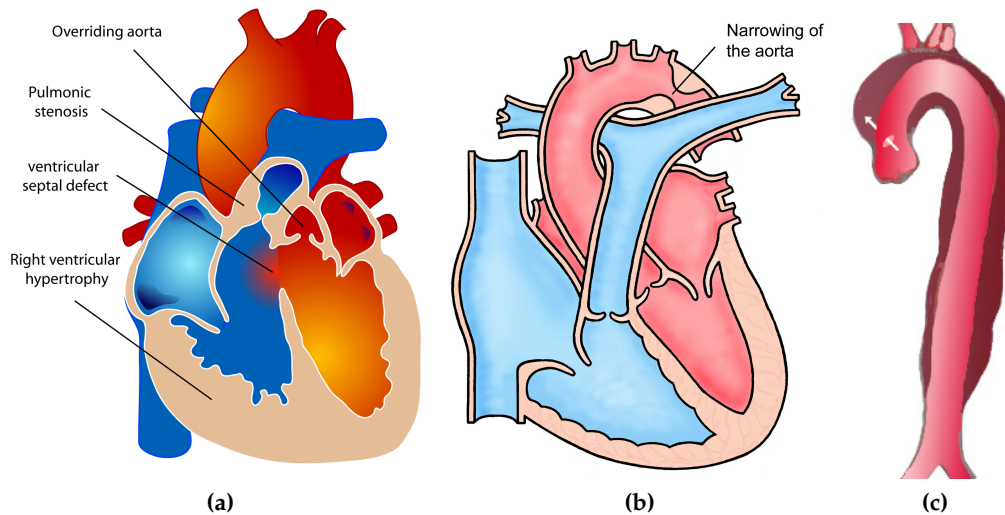


**Figure 2:** Illustrations of three CVDs: (a) tetralogy of Fallot with its four components, (b) aorta coarctation depicted as narrowing at the aortic arch and (c) aorta dissections with false vessel lumen. (Image (a) © Mariana Ruiz / Wikimedia Commons / Public Domain, image (b) from Yorkshire and Humber Stroke and Cardiac Networks with © Crown Copyright and image (c) © User: JHeuser / Wikimedia Commons / CC-BY-SA-3.0 / GFDL.)

of the constant resistance time. (4) An *overriding* aorta denotes a special malposition, where the aorta is positioned directly over a VSD instead of the left ventricle.

- **Congestive heart failure:** A *congestive heart failure* (CHF) is diagnosed when the heart is not able to supply the body with enough blood. Possible reasons are a limited pump capacity or an abnormal amount of retrograde flow. The latter can occur during the diastole from the aorta back into the left ventricle or from the pulmonary artery back into the right ventricle, if the corresponding valve does not close properly. Another failure can be related to the mitral valve, which can close abnormally and cause a back flow of blood into the atrium. Heart valve failures may be congenital or acquired. The percentage of backflow is called *regurgitation fraction*. While a small amount of up to 5% is considered as normal, higher percentages indicate a CHF. Depending on the affected vessel, aorta or pulmonary artery, it is termed aortic or pulmonary insufficiency.
- **Aorta ectasia and coarctation:** An *ectasia* denotes a local dilation of the aorta due to a weakened vessel wall. If the vessel diameter is more than 1.5 times larger than the original size, it is called an aortic *aneurysm*. On the contrary, a *coarctation* denominates an abnormal narrowing of the aortic arch and can cause higher flow speed (see Fig. 2b). This higher speed increases the pressure on the vessel wall and might promote the formation of aortic aneurysms.
- **Aorta dissection:** An *aortic dissection* is caused by a tear in the inner aortic wall, which allows the blood to flow between the layers of the wall (see Fig. 2c). It forces the layers apart and develops a "false" lumen, which bears a high risk of rupture. A rupture can lead to a massive and acute blood

loss resulting in a high mortality rate. As a result, the blood supply by this affected vessel is reduced and can lead, for example, to a heart attack.

- **Valve defects:** Congenital malformations of valves lead either to an insufficient shutting (see also CHF) or increased flow speed during diastole and systole, respectively. For example, a *bicuspid aortic valve* (BAV) is the most common congenital aortic valve malformation. Normally, the aortic valve consists of three valvular leaflets, but in BAV patients two of them are fused together. As a result, BAVs show an usual amount of backward blood into the left ventricle during the diastole and high outflow jet during systole.
- **Marfan syndrome:** The *Marfan Syndrome*<sup>2</sup> is a genetic disorder of the connective tissue. It results in a weakening of the connective tissue and may contribute to the formation of an aorta ectasias and aortic aneurysm.
- **Vascular stenosis:** A *vascular stenosis* is an abnormal narrowing of the vessel lumen often caused by atherosclerosis made up mostly of a local accumulation of lipids, known as plaques.
- **Cerebral aneurysms:** Similar to an ectasia and aortic aneurysm, a *cerebral aneurysm* is a pathological vessel dilation of a cerebral artery, which bears a high risk of rupture. They are caused by several factors such as genetics, vessel morphology, hemodynamics and other clinical or epidemiological factors (e. g., smoking, alcohol consumption and hypertension).

The diagnosis and prognosis of the aforementioned CVDs are largely based on the vessel morphology obtained by computer tomography (CT) and magnetic resonance imaging (MRI) as well as functional information from cine scans and ultrasound (US) [135]. However, a CVD often reveals an anomalous hemodynamic behavior compared to a normal vasculature. Thus, clinicians and biomedical researchers are increasingly interested in a quantitative and qualitative investigation of hemodynamic measures to understand their influence on the progression and outcome of the diseases. Moreover, a deeper understanding of this correlation can be used to establish an optimized treatment procedure. A particular field of application is cerebral aneurysms where its pathology is discussed in the next section in more depth.

### 2.3 CEREBRAL ANEURYSMS

Cerebral aneurysms or *intracranial aneurysms* belong to the category of cerebrovascular diseases with an overall prevalence of about 3% to 7% [175, 349]. The percentage is higher in patients who have had kidney disease or a positive family history of a former rupture or aneurysm. Women and people older than 50 years also have higher prevalence. Improvements in medical imaging and an increased number of patient examinations have led to more incidental findings of unruptured aneurysms. Although cerebral aneurysms may occur at different locations of the brain arteries, their occurrences are typical on arteries of the *Circle of Willis*, which is the vessel base of the brain. In Figure 3 the most common locations of cerebral aneurysms at the Circle of Willis are illustrated.

<sup>2</sup> Named after the French pediatrician who first described this disease in 1896.

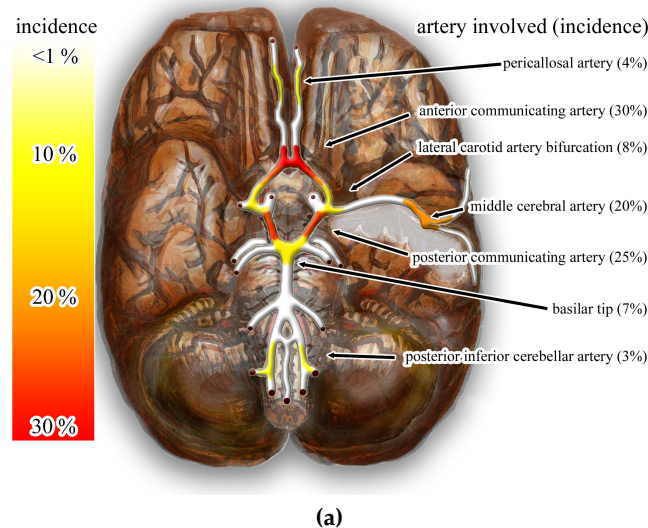


**Figure 3:** Indication of the most common locations of cerebral aneurysms. The majority of aneurysm develop on arteries of the Circle of Willis, which is at the base of the brain. (Image © Nicholas Zaorsky / [Wikimedia Commons](#) / CC-BY-SA-3.0.)

Every unruptured aneurysm bears the risk of rupture resulting in a *subarachnoid hemorrhage* (SAH), which is a subtype of stroke. An SAH leads to a bleeding into the subarachnoid space with critical consequences for the patient, e. g., severe cognitive impairments, depression or even death. The average annual rupture rate of cerebral aneurysms is about 0.6% to 1.4% [166, 361] with a fatality rate between 40% and 60% [227]. Important risk factors for a rupture are the aneurysm size, genetic factors (e. g., Japanese and Finnish descendants as well as patients with a family history of SAHs) and epidemiological factors (e. g., female gender, age older than 60, smoking, excessive alcohol consumption and hypertension).

In clinical practice, the aneurysm's geometric size is the most important measure for the risk of rupture: larger aneurysms are more likely to rupture than smaller aneurysms. Several studies have shown that cerebral aneurysms with a diameter smaller than 10 mm have a risk of rupture of about 0.1% to 0.8%, larger than 10 mm about 1.2% to 7.1% and larger 25 mm over 40% per year [88, 166, 364]. Nevertheless, a considerable amount of small aneurysms also rupture and the investigations show that the mechanisms responsible for the initiation, growth and rupture of an aneurysm are not well understood. In addition to the aforementioned risk factors, wall biomechanics, the extravascular environment and *hemodynamics* are also involved [301]. For physicians, however, a reliable risk assessment is vital because the decision to treat an aneurysm, with the inherent risk of complications, has to be balanced against the risk of rupture. This is also crucial in cases of multiple aneurysms for the decision as to which one should be treated first and what treatment option should be chosen.

In the context of this multi-factorial problem, recent studies have shown that certain hemodynamic information plays an important role in the assessment of aneurysm progression and rupture [64, 301, 370]. It is also assumed that comprehensive knowledge about hemodynamic information can also be useful for patient-specific treatment planning. Thus, cerebral aneurysms are one of the most common CVDs with increased investigations of their embedded hemodynamics in

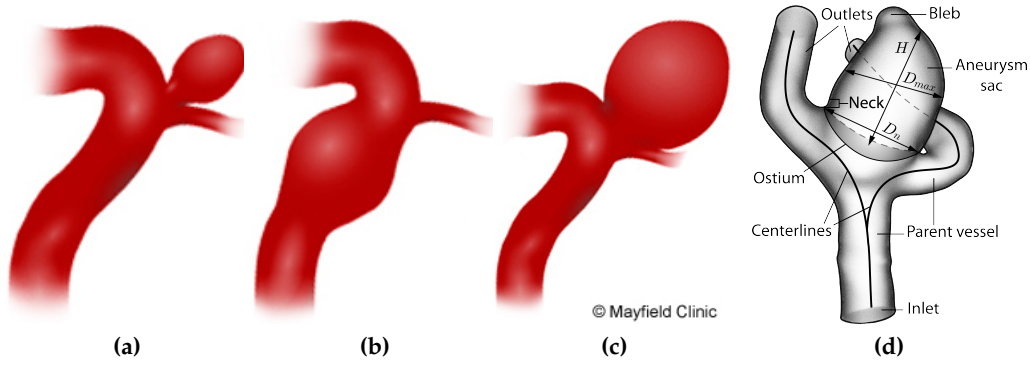


**Figure 4:** The three different shape types of cerebral aneurysms: (a) saccular as most common type, (b) fusiform and (c) giant aneurysm. An illustration of different anatomical landmarks and measurements for cerebral aneurysms is shown in (d). (Images (a) - (c) reprinted with kind permission from © Mayfield Clinic.)

recent years and they will be discussed in more detail in Chapter 3. In the following, we describe certain morphological characteristics and treatment procedures for cerebral aneurysms.

### 2.3.1 Morphological Classification and Characterization

Cerebral aneurysms can be classified and characterized in terms of their shape and size measurements. There exist three main types of aneurysm shapes: *saccular*, *fusiform* and *giant* [44, 116]. The most common type is a saccular shape (prevalence of about 80%) consisting of a neck or narrow stem with a berry-shaped aneurysm sac. Fusiform aneurysms exhibit no distinct neck or stem and are spindle-shaped. Giant aneurysms are either saccular or fusiform with more than 2.5 cm in diameter, frequently with a wide neck. All three shape types are illustrated in Figures 4a to Figure 4c.

In addition to the shape classification, clinicians also refer to certain anatomical landmarks and size measurements to characterize cerebral aneurysms. This information is used mainly to assess the risk of rupture as well as for treatment decisions and treatment planning [200, 218, 361]. In Figure 4d the most relevant landmarks and measurements are illustrated, which are also used throughout the thesis and defined as follows:

- **Parent vessel:** The parent vessel is the affected vessel where the aneurysm has evolved. In most cases it is an artery with one or multiple inlet and outlets.
- **Aneurysm sac:** The aneurysm sac or dome represents the vascular lumen of the aneurysm and describes the spatial extension of the pathological vessel dilation. Due to the widening, the vessel wall of the aneurysm sac is thinner compared to the wall of the parent vessel, which causes the increased risk of rupture.
- **Bleb formations:** Bleb formations are local outpouchings of the aneurysm sac and sometimes denoted as lobes, daughter sacs or satellites. They may re-



sult from a former rupture and have been identified as a factor for increased risk of future rupture.

- **Ostium:** The ostium describes the neck contour around an aneurysm. As a consequence, the ostium is only defined for saccular aneurysms. The imaginary ostium surface separates the aneurysm sac from the parent vessel.
- **Centerlines.** The centerlines refer to the parent vessel and describe one or multiple imaginary midlines between inlets and outlets as well as between outlets.
- **Neck.** The neck describes the stem between the parent vessel and the aneurysm sac. It can be narrow or wide and is defined only for saccular aneurysms.
- **Aneurysm height:** The height  $H$  is the maximum perpendicular distance from the aneurysm wall to the neck.
- **Maximum diameter:** The maximum diameter  $D_{\max}$  of the aneurysm sac is measured almost parallel to the neck and at the largest separation between the aneurysm walls. Furthermore, from cooperation with neuroradiologists for this thesis it has emerged that not only one maximum diameter is measured but multiple diameters to assess the volume of the aneurysm sac.
- **Neck diameter:** The diameter of the neck  $D_n$  is measured as the largest width of the neck.
- **Aspect ratios:** Based on the aforementioned dimension measurements the following aspect ratios are obtained:  $H/D_n$ ,  $D_{\max}/D_n$ , and  $D_{\max}/H$ . These ratios can also be used to classify the shape of an aneurysm sac as more spherical or ellipsoidal.

In addition to these landmarks and measurements, Ma et al. [218] introduced further quantitative shape information, such as convexity ratio, bottleneck factor and curvature. For this information, however, no statistical studies exist that investigate the influence of these geometrical characterizations on the risk of rupture and treatment planning.

### 2.3.2 Treatment Procedures

The diagnosis and detection of cerebral aneurysms can be incidental (asymptomatic) or due to investigations after specific symptoms occur, e.g., a sudden and severe headache, vision impairment or loss of consciousness. If one or multiple aneurysms are found, they can be unruptured or already ruptured and the decision about an appropriate treatment procedure has to be made [346]. Every treatment, however, carries a risk of complication. Thus, the decision to treat an aneurysm has to be balanced against the risk of rupture. Furthermore, in cases of multiple aneurysms, the question arises as to which of them should be treated first. Important factors influencing this decision are:

- aneurysm location and its anatomical access,

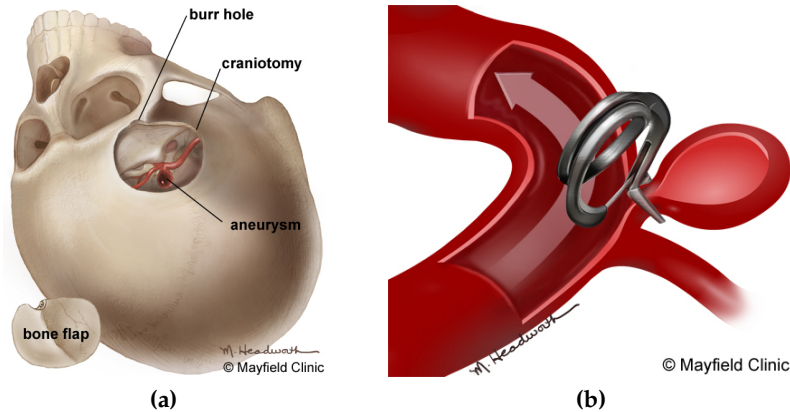


**Figure 5:** Illustration of the surgical clipping procedure to treat cerebral aneurysms: (a) performing a *craniotomy* to get access to the aneurysm, (b) a titanium clip is placed across the neck to block normal blood from entering the aneurysm. (Images reprinted with kind permission from © Mayfield Clinic.)

- aneurysm size,
- former SAH,
- patient's age, life expectancy and physical condition.

The treatment can be categorized in *surgical* and *endovascular* procedures. From ancient times until now it has undergone gradual improvement to increase the outcome, to decrease treatment risk and to permit treatments of more complicated aneurysm configurations. The treatment aims to completely block off the aneurysm sac from the flow of the parent vessel, which induces a thrombus formation (so-called *embolization*), within the aneurysm lumen. Later, the vessel wall at the neck is remodeled due to a reconstruction of the endothelium, the thin cell layer that lines the inner surface of the vessel wall. Finally, the aneurysm shrinks and the natural blood flow circulation is restored. In the following, we briefly describe the two aforementioned procedures and refer to Wong et al. [367] for further details.

### 2.3.2.1 Surgical Treatment

The first description of a cerebral aneurysm treatment was dated back to 2725 BC, when an Egyptian physician used a fire-glazed instrument to treat an incidentally found aneurysm during an open head surgery. However, further developments did not occur until after AD 200 with various degrees of success [265]. Rapid progress was made in the 1800s by John Hunter, who introduced the procedure of *ligations* of the affected artery. Until the early 1900s this kind of treatment became the standard for incidentally exposed cerebral aneurysms but it was still associated with high levels of morbidity and mortality. No occlusion tests were carried out to predict whether a patient could tolerate the vessel sacrifice.

Thus, a more selective ligation arose by the wrapping and direct suture ligation of the aneurysm neck, which was later replaced by the *clipping procedure*. After performing a *craniotomy* and exposing the aneurysm, a microsurgical *titanium clip* is placed across the aneurysm neck to prevent blood from entering, as illustrated

in Figure 5a and Figure 5b, respectively. Finally, the aneurysm sac is punctured with a needle release the filled blood and to invoke an atrophy of the aneurysm.

The surgical modality offers the advantage of a direct aneurysm occlusion associated with a significantly low rate of recurrence. However, this is achieved with the burden of an open head surgery including patient discomfort, longer length of hospital stays and operative risks. Furthermore, for aneurysms which cannot be exposed, clipping is not applicable. Nevertheless, due to its direct vessel repair and further developments, microsurgical clipping is still used in the treatment of cerebral aneurysms to this day.

### 2.3.2.2 Endovascular Treatment

Parallel to the development of microsurgical clipping, endovascular techniques arose at the end of the 20th century. In an endovascular procedure, the carotid artery is punctured and a microcatheter is introduced guided by intra-operative CT or MRI imaging to the proper artery section. Over the tip of the microcatheter a detachable device can be deployed at a specific artery section. For cerebral aneurysms a so-called *Guglielmi Detachable Coil*<sup>3</sup> (GDC) is introduced to induce a thrombus formation [140].

The microcatheter is placed in the aneurysm sac where an electrically detachable platinum guide wire is advanced through the microcatheter and is released to a coil, which partially fills the aneurysm. A GDC is relatively soft, retrievable and adopts the shape of the aneurysm well. If one coil does not fill out the aneurysm lumen sufficiently, multiple coils will be placed until the lumen is packed. This procedure is illustrated in Figure 6a and Figure 6b. Due to the coil packing, the blood flow speed decreases and induces a thrombus formation within the aneurysm sac that prevents the normal blood flow from entering the sac.

For wide-necked aneurysms, however, standard coiling is not feasible because the coils may not be able to remain in the aneurysm sac properly and could occlude the parent vessel. Thus, *balloon-assisted coiling* techniques (also known as *remodeling techniques*) were introduced to close off the neck of the aneurysm temporarily. For balloon-assisted coiling, two microcatheters are utilized. The first one is used to place a deflated balloon in front of the aneurysm neck, followed by the second catheter into in the aneurysm. Before a coil is deployed and detached, the balloon is inflated and covers parts or the whole of the aneurysm neck. If the coil is seen to be fixed in the aneurysm lumen after its deposition, the balloon is deflated to prevent a thrombus formation in the parent vessel. This procedure is repeated until the aneurysm is packed and the balloon is finally removed.

Beside the advantage of treating wide-necked aneurysms, balloon-assisted coiling enables a higher packing density and a fast hemostasis, i.e., cessation of bleeding, in the case of an acute rupture. On the contrary, two microcatheters are needed, which is associated with an increased potential of procedural complications and thromboembolic events. Furthermore, there is still an aneurysm recurrence rate of between 15% and 30% [367].

To overcome these drawbacks, another approach, *stent-assisted coiling*, was suggested and developed in the early 2000s. The idea behind this procedure is to deploy a *stent* along the wide aneurysm neck to act as a non-occlusive support

<sup>3</sup> Named after its inventor, the Italian neuroradiologist Guido Guglielmi in 1990.



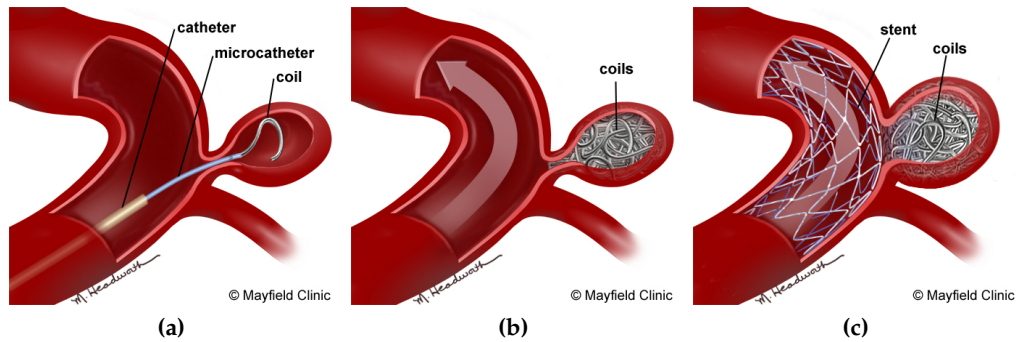


**Figure 6:** Illustration of endovascular coiling procedures to treat cerebral aneurysms: (a) a microcatheter is placed into the aneurysm sac, (b) through the microcatheter one or multiple coils are deployed that fill the sac to prevent the blood from entering the aneurysm. For wide-necked aneurysms a stent is detached for the aneurysm neck in (c) to prevent the coils dropping out. The stent remains in the vessel after the procedure. (Images reprinted with kind permission from © Mayfield Clinic.)

and scaffold for coil embolization, illustrated in Figure 6c. The stent is a metal mesh device (usually made of nitinol), which is pushed through the microcatheter and remains at the neck after the coiling procedure is performed. First studies have shown that stent-assisted coiling seems to have a significant decrease of aneurysm recurrences but is also associated with a higher fatality rate compared to coiling with or without remodeling techniques [262].

In clinical practice, endovascular treatment with advanced GDC devices supported by remodeling techniques are the most frequent treatment procedure for cerebral aneurysms compared to surgical clipping today. The shorter length of hospital stays and lower operative risk makes coiling the cornerstone of selective aneurysm embolization. However, even for advanced coiling procedures some difficulties remain, such as intra-operative aneurysm rupture, vessel wall perforation and uncoilable aneurysms like fusiform aneurysms.

As a result, flow diversion is suggested as a new endovascular treatment approach in recent years. So-called *flow diverters*<sup>4</sup> aim for a reconstruction and remodeling of the vessel wall to restore natural blood flow circulation and to provide a permanent, long-term occlusion of the aneurysm. Flow diverters are only placed in the parent vessel rather than in the aneurysm lumen. Thus, no coils are needed, which decreases the risk of vessel perforation and intra-operative aneurysm rupture. Available devices are similar to stents but consist of a higher metal coverage of the inner vessel wall due to an increased mesh density. First studies of endovascular reconstructions with flow diverters show an effective treatment of wide-necked, fusiform, large and giant unruptured aneurysms with a high occlusion rate and relative low rate of flow diversion-related morbidity and mortality. However, they also reveal technical difficulties in the deployment and delayed clinical complications, e. g., delayed morbidity and fatality [51, 366].

<sup>4</sup> In the literature the term *flow diverter* denotes a generic name for stents that exhibit a specific design to divert blood flow.

## 2.4 VASCULAR IMAGING

For the diagnosis of cardiovascular, cerebrovascular and peripheral vascular diseases, vascular imaging is necessary. The history of vascular anatomic imaging began over 100 years ago, shortly after the seminal experiments on X-rays, discovered and conducted by Wilhelm Conrad Röntgen in 1895 [112, 135]. With radiographic measurements that are supported by primitive and toxic contrast agents like salt or strontium bromide, first angiographic images of the vasculature were achieved in 1896 and 1927, respectively. Further developments of image technology and less toxic contrast agents resulted in surgical interventions and formed the foundation for the field of interventional radiology.

In 1929 the first cardiac catheterization was conducted, followed by the first selective coronary angiogram in 1958, whereby, in both cases, a contrast agent was injected in the vessels of the heart via an inserted catheter. A subsequent radiographic examination was used to gain an image of the contrast enhanced vascular system. From these initial experiments, angiographic imaging used for the diagnosis and treatment of vascular disease has become one of the most commonly performed invasive procedures in the world [135]. Over the last few decades, advances in angiographic modalities have contributed to a more detailed morphological depiction of the vasculature with its pathological diseases and to safer imaging procedures.

In the following, all relevant modalities are described briefly and are categorized in *minimally invasive* and *non-invasive modalities*. Minimal-invasive modalities require minimal damage of the skin at the point of instrument entrance, e.g., a catheter or an injection in contrast to non-invasive modalities.

### 2.4.1 Minimally Invasive Image Modalities

The most frequently used angiographic image modalities are based on minimally invasive vessel contrast enhancement. Commonly, a catheter is placed into the affected vessel with a subsequent injection of contrast agent. A syringe can also be used to apply the contrast agent in a vein. Depending on the utilized imaging modality, the contrast medium is radio-opaque for X-ray techniques or alters the emitted radio frequency signal from the body in magnetic resonance imaging. In clinical practice, the following modalities are currently used for vascular depiction.

#### 2.4.1.1 Digital Subtraction Angiography

The *digital subtraction angiography* (DSA) is an X-ray projection technique and involves a radio-opaque contrast agent injection. The image acquisition is performed on an angiographic unit consisting of a rotatable and moveable C-arm (the X-ray source and detector), a stationary table (gantry) for the patient, and equipment for monitoring and post-processing. An example setup of a modern angiographic unit is shown in Figure 7a [258]. The DSA image is generated by subtracting a pre-contrast image (the so-called *mask*) from the contrast enhanced image. As a result only the vessels remain visible and background structures are removed, as shown in Figure 7b.

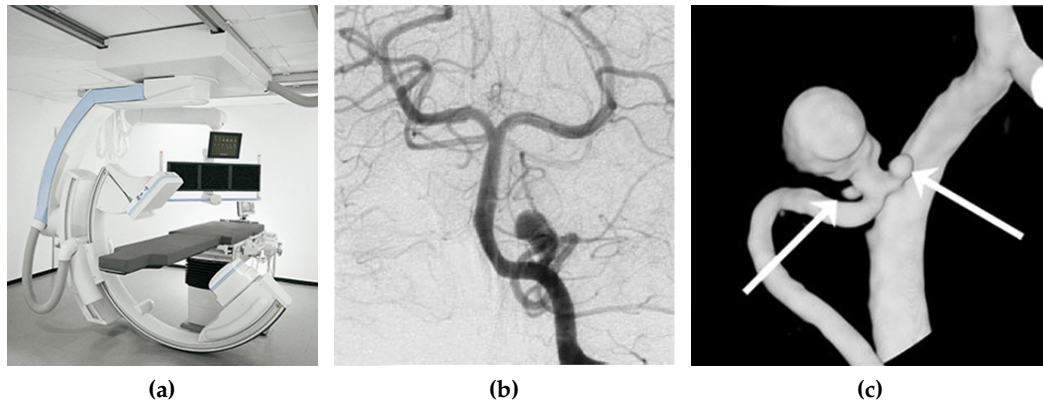


**Figure 7:** (a) Modern commercial angiographic unit with C-arm, gantry and monitoring system. The DSA image of a cerebral aneurysm (b) does not reveal the two additional microaneurysms that are visible in the volume rendering (c) of the same aneurysm that is based on 3D-RA images. (Image (a) by **SIEMENS** (SIEMENS AG Healthcare Sector, Erlangen, Germany), (b) and (c) reprinted from Van Rooij et al. [341] © ASNR 2008 with kind permission of the American Society of Neuroradiology.)

The DSA procedure can be performed in real time, exhibits a sufficient resolution to examine the vascular structure and provides image guidance for all interventional procedures used in the treatment of vascular diseases, e. g., endovascular procedures for cerebral aneurysms. Therefore, DSA was generally seen as the gold standard in angiographic imaging in the past, has crucially contributed to the understanding of the natural history of vascular disease and plays an important role in its treatment to this day [135].

However, due to its 2D projection of complex 3D vascular structures, there are also some limitations and image artifacts in the DSA. The most relevant limitations are vessel overlaps, vessel foreshortening and variable magnification of vessel parts, which may lead to a misrepresentation or misdiagnosis of diseases [135]. For example, studies have shown that during surgery of symptomatic aneurysms up to 12% of small and incidental aneurysms were found that were missed in the DSA imaging [341]. Thus, the entire angiographic examination is dependent on the angiographer's visual skills, knowledge of the vascular tree and experience in identifying and selecting optimal views. Additionally, the contrast agent injection relies only on one artery. Multiple, subsequent DSA procedures are necessary to image a complex arterial system.

#### 2.4.1.2 3D Rotational Angiography

*Rotational angiography* (3D-RA), also called 3D-DSA, is a relatively new imaging technique to overcome the limitations of DSA imaging. 3D-RA acquires the same images as DSA but is less dependent on the acquisition parameters, such as view selection or timing of contrast agent injections. It provides multiple and sequential projection views, which can be reconstructed into a 3D image dataset of the vascular structure. Additionally, less radiation and contrast agent are needed during image acquisition [135].

On current angiographic units, the acquisition process is based on a high-speed rotation and translation of the C-arm around and along the volume of interest

of the patient. The obtained DSA images are then post-processed by advanced 3D volumetric reconstruction algorithms to generate a tomographic, i.e., cross-section, representation of the individual 2D slices. Typical clinical resolutions are  $512 \times 512 \times 256$  in the x-, y-, and z-axis with a voxel size of about  $0.5 \times 0.5 \times 0.5$  mm. Finally, the 3D dataset can be visualized with, e.g., advanced volume rendering techniques to reveal the 3D vascular structure. Due to the standardization and the less operator-dependency compared to DSA imaging, 3D-RA is seen as the new gold standard for accurately identifying vascular diseases [135, 341]. As an example, Figure 7c shows a volume rendering of the same aneurysm as in Figure 7b but acquired with 3D-RA imaging. The two small additional aneurysms were missed in the corresponding single DSA images because inappropriate projection views were chosen.

#### 2.4.1.3 Computed Tomography Angiography

*Computed tomography angiography* (CTA) is a cross-sectional imaging procedure based on computer-processed X-ray absorption profiles of a radio-opaque contrast agent injection. The image generation is the same as for conventional CT imaging [46, 176]. First, a  $180^\circ$  rotation of the X-ray source and detector around a region of interest (ROI) of the patient is performed to collect several 1D X-ray absorption profiles. Second, by utilizing the filtered back projection algorithm, the 1D profiles are reconstructed into a 2D cross-section or slice of the currently scanned body part. With additional rotations, neighbored slices can be obtained.

Modern computer tomography scanners are able to collect up to 64 or 320 slices in one rotation, called multi-slice or multidetector CTs, resulting in a decreased acquisition time, radiation exposure, less amount of contrast agent, and increased temporal and spatial resolution. The final image intensities represent the density or absorption values in Hounsfield units<sup>5</sup> (HU) of the scanned structures. Current clinical resolutions are  $512 \times 512 \times 256$  in the x-, y-, and z-axis with a voxel size of  $0.35 \times 0.35 \times 0.5$  mm.

Similar to 3D-RA, the resulting 3D dataset provides a structural representation of the scanned anatomy, which is utilized for diagnostic purposes. One advantage is the correlation between HU values and the anatomical structures, which range from -1000 HU (air) through 0 HU (water) to above +1000 HU (e.g., bones and metal). Other structures and tissues lie between these values, such as muscles and blood (+40 HU), soft tissue (-300 to -100 HU) and fat (-80 HU).

The application of contrast agent in CTA shifts the HU value of blood to the HU range of bones, which enhances the contrast to the surrounding soft tissue. This enhancement supports the visual investigation of the blood vessels and simplifies subsequent segmentation approaches for further post-processing, e.g., surface mesh generation or edge-enhanced volume rendering. The similar contrast to bone structures, however, impedes segmentation approaches to distinguish between both structures when they are present in the scanned volume, e.g., in intracranial sections. A 3D-RA does not exhibit this disadvantage and requires a lower radiation dose. However, CTA is the imaging modality of choice in clini-

<sup>5</sup> Named after the British electrical engineer Sir Godfrey N. Hounsfield who is seen as having invented CT imaging in 1969.

cal practice for the first diagnosis of cardiovascular diseases because of its fast acquisition time, immediate availability and high spatial resolution [46].

#### 2.4.1.4 Contrast-Enhanced Magnetic Resonance Angiography

Similar to CTA, *contrast-enhanced magnetic resonance angiography* (CE-MRA) imaging is an acquisition procedure to obtain 2D cross-sections or 3D volumes of the body's anatomy. In contrast to CTA, CE-MRA is based on the MRI technique, which does not use ionizing radiation but the magnetic moment of hydrogen atomic nuclei [208]. No critical side effects from the magnetic fields and radio waves have yet been reported. Since the physical principles of MRI acquisition are also important for the understanding of MRI-based flow measuring (see Sec. 2.5), we present the fundamentals below. A comprehensive and recent description of basic MRI concepts can be found in Hashemi et al. [146].

MRI exploits an important property of the atomic nuclei, the so-called *spin*. The spin is a rotation about an arbitrary magnetization vector  $\vec{m}_{\text{spin}}$  and exhibits a magnetic moment (see Fig. 8a, bottom). Thus, each nucleus represents a tiny magnet and for MRI, the hydrogen nucleus is of special interest because it is the most common nucleus in living tissue.

In an MRI scanner, a strong magnetic field  $B_0$  is applied to the subject, which causes an alignment of the spin magnetization vector  $\vec{m}_{\text{spin}}$  in the direction  $\vec{m}_0$  of the external magnetic field (see Fig. 8a, top). The spins precess around  $\vec{m}_0$  with a frequency known as *Larmor frequency* and establish a *longitudinal magnetization*. Next, the aligned nuclei are excited with a specific external radio frequency

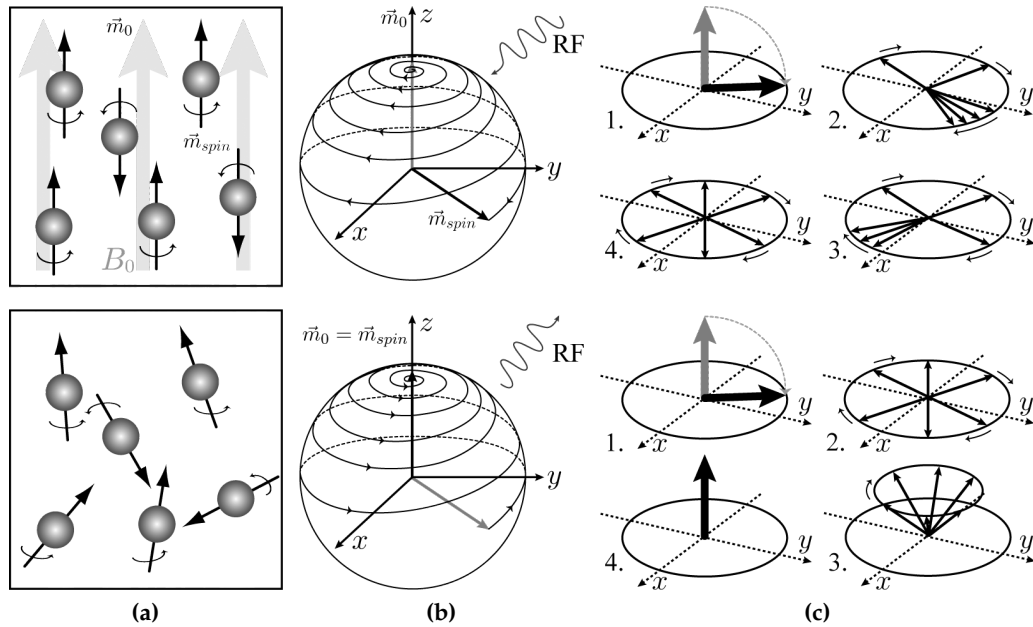


**Figure 8:** Physical principles of MRI imaging: (a, bottom) nucleus spin about an arbitrary magnetization vector  $\vec{m}_{\text{spin}}$ , (a, top) alignment of each  $\vec{m}_{\text{spin}}$  to the direction  $\vec{m}_0$  of the external magnetic field  $B_0$ , (b, top) excitation with RF signal and subsequent establishment of transversal magnetization, (b, bottom) relaxation of the spins and characteristic RF signal emission, (c, top) illustration of longitudinal relaxation and (c, bottom) transversal relaxation.



(RF) signal. The RF signal causes a resonance in the atomic nuclei, which rotates the magnetization vector  $\vec{m}_{\text{spin}}$  in the plane transverse to  $B_0$  and establishes a *transversal magnetization* (see Fig. 8b, top).

After the RF signal is turned off, the magnetization vector is rotated back to its thermodynamic equilibrium, which corresponds to the direction of the external magnetic field. During this relaxation, a RF signal is emitted, which is measured by receiver coils in the scanner (see Fig. 8b, bottom). Thereby, the signal strength and decay is proportional to the density of hydrogen nuclei in the individual tissue and fluid types, such as muscles, bones and blood. The spatial encoding for the excitation is achieved by sequentially imposing the external magnetic field with small varying magnetic fields, so-called *gradient fields*. Consequently, nuclei in different spatial locations experience different magnetic fields, and thus have different precession frequencies. This results in RF signals that have different frequencies and phases depending on the spatial location they were emitted from. By means of the *Fourier transformation*, each signal is assigned to its spatial location in the measured slice or volume and is used for the final image reconstruction. Here the reconstructed intensity values of the signals are converted to gray values where high intensities correspond to bright values and low intensities to dark values.

In general, three common MRI sequence scans can be obtained that are utilized to encode different kinds of tissue in the gray values.

- **$T_1$ -Sequence:** This sequence measures the *longitudinal relaxation time*, which is a time constant that it takes for the longitudinal magnetization vector  $\vec{m}_{\text{spin}}$  to recover, i. e., to align with  $\vec{m}_0$ , and describes the decay of the emitted RF signal (see Fig. 8c, bottom). For example, this sequence results in bright values for fat and dark values for water.
- **$T_2$ -Sequence:** This sequence measures the *transversal relaxation time*, which is a time constant for decaying the transversal magnetization (see Fig. 8c, top). Typically,  $T_2$  is shorter than  $T_1$  and represents fat darker than water.
- **$T_2^*$ -Sequence:** This sequence is related to the transversal relaxation time but exhibits a shorter time constant due to inhomogeneities in the magnetic field. Typically,  $T_2^*$ -sequences are used to decrease imaging time because the time to neutralize the inhomogeneities is omitted when measuring.

Compared to CT imaging, MRI exhibits a much lower contrast of bone structures but a higher detail of soft tissue, has a longer scanning time and exhibits some artifacts such as inhomogeneous gray value distribution due to inhomogeneities in the magnetic field. Furthermore, no direct correlation between gray values and tissue type exist, which impedes the segmentation.

In CE-MRA imaging, a contrast agent is injected, which shortens the  $T_1$  relaxation time of blood. This results in an enhanced contrast of the vessel lumen flushing by the blood compared to the surrounding tissue. Similar to CTA the acquired slices can be composed as volume datasets with a common clinical resolution of about  $512 \times 512 \times 256$  with a voxel size of  $0.7 \times 0.5 \times 0.9$  mm using a field strength of 1.5 or 3 Tesla (T). For clinical and biomedical research purposes, MRI scanner of up to 7 T with a spatial resolution of  $0.26 \times 0.26 \times 0.3$  mm are utilized. In general, the higher the field strength is, the higher the signal-to-noise ratio (SNR) of the

volume datasets and image quality. For other MRA imaging modalities we refer to the comprehensive overview of Suri et al. [314].

#### 2.4.2 Non-Invasive Image Modalities

Angiographic imaging that uses invasive modalities, measures the contrast enhancement of the blood by means of contrast agent distributions. However, this requires the administration of contrast agent injections, which bears certain risk factors for developing severe reactions like allergies and cardiac diseases. Non-invasive angiographic imaging does not require any injections but takes advantage of certain blood flow properties. Available techniques are based on MRI and ultrasound.

##### 2.4.2.1 Time-of-Flight MRA

*Time-of-Flight angiographic imaging* (TOF-MRA) is an MRI sequence based on a flow-related enhancement of the vessels [314, 162]. For an anatomical ROI a rapid  $T_1$ -sequence is performed. The static tissue in the ROI loses much of its longitudinal magnetization, i.e., the tissue is highly magnetized (saturated) by means of the external RF signal, which results in a faster decay of the emitted RF signal. When blood flows into the ROI, the hydrogen nuclei in the blood are unsaturated and establish a higher longitudinal magnetization than the static tissue. Consequently, the nuclei emit a much stronger RF signal, which results in higher intensity values for blood vessel lumen than for the surrounding tissue.

Since TOF-MRA depends on flowing blood, ROIs with slow or turbulent flow, e.g., in giant cerebral aneurysms, may lead to an RF signal extinction and the vessel lumen not being well enhanced. In comparison to CE-MRA, the TOF-MRA can be used as a complimentary method or in cases where contrast agents cannot be administered.

##### 2.4.2.2 Ultrasound

US imaging, also called sonography, utilizes high frequency sound waves (2 to 18 MHz) to image the body's internal soft tissue structures, e.g., muscles, organs or vessels, and their movement. Additionally, it is able to capture *in vivo* blood flow dynamics such as flow direction and speed. The choice of frequency is a trade-off between the spatial resolution of the image and imaging depth. Lower frequencies produce lower resolution but penetrate deeper into the body and higher frequency sound waves achieve higher resolution but are scattered and absorbed by smaller structures due to their shorter wavelength.

The image generation is accomplished in real time and consists of three steps: (1) producing the sound waves, (2) receiving echoes and (3) interpreting those echoes. The body is exposed to the sound waves by means of a small piezoelectric transducer (probe) that can be focused to a desired body depth. During penetration, the sound waves are reflected wherever there are density changes, especially from the layers between different tissues. Some of the reflected sound waves are received by the transducer and transformed into electrical pulses. Each pulse or echo is analyzed according to its transit time, depth and strength. In general, these values are coded into gray values to form a 2D slice image with white as strong and black

as zero echo. There are several modes of US imaging, e.g., the *color Doppler US*, for capturing the aforementioned blood flow dynamics, which is described briefly in the next section.

In addition to 2D imaging, current US scanners are also able to generate 3D images by acquiring a series of adjacent 2D images. US imaging is cost-effective, achieves a high spatial resolution for high frequency sound waves and has no known long-term side effects. However, the image quality and interpretation is operator-dependent, which requires a high level of skills and experience. Furthermore, US is limited to a relatively small field-of-view and is significantly prone to noise, which impairs considerably the image quality. For a more detailed description of US physics and application we refer to Gibbs et al. [130].

## 2.5 FLOW MEASUREMENT WITH 4D PHASE-CONTRAST MRI

Phase-contrast MRI is a special MRI sequence to obtain time-resolved, non-invasive 3D flow information and is often referred to as 4D PC-MRI.<sup>6</sup> In particular, the 4D flow velocity is captured at each measured voxel for a certain period of time, usually one cardiac cycle. Here the velocity value encodes the direction vector and the blood flow speed as the length of the vector. Due to considerable progress in recent years, a variety of established applications in quantifying cardiovascular function and hemodynamics exist [308]. In general, MRI acquisition is sensitive to motion like patient movement or breathing, which leads to several image artifacts, e.g., blurring and ghosting. For 4D PC-MRI measuring, however, the intrinsic motion sensitivity of MRI is exploited to obtain quantitative information about blood flow. This section describes the fundamental theory behind phase-contrast MRI and certain artifacts that could occur during image acquisition. Additionally, the section ends with a short overview of other flow measurement approaches, which are mostly used for *in vitro* experimental studies.

Note, in the related flow literature, the meanings of the terms flow **velocity** and **speed** are used ambiguously. In the 4D PC-MRI flow measuring domain it is well established to refer to velocity as the flow *direction vector* and speed as the *length of the direction vector*. In the CFD domain, flow velocity also means flow direction but speed is mostly referred to as *velocity magnitude*. Throughout the thesis and for the sake of consistency we use the term velocity and speed as described for the 4D PC-MRI domain.

### 2.5.1 Data Acquisition Principles

In the following, we describe the basic principles for 4D PC-MRI flow acquisition. For a more elaborated description, we refer to Lotz et al. [215] and Markl et al. [221]. Phase-contrast MRI builds on hydrogen nucleus spin physics, which was introduced in the section about CE-MRA image acquisition (see Sec. 2.4.1). It exploits the property that the Larmor frequency at which the magnetization vector

<sup>6</sup> In the literature this sequence is also termed as: *flow-sensitive 4D MRI*, *4D flow MRI*, *time-resolved 3D velocity mapping* or *four-dimensional quantitative flow* (4D Qflow).



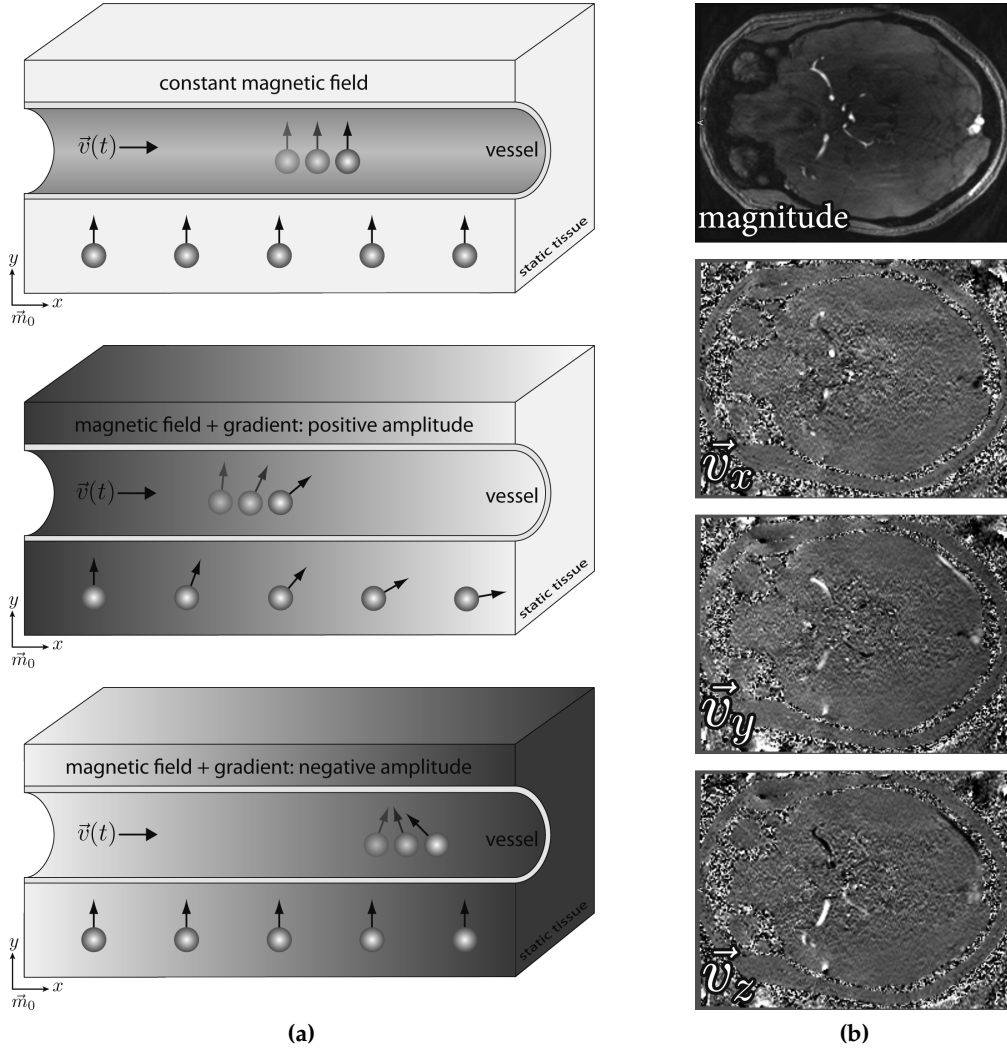


**Figure 9:** Illustration of the acquired phase shift in 4D PC-MRI: (a, top) based on a constant magnetic field stationary and moving spins do not acquire a difference in the phase of their rotation around  $\vec{m}_0$ , (a, middle) a spatially varying magnetic field caused by an imposed linear gradient with positive amplitude leads to a phase shift along the gradient direction, (a, bottom) a subsequent gradient with negative amplitude cancels out the phase shift in the static tissue but for the moving spin the phase shift remains and is linear to the speed along the gradient. The resulting 4D PC-MR images consist of one magnitude image (b, top) and three phase images (b, lower three) that represent the anatomy with the contrast-enhanced vessel lumen and flow speed in each of the three direction, respectively. (Image (a) is based on Lotz et al. [215] and Van Pelt et al. [336].)

$\vec{m}_{\text{spin}}$  of a spin is precessing around  $\vec{m}_0$  depends on the external magnetic field strength  $B_0$ . For a constant magnetic field, spins in stationary tissue and moving spins with velocity  $\vec{v}(t)$  at time point  $t$  acquire no difference in their Larmor frequency around  $\vec{m}_0$ , i.e., no difference in the phase of rotation (see Fig. 9a, top). However, by varying the magnetic field spatially the spins will experience different magnetic field strengths and precess with different Larmor frequencies along the varying magnetic field (see Fig. 9a, middle).

The variation of the magnetic field is induced by imposing the constant magnetic field with a bipolar linear gradient, the so-called *velocity-encoding gradient*.

This gradient consists of a positive and a negative amplitude that is applied successively after the nuclei are excited by the external RF signal and the spins are flipped into the transverse plane of  $B_0$ . The positive gradient pulse induces a *phase shift* for the moving and stationary nuclei due to the varying field strength. The subsequent negative gradient cancels out the phase shift in stationary nuclei but a phase shift in the moving nuclei remains, which is linear to the nuclei's speed along the gradient direction (see Fig. 9a, bottom). After the positive and negative gradient pulses are released, the spins start the relaxation and emit an RF signal, i. e., an echo wave, that encodes the phase shift. The procedure of RF excitation and the subsequently imposing with the bipolar gradient is accomplished for the x-, y- and z-directions. Similar to standard MRI, each emitted signal is reconstructed into a spatial location by means of the Fourier transformation.

The inhomogeneities of the external magnetic field  $B_0$  cause additional background phase offsets that are added to the phase shift, denoted as  $\phi^1$ . In order to compensate these offsets, a reference measurement  $\phi^2$  is performed that consists only of the background phases and is subtracted from  $\phi^1$ . Due to the Fourier transformation,  $\phi^1$  and  $\phi^2$  consist of complex signals and their subtraction commonly results in two kinds of images: the *magnitude image* and *phase images*. The magnitude image corresponds to the length of the magnetization vector  $\Delta\vec{m}_{xy}$  that results from the difference between the phase shift images  $\phi^1$  and  $\phi^2$ . In general, three magnitude images are acquired one image for each direction, which are often averaged to one final magnitude image. The intensity values represent the different anatomical tissue structures including the contrast-enhanced vessel lumen (see Fig. 9b, top).

The phase images correspond to the individual phase shift difference  $\Delta\phi_i$  between the phase angles in  $\phi_i^1$  and  $\phi_i^2$  as:

$$\Delta\phi_i = \phi_i^1 - \phi_i^2 \text{ with } i = x, y, z.$$

Thus, for each gradient direction one phase image is acquired where each value is proportional to the local flow speed in that direction. Based on  $\Delta\phi_i$ , three intensity images are calculated that represent the velocity components of the final measured flow vector  $\vec{v} = (v_x, v_y, v_z)$  with:

$$\vec{v}_i = \frac{\Delta\phi_i}{\pi} v_{ENC}, \text{ with } \vec{v}_i \in [\pm v_{ENC}]. \quad (1)$$

Thereby, the  $v_{ENC}$  or *velocity-encoding* parameter represents the speed limit expected in the vessel of interest and is typically defined in cm/s. The  $v_{ENC}$  has to be defined by the user before the flow measurements start since it is used to adjust the strength and duration of the bipolar gradients. Phase shifts are measured in degrees in the range of  $-/+180^\circ$  and all measured speed values should be in this range. The amplitudes of the bipolar gradients are calculated so that the maximum speed corresponds to a phase shift of  $180^\circ$ . Measured flow speed values outside the  $v_{ENC}$  lead to *velocity aliasing* artifacts, which will be discussed in Section 2.5.2.

In the three phase images, stationary tissue appears noisy gray, flow in one direction appears brighter and flow in the opposite direction appears darker (see Fig. 9b, lower three). By triggering on electrocardiography, it is possible to create a collection of 3D images each covering different time steps of the cardiac cycle.

REGION	VENC [CM/s]	VOLUME [#VOXEL]	SPATIAL RES. [MM]	TEMPORAL RES. [MS]	SCAN TIME [MIN]
Intracranial arteries	80-100	512×512×60	1.0×1.0×1.6	40-60	15-20
Aorta	150-200	192×128×32	1.7×2.0×2.0	40-50	19-22
Whole Heart	150-200	116×116×40	2.5×2.5×2.5	40-50	19-22
Pulmonary artery	100-150	256×256×256	2.0×2.0×2.0	40-50	10-20
Renal arteries	40-80	256×256×256	1.0×1.0×1.0	40-50	8-12

**Table 2:** Overview of different vascular regions, typical imaging parameters and scan times that are utilized for 4D PC-MRI. (Data from Markl et al. [221, 222].)

For clinical research, MRI scanners of 1.5 or 3 T magnetic field strengths are used, which usually acquire images of size  $128 \times 128 \times 50$  voxels with a spatial resolution of  $2.0 \times 2.0 \times 2.5$  mm, over up to 25 time steps with a temporal resolution of approximately 40-50 ms [221]. In biomedical research, MRI scanners of up to 7 T are used, which results in an increased spatial resolution of about  $0.75 \times 0.75 \times 0.8$  mm for an image matrix size of usually  $256 \times 256 \times 64$  voxel. Only this relatively high spatial resolution ensures that also small vessel sections and vascular diseases are sampled sufficiently, e. g., cerebral arteries or aneurysms with diameters of a few millimeters.

In Table 2 an overview of different vascular regions with typical imaging parameters and scan times is provided for a given cardiac period of about 1000 ms. The acquisition parameters are based on recent clinical research reports and accomplished on clinical 1.5 and 3 T scanners [66, 111, 221]. Note, these parameters influence each other with trade-offs between spatial and temporal resolution as well as total scan time. For example, the scan time depends not only on the heart rate but also on the spatial resolution. A doubling of the spatial resolution would lead to a quadrupling of the scan time.

### 2.5.2 Accuracy and Artifacts

The main drawback of *in vivo* flow measuring is the lack of a ground truth [215]. All available techniques including PC-MRI exhibit artifacts and a limited accuracy. Existing studies reveal different degrees of accuracy depending on the performed comparison. Studies that compare PC-MRI measuring of flow in the ascending aorta and in the pulmonary artery between phantoms and volunteers have shown an average difference of 5%. Compared with the Doppler US technique, PC-MRI measuring exhibits a good correlation but shows lower peak speed values. However, investigations of US flow measuring reported a tendency to overestimate peak speed values by up to 25% and to overestimate mean flow speed in large vessels. Other studies consider comparisons between PC-MRI and *invasive* techniques based on thermodilution or the ink-indicator method [215].

Since these techniques are highly operator-dependent and sensitive to respiratory movements, corresponding comparisons show discrepancies of between 10% and 60% for cardiac output. As mentioned in the former subsection, the accuracy of PC-MRI measuring is higher in larger vessels, e. g., aorta, than in smaller vessels, e. g., intracranial arteries, due to the limited spatial resolution of PC-MRI. For smaller vessel diameters the velocity information are only captured by a few voxel. Thereby, the *partial volume effect* becomes larger due to the higher influence of noise at the vessel border from the surrounding static tissue.

In addition to a limited accuracy, several artifacts and errors could occur during PC-MRI acquisition, which additionally impair the quality of the measured flow information. These artifacts are caused by various factors, e. g., scanner hardware, parametrization of the phase-contrast sequence and motion of the subject. In the following, a brief description of the most important artifacts is provided. For further details, we refer to Section 3.3.1 and to Lotz et al. [215].

#### 2.5.2.1 Background Phase Distortions

Inhomogeneities in the external magnetic field, eddy currents and concomitant gradient terms cause background phase distortions or *phase offsets*, which result in an incorrect velocity measurement [152, 201]. The distortion is assumed to be a spatially and temporally slowly varying image gradient, which is added to the phase images that encode the flow speed in the three dimensions. Since flow assessment is determined by integration over time and space, relatively small speed offsets can lead to significant errors in mean volume flow, stroke volume and cardiac output.

#### 2.5.2.2 Velocity Aliasing

In Section 2.5.1 the  $V_{ENC}$  parameter was introduced. Measured speed values larger than the adjusted  $V_{ENC}$  value will result in velocity aliasing artifacts, so-called *phase wraps*. For example, a flow speed of  $1.5 V_{ENC}$  in x-direction with an adjusted  $V_{ENC}$  of 100 cm/s results in a phase angle of  $270^\circ$  after Equation 1 is solved for  $\Delta\phi$ . Since the resulting phase angle exceeds the allowed range of  $-/+180^\circ$  it will be interpreted as  $-90^\circ$ , which results in a final speed  $\vec{v}_x$  of  $-0.5 V_{ENC}$  instead of  $1.5 V_{ENC}$ . A phase-wrap occurs that is characterized by a flipped flow direction and reduced speed value. However, a  $V_{ENC}$  that is too high results in less accurate measurements because noise increases with a larger  $V_{ENC}$  and flow becomes compressed to a narrow range. The closer the  $V_{ENC}$  is to the maximum expected speed, the more precise the measurement is (see Tab. 2) [221]. A correction of velocity aliasing artifacts is called *phase unwrapping* and can be achieved by adding a multiple of  $2\pi$  to the unwrapped velocity value in the phase images.

#### 2.5.2.3 Noise

As for all MR imaging techniques, phase contrast velocity images suffer from noise that can lead to errors in the acquired velocity values. There exist many factors that introduce noise, such as magnetic inhomogeneities and the strength of the external magnetic field as well as large  $V_{ENC}$  values. Therefore, the noise distribution follows a *Rician distribution* and it can be shown that the noise in the phase images

is inversely related to the SNR in the corresponding magnitude images. Thus, for a given SNR the velocity noise is determined by the user-selected  $V_{ENC}$ , resulting in a trade-off between the minimum and maximum detectable speed sensitivity needed to avoid aliasing [221]. For optimal noise performance, the smallest possible  $V_{ENC}$  should therefore always be selected. Additionally, the higher the field strength of the external magnetic field, the higher the SNR. This results from the stronger signal emitted by the hydrogen nuclei.

### 2.5.3 Other Flow Measurement Approaches

In addition to 4D PC-MRI flow measuring, there exist other modalities, which are able to measure flow velocity. In the following, we briefly present four relevant modalities including US and three optical approaches. With the exception of US, they are only able to measure *in vitro* velocity data in patient-specific vessel or phantom models. In the context of hemodynamic investigations, these modalities are utilized for assessing the state of certain CVDs, for validation purposes with other blood flow acquisition modalities such as 4D PC-MRI or CFD simulations and for the extraction of CFD boundary conditions. Compared to 4D PC-MRI, they sometimes achieve a higher spatial and temporal resolution or are able to capture flow quantities in real time.

#### 2.5.3.1 Doppler US

In the former section, we described US as an important imaging modality that is able to capture internal soft tissue structures, e. g., vessels, in real time. In addition to 4D PC-MRI, US measurement is the only image acquisition that is also able to capture flow speed and direction *in vivo* and *non-invasively* [130]. Compared to 4D PC-MRI, it exhibits a higher spatiotemporal resolution but it is not able to capture three-directional velocity information. The direction information is related to the orientation of the measured blood flow as towards or away from the transducer for the current 2D field of view. Flow speed and direction are obtained by exploiting the *Doppler effect*<sup>7</sup>.

The Doppler effect or Doppler shift describes the change of frequency of a wave for an observer moving relative to the wave source. The frequency increases when approaching, is identical when passing and decreases when receding from the observer. Applied to the blood flow, the frequency shift results from the moving blood cells with respect to the transducer. A Doppler system compares the transmitted waveform with the received and reflected waveform for the change of frequency. A negative shift, i. e., higher returning frequency, corresponds to blood flow towards the transducer and a positive shift, i. e., lower returning frequency, represents blood flow moving away from the transducer. Based on the receiving frequency, the blood flow speed can be derived, which is proportional to the size of the shift. The speed is utilized to determine states of certain CVDs, such as stenosis or congestive heart failures (see Sec. 2.2). In color Doppler US, the signed shift is color-coded where red is usually used to indicate flow toward the transducer and blue for flow away from the transducer.

<sup>7</sup> Named after the Austrian physicist Johann Christian Doppler who proposed this phenomenon in 1842.



Since the Doppler shift is highly dependent upon the angle between the beam of ultrasound and the moving blood flow, the accuracy of the resulting image depends on the operator's skills and expertise. The backscatter behavior of the flowing blood also influences the image accuracy and can be improved by using gas-filled microbubbles as an injected contrast agent. This procedure, however, would require a minimally invasive intervention. Finally, US waves have trouble penetrating high density bone structures, which results in a very limited application of Doppler US in transcranial flow measurement [110]. Nevertheless, sonographic measurements are currently the clinical routine method for a detailed quantitative analysis of *in vivo* cerebral blood dynamics.

### 2.5.3.2 Laser Doppler Velocimetry

*Laser Doppler velocimetry* (LDV) is an optical technique that also exploits the Doppler effect to quantify flow velocity [333]. It utilizes a system of two beams of collimated and coherent laser lights that intersect at a certain focus point within a vessel cross-section. This intersection results in a characteristic interference pattern or *fringes*. As a particle (either naturally occurring or induced) enters the interference fringes, it reflects light that is collected by an optical sensor. The reflected light exhibits a frequency shift that is proportional to the velocity component perpendicular to the fringes. A combination of three laser systems with different wavelengths enables the simultaneous and accurate measurement of the three-directional velocity information of that particle. As a consequence, LDV can only capture one particle at a time in a given vessel cross-section. Spatiotemporal coverage requires a time-dependent sampling of many particles distributed across the cross-section.

Due to its optical setup, LDV is only capable of measuring *in vitro* flow based on patient-specific vessel or phantom models [31]. Therefore, the model and measured fluid must be transparent and free of refractions. Typically, the models are made of glass, plexiglass or silicone, and an artificial fluid with small tracer particles, e.g., glass beads, is used instead of blood to prevent absorption of the laser light. The artificial fluid exhibits several properties including transparency at the wavelengths of the laser lights, the same refraction index as the model's material and flow properties similar to blood.

### 2.5.3.3 Particle Image Velocimetry

*Particle image velocimetry* (PIV) is also an optical technique to obtain instantaneous velocity measurements of *in vitro* blood flow [333]. As with LDV, the optical setup consists of a transparent vessel model and artificial fluid, which is seeded with tracer particles. In contrast to LDV, however, the particles have a different refraction index to the surrounding fluid and PIV is able to capture 2D or even 3D vector fields at one time. Thanks to high speed data processing, these flow fields may be visualized in real time. For a 2D vector field, a laser beam with short pulse durations is expanded into a cross-section plane of the model. Since the refraction index of the particles differs from the fluid, only the particles flowing through the plane are illuminated. A camera system records two separate frames that represent the visible particles of two successive exposures. With the help of *image processing* and *cross-correlation techniques*, the two frames are analyzed to estimate average displacement vectors for small regions of visible particles. These vectors

are converted into in-plane velocity vectors based on the known time between two successive exposures and the physical size of the image pixel. For the measurement of 3D vector fields, a 3D volume is illuminated and captured by a setup of multiple camera systems.

The particle density for PIV is crucial and has to be properly adjusted. A too low density results in a poor representation of the real vector field. A too high density may alter the blood-like flow behavior or prevents the detection of individual particles in the captured images. Compared to LDV, the accuracy of the derived vector fields is lower because of both the more distant particle positions and the spatially averaged velocity vectors that result from the image processing.

#### 2.5.3.4 Particle Tracking Velocimetry

A variation of PIV is *particle tracking velocimetry* (PTV), which is able to track single particle trajectories in 2D and 3D [333]. In contrast to PIV, a lower density of seeded tracer particles is used to enable the tracking of single particles over time. For 2D trajectories the same procedure as for the PIV measurement in 2D is used with the difference that individual particles are tracked for several frames. The tracking of 3D trajectories requires up to four calibrated camera systems including reference points that are installed in an angular configuration. The flow volume is illuminated with pulsatile laser beams or LEDs and for each successive exposure the cameras simultaneously capture the visible particle positions. With the help of image processing techniques, individual and corresponding particles in the different images are identified and their 3D locations are calculated. Once the particles are localized, pairs of particles are matched in the successive frames to track their trajectory. Thanks to the calibrated camera systems, the world coordinates of the particles are known, which are used to determine the local flow speed of the trajectory. PTV achieves a higher accuracy than PIV because individual particles are tracked instead of an averaged velocity vector for small regions of visible particles. Compared to LDV, the accuracy is lower but enables a 3D tracking of individual particles instead of a single point in the fluid at any one moment.

## 2.6 SUMMARY AND CONCLUSION

The large impact of CVDs on the global population means that medical research focuses on early diagnosis and optimized treatment planning. CVDs cause a pathological altering of a vascular region that results in a weakened vessel wall, decreased blood supply or unusual change of blood flow with serious consequences for the patient. Thus, a detailed and reliable morphological depiction of the pathological region is relevant for assessing the state of a certain disease. Thanks to advanced image modalities such as 3D-RA and CE-MRA, high-resolution vascular images with reduced radiation exposure and scanning time are available nowadays. In this context, TOF-MRA is becoming more and more relevant since no radiation or contrast agent are used and it provides high soft tissue and vessel detail. However, for intra-operative imaging, e. g., for endovascular treatment of cerebral aneurysms, DSA imaging is still the gold standard.

In addition to vascular imaging, the diagnosis and assessment of CVDs rely also on *in vivo* flow quantification, such as flow rate or speed estimations by means of

Doppler US. Moreover, studies have shown that morphological or epidemiological information such as the size of an aneurysm or patient age alone may not be sufficient risk factors. An increasing community of cardiovascular physicians and biomedical researchers are convinced that the blood flow behavior or *hemodynamics* also play an important role for the initiation, evolution and outcome of CVDs. In current clinical routine, Doppler US is utilized to obtain *in vivo* flow information. With Doppler US it is possible to measure the flow in real time with a high spatial resolution. However, no volumetric flow can be obtained, which makes the investigation of 3D flow structures difficult. Furthermore, the utilization of Doppler US is restricted to certain structures, which enable a penetration of the US waves.

With the advent and advances of 4D PC-MRI, however, domain experts are able to measure *in vivo* 3D blood flow over the cardiac cycle. Although the acquired flow information does not represent a gold standard and exhibits uncertainty due to the limited spatial resolution and image artifacts, it can be used to evaluate the hemodynamics quantitatively and qualitatively. Currently, it is applied in clinical research for a variety of anatomic regions, such as the heart, aorta and the cerebral artery system. First results are promising since they reveal abnormal flow quantities and behavior, such as sudden changes of flow rate, speed and flow direction, which are seen as indicators of certain CVDs, e.g., stenosis, aorta dissections or heart valve failures. The acquisition of volumetric blood flow information, however, is not restricted to *in vivo* flow measuring. In recent years, considerable progress has been made in CFD simulations to model the complex patient-specific hemodynamic behavior. These simulations are based on reconstructed vessel surfaces as well as on boundary conditions derived mostly from 4D PC-MRI or US. Thus, the possibility of high resolution image data acquisition as well as advances in 4D PC-MRI measuring and its post-processing, support the usage of CFD blood flow modeling. Based on reliable blood flow modeling, various forms of virtual treatment can also be conducted that provide clinically pertinent information for treatment decisions and optimizations, e.g., in flow diverter design.

The potential of acquiring instantaneous 3D flow information by means of measurement and simulation leads to the following three conclusions:

- **Data post- and pre-processing:** Measured and simulated blood flow information requires several post- and pre-processing steps before it can be utilized. The 4D PC-MRI datasets generally require a correction in terms of the inherent artifacts, such as noise and phase wraps. For a reliable and patient-specific blood flow simulation, several image and geometric processing steps are necessary. Among other things, this involves a segmentation process and geometric mesh optimizations to achieve high-quality vessel surfaces.
- **Different fields of application:** Once flow information is obtained, it can be investigated in different fields of cardiovascular applications. Several research questions arise that focus on the identification of prominent hemodynamic characteristics in both healthy and pathological cases. Additionally, the knowledge about healthy blood flow behavior may promote the development of patient-specific treatment options to correct the pathological flow behavior.
- **Quantitative and qualitative analysis:** The investigation of hemodynamic information requires an efficient quantitative and qualitative data analysis. The



acquired volumetric flow data are complex and need tailored approaches for less experienced domain experts such as physicians in terms of vector field and multiparameter analysis. Relevant to this thesis is a qualitative analysis that focuses on an efficient visual exploration of both the hemodynamic information and the enclosed vessel anatomy. These two kind information are correlated with each other and require an embedded visualization.

The following chapters elaborate these conclusions in more detail, present relevant investigations of cardiovascular research as well as discuss and propose visual exploration approaches.

## 3.1 INTRODUCTION

In recent years, the role of hemodynamics has become more and more relevant for the investigation and treatment planning of CVDs. Studies have shown that certain characteristics of hemodynamic information are indicators of disease prognosis and have an influence on the outcome of the disease. For example, abnormal hemodynamics in the aortic vessel may imply a congenital heart disease such as a BAV (see Sec. 2.2). Patients with a BAV demonstrate a nested helical aortic flow with an eccentric flow jet. This is assumed to be a relevant risk factor for aorta ectasia development [158]. Furthermore, it has been shown that hemodynamic characteristics influence the risk of rupture in cerebral aneurysms [63, 64]. In the case of multiple aneurysms, the decision arises as to which one should be treated first and what treatment option should be chosen. Each existing treatment option carries a risk of complication and the decision to treat an aneurysm has to be balanced against the risk of rupture. Thus, investigations of hemodynamic behavior are of great interest to optimize patient-specific treatment options and to support the decision process.

The term *hemodynamics* is derived from the Greek words for blood (*haima*) and power (*dynamis*). It describes the fluid mechanics of blood in the vessels depending on different conditions, such as the vessel geometry, vessel wall elasticity and the viscosity of the blood. Hemodynamic information comprises all *quantitative* and *qualitative parameters* that describe the blood flow behavior within the vessels and onto the vessel wall. Note, hemodynamics do not only refer to vessels but also to heart chambers, but for the scope of this thesis we mostly consider hemodynamics in blood flow vessels.

This chapter starts with an overview of relevant hemodynamic information, the clinical and biomedical research domains as major application areas and current data analysis methods (Sec. 3.2). As the data analysis relies on either measured or simulated flow information, we present necessary post-processing steps for measured flow datasets (Sec. 3.3) as well as data acquisition steps for simulated flow datasets (Sec. 3.4). Subsequently, relevant applications of hemodynamic information in the clinical research domain (Sec. 3.5) and the biomedical research domain (Sec. 3.6) are presented. For this thesis, we focus on simulated hemodynamics in the biomedical domain for the investigation of cerebral aneurysms. We also provide an overview of available software tools and frameworks to accomplish the data processing and analysis (Sec. 3.7) as well as some further related literature and recent progresses on this topic (Sec. 3.9). Finally, we derive important implications for the thesis and remaining chapters, respectively (Sec. 3.9).

### 3.2 HEMODYNAMIC INFORMATION AND APPLICATION AREAS

Hemodynamic information is complex and consists of several parameters, such as scalar values, vectors and flow structures, which can be spatial- and time-dependent. Some of them are relevant in general, some only for certain CVDs. Thus, this section provides an overview of important hemodynamic information, including a classification and introduction, based on reviews of the domain-specific literature. This literature denotes the individual kinds of information ambiguously as *parameter*, *feature*, *measure* or *characteristic*. For the sake of clarity, we use the term *parameter* for the remainder of the thesis.

All parameters can be classified as *quantitative* or *qualitative*. The list of parameters is not an exhaustive list of all hemodynamic information but the most relevant according to recent clinical and biomedical research reports. The overlap between the two classifications indicates that for some parameters a clear distinction is hard to make. For example, the assessment of flow complexity as a qualitative parameter can be made on the computation of certain vorticity measures as quantitative scalars. The final decision, however, as to whether the flow is simple or complex is currently made according to observations by the domain expert.

#### 3.2.1 Quantitative Parameters

Quantitative parameters are hemodynamic information that can be explicitly measured or computed by a formula description. Thus, they can be expressed with a scalar value, a vector or a tensor [188]. The following list introduces several of them including their notation for the remainder of the thesis. For a comprehensive overview of quantitative parameters we refer to Cebal et al. [64].

- **Velocity:** The most obvious and important quantitative parameter is the blood flow velocity  $\vec{v}$ . As mentioned in Section 2.5 the velocity comprises the direction of the flow along with its speed denoted in cm/s or m/s. The velocity as spatial- and time-dependent information represents the basis for all other quantitative and qualitative parameters. Thus, a reliable acquisition of the velocity field  $\mathbf{V}$  is crucial for a valid hemodynamic analysis.
- **Pressure:** The fluid pressure  $q$  is the kinetic energy per unit volume of a flowing fluid particle and often denoted in pascal (Pa). For incompressible fluids, which is assumed to be the case with blood, it is defined as:

$$q = \frac{1}{2} \rho \|\vec{v}\|^2, \quad (2)$$

with  $\rho$  as the constant fluid density and  $\|\vec{v}\|$  as the flow speed. Since the pressure depends on the flow speed, it is also a spatial- and time-dependent parameter.

- **WSS and MWSS:** The *wall shear stress* (WSS) is a spatial- and time-dependent scalar that represents a force tangential to the vessel wall caused by the flow-

ing blood along the wall. The WSS is based on the WSS vector  $\vec{\tau}_{wss}$ , which can be calculated as:

$$\vec{\tau}_{wss} = \mu \frac{\partial \vec{u}_t}{\partial \hat{n}}, \quad (3)$$

where  $\mu$  is the absolute viscosity of the blood (a measurement of the "thickness" or resistance of the blood),  $\vec{u}_t$  is the velocity tangential to the wall and  $\hat{n}$  is the normal to the wall. The WSS is then the magnitude of  $\vec{\tau}_{wss}$

$$WSS = \|\vec{\tau}_{wss}\|, \quad (4)$$

and denoted in Pa [240]. A related measure is the *maximum* WSS (MWSS) over each vessel surface point  $\mathbf{p}$  of a certain wall region  $A_{wall}$  and is calculated as:

$$MWSS = \max_{\mathbf{p} \in A_{wall}} \|\vec{\tau}_{wss}(\mathbf{p})\|. \quad (5)$$

As a consequence, the MWSS represents only a time-dependent scalar value and is spatially independent in terms of the local wall region  $A_{wall}$  [64].

- **OSI:** The *oscillatory shear index* (OSI) indicates flow disruption like crossing or reversing flow at the vessel wall over time [306]. More formally, the OSI describes the WSS vector acting in directions other than the direction of the temporal mean WSS vector and is calculated as:

$$OSI = \frac{1}{2} \left( 1 - \frac{\left\| \int_0^T \vec{\tau}_{wss} dt \right\|}{\int_0^T \|\vec{\tau}_{wss}\| dt} \right), \quad (6)$$

with  $T$  as the time for a cardiac cycle. Equation 6 represents the ratio between the magnitude of the time averaged WSS vector and the time-average of the WSS magnitude. Thus, the OSI is a dimensionless parameter and ranges from 0 to 0.5, indicating non-cyclic variation of the WSS vector and the 180° deflection of the WSS vector, respectively.

- **Volumetric flow rate:** The *volumetric flow rate*  $Q$  is a parameter that determines the amount of fluid volume passing through a given surface per unit time. Thus, it is a spatial- and time-dependent parameter and often denoted in  $\text{cm}^3/\text{s}$  or  $\text{m}^3/\text{s}$ . Formally, it is defined as:

$$Q = \|\vec{v}\| A \cos(\theta), \quad (7)$$

with  $\|\vec{v}\|$  as the flow speed,  $A$  as the surface area through which the volume passes, and  $\theta$  as the angle between the velocity vector  $\vec{v}$  and surface normal  $\hat{n}$ .

- **Regurgitant fraction:** The *regurgitant fraction*  $R_{frac}$  is the percentage of blood that flows back from one vessel section into another, e.g., from the pulmonary artery or aorta back into the corresponding ventricles or from the

ventricles into the atria. It is caused by an insufficient shuttering of the valves and may indicate a CHF (see Sec. 2.2). It is defined as:

$$R_{\text{frac}} = \frac{Q_b}{Q_f} 100\%, \quad (8)$$

with  $Q_b$  and  $Q_f$  as backward and forward volumetric flow rate, respectively.

- **Turnover time:** The *turnover time* (ToT) or *residence time* indicates the average amount of time a blood flow particle remains in a particular vessel region. The turnover time begins from the moment the particle enters the vessel region until the same particle leaves the region again. The definition of the ToT is as follows:

$$\text{ToT} = \frac{V_R}{Q_I}, \quad (9)$$

with  $V_R$  as the volume of the vessel region and  $Q_I$  as the inflow rate into the region. With respect to the vessel volume and the averaged inflow rate, the ToT is a spatial- and time-independent parameter and often denoted in seconds. Furthermore, it is used to quantify flow stasis, which can indicate a thrombus formation in a vessel region.

### 3.2.2 Qualitative Parameters

Qualitative hemodynamic parameters are used to describe certain blood flow patterns in the velocity field. In contrast to quantitative parameters, their investigation is based more on a visual flow inspection than on a mathematical definition. They provide a qualitative description of the velocity field in terms of direction, speed and interaction with the surrounding vessel wall. Often, they are used as a starting point for a deeper quantitative analysis using the aforementioned quantitative parameters. In the following, informal descriptions of relevant qualitative parameters are presented that can be found in recent reports by Cebal et al. [63], Markl et al. [222] and Chien et al. [75].

- **Laminar vs. turbulent flow:** A very basic flow parameter is the evaluation in terms of *laminar* or *turbulent* flow. The flow is assessed as laminar if the particles are flowing mostly parallel to each other and to the boundary wall without disruptions. Additionally, if the flow is around and along a common center axis *helical* flow occurs but this is still considered as laminar due to the regular and parallel blood flow layers of the particles. The flow is assessed as turbulent if it is irregular with randomly and rapidly fluctuating velocities as well as flow instabilities. Thereby, turbulent behavior depends mainly on the flow speed, its viscosity and the boundary geometry. The transition between laminar and turbulent flow can be described with the so called *Reynolds* number (Re). The Re number is a dimensionless quantity that is defined as the ratio between inertial forces to viscous forces [188]. In general, laminar flow occurs for low and turbulent flow for high Re numbers but there is no unique Re number that indicates a complete turbulent flow. For example, the transition interval between laminar and turbulent for a stationary flow

in an indefinitely long pipe is between 2300 and 4000 Re. For other flow and boundary conditions much larger Re numbers are required to establish turbulences. For blood flow in the human body, however, Re numbers between 200 and 400 occur in most cases. Thus, only laminar flow behavior is assumed in the context of human blood flow.

- **Vortices:** A vortex is a very fundamental flow structure in fluid dynamics and vector field analysis. However, no exact definition of vortices exists. In more general flow domains, a vortex is described as rotating or swirling motion in the flow field, where particles tend to curl back on themselves. Vortices are often associated with a slow flow speed relative to their surroundings. Moreover, even complex vortex structures exhibit still a laminar flow behavior.
- **Recirculation:** A *recirculation* occurs when flow from a forward stream flows back into a separation zone. For example, this happens beyond each heart valve in both ventricles. A recirculation may also indicate vortex structures.
- **Flow complexity:** The *complexity* of flow can be categorized into *simple* or *complex*, depending on the number of vortices. The flow complexity is considered as simple if only one recirculation or vortex structure occurs in a particular vessel region. If the flow exhibits flow separations or multiple vortex structures, it is seen as complex.
- **Flow stability:** The *flow stability* evaluates the persistence of certain flow patterns like vortex structures or flow separations during the cardiac cycle. A flow separation denotes the separation of flow from an adjacent wall. This tends to happen by virtue of the forward momentum of flow relative to a curving, irregular or discontinuous vessel boundary, e. g., flow that separates from the inner curvature of the distal aortic arch. The flow is considered as *stable* if these patterns do not move or change. In *unstable* flow, vortex structures or flow separations move, are created or destroyed during the cardiac cycle.
- **Inflow jet:** The *inflow jet* (also called *slipstream*) is a flow structure within a certain vessel region that consists of parallel inflow of a high speed compared to other parts in that region. The jet is evaluated as *concentrated* or *diffuse*, depending on its thickness and penetration depth into the vessel region.
- **Impingement zone:** With the presence of an inflow jet, an *impingement zone* on the vessel wall can occur. It is the region on the wall where the inflow jet is seen to impact the wall for the first time and changes its direction or disperses. The size of that region is either evaluated as *large* or *small* based on the ratio between the area of the impingement zone and the area of the relevant vessel wall.

### 3.2.3 Application Areas

The application of hemodynamic information can be mainly grouped into the *clinical research domain* and *biomedical research domain*. For the clinical domain, the

domain experts are mainly physicists and clinicians, such as cardiologists and radiologists. The domain experts in the biomedical domain are mostly engineering researchers, such as CFD simulation experts and computational scientists, as well as clinicians from the clinical domain. For some applications, both domains share the same type of domain experts, e. g., the investigation of measured vs. simulated flow in patient-specific vascular systems involves physicists, CFD engineers and clinicians.

In general, the clinical research domain relies on measured flow and the biomedical domain on simulated hemodynamic information. For both domains the acquired hemodynamic information is integrated into a similar workflow pipeline that consists of three main steps, as shown in Figure 10:

1. **Data acquisition:** The first step is the data acquisition itself that comprises either flow measuring or simulation, both with individual processing steps. The measured flow datasets require some *post-processing* including correction of image artifacts, vessel segmentation and surface reconstruction. The simulation of blood flow involves some *pre-processing*, such as vessel segmentation from the patient-specific image data, volume grid generation and modeling of the simulation. In general, the data acquisition of simulated flow data is more time-consuming and less semi-automatic than for measured flow datasets. Each pre-processing step strongly influences the subsequent step and the final simulation results.
2. **Data analysis:** Based on the obtained flow data, the data analysis follows and consists of a *quantitative* and *qualitative analysis*. The data analysis aims to answer several research questions depending on the application area. In the context of this thesis, the qualitative analysis is of main interest, in particular the visual exploration.
3. **Specification of hypotheses and tasks:** In most cases, the data analysis starts with an exploration phase of the hemodynamic information but potentially leads to hemodynamic indicators that may correlate with a CVD. Based on these indicators, particular *hypotheses* can be specified and validated by the data analysis on a broader range of datasets. In addition to hypotheses, specific *tasks* can be derived that are also accomplished by the data analysis. Tasks can result from confirmed hypotheses or inherently defined by the domain expert based on justifiable assumptions, e. g., the altering of the turnover time after a virtual treatment procedure in cerebral aneurysms since a long turnover time promotes thrombus formations. Hypotheses and tasks can also be utilized to validate the data acquisition step, e. g., validation of the corrected image artifacts in measured flow data or validation of the simulation model.

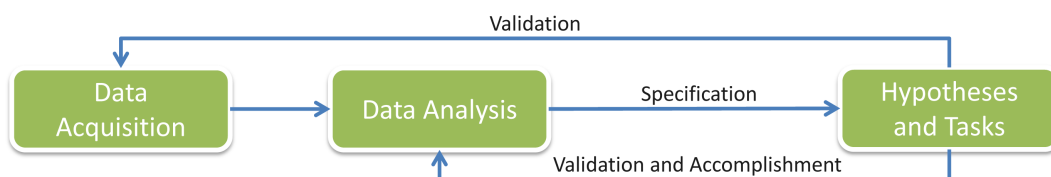


**Figure 10:** General workflow for the application of hemodynamic information in the clinical and biomedical research domain.

In the following, we provide an overview of both domains and present their leading research questions.

#### 3.2.3.1 Clinical Research Domain

The clinical research domain deals with the investigation of hemodynamics in a clinical environment but is not yet established in a clinical workflow. It focuses on the hemodynamics in healthy subjects and patients to identify specific flow behavior. The goal of the clinical research is to understand how abnormal flow may promote or worsen CVDs in certain vascular regions. Various research groups aim for this goal and are promoting the development of improved hemodynamic data acquisition, data analysis and the clinical acceptance of volumetric hemodynamic information in diagnosis and treatment planning. In order to accomplish these developments, the following leading research questions can be derived from the proposed works [221]:

**CD<sub>1</sub>:** What are the hemodynamics in healthy subjects?

**CD<sub>2</sub>:** What is the link between altered hemodynamics and CVDs in patients?

**CD<sub>3</sub>:** To what extent do the hemodynamics change after a treatment procedure is performed?

An important tool for answering these questions is the utilization of PC-MRI flow measurements, especially 4D PC-MRI (see Sec. 2.5), in healthy subjects and patients. Substantial developments in 4D PC-MRI offer the ability to measure and to visualize the volumetric, spatiotemporal behavior of complex blood flow patterns in a clinical environment. These developments provide the potential to obtain comprehensive *in vivo* information on normal and pathologically altered hemodynamics in different vascular regions and particular CVDs. Thus, 4D PC-MRI is seen as a valuable complement to 2D PC-MRI measurements and colored Doppler US, which are established flow measuring modalities in clinical diagnosis and follow-up studies.

#### 3.2.3.2 Biomedical Research Domain

With increasing developments in accurate and non-invasive cardiovascular imaging, the capabilities to diagnose and treat CVDs have been significantly improved. Progress in the aforementioned *in vivo* 4D PC-MRI flow measurement facilitates the clinical understanding how hemodynamic characteristics have changed in the presence of certain CVDs or after treatment procedures and what influence they might have on the CVD development. However, there is still scarce knowledge about how the disease genesis, evolution and outcome are influenced by the hemodynamics and vice versa. Furthermore, techniques and methods available in the clinical research domain are not able to reliably predict the flow behavior altered by means of different treatment options.

For these applications, the biomedical research domain comes into play and aims for two research goals. First, it focuses on a more detailed view of how hemodynamic parameters influence the initiation, development and outcome of certain CVDs. This ranges from patient-specific fluid modeling and risk assessment, to identifying new relevant hemodynamic parameters and investigations into how



hemodynamic forces affect the endothelial cells of the vessel wall. These cells play an important role in the development of CVDs [81]. Second, domain experts are interested in the evaluation of new and advanced treatment options with respect to their outcome and the altered hemodynamics. For example, they are aiming for a patient-specific flow diverter configuration that occludes a cerebral aneurysm completely without coil placements (see Sec. 2.3.2).

The biomedical research domain is placed in a *preclinical environment* and is based more on basic research than on clinical applications. Biomedical engineers and computer scientists in this domain test hypotheses and consider their current investigations to be still in the exploration phase [59]. Due to the complexity of the mechanisms that lead to the development of a certain CVD, they utilize patient-specific, image-based numerical models to assess CVDs and to support treatment decisions.

Advanced CFD *simulations* are mainly used here since they are seen as a promising tool for revealing pathophysiologies (biological processes that lead to abnormal conditions) and for investigating the effect of different factors independently. The effectiveness of CFD simulations has already been proven in other research domains such as aircraft design, logistics and weather forecasting. Increased computing power has made it possible to tailor these simulations towards the conditions found in a particular subject or patient [180]. Thus, it supports very well the concept of *personalized medicine* along with other advances in many medical research areas. The division of cardiovascular diseases at the National Heart, Lung and Blood Institute states in their strategic plan [244]:

*"Personalized medicine uses enabling technologies, along with clinical and environmental information about an individual, to tailor prevention, management, or treatment of a disease or condition for that individual."*

Among these technologies, CFD simulations promise to provide additional information that may be helpful for personalized risk assessment and in therapeutic decision making. At the same time, clinicians raise important critical points regarding the potential utility of CFD [59, 178, 180]. The main criticisms are:

- CFD simulations are based on assumptions that might make results questionable.
- A large number of hemodynamic parameters have arisen that are confusing or conflicting.
- The investigations are performed on a small number of cases at single centers with single population data, which are still too small to yield strong statistical results or make the results entirely objective.

These observations are still a current problem and biomedical researchers are aware of this. However, to make the computational problem tractable, approximations and assumptions are necessary as a trade-off between accuracy, cost and feasibility. It is important to understand the effect of the approximations on the resulting hemodynamic behavior, which can then be evaluated with *in vivo* or in *in vitro* observations. CFD modeling is well-suited for this kind of analysis since individual factors can be explored independently. The confusing and conflicting

findings are mainly a result of non-standardized modeling approaches and investigations of hypotheses. Thus, the observed divergences are unavoidable and often necessary in this domain.

Biomedical researchers explore different points of view and depths of a problem, which confirms existent findings or, alternatively, results in new and different findings. In order to provide clinically pertinent information that will help improve clinical practice, these inconsistent results must be resolved. To accomplish this goal, more studies on large multicenter and multi-population datasets as well as unified modeling approaches are necessary. Furthermore, the CFD simulation has to be integrated into the clinical workflow accompanied with computational tools to analyze the resulting flow data. This includes tailored qualitative and quantitative analysis methods that have to be user-friendly and efficient. Ideally, the CFD simulation and analysis should be integrated into clinical workstations similar to the preliminary implementations in some MRI scanners for the analysis of measured flow data [20].

In order to summarize the two research goals at the beginning and the purpose of patient-specific hemodynamic modeling, the following leading research questions can be derived:

- BD<sub>1</sub>:** Which hemodynamic models are reliable for predicting patient-specific flow behavior according to findings in clinical data?
- BD<sub>2</sub>:** What are the correlations between certain hemodynamic parameters and the underlying histological mechanisms of CVDs?
- BD<sub>3</sub>:** What are the correlations between certain hemodynamic parameters and the outcome of CVDs?
- BD<sub>4</sub>:** Is the modeling of patient-specific hemodynamics capable of supporting the concept of *personalized medicine*, e. g., virtual treatment planning?

#### 3.2.4 Data Analysis

The complex nature of measured and simulated flow data (volumetric and unsteady) and the surrounding anatomical context require a qualitative and quantitative analysis to obtain pertinent clinical information. The review of domain-specific literature reveals that qualitative analysis by means of a visual exploration is the most prominent way to get insights into the individual flow behavior. Quantitative analysis complements the visual exploration by providing measurements of quantitative parameters, such as flow rates, peak flow speeds and regurgitant fractions.

In the following, an overview of the most relevant methods for both analysis types is given. In Section 3.7, we present and review some existent software systems and frameworks that have been developed for different processing and analysis steps in the medical and biomedical research applications. They incorporate some of the subsequent qualitative and quantitative methods. An appropriate understanding of how these methods are used to investigate the aforementioned research questions is necessary to derive implications for this thesis, in particular for visual exploration.

### 3.2.4.1 Qualitative Analysis

Qualitative analysis mostly utilizes *multi-planar reformations* (MPR) and *cut planes*, height fields as well as established volume and flow visualization techniques [63, 221, 305, 334]. An MPR is a common image reconstruction method for volume datasets. It is a planar cross-section that is either aligned freely or according to the three standard views sagittal, coronal or transversal. With respect to the 4D PC-MRI datasets, the MPR are applied to the magnitude and phase images. Cut planes (also called probe planes) are similar to MPRs but refer to cross-sections in numerical grids of CFD simulations. MPRs and cut planes resample local velocity information based on a user-defined density of regularly distributed in-plane sample points. Typically, the resampled information is color-coded according to the flow speed or individual components of the velocity vector. In order to provide an anatomical context during the alignment of the MPR or cut plane, a semitransparent volume rendering of the magnitude images or vessel surface rendering is often utilized.

In Figure 11a, an MPR example by Sørensen et al. [305] is shown for a freely reformatted slice (left) with two time points of in-plane flow along the up-down axis. An example of cut planes is presented in Figure 11c (top) by Karmonik et al. [180] where a patient-specific simulation of the hemodynamics in an aortic dissection was performed. MPR and cut plane are color-coded according to the flow speed whereby the direction of resampled measured flow is depicted in a red-to-blue color scheme comparable to the color coding of color Doppler US. Spatiotemporal quantitative parameters, such as flow speed or WSS magnitude are visualized mostly by isosurface renderings and surface color coding as presented in Figure 11c (bottom). The WSS magnitude for the peak systole is visualized on the vessel surface with high values for the true lumen compared to the false lumen.

The flow visualization techniques primarily include *2D/3D vector glyphs*, *streamlines* and *pathlines*. Similar to the MPR and cut plane visualizations, these geometric representations are often color-coded according to the local flow speed and are utilized to assess the qualitative flow parameters, such as vorticity, flow complexity and inflow jets. To provide an anatomical context, they are embedded in a standard orthogonal view plane of the anatomical image data, in the MPR or cut plane or in the surface rendering of vessel geometry. Vector glyphs are a direct visualization method to convey the velocity values at each voxel with an arrow-like primitive. They are oriented and scaled according to the underlying flow direction and speed. To avoid visual clutter and occlusion, they are often restricted to the MPR or cut plane as shown in Figure 11b from Unterhinninghofen et al. [334]. The cone primitives depict a vortex in the left ventricle at mid-diastole.

Streamlines and pathlines are *integral lines* that need seeding locations as a starting point for the integration through the velocity field. These seeding locations are placed either by user-defined emitter planes orthogonal to the vessel centerline or freely placed in the vessel region. Streamlines are lines through the velocity vector field that are tangent to the velocity vectors everywhere at a particular point in time. However, velocity fields in vessels are time-varying and streamlines do not represent the unsteady flow of particles through the vessel. Pathlines are lines through an unsteady vector field that are tangent to the velocity vectors every-

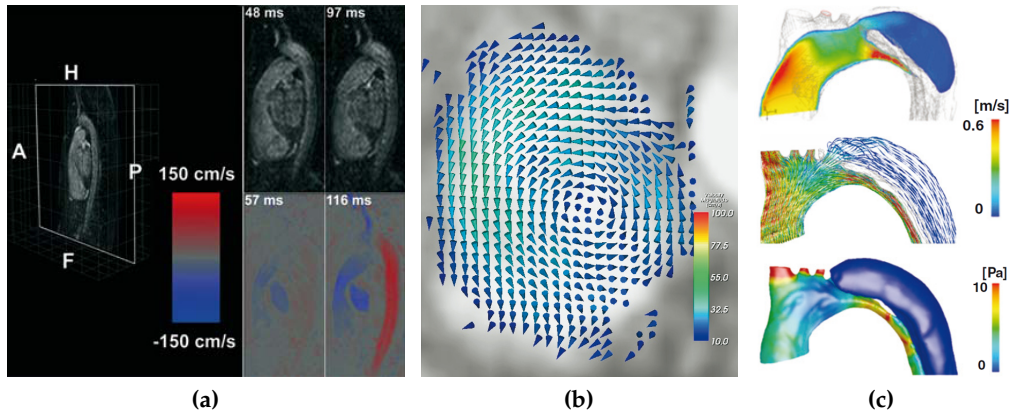


**Figure 11:** Standard visual exploration techniques for a qualitative analysis of measured and simulated flow datasets: (a) an MPR view of two time points of an aortic flow dataset that are color-coded according to flow speed in the up-down direction, (b) color-coded arrow glyph representation aligned to flow direction in an MPR view as well as (c) color-coded cross-section (top), pathlines (middle) and surface coloring (bottom) in a simulated aortic flow dataset. (Image (a) reprinted from Sørensen et al. [305] © Springer Science and Business Media 2005 with kind permission from Springer Science and Business Media, (b) reprinted from Unterhinninghofen et al. [334] © Elsevier 2008 with kind permission from Elsevier, (c) reprinted from Karmonik et al. [180] with kind permission from Houston Methodist.)

where at different points in time. These points correspond to the position of the particles as they move through the velocity field over time. If the velocity field is , streamlines and pathlines are identical. A more detailed description of these standard flow visualization techniques will be presented in Section 4.2.2. An example of an embedded pathline visualization is given in Figure 11c (middle) for the aortic dissection case. Laminar flow is visible in the aortic lumen before the entrance tear and in the true aortic lumen. In contrast, flow is disturbed immediately after the entrance tear in the false lumen, most likely due to flow deceleration.

#### 3.2.4.2 Quantitative Analysis

Quantitative analysis focuses on the investigation of parameters that can be directly measured, simulated or estimated by their formal definition, i.e., quantitative parameters. The analysis comprises *statistical methods* as well as *local* and *regional quantification*. Standard statistical methods are, for example, the Student *t* test, scatter or Bland-Altman plots and bar charts to estimate statistical significance and to derive correlations between different parameters [104]. Local and regional quantification restricts the analysis to a region of interest and often require a (time-consuming) manual definition of these regions.

*Local quantification* relies on one or multiple vessel cross-sections that are utilized to obtain several profiles, e.g., volumetric flow rates and speed values, over the cardiac cycle. For 4D PC-MRI, these cross-sections correspond to MPRs with user-defined 2D contours around the inner border of the vessel of interest and are applied to the magnitude or phase image datasets. As an example, Figure 12 shows the application of a volumetric flow volume profile for a patient with an aortic insufficiency caused by a valve malformation [69]. In Figure 12a the slice of interest

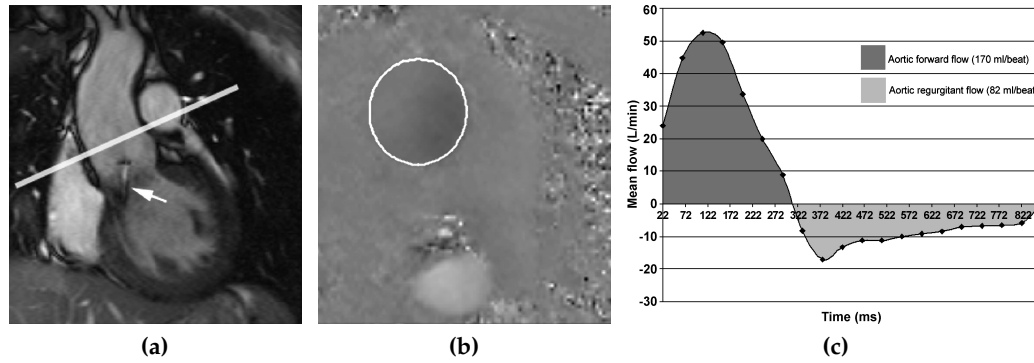


**Figure 12:** Quantitative flow analysis of a patient with aortic insufficiency: (a) indication of an MPR (white line) in the magnitude image, (b) the corresponding MPR view of the phase image with a user-defined contour around the inner border of the aorta, (c) mean volumetric flow rate profile over a cardiac cycle shows significant regurgitant flow volume. (Images reprinted from Chai et al. [69] © Informa Healthcare 2005. Reproduced with kind permission of Informa Healthcare.)

is indicated in the magnitude image dataset and the corresponding MPR view of the phase image together with the user-defined vessel wall contour of the aorta is shown in Figure 12b. This contour is adapted on all corresponding phase images throughout the cardiac cycle to generate the flow profile in Figure 12c. The dark shaded area above the x-axis represents the forward flow volume and the light shaded area represents the regurgitant flow volume. The regurgitant fraction is about 48%, which indicates a severe aortic valve regurgitation.

To identify correlations between quantitative and qualitative flow parameters, both types of analysis are sometimes combined. This is illustrated in Figure 13a for a patient with an ascending aortic aneurysm where the combined analysis is used to evaluate the impact of altered flow patterns on the volumetric flow volume and on WSS [222]. For the peak systole, the velocity field is depicted with color-coded streamlines seeded at two emitter planes (black lines). The streamlines are embedded in the generated vessel surface as the anatomical context. Next to each emitter plane, a corresponding polar plot of the WSS distribution and volumetric flow profile is shown. The polar plot view depicts the cross-section of an emitter plane with a circular shape subdivided into 16 segments. The segments define the anatomical locations (left, right, inner and outer curvature) of the WSS distribution derived from the 2D contour.

*Regional quantification* relies on flow analysis in decomposed vessel or chamber sections, e. g., the separation of the aneurysm sac from the parent vessel to compute the turnover time. Pathlines are often used since it is assumed that every pathline represents the movement of the amount of blood defined by the emitter density. In the work of Eriksson et al. [99], this pathline-based quantification is applied to measure intraventricular flow distribution and flow volume of the left ventricle in a healthy subject, shown in Figure 13b and Figure 13c. First, the lumen of the left ventricle was segmented at the times of systole and diastole. Then, pathlines were emitted at each voxel in the segmented lumen starting from the systolic contraction. Each pathline was traced in the forward and backward direction until the diastolic relaxation was reached. The segmented lumen at the diastole was utilized to determine if and where the pathlines left the ventricle. Based on



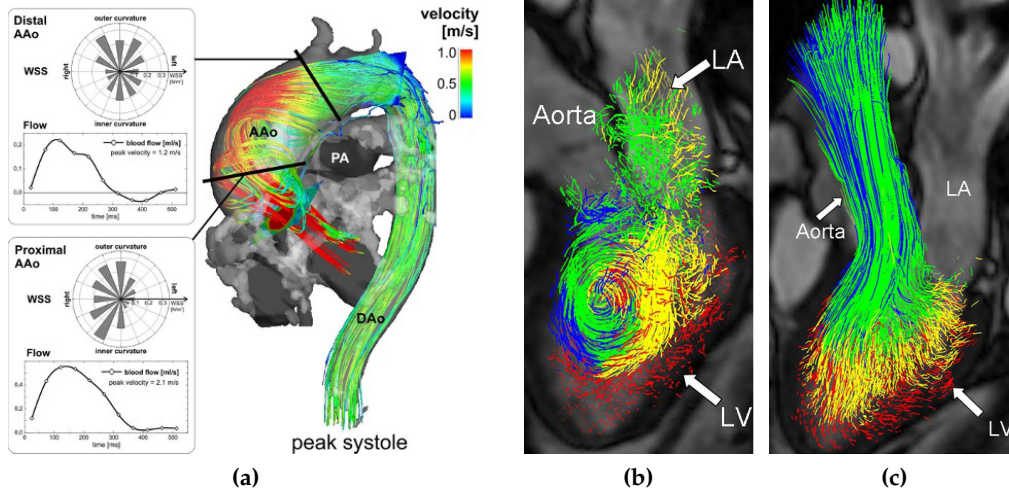


**Figure 13:** A combination of qualitative and local quantitative data analysis of measured blood flow at peak systole is shown in (a). The flow behavior is depicted with color-coded streamlines and the two polar plots show the quantitative WSS distribution for a patient with an aortic aneurysm. In (b) and (c) an example of regional quantifications to measure intraventricular flow transit is presented. The flow is decomposed into "direct flow" (green), "retained inflow" (yellow), "delayed ejection flow" (blue) and "residual volume" (red) at diastole (b) and systole (c). (Image (a) reprinted from Markl et al. [222], (b) and (c) reprinted from Eriksson et al. [99] with © Creative Commons / CC-BY-2.0.)

this information, the pathlines were automatically separated into four different components of flow:

- **direct blood flow** that enters the ventricle during diastole and leaves it during systole, entering the aorta,
- **retained blood inflow** that enters the ventricle during diastole but does not leave it during systole,
- **delayed ejection blood flow** that starts and resides inside the ventricle during diastole and leaves it during systole and
- **residual blood volume** that remains within the ventricle for at least two cardiac cycles.

Finally, the blood volumes for every component were calculated by multiplying the number of corresponding pathlines by the volume of the voxel where each pathline was emitted.

### 3.3 POST-PROCESSING OF 4D PC-MRI DATASETS

The acquisition of 4D PC-MRI datasets offers domain experts in the clinical domain the possibility to investigate *in vivo* flow in terms of normal and abnormal flow behavior. However, before a reliable data analysis can be conducted, the acquired 4D PC-MRI flow datasets need to be post-processed. In this section, we describe the major processing steps, which are summarized in Figure 14. Based on the phase and magnitude image datasets, the processing steps involves the

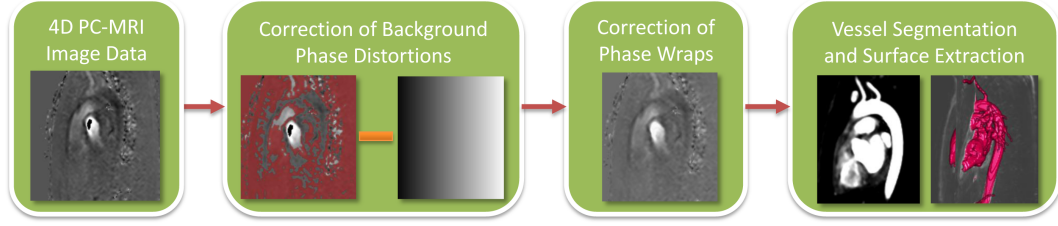


**Figure 14:** Overview about the post-processing pipeline of 4D PC-MRI image data: (a) phase and magnitude image data with artifacts, (b) correction of background phase distortions by subtracting fit planes, (c) correction of phase wraps and (d) vessel segmentation and surface extraction for masking and visualization, respectively.

correction of image artifacts (Sec. 3.3.1) and the vessel segmentation (Sec. 3.3.2). The correction of image artifacts focuses on the reduction of background phase distortions and phase wraps. The subsequent vessel segmentation can be used for static tissue masking and for vessel surface reconstruction as geometrical context visualization.

### 3.3.1 Correction of Image Artifacts

In general, the measured 4D PC-MRI flow datasets consist of three magnitude and phase image datasets, one magnitude and phase image dataset for each direction. Depending on the MRI scanner, the magnitude images may also be combined as one magnitude image dataset. The phase images exhibit certain artifacts like background phase distortions, phase wraps and noise (see Sec. 2.5.2). For a reliable flow analysis, these artifacts have to be corrected and minimized. In addition to the artifact reduction, the noisy flow information of the surrounding (static) tissue should be excluded from the analysis to reduce visual clutter and error-prone quantifications. This requires a segmentation of the vessel lumen that masks the vessel from its background. The segmentation mask can also be utilized later to define a vessel volume or a surface rendering as an anatomical context visualization. In the following, we describe these processing steps.

#### 3.3.1.1 Correction of Background Phase Distortions

The first step consists of the correction of the phase offset error introduced by eddy currents and concomitant gradient terms. This offset distorts the true velocity component at a pixel position  $(x, y)$  for a given time step  $t_i$  in each of the three acquired phase image planes. This error can be corrected by fitting a higher polynomial surface through the time average of stationary tissue in the phase images and subtracting this surface from all phase images [201]. This approach is based on several observations. First, the measured velocity component  $\vec{v}(x, y, t_i)$  is an additive combination of the true velocity component  $\vec{v}_{\text{true}}(x, y, t_i)$ , the corresponding phase offset error  $\vec{v}_{\text{off}}(x, y, t_i)$ , and a zero-means noise  $\vec{v}_{\text{noise}}(x, y, t_i)$ , formally described as:

$$\vec{v}(x, y, t_i) = \vec{v}_{\text{true}}(x, y, t_i) + \vec{v}_{\text{off}}(x, y) + \vec{v}_{\text{noise}}(x, y, t_i). \quad (10)$$

Second,  $\vec{v}_{\text{true}}(x, y, t_i)$  equals to zero for stationary tissue (see Sec. 2.5.1). Thus, if the phase error is considered as constant while measuring, it can be estimated from the corresponding temporally averaged velocity phase images  $\vec{v}_{\text{stat}}(x, y, t_i)$ :

$$\vec{v}_{\text{off}}(x, y) = \frac{1}{n} \sum_{i=1}^n \vec{v}_{\text{stat}}(x, y, t_i), \quad (11)$$

with  $n$  as the number of acquired time steps. Third, it has been shown that the spatial distribution of this error has at least a quadratic order. This distribution can be approximated by fitting a two-dimensional quadratic surface through the computed phase offset error pixels in stationary tissue. By subtracting the fitted surface from the corresponding phase image, the phase offset error is corrected.

For the computation of Equation 11 the separation of stationary from non-stationary pixels is necessary. This is performed by analyzing the standard deviation  $\sigma(x, y)$  at each pixel, which equals to:

$$\sigma(x, y) = \sqrt{\frac{1}{n-1} \sum_{i=1}^n (\vec{v}(x, y, t_i) - \vec{v}_{\text{avg}}(x, y))^2}, \quad (12)$$

with  $\vec{v}_{\text{avg}}(x, y)$  as the time average of  $\vec{v}(x, y, t_i)$ . Since stationary tissue exhibits no or little velocity variation, pixels are identified as stationary if their  $\sigma(x, y)$  is below a certain user-defined threshold value. Lankhaar et al. [201] estimated the 25% percentile of all  $\sigma(x, y)$  as an appropriate value. However, depending on the dataset, this value should be adapted properly to avoid the selection of non-stationary pixels.

### 3.3.1.2 Correction of Phase Wraps

In the second step, phase wraps are corrected, which occur in cases of velocity aliasing when the measured speed value exceeds the adjusted  $v_{\text{ENC}}$  value. Most commonly, these artifacts are detected and corrected by iterative approaches, which investigate the local neighborhood around a pixel. A well established method is presented by Díaz et al. [89], who propose a *reliability measure* based on the local neighborhood. For each pixel position  $(x, y)$  and time step  $t_i$  in a particular phase image, the reliability value  $R(x, y, t_i)$  is defined as:

$$R(x, y, t_i) = \frac{1}{D(x, y, t_i)}. \quad (13)$$

Here,  $D(x, y, t_i)$  is the second derivative at the current pixel and can be calculated by a  $3 \times 3$  convolution kernel:

$$D(x, y, t_i) = \sqrt{H^2(x, y, t_i) + V^2(x, y, t_i) + D_1^2(x, y, t_i) + D_2^2(x, y, t_i)}$$

with



$$\begin{aligned}
H(x, y, t_i) &= \vec{v}(x+1, y, t_i) - 2\vec{v}(x, y, t_i) + \vec{v}(x-1, y, t_i) \\
V(x, y, t_i) &= \vec{v}(x, y+1, t_i) - 2\vec{v}(x, y, t_i) + \vec{v}(x, y-1, t_i) \\
D_1(x, y, t_i) &= \vec{v}(x+1, y+1, t_i) - 2\vec{v}(x, y, t_i) + \vec{v}(x-1, y-1, t_i) \\
D_2(x, y, t_i) &= \vec{v}(x+1, y-1, t_i) - 2\vec{v}(x, y, t_i) + \vec{v}(x-1, y+1, t_i).
\end{aligned}$$

The value  $R(x, y, t_i)$  is a measurement of how likely the current velocity value at  $(x, y, t_i)$  represents a phase wrap. The lower the change of neighboring velocity values, the more reliable the current velocity value is. A phase wrap  $\vec{v}_{\text{wrap}}(x, y, t_i)$  is detected if  $R(x, y, t_i)$  is below a user-defined threshold  $\epsilon_{\text{rel}}$  and is unwrapped according to Hennemuth et al. [152] with:

$$\vec{v}(x, y, t_i) = \vec{v}_{\text{wrap}}(x, y, t_i) + 2 \text{ vENC} \frac{\vec{v}_{\text{wrap}}(x, y, t_i)}{|\vec{v}_{\text{wrap}}(x, y, t_i)|}. \quad (14)$$

This unwrapping procedure is repeated until a user-defined number of iterations is reached or all  $R(x, y, t_i)$  values are above  $\epsilon_{\text{rel}}$ .

### 3.3.1.3 Reduction of Noise

In the next step, random noise is identified and reduced. Noise is mainly introduced due to a large vENC value (see Sec. 2.5.2), regions of air and limited scanner sensitivity. In addition to standard image processing methods like *median filtering*, other approaches exist to reduce this kind of noise. In Bock et al. [27] noisy regions are removed by thresholding low signal intensity values in the magnitude images. Regions which are below 10% of the maximum value are selected and excluded from the phase images. Another method is proposed by Walker et al. [350], who identify noisy regions in phase images according to large standard deviations (see Eq. 12).

For each velocity component  $v_x$ ,  $v_y$  and  $v_z$ , a standard deviation image  $\sigma(x, y, v_x)$ ,  $\sigma(x, y, v_y)$  and  $\sigma(x, y, v_z)$ , respectively, is computed. Based on these images, three masking images  $\vec{v}_{\text{mask}}(x, y, v_x)$ ,  $\vec{v}_{\text{mask}}(x, y, v_y)$  and  $\vec{v}_{\text{mask}}(x, y, v_z)$  are derived with pixel values of 1's if the corresponding standard deviation value exceeds a user-defined threshold value and 0's otherwise. The three masking images are summed up as a final noise masking image  $\vec{v}_{\text{noise}}(x, y)$  with

$$\vec{v}_{\text{noise}}(x, y) = \vec{v}_{\text{mask}}(x, y, v_x) + \vec{v}_{\text{mask}}(x, y, v_y) + \vec{v}_{\text{mask}}(x, y, v_z). \quad (15)$$

The noise masking image is used to cancel out noise regions from the phase images as follows:

$$\vec{v}(x, y, t_i) = \begin{cases} \vec{v}(x, y, t_i) & , \text{ if } \vec{v}_{\text{noise}}(x, y) < 3 \\ 0 & , \text{ otherwise.} \end{cases} \quad (16)$$

Thereby, the phase image values in  $\vec{v}(x, y, t_i)$  correspond to the current post-processed values, i. e., after the correction of phase errors and phase wraps.

### 3.3.2 Vessel Segmentation and Surface Reconstruction

The last image processing step consists of the vessel lumen segmentation for excluding flow information outside the vessel and for additional anatomical context visualizations by means of volume or surface rendering. Independent of the utilized segmentation method, a well defined contrast between vessel lumen and background is necessary. In general, this can be accomplished by computing either a *time-averaged phase contrast MRA* (PC-MRA) or a *temporal maximum intensity projection image* (TMIP). The PC-MRA image  $I_{PC-MRA}(x, y, z)$  was proposed by Bock et al. [27] and is calculated from the magnitude image  $v_{mag}(x, y, z, t_i)$  as well as from the post-processed phase image  $\vec{v}(x, y, z, t_i)$  by:

$$I_{PC-MRA}(x, y, z) = \frac{1}{n} \sum_{i=1}^n \left( v_{mag}(x, y, z, t_i)^2 \sum_{j=1,2,3} (\vec{v}(x, y, z, t_i)^2)_j \right), \quad (17)$$

with  $(x, y, z)$  as the spatial location in the corresponding image and  $t_i$  as the measured time step within the cardiac cycle out of a total number of  $n$  time steps. The TMIP image  $I_{TMIP}(x, y, z)$  was introduced by Van Pelt et al. [337] and relies solely on the phase image. It is computed by determining the maximum speed value at each voxel position over each time step  $t_i$  of the cardiac cycle. Formally, this can be expressed as:

$$I_{TMIP}(x, y, z) = \max(\|\vec{v}(x, y, z, t_i)\|), \text{ for } i \in [1, n]. \quad (18)$$

In practice, we noticed no considerable difference between the PC-MRA and TMIP image because both approaches utilize a similar computation scheme to identify the maximum value at each voxel. Based on the image data, they represent the maximum vessel lumen extent over the cardiac cycle. The PC-MRA image is computationally more expensive compared to the TMIP image but tends to be more robust in terms of outliers due to the temporal averaging. Additionally, two other observations were made.

First, the enhanced vessel-to-background contrast of the PC-MRA and TMIP image is considerably higher for vessels near to the heart, e. g., the aorta, and almost similar for more distant vessels, e. g., cerebral vessels, compared to the original magnitude image. This results from higher peak flow speed values near the heart during the systole. The second observation relies on anatomical vessel movements during the cardiac cycle. The PC-MRA and TMIP images are both static, which also results later in a static segmentation mask and vessel anatomy. However, for vessels near the heart the anatomical movement can be strong compared to distant vessels. Since both images represent the maximum vessel extent, this may lead to an error-prone analysis during the diastole. In this relaxation phase, the vessel diameter becomes smaller and more noisy flow information at the vessel border influences the qualitative and quantification analysis, e. g., distracting integral lines or erroneous flow rate estimations. This has to be considered during the user-defined 2D contour definition for the local quantification procedure (see Sec. 3.2.4).

Note, the computation of a PC-MRA or TMIP image is not mandatory, since for some PC-MRI acquisitions, a prior TOF-MRA or CTA imaging is performed, which

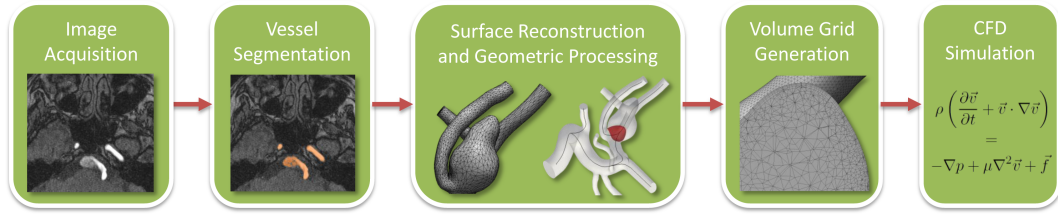


**Figure 15:** General workflow pipeline to obtain simulated and patient-specific hemodynamic information in the biomedical research domain.

can also be used as input for the segmentation and masking processes. However, due to different acquisition times as well as subject and respiratory movements, small spatial offsets can occur between anatomical and 4D PC-MRI datasets. Typically, this requires an additional non-rigid registration process.

Based on the PC-MRA or TMIP image, the vessel segmentation is performed. Because of the high vessel-to-background contrast in these images, a standard region growing or interactive watershed transformation is used to segment the vessels [142, 152]. In order to generate the vessel geometry, the Marching Cubes algorithm [214] is applied either directly to the contrast-enhanced images [337] or to the resulting segmentation mask. Depending on the image quality and vessel geometry, advanced segmentation and geometry processing may be necessary to correct the influence of noise and the partial volume effect as well as to decompose vessel sections for visualization purposes, e. g., to hide certain vessel structures. We refer to the data acquisition pipeline for simulated flow data in Section 3.4 for a more detailed discussion of these processing steps.

### 3.4 DATA ACQUISITION FOR SIMULATED HEMODYNAMICS

In Section 3.2.3 we have introduced the potentials and challenges of simulated hemodynamics in the biomedical research domain regarding clinically relevant information for the initiation, development and treatment of CVDs. In order to obtain patient-specific and simulated flow information, a workflow pipeline of five processing steps is necessary, as shown in Figure 15:

1. Patient-specific **image acquisition** of the vascular system of interest.
2. Reliable **vessel segmentation** of all necessary vascular sections.
3. **Vessel surface reconstruction** and its **geometric processing** to obtain high-quality surface meshes and anatomical landmarks.
4. **Volume grid generation** based on a surface mesh to establish a numerical grid for the simulation.
5. **CFD simulation** by incorporating boundary conditions and an approximated blood flow simulation model.

Depending on the anatomical application and vascular image data quality, each step can be more or less complex and time-consuming. Due to the high variation of vessel and CVD morphology among healthy subjects and patients, a completely

automatic approach is currently not feasible. Thus, the process steps are accomplished by the operator, i. e., the domain expert, and by (semi-)automatic computational methods, which make the processing non trivial, often time-consuming and operator-dependent.

For a reliable and streamlined data acquisition, it is crucial that the aforementioned steps are integrated into an efficient workflow with minimized operator-intensive tasks, high level decisions by the operator and reduced parameter settings [8]. With respect to the need for large-scale studies, robustness, reproducibility and efficiency are required as well as flexibility for other anatomical contexts. It is a challenging task to fulfill these requirements and is not yet resolved in this domain. In the following, we describe each pipeline step and its implementation based on several works that were proposed by different research groups [8, 12, 61, 311, 321]. Here we also incorporate practical experiences from our own research and cooperation partners including clinicians and biomedical engineers.

#### 3.4.1 Image Acquisition

Subject- or patient-specific modeling requires the individual spatial morphology of the vessel and CVD anatomy. Thus, volumetric images are acquired by vascular image modalities such as 3D-RA, CTA or TOF-MRA (see Sec. 2.4). These images are often obtained in combination with a CVD diagnosis in the clinical routine. For the subsequent processing steps, a well-defined vessel lumen boundary in the image data is necessary. However, several image artifacts may occur due to the physical conditions of the subject or patient, the anatomical region and current CVD as well as due to the limited spatiotemporal resolution of the image acquisition modality. This primarily includes motion artifacts, inhomogeneous intensity distribution in the vessel lumen due to contrast bolus dynamics, so-called *flushing*, beam hardening artifacts and blending due to the partial volume effect.

Two examples of common artifacts for cerebral aneurysms are demonstrated in Figure 16 obtained with CTA imaging. In Figure 16a blending artifacts between the parent vessel and the aneurysm caused by the partial volume effect can be seen. This is highlighted in Figure 16b of the corresponding direct volume rendering visualization (outlined arrow). A flushing artifact is shown in Figure 16c for a giant aneurysm. As a consequence, a low defined vessel lumen boundary occurs, as depicted in Figure 16d (filled arrow) together with additional blending artifacts at two parent vessels (outlined arrow). These artifacts have a strong influence on the subsequent segmentation and surface reconstruction. Moreover, the final simulation is based on the surface boundary and it is shown that the simulated hemodynamics have a strong dependency on this spatial boundary [318].

In addition to the morphological image data, PC-MRI flow measuring can be performed to serve as boundary conditions for the simulation or for comparison purposes. The acquisition capability depends on the physical condition of the patient and the available technical equipment in the clinical or research settings. If it is feasible, 2D or 4D PC-MRI scans are utilized to derive velocity information at specific vessel cross-sections or from a 3D spatial volume.

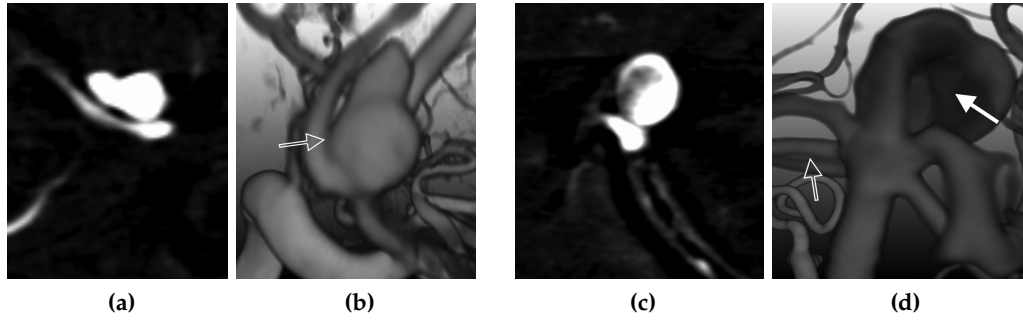


**Figure 16:** Two examples of common image artifacts for cerebral aneurysms obtained with CTA. In (a) the partial volume effect leads to blending artifacts between the parent vessel and the aneurysm highlighted in (b, outlined arrow) of the volume rendering visualization. In (c) a flushing artifact of a giant aneurysm is shown, which results in a vessel lumen boundary with low definition as presented in (d, filled arrow) of the corresponding volume rendering. Additionally, blending artifacts are shown (outlined arrow).

### 3.4.2 Vessel Segmentation

Based on the acquired image data, the lumen of the relevant vessel sections has to be segmented. The segmentation is used to reconstruct the geometry of the vascular segments, which will later define the computation domain for the CFD simulation. In order to get reliable subject-specific simulation results, an accurate geometric model of the underlying anatomical vessel section is a key requirement. It is known that the flow has a strong relation and is highly sensitive to the enclosing geometry [318]. Thus, the segmentation process is one of the most important steps in patient-specific modeling. The challenges of the segmentation process are the image artifacts described in the previous section that make it difficult to separate vessel lumen and background.

Various pieces of research work exist for vascular segmentation. Depending on the modality of the image data, the anatomical vessel region and the field of application, different approaches and schemes exist. Since it is beyond the scope of the thesis to provide an overview of all relevant methods, we only present those that are relevant in the current domain. For the interested reader we refer to Lesage et al. [209] for a state-of-the-art review on vascular segmentation.

#### 3.4.2.1 Intensity-Based Methods

The simplest way to segment the vessel lumen is to use the absolute image intensity values. The most utilized method is *thresholding* here, which classifies all voxels as vessel lumen that are greater than a global user-defined threshold. Approaches also exist that determine the threshold automatically, e.g., based on a histogram analysis or known gray value distributions. Especially for CTA image datasets, the correlation between HU values and tissue type can be exploited. It is often associated with a trial-and-error process whereby the threshold is increased or decreased until a plausible result is achieved.

Although it is a simple and fast approach, thresholding has some disadvantages. First, it is not robust against low vessel lumen contrast and intensity changes due to noise, the partial volume effect or contrast bolus dynamics. This can lead to

blending artifacts between two near vessel segments as well as to an over- and under-defined segmentation (see Fig. 16a and Fig. 16b). The invalid results have to be corrected manually, which is time-consuming. The correction is performed either on the segmented image data or on the reconstructed geometric model. This post-process increases the operator-dependency and decreases the reproducibility. An additional disadvantage of thresholding is its sensitivity to variations of the threshold, which further increases the operator-dependency. Small changes of the threshold lead to a relatively large change in the segmented vessel lumen due to the steep changes in intensity values at the true lumen boundary.

*Region growing* approaches can be used to perform the segmentation according to local intensity values. From interactively placed seed points or regions within a vessel, neighboring voxels are iteratively extended until they break a homogeneity criterion, e. g., deviation from a given intensity value. The growing stops once no neighboring voxel can be added to the current segmentation. In comparison to a global thresholding, region growing is also computationally efficient but ensures connected regions based on the seeding locations. Additionally, it explores datasets sparsely, which is an advantage for large datasets. Region growing is also sensitive to noise and image inhomogeneities or can lead to holes and leakages in the segmentation. Thus, different algorithmic enhancements are available, which include exclusion criteria [235], locally adaptive region growing [372] and wave propagation schemes [270]. All these improvements try to ensure well-defined vessel boundaries and to capture vessel topology, e. g., bifurcations, during the growing process.

#### 3.4.2.2 Explicit Deformable Models

Another popular class of vessel segmentation techniques are deformable models, also known as active contours or *snakes*, that rely on an explicit parametric contour description [229]. They evolve a 2D contour or 3D surface according to *external forces* derived from the image data and *internal forces* based on the contour geometry and its regularity. The initial contour is typically placed manually within the vessel and the evolution stops once it reaches an equilibrium. As an example, Cebal et al. [58] reconstruct an initial surface within the cerebral vessels by using a region growing segmentation followed by an isosurface extraction. The selection of the intensity values for the homogeneity criterion of the region growing is carried out on a trial-and-error basis. The extracted isosurface model is then deformed according to the image gradient (external forces) and surface curvature (internal forces).

In comparison to image-based methods, the resulting contours do not suffer from leakage and hole artifacts due to the internal and external force controlling. Furthermore, a subvoxel segmentation is achieved, which avoids additional post-processing efforts to minimize staircase artifacts in the reconstructed vessel mesh. Despite the desirable features, like inherent connectivity and smoothness, classical deformable models have two primary limitations. First, if the initial contour shape differs considerably from the actual vessel boundary, a dynamical reparametrization of the contour is necessary, which can be challenging. For example, this can happen in the case of a pathological vessel dilatation such as an aneurysm. The second limitation relies on the difficult adaption to a change of the



local vessel topology, e. g., branching. A re-parametrization is necessary every time if a topology change occurs. Thus, several improvements have been proposed such as topology-adaptive contours [229] and avoiding self-intersection artifacts [85].

### 3.4.2.3 Implicit Deformable Models

An extension of classical active contours is found in implicit deformable models that use *level set segmentation* methods [259]. In contrast to explicit deformable models, they exhibit the advantage of an inherent topological flexibility in terms of an implicit contour evolution [5]. The general idea is to embed a contour into a higher dimension scalar function  $\phi$ , the level set function, such that the contour is the zero-level contour of  $\phi$ . The temporal evolution of the level set function  $\phi_t$  is described by a *partial differential equation* (PDE), which incorporates image features (external forces) as well as shape and smoothness constraints (internal forces). In general, the definition of the PDE involves: an initialization strategy, some regularization strategies to be robust against noise, and the choice of a feature that defines the external force terms.

As an example of application, we illustrate this approach according to Antiga et al. [8]. They define  $\phi_t$  at voxel position  $\mathbf{x}$  as follows:

$$\phi_t = -w_1 G(\mathbf{x}) \|\nabla \phi\| + 2w_2 H(\mathbf{x}) \|\nabla \phi\| - w_3 \nabla P(\mathbf{x}) \cdot \nabla \phi. \quad (19)$$

The first term  $G(\mathbf{x})$  represents the contour inflation and is controlled by a speed value dependent on local image features, commonly the image gradient or shape constraints, e. g., rigidity. The second term  $H(\mathbf{x})$  describes the smoothness constraints that use the mean curvature of the current zero-level contour. The last term  $P(\mathbf{x})$  represents the advection of the zero-level contour, which pushes it towards certain image features defined by a feature image. The authors choose  $P(\mathbf{x}) = \|\nabla I\|$  as the magnitude of the image gradient. Finally, the user-defined weights  $w_1$ ,  $w_2$ , and  $w_3$  control the influence of each term on the contour evolution.

After  $\phi_t$  is evolved, it separates the image domain into negative values (inside) and positive values (outside). By default, the initial level set function  $\phi_0$  is obtained by placing two seed points  $s_1$  and  $s_2$  at the two ends of a vessel branch (see Fig. 17a). Starting from these seed points, two independent wave fronts are propagated following the so-called *Eikonal PDE equation*, which is numerically approximated by the fast marching method [299]. Here the propagation speed is proportional to the underlying image intensity values. The result of the fast marching method consists of two scalar fields  $T_1$  and  $T_2$ , which represent the arrival times in each point of the image domain (see Fig. 17b). The initial function  $\phi_0$  is then defined as

$$\phi_0 = \nabla T_1 \cdot \nabla T_2. \quad (20)$$

For more than one vessel segment, this propagation is repeated for each branch and the different scalar fields are merged into one final function  $\phi_0$ . The authors also provide a strategy in the case of non-tubular vessel structures like aneurysms. For this, several seed and target points are manually placed, e. g., in the aneurysm and in the parent vessel, and  $\phi_0$  is then defined as the arrival times when the first target is reached. The region where  $\phi_0$  in Equation 20 is negative, i. e., the propa-

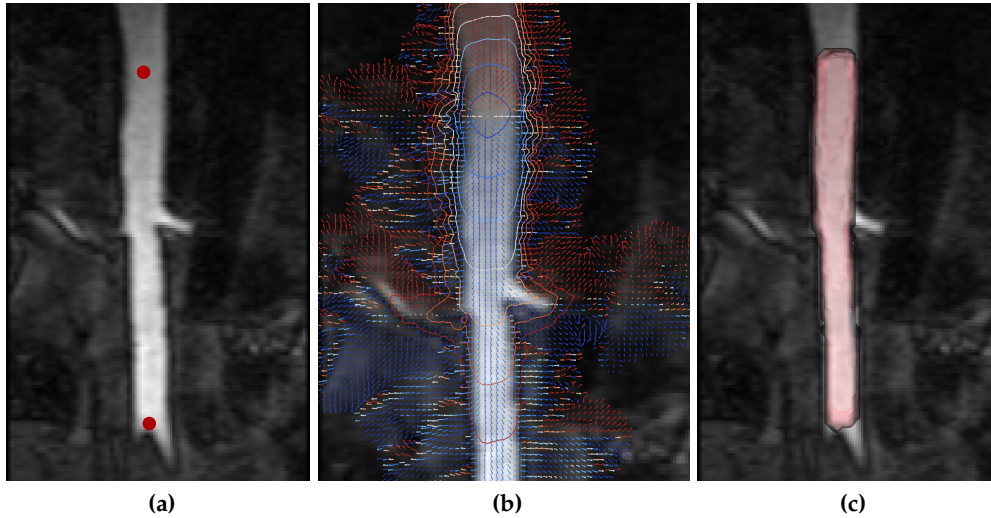


**Figure 17:** Vessel segmentation steps using implicit deformable models according to Antiga et al.: (a) placing of two seed points from which two initial scalar fields are propagated that correspond to the arrival times at each point based on the Eikonal PDE equation. Contour lines of one scalar field and vector plots of its gradient are shown in (b). The zero-level between the two scalar fields is shown as isosurface in (c), which is used as an initial level set function. The temporal evolution of the level set function is controlled by external forces, e. g., image features, and internal forces, e. g., shape constraints. (Images reprinted from Antiga et al. [8] © Springer Science and Business Media 2008 with kind permission from Springer Science and Business Media.)

gation fronts are directed towards each other, is used as an initial level set function. In order for it to be more robust against image noise and to produce smooth segmentation results, the authors present several regularization schemes. This can include: noise suppression by using image smoothing filters, e. g., anisotropic diffusion filters [137] to preserve features, steering the segmentation along the vessel direction by incorporating contour curvature constraints or surface smoothing of the extracted final vessel surface with non-shrinking filters [320]. A perfect regularization scheme, however, does not exist and it depends on the image type and the vessel morphology.

Since implicit deformable models synthesize low-level and high-level image information with topological flexibility, it is one of the most favored approaches for vessel segmentation [8, 321]. However, some aspects have to be considered. The indirect handling of topology changes in a vessel tree, due to the temporal evolution of the level set function, comes with an elevated computational cost and, in practice, special algorithmic care has to be taken to ensure convergence [209].

Furthermore, the weighting parameters that control the influence of each term in the PDE as presented in Equation 20 need to be adjusted properly to achieve satisfactory results. For some pathological vessel locations that differ strongly from the normal vessel geometry, this could be challenging and there may even be no parameter setting that ensure both high local deformation and smoothness. To overcome these limitations, implicit deformable models can be adapted to a particular vascular disease by means of training datasets from which appropriate features for the external forces can be derived. For example, this has recently been proposed and validated by Bogunovic et al. [30] for an automatic segmentation of



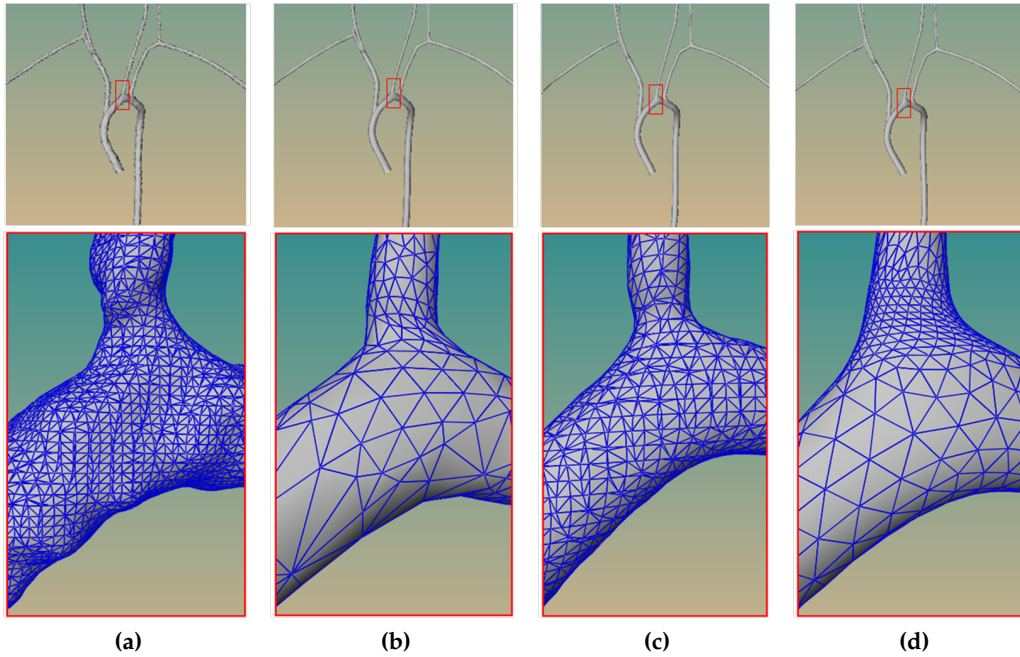


**Figure 18:** Different results of surface extraction methods: (a) marching cubes, (b) subdivision surface reconstruction, (c) MPUI approach by Schumann et al. [297] and (d) scale-adaptive MPUI method by Wu et al. [369]. (Images reprinted from Wu et al. [368] © Elsevier 2013 with kind permission from Elsevier.)

cerebral aneurysms in 3D-RA and CTA images. The authors also include a vessel enhancement or *vesselness filter* by Frangi et al. [113] to control the fast marching method for the initial level set function.

### 3.4.3 Surface Reconstruction and Geometric Processing

Once the segmentation is completed, a triangulated surface mesh has to be extracted describing the *vessel lumen boundary*. In the case of an explicit deformable model, the surface is already defined due to the geometrical model itself. For the intensity-based methods or implicit deformable models, the standard Marching Cube algorithm (MC) [214] can be utilized. The input for MC is either a binary segmentation mask or the scalar field of the evolved level set function (see Fig. 17c and Fig. 18a).

As an alternative to the MC algorithm, Schumann et al. [296] present a surface extraction approach by utilizing the *Multi-level Partition of Unity Implicits* (MPUI) by Ohtake et al. [257], which generates a smoother surface approximation compared to MC. The input of the MPUI method is also a binary segmentation mask from which a point cloud is generated. For each point, an implicit function is defined and accumulated to obtain a global implicit function. Bloomenthal's implicit polygonizer is then used to generate the polygonal surface based on this function [26]. As a result the MPUI method provides a smooth piecewise quadratic surface approximation compared to the linear approximation of MC shown in Figure 18b. In an additional step, Schumann et al. [296] improve the triangle quality by remeshing the surface mesh to obtain equilateral triangles. Wu et al. [369]

improve some processing steps of the MPUI approach to achieve a good balance in terms of smoothness, accuracy, triangle quality and surface size. They use the point cloud generation of Schumann et al. [296] but utilize a more robust normal estimation for each point by means of a covariance analysis. Subsequently, they choose a more robust implicit surface reconstruction method, so-called *Poisson surface reconstruction*. This method is more robust in terms of recovering fine details in noisy image data and does not need the accumulation of local implicit functions to obtain a global implicit function. Finally, the authors propose a polygonization algorithm that is adaptive to the local curvature. Compared to the original approach of Schumann et al. [296] without the additional remeshing step, the resulting surface mesh exhibits almost equilateral triangles that are adaptively scaled to local curvature characteristics. Surface areas with high curvature are represented by smaller triangles, whereas triangles become larger in low-curvature regions. Here the triangle size gradually changes from small to large as can be seen in Figure 18c.

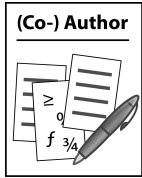
In Figure 18c an example of a *model-based* subdivision surface reconstruction algorithm [216] is presented. The resulting surface mesh also shows equilateral-shaped and adaptive triangle sizes with smooth transitions. However, a quantitative analysis by Wu et al. [369], exhibits a lower surface accuracy compared to both MPUI approaches. The maximum error for the subdivision algorithm is larger than twice a voxel size while the *model-free* methods of Schumann et al. [296] and Wu et al. [369] achieve a maximum error that is less than a voxel size. Moreover, because of the simplified assumptions of model-based surface reconstruction methods, only circular-shaped cross-sections can be achieved. These assumptions may not represent the vessel morphology in the image data and is therefore inappropriate for vessel diagnosis. For example, pathological vessel malformations, such as aneurysms or stenoses, might generally have non-circular shapes.

Independent of the surface extraction approach, the generated initial surface is not yet usable for a reliable CFD simulation. Since the vessel geometry is the main impact factor on the resulting simulated flow data, a reliable surface representation is important [154, 318]. Further geometric processing steps are necessary to obtain a valid CFD surface mesh and to extract anatomical landmarks, which are useful for the CFD data analysis.

#### 3.4.3.1 Removal of Surface Artifacts

Depending on the image quality and the segmentation method, different surface artifacts occur, such as over- and under-segmentation, merged vessel sections, narrowing and noise (see Fig. 19a). The severity of these artifacts is increased especially in cases of small and neighboring vessels with a low vessel-to-background contrast and larger influence of the partial volume effect on the segmentation. The first step to remove over-segmentations and merged vessel sections is to cut out a ROI with a subsequent *connected component analysis* of the remaining surface meshes [294]. This excludes irrelevant vessel parts and small disconnected surfaces, e. g., noisy regions. In a second step, merged vessel sections have to be separated and remodeled since the CFD simulation would assume these regions to be connected domains, which does not describe the real vessel morphology and topology. Note, the separation can also be accomplished during the segmentation by incorporating barriers or exclusion regions. This leads to an iterative procedure

between vessel segmentation and its surface reconstruction. A remodeling is also necessary in cases of under-segmentations or narrowing, e.g., due to a weakly defined vessel lumen boundary (see Fig. 16d). It requires a local adaptive surface inflation of the affected region controlled by a validation with the original image data.



Mönch et al. [239]

With respect to surface noise and staircases, volume-preserving and context-aware mesh smoothing approaches can be utilized [239, 320]. In the work of Mönch et al. [239], in which the author of the thesis was involved, a method is presented that automatically identifies and quantifies staircase artifacts. This is accomplished by comparing the surface normal with the z-axis orientation of the image data stack. The quantification is then used to parametrize uniform smoothing algorithms, e.g., Laplace+HC [13]. As a result, artifacts can be adaptively smoothed while accuracy and features are preserved in non-artifact areas of the vessel surface. This context-aware smoothing approach was also utilized to smooth a cerebral aneurysm surface that exhibited staircase-like artifacts, e.g., after surface cuts of merged vessel sections. The approach was quantitatively compared with a manual correction that was seen as gold standard, standard Laplace and Laplace+HC smoothing as well as both smoothing approaches with context-aware parametrization. Based on the resulting meshes, CFD blood flow simulations were performed and the differences between the resulting hemodynamic information at the smoothed locations were compared, in particular maximum flow speed and WSS.

The context-aware smoothing with Laplace+HC demonstrated the lowest distance changes (0.4 mm) and volume shrinkage (-1.5%) compared to a manual correction. Standard Laplace and Laplace+HC smoothing always yielded larger differences. In terms of the hemodynamic information, each smoothing approach achieves higher values compared to the manual smoothing. However, the context-aware smoothing approach demonstrated the lowest differences with  $\approx 6\%$  for the maximum flow speed and  $\approx 67.5\%$  for the MWSS. The relatively large WSS difference results from small remaining staircase-like artifacts that were not possible to smoothed completely without causing a strong volume shrinkage.

In general, the vessel separation and remodeling are performed manually as a time-consuming and user-dependent task, which can take several hours depending on the severity of the artifacts. Available modeling tools, which are presented in Section 3.7, can be used to accomplish these tasks. The manual correction, however, is questionable since the estimation of the real vessel morphology depends on the user's judgment and is hard to reproduce or to validate. A reliable automatic or semi-automatic approach is still lacking and remains an important goal for future work. Thus, a review of the resulting vessel surface with clinical experts, such as neuroradiologists or cardiologists, is important, who should be involved in the reconstruction process.

### 3.4.3.2 Extraction of Anatomical Landmarks

After the removal of surface artifacts, the extraction of certain anatomical landmarks is performed (see Sec. 2.3.1). These landmarks can be utilized to support advanced vessel surface processing, e.g., vessel decomposition, to quantify vessel pathologies, e.g., the grade of a stenosis, or for the visual exploration of the flow

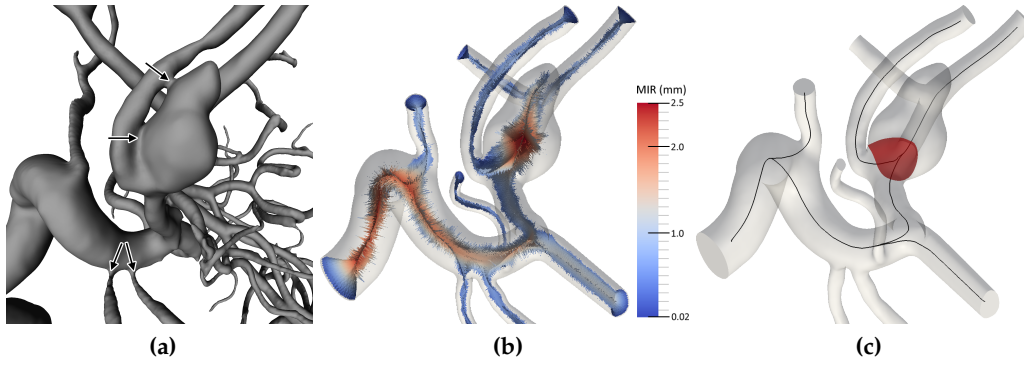


**Figure 19:** Example of surface artifact removal and anatomical landmark extraction for a cerebral aneurysm: (a) initial reconstructed surface with highlighted artifacts (arrows) and (b) after their removal. Additionally, the embedded Voronoi diagram is shown color-coded according to the maximum inscribed sphere radii (MIR). In (c) several extracted centerlines (black) and the ostium (red) can be observed.

data. Here the most relevant landmark is the *vessel centerline*, which can be extracted by exploiting the embedded 3D *Voronoi diagram* [7] or other proposed 3D skeletonization approaches, such as distance transformations, thinning algorithms or level set methods [147]. We shortly describe the approach by Antiga et al. [7] due to its robustness regarding pathological vessel morphologies. The centerline extraction relies on the concept of the medial axis of the reconstructed vessel surface, which can be approximated by the Voronoi diagram lying inside the surface [87]. Each point on this embedded Voronoi diagram is associated with a maximum inscribed sphere touching the surface at at least four points (see Fig. 19b). On the Voronoi diagram an action field is computed as the inverse of the local sphere radii. Given this action field, the Eikonal equation, i.e., the arrival times, from seed to target points on the Voronoi diagram are solved by means of the fast marching method (see Sec. 3.4.2). Seed and target points are specified at the vessel inlets and outlets by the user. The centerlines are then extracted by backtracing the path from target to seed points with a gradient descent method (see Fig. 19c).

Depending on the specific anatomical structure, additional landmarks can be extracted. As an example, the ostium and certain axes of saccular cerebral aneurysms are relevant for quantifications or local flow analysis (see Sec. 2.3.1). Neugebauer et al. [246, 250] propose a robust method to reconstruct these landmarks (semi-)automatically based on geometrical descriptions provided by several clinicians. Given a manually selected point on the aneurysm sac and a centerline, four connected control points around the aneurysm neck are computed. The initial ostium contour is then smoothly bended around the parent vessel until the geodesic distance between the control points corresponds to the local mean parent vessel diameter. In a final step, the ostium contour is regularly triangulated to provide a well-defined ostium surface (see Fig. 19c).

Based on the extracted ostium, several axes and diameters can be derived, such as the *central aneurysm axis* (CAA) and the maximum diameter. In a subsequent work, the authors utilize the centerline, ostium surface and the CAA to provide an anatomy-guided flow exploration, which we present in more detail in Chapter 4. Furthermore, the authors suggest using the detected ostium regions as a basis for an aneurysm decomposition into the sac and its parent vessel. A decom-

position would facilitate a surface model-to-model comparison regarding surface-based physiological and hemodynamic parameters.

In a recent work, Jiang and Strother [171] focus on such a reliable and reproducible decomposition with a subsequent mapping of the separated aneurysm onto a 2D disc. For the decomposition they combine different geometric information, such as the local curvature and a distance metric defining the spatially varying deviation from the parent vessel, to construct a harmonic function. The function computes a scalar field on the vessel surface from which a characteristic iso-line is extracted that represents the border between the aneurysm sac and the parent vessel. The decomposed aneurysm surface is then mapped to a 2D disc to compare hemodynamic surface parameters such as the WSS and pressure.

#### 3.4.3.3 *Inlet and Outlet Preparation*

Geometric processing is also required for the preparation of the vessel's inlets and outlets. At these locations certain boundary conditions for the CFD simulation are later defined, such as a speed and pressure profiles. In order to ensure a full development of these conditions, the inlets and outlets have to be cut orthogonal to the local vessel direction. Here a sufficient cylindrical vessel extension of several centimeters at both ends has to be provided before the flow enters the computational domain of interest. The cutting and extension can be accomplished manually by means of available modeling tools or semi-automatically by using the centerlines to define the cutting planes and extension direction [8]. Note, an extension is only necessary if no sufficient straight segments of the upstream and downstream geometry are available, e. g., the parent vessel ends with a strong axial curvature. In the case of a required extension, its shape must provide a smooth transition between the boundary sections to avoid error-prone flow disturbances during the simulation. Advanced surface deformation methods can be applied to the cylindrical geometry, such as a thin plate spline or gradient-based deformation [39], to smoothly align the circular section with the vessel cut section.

#### 3.4.3.4 *Improvement of Mesh Quality*

Once the shape of the vessel model has been finalized, the quality of the surface triangulation has to be improved. A highly regular surface mesh in terms of *connectivity* and *geometry* is necessary for the subsequent generation of the numerical CFD volume grid. The generation of such a grid is based on the vessel surface triangulation and its high quality is required to ensure convergence of the CFD solution as well as minimization of numerical errors and singularities. In Figure 20a the finalized shape of an aneurysm surface and its superimposed triangulation are shown. The triangles exhibit irregular shapes and vertex valences (i. e., number of incident vertices), especially at low curvature regions and at cut sections.

According to Alliez et al. [3], a high-quality triangulation exhibits the following three properties: well-shaped triangles, i. e., ideally equilateral, uniform vertex density and smooth gradation of triangle sizes depending on the local curvature. Thus, a remeshing of the initial triangulation is necessary to achieve these properties. Existing approaches can be roughly classified as being *greedy*, *variational* or *incremental* [38]. Greedy methods commonly use a series of local modifications at



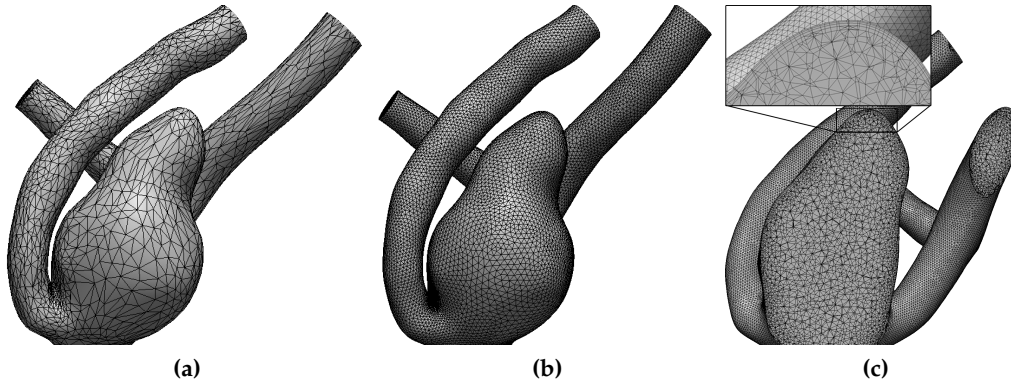


**Figure 20:** Improving mesh quality and volume grid generation: (a) the finalized vessel surface shape exhibits a low mesh quality with irregular triangle shapes and vertex valences, (b) improved mesh quality after a remeshing algorithm was applied, (c) section cut through the volume grid shows prism cell layers at the wall and tetrahedral cells for the interior.

one time, such as edge collapse, edge flip and vertex insertion, until the desired properties are satisfied.

Variational methods consider the initial mesh as an optimization problem where an energy functional is minimized. Here the mesh is globally or locally parametrized onto a 2D domain with a subsequent relaxation, e. g., vertex relocation or vertex insertion until convergence. The final triangulation is then projected back into the 3D space with an improved mesh quality [2, 313]. Incremental methods combine both refinement and decimation by means of the aforementioned local modifications, possibly interleaved with a relaxation procedure controlled by a local parametrization [36]. For the interested reader, we refer to Botsch et al. [38] for a more detailed description and to Alliez et al. [3] for an overview of recent advances in surface remeshing.

In daily practice we utilize an advancing front remeshing algorithm, which is one of the incremental approaches [295]. At first the user has to select the cut edges at the inlets and outlets as feature edges and defines a certain maximum triangle size. Starting at these edges the fronts are then propagating towards each other. During the propagation, local mesh modifications are performed, such as edge flipping or vertex insertion, that are supported by the underlying initial triangulation. Here the defined features are preserved. The result can be seen in Figure 20b. In comparison to a variational approach, no complex 2D parametrizations or previous cutting into topological discs are necessary.

Note that the additional remeshing step is also necessary when the surface reconstruction is realized with the aforementioned MPUI approach by Wu et al. [369]. Although this method achieves well-shaped triangles with smooth transitions, badly-shaped triangles occur at the inlets and outlets after the cutting.

#### 3.4.4 Volume Grid Generation

Based on the improved vessel surface triangulation, the numerical volume grid for the subsequent CFD finite element or volume analysis is generated. The most common approach is to use an advancing layer method by filling the vessel lumen

with unstructured tetrahedral cells starting from the surface into the lumen along the surface normal [285]. In general, such elements are called *computational* or *volume cells*.

For hemodynamic CFD solutions close to the wall, a higher density of computational cells is required and they should be aligned with the local orientation of the vessel surface. This increased density is necessary because the flow speed gradients at the boundary are higher than at the vessel center. In order to capture small changes of flow speed, a higher resolution of the volume grid is required, which results in an *adaptive volume grid generation*. Thus, a boundary layer is defined that is filled with a stack of prisms followed by tetrahedral cells for the interior [8, 284]. This can be observed in Figure 20c where a magnified view of clipped grid faces through a cerebral aneurysm is presented. The size, thickness and number of the prism and tetrahedral cells can be controlled either by the local triangle edge length of the surface mesh or according to certain mesh metric fields.

The definition of that metric field is accomplished by setting a measure at each initial cell followed by a subsequent cell subdivision until the measure fulfills certain conditions. A reasonable measure would be the flow speed gradient based on a precomputed CFD simulation on an initial volume grid. The subdivision stops once the gradient is below a certain threshold.

A more accurate but computationally more expensive approach is presented by Sahni et al. [284, 285]. At each grid point of the cells, a symmetric Hessian matrix of the precomputed flow field is defined where the eigenvectors of the matrix represent the principal directions of speed changes. The main idea is that a large eigenvalue implies a high error rate in the corresponding direction of its eigenvector where small element sizes are desired. Conversely, a low eigenvalue is associated with a low error rate and suggests that the element size can be large in this direction. Thus, the grid resolution is adaptive in terms of local flow features resulting in an increase in both the computational efficiency and the accuracy of hemodynamics at these locations, e. g., near-wall information.

The number of computational cells depends on the vessel volume and embedded structures such as stents for cerebral vessels, which have to be incorporated into the volume grid generation. Typically, it can range from 100,000 to 3,000,000 cells for non-embedded and over 10,000,000 cells for embedded structures [169]. The spatial resolution varies between 0.02 and 0.08 mm volume diagonal of a cell.

### 3.4.5 CFD Simulation

The final step of the data acquisition is the simulation of the blood flow. Typically, this is accomplished by the already mentioned CFD simulation, which is an established numerical method within the domain of fluid mechanics to solve and analyze fluid flow problems [121, 188]. Here the blood flow is modeled mostly as *incompressible Newtonian fluid*, i. e., it has constant density and viscosity. Theoretically, blood is considered to be a compressible, non-Newtonian fluid (a suspension of red and white blood cells as well as platelets) but in practice this is mostly not assumed. The change of flow properties by means of compression arises only in high flow speed ranges, e. g., speed of sound and higher in the blood medium. Since the blood flow speed is much lower, the influence of compression is very low and negligible. Furthermore, studies have shown that non-Newtonian effects

in large arteries are also minimal and can be neglected. However, in regions of slow flow speed this approximation is not entirely justified and further investigations are required [301]. Because of this open issue and the increased computational costs that would arise with a non-Newtonian model, most research groups do not utilize it.

The corresponding fluid model can be described by the three-dimensional unsteady incompressible Navier-Stokes equations [188]:

$$\nabla \cdot \vec{v} = 0 \quad (21)$$

$$\rho \left( \frac{\partial \vec{v}}{\partial t} + (\vec{v} \cdot \nabla) \vec{v} \right) = -\nabla p + \mu \nabla^2 \vec{v} + \vec{f}. \quad (22)$$

Equation 21 defines the incompressible property as zero divergence of the flow velocity vector  $\vec{v}$ . This represents a vector field without sources and sinks or a vector field with constant density and volume. The left-hand side of Equation 22 defines the inertia per unit volume composed by the unsteady and convective acceleration  $\frac{\partial \vec{v}}{\partial t}$  and  $\vec{v} \cdot \nabla \vec{v}$ , respectively, with  $\rho$  as density. The convective acceleration describes the change of speed over position, e. g., due to a narrowing in a tube, instead of over time  $t$ . The right-hand side represents the divergence of stress and body forces  $\vec{f}$ , e. g., gravity or centrifugal force, per unit volume. The divergence of stress is composed by the pressure gradient  $\nabla p$  and the viscosity  $\mu$ , which is represented by the vector Laplacian of  $\vec{v}$ . The vector Laplacian is interpreted as the difference between the velocity at a point and the mean velocity in a small volume around it.

The Navier-Stokes equations require a solution of nonlinear PDE, which are typically approximated with a *finite element* or *volume* method simulation. Here the simulation is based on discrete, i. e., finite, cells, represented by the aforementioned prisms and tetrahedrons of the generated volume grid. The numerical approximation of the exact solution is accomplished by defining certain boundary conditions and defining a system of linear equations that have to be solved, e. g., with Newton's method. For each cell and each flow parameter, one linear equation has to be defined. As an example, the computation of the three velocity vector components and the pressure from Equation 22 requires four equations at each cell. Given a volume grid with 1,000,000 cells, a system of 4,000,000 equations has to be solved. Depending on the computational resources, this may take several hours or days. Based on the simulated flow vectors and pressure values at each grid point, other hemodynamic parameters, such as WSS and OSI, are also derived after the simulation in a post-processing step [188]. Typically, the temporal coverage comprises a complete heart cycle of 0.8-1 sec. with a temporal resolution of about 0.0025 to 0.005 ms between each time step.

The boundary conditions comprise a pulsatile flow speed and pressure profiles at the inlets and outlets. Furthermore, no *fluid-structure interaction* (FSI) and no *slip-boundary*, i. e., flow speed is zero at the vessel wall, are assumed. The profiles may be derived from 2D or 4D PC-MRI measurements, from US measurements (see Sec. 2.5.3), from the literature or derived from *in vitro* experiments. The assumption of a rigid vessel wall is mainly due to a lack of information regarding arterial wall properties such as elasticity and thickness. These properties are highly



patient-specific and current image acquisition techniques are not able to capture this information *in vivo*.

It is important to note, however, that there is an ongoing debate about the influence of rigid and non-rigid vessel wall assumptions on the resulting hemodynamic behavior [321]. Promoters of FSI emphasize the influence of flow speed and pressure on the vessel deformation and vice versa, especially for large vessels near to the heart, such as the aorta. Heart muscle contraction, moving heart valves and the surrounding anatomical context, e.g., organs or bones, can greatly influence the vessel deformation. Thus, the extraction of reliable vessel wall properties and modeling of FSI represent two of the major challenges in the field of cardiovascular flow simulation.

In recent years, a strong alternative to the CFD simulation of hemodynamics based on Navier-Stokes and unstructured volume grids is the so-called *lattice Boltzmann simulation* (LBS) [271]. The LBS is also a CFD method for fluid simulation but it solves the Newtonian fluid equations by discretization of the Boltzmann equation, which models the kinetic transport of particles. It incorporates the essential physics of the particles, such as their mass and momentum, as well as the aforementioned boundary conditions.

It is also possible to derive the Navier-Stokes equation from the Boltzmann equation under the assumption that the density variation is small. In contrast to the classic CFD approach, the LBS is considered to be *meshless* in the sense that it does not require the generation of an unstructured volume grid. Instead, the vessel anatomy is sampled by a regular voxel grid or *lattice*, which is utilized to seed a set of fictitious particles. The computational costs to solve the Boltzmann equations are similar to the Navier-Stokes equations but the overall time is shorter because of the less resolute grid.

Similar to the classic CFD approach the accuracy of the LBS method also depends on the lattice resolution. A lower spatial resolution also results in a lower accuracy, which can only be overcome by a larger number of smaller voxel cells. Depending on the vessel geometry shape, however, this would lead to a computational effort similar to that of the classic volume grid approach. Nevertheless, due to the omitted and time-consuming processing step of the unstructured volume grid generation including prior surface mesh optimization, the LBS method becomes "attractive" for biomedical researchers in hemodynamic modeling [271]. Throughout the thesis, however, we utilize only hemodynamic information based on the Navier-Stokes equation and on volume grids because this is still an established approach for most of the major research groups, including our cooperation partners.

### 3.5 CLINICAL RESEARCH APPLICATIONS OF 4D PC-MRI

Advances in 4D PC-MRI flow measuring combined with reliable post-processing promotes the application of flow analysis for different vascular systems and diseases. Domain experts, such as cardiologists and biomedical physicists, have a particular interest in the exploration and understanding of flow patterns for both healthy subjects and patients with a certain CVD. In this section, we present an overview of the most prominent applications of flow analysis in the clinical research domain. Here we incorporate the three leading research questions **CD<sub>1</sub>-**

$CD_3$  of this domain (see Sec. 3.2.3) and provide information about normal and abnormal hemodynamics in different anatomical regions and associated CVDs. This overview is also later used to derive implications for this. For a more comprehensive presentation of 4D PC-MRI flow applications, we refer to the recent work of Markl et al. [221].

### 3.5.1 Heart and Great Vessels

Due to the great clinical importance and their relatively large sizes, flow analysis in the heart and great vessels are of main interest. This primarily includes investigations of the heart chambers, their valves, the aorta and the pulmonary arteries. Relevant CVDs are, for example, valve defects, aorta coarctation and aneurysms or the tetralogy of Fallot (see Sec. 2.2).

Studies of the flow in healthy hearts identified asymmetric, regionally constrained vortices near the mitral and tricuspid valves during diastolic inflow [181, 222]. Flow quantifications in terms of the average flow volume through the four heart valves have been measured [278]. Additionally, regional quantification (see Sec. 3.2.4) in the left ventricle reveals that direct flow and residual volume are the largest components of the end-diastolic volume. In contrast to this, it has been observed in patients with heart muscle diseases that the characteristics of the vortices and direct flow were considerably changed in the left ventricle [54, 99]. An increased vortex flow was also observed in the right ventricle and pulmonary artery in patients who had had a VSD surgery compared to healthy subjects [111]. For patients with valvular insufficiency, regurgitation could be observed accompanied by a lower average flow volume for all four heart valves [278]. The ability to measure and assess ventricular flow performance creates the potential for an early diagnosis, treatment options and prognosis.

A topic of considerable interest is also the blood flow in the aorta. Several studies on healthy subjects have shown accelerated flow speed through the aortic valve and a right-handed helical outflow in the ascending aorta during late systole [220, 222]. This is shown in Figure 21a. During diastole, retrograde flow along the inner curvature of the ascending aorta was observed. Normal distributions of WSS and OSI in the entire aorta have been identified to provide a reference for the examination of patients with aortic diseases [118].

Compared to normal subjects, irregular flow patterns and significantly different flow characteristics were found in patients with altered vessel morphology caused by vessel diseases and during aging. For example, patients with aneurysms exhibit abnormally pronounced helical or vortical flow features as shown in Figure 21b [220]. In patients with a bicuspid aortic valve, an ascending aortic aneurysm and an aortic coarctation, an aberrant and complex peak systolic flow behavior has been observed. Especially eccentric flow jets and a skewed WSS profile have been identified, as illustrated in Figure 21c [221]. Some studies suggest that these flow patterns play an active role in aneurysm progression and are not only consequences of dilatation [156, 158]. This assumption, however, is still in debate because similar flow has been observed in aortas that are not (yet) dilated [221].

There is also growing evidence that diastolic retrograde flow in the descending aorta may be an indicator of the presence of complex plaque, shown in Figure 22a. This extends the hazard of a potential stroke mechanism to all brain territories.

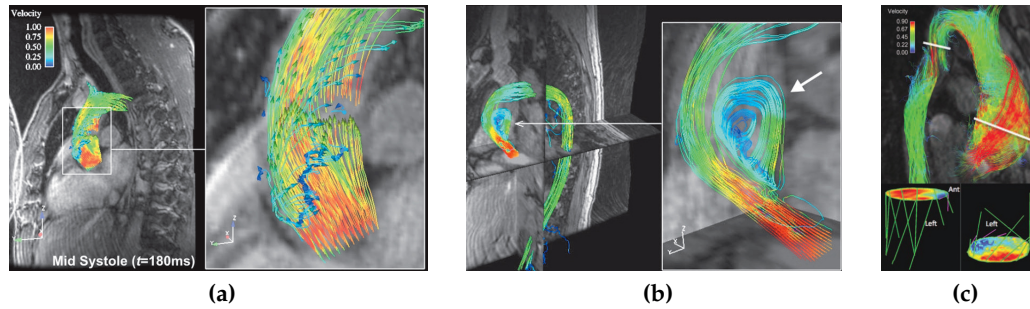


**Figure 21:** Differences in flow patterns in the ascending aorta between a healthy subject and pathological cases during mid and late systole: (a) increased flow speed and right-handed helical outflow in a healthy subject, (b) abnormal vortical flow in a patient with an aorta aneurysm and (c) eccentric flow jets and skewed WSS distribution in a patient with a bicuspid aortic valve. (Images (a) and (b) reprinted from Markl et al. [220] © Wolters Kluwer Health 2004 with kind permission from Wolters Kluwer Health, image (c) reprinted from Markl et al. [221] © John Wiley and Sons 2012 with kind permission from John Wiley and Sons.)

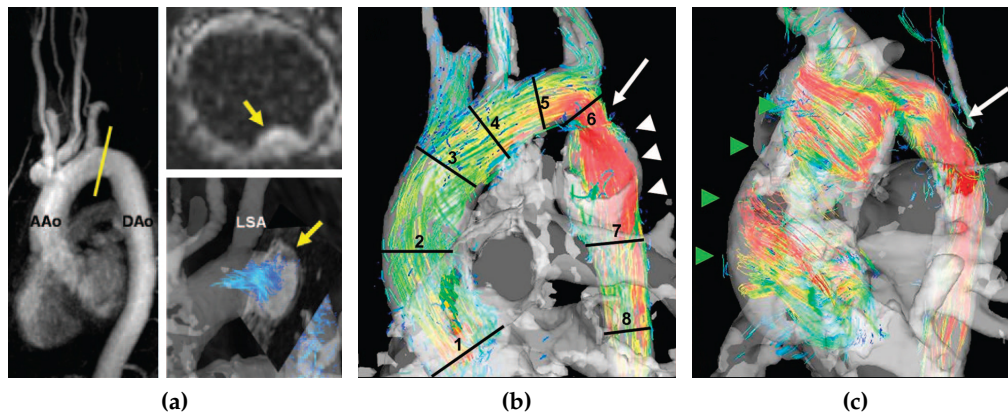


**Figure 22:** (a) Potential correlation between plaque formations (yellow arrow) in the descending aorta (DAo) and abnormal retrograde flow into the carotid arteries. Altered flow patterns and morphological changes after aortic coarctation (CoA) repairs in two patients: (b) restenosis at the region of the CoA repair (white arrow) leads to accelerated flow speed and post-stenotic aneurysm formation (white arrowheads), (b) accelerated flow speed (white arrow) and increased helical flow in the ascending aorta (green arrowheads). (Image (a) reprinted from Harloff et al. [145], (b) and (c) reprinted from Frydrychowicz et al. [117] © Wolters Kluwer Health 2011 with kind permission from Wolters Kluwer Health.)

The phenomenon that plaque in the descending aorta could be a source of stroke had never been considered before [145]. It was possible to confirm the hypothesis that atherosclerosis and the aging process influence the flow behavior in the aorta. Studies have shown that the presence of atherosclerosis leads to an increased retrograde flow speed and lower flow speed during systole. The same hemodynamic behavior was observed for healthy but older subjects [29].

Domain experts are also interested in the alteration of hemodynamics after repairing certain aorta diseases to validate the resulting blood flow behavior [117, 157]. In Figure 22b and Figure 22c the resulting morphology and blood flow after coarctation repair for two patients are shown. Corresponding studies revealed a

marked flow acceleration, an increase of WSS accompanied by a decreased OSI, and disturbing flow patterns (also called secondary flow patterns) like helical flow at the location of the coarctation repair. These findings also reveal an apparent deterioration of the morphology, such as post-stenotic dilatation or aneurysm as well as a re-stenosis after the treatment. However, larger studies and follow-up imaging are needed to further evaluate the association between altered flow and post-intervention [157].

In addition to the aorta, the main pulmonary artery is also considered for blood flow analysis in large vessels. An important question is to identify characteristic flow patterns that could indicate the presence of pulmonary arterial hypertension (PAH) in patients who are suspected to have it. PAH leads to heart failures and considerable decrease in exercise tolerance due to shortness of breath. Recent reports have shown that in PAH patients, the flow patterns in the pulmonary artery differ significantly from those seen in healthy subjects [150, 274]. Some of the main findings are the onset and presence of retrograde flow as well as vortex structures that may be caused by the retrograde flow. Pulmonary regurgitation was also observed in patients with repaired tetralogy of Fallot. Furthermore, increased helical and vortical flow patterns occurred in the majority of cases compared to mostly laminar flow in healthy subjects [111].

### 3.5.2 Carotid Arteries

The assessment of the severity and progression of internal carotid artery (ICA) stenosis is of clinical interest since high-grade stenosis constitutes a major source of ischemic stroke [144]. Such a stenosis results from atherosclerosis caused by plaque formation at the ICA wall. In this context, clinical flow assessment mainly aims to achieve two research goals. First, a reliable evaluation of local hemodynamics in healthy subjects and patients as well as changes in the hemodynamics after a revascularization procedure was performed. Second, the identification of certain flow parameters that influence the development of atherosclerosis and plaque.

For healthy subjects, consistent flow patterns of complete vessel filling and helical flow were observed. In patients with an ICA stenosis, these two patterns are considerably altered and show a low grade of vessel filling and the absence of helical flow. After a revascularization procedure, the level of vessel filling and helical flow was partly restored. This is partly shown in Figure 23a. The stenosis caused a reduced flow through the vessel lumen, which it was possible to restore after a revascularization procedure.

For the occurrence and development of atherosclerosis, studies have revealed a close link to local hemodynamic characteristics, such as flow deceleration, recirculation, reduced WSS and elevated OSI [74]. It is suggested that lowered WSS and increased OSI are potential parameters that promote atherosclerosis. These parameters are potentially linked to future growth of such lesions whereas an increased WSS protects against atherosclerosis. In patients after surgical revascularization of previously high-grade ICA stenosis, the wall parameter distribution was similar to that observed in healthy subjects [223].



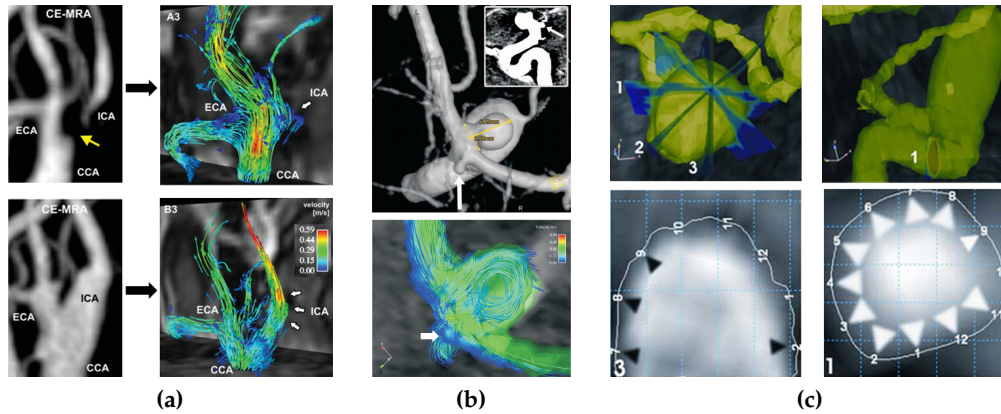


**Figure 23:** Hemodynamic information of measured blood flow in pathological carotid arteries. In (a, bottom) a stenosis in the ICA led to a reduced flow filling (yellow arrow) but it was possible to restore the vessel after a revascularization procedure (a, top). A cerebral aneurysm shows complex vortical flow patterns (b) and reduced WSS at the wall (c, left) compared to its parent vessel (c, right). Black arrowheads indicate 0%-39.5%, no arrow heads 40%-59.9% and white arrow heads 60-100% of mean parent vessel WSS distribution. (Image (a) reprinted from Harloff et al. [144] © John Wiley and Sons 2009 with kind permission from John Wiley and Sons, (b) and (c) reprinted from Meckel et al. [231] © Springer Science and Business Media 2008 with kind permission from Springer Science and Business Media.)

### 3.5.3 Intracranial Hemodynamics

In the past, it was not possible to obtain reliable flow information about the small intracranial vessels and their pathologies due to the low spatial and temporal resolution of existent MRI scanners. The application of Doppler ultrasound was also very limited because of the surrounding bone structures. However, with recent progress in 4D PC-MRI, e.g., higher magnetic field strength, improved image sequences and more accurate  $v_{ENC}$  adjustments, investigations of volumetric intracranial hemodynamics are becoming feasible in the clinical research domain. Here, 4D PC-MRI provides several advantages compared to common transcranial Doppler US, such as complex 3D flow feature depiction and no sound propagation problems due to bone structures [362].

However, studies have shown that 4D PC-MRI acquisition captures lower peak flow speed values in comparison to Doppler US due to the lower spatial and temporal resolution. Current clinical research interests focus mainly on the depiction of measured hemodynamics in healthy subjects and in patients with cerebral aneurysms or stenosis. This also includes the investigation to what extent different MRI parameters, such as the magnetic field strength, parallel imaging and different temporal resolutions, influence the quality of the acquired data [19].

In studies on cerebral aneurysms, complex vortical flow patterns were observed as shown in Figure 23b for a patient with two adjacent aneurysms at the basilar artery [231]. Moreover, the spatial and temporal evolution as well as the magnitude of the vortices differed markedly between different aneurysms. Temporally varying vortices were demonstrated in wide-necked aneurysms while more stable vortices were seen in narrow-necked aneurysms. In addition, diffuse inflow jets were correlated with aneurysms with stable flow patterns while concentrated in-

flow jets were more likely in aneurysms with unstable flow patterns. It is assumed that the second type of aneurysm may have a higher likelihood of rupture [63, 159].

For WSS, a reduced magnitude on the aneurysm wall was seen compared to the parent vessel. An example is shown in Figure 23c for a saccular aneurysm at the ICA. For two cross-section planes, one in the aneurysm and one in the ICA, the temporally averaged WSS is derived at several positions on the segmented aneurysm and vessel wall. A significantly lower WSS distribution for the aneurysm plane can be clearly recognized. This correlation leads to the hypothesis that regions with low WSS may promote aneurysm growth. However, further studies are needed to establish a direct link between particular flow patterns and different aneurysm geometries.

### 3.5.4 Hepatic and Peripheral Vessels

The examination of hepatic flow, including arteries and veins, is another interesting field of clinical application. Similar to the previous applications, current investigations focus on the estimation of normal and abnormal blood flow behavior in healthy subjects and patients, respectively. For example it is known that liver cirrhosis changes the hepatic flow behavior. Recent results showed significant alterations in flow direction and speed in cirrhosis patients compared with age-matched and younger control groups [310]. An example is shown in Figure 24a where the flow in the portal venous system of a patient with cirrhosis is visualized. The flow visualization reveals vortical and retrograde flow, which does not

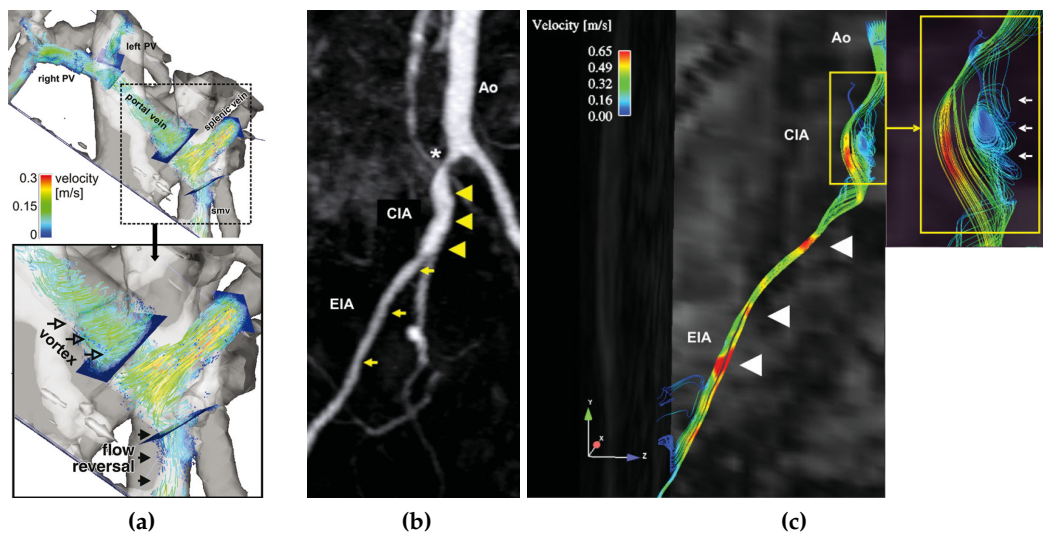


**Figure 24:** Flow patterns in pathological hepatic and peripheral vessels. In (a), unusual retrograde and vortical flow in the portal vein (PV) of a patient with liver cirrhosis are shown. In (b), an MIP of a peripheral artery reveals a stenosis (asterisk) with a post-stenosis dilatation (yellow arrowheads). Although vortical flow can be observed within the dilatation (inset), flow acceleration occurs not at the stenosis but in the subsequent artery (white arrowheads). (Image (a) reprinted from Stankovic et al.[310] © RSNA 2012 with kind permission from the Radiological Society of North America, (b) and (c) reprinted from Frydrychowicz et al. [119] © John Wiley and Sons 2007 with kind permission from John Wiley and Sons.)

occur in healthy subjects. These findings with 4D PC-MRI were validated with color Doppler US measurement and show significant correlation. Future studies will also focus on hemodynamics related to portal vein hypertension as well as changed vein flow during the course of the day and after ingesting a meal [221].

The acquisition and analysis of hemodynamic information also becomes relevant for peripheral vessels to assess corresponding occlusive diseases. In addition to anatomical image data, such as CE-MRA or CTA, the severity of the occlusion can be characterized by additional flow information. Doppler US is commonly used in peripheral vessels to obtain relevant flow information due to its high spatial and temporal resolution. However, as mentioned earlier, it suffers from a high operator-dependency and no volumetric flow information can be obtained. Advanced 4D PC-MRI overcomes these restrictions and has been successfully applied to capture relevant flow characteristics in healthy subjects and patients [119].

An example is shown in Figure 24 of a patient with a peripheral arterial occlusion due to a stenosis at the *common iliac artery*. In Figure 24b a maximum intensity projection (MIP) of a CE-MRA reveals the stenosis (denoted with an asterisk). The MIP also demonstrates a pathological dilatation after the stenosis (yellow arrowheads) and a general reduction in the vessel diameter (yellow arrows) throughout the entire *external iliac artery* (EIA). The narrowing results from non-calcified plaques. The corresponding flow visualization is presented in Figure 24c with color-coded streamlines according to the speed at the peak flow. The visualization reveals no speed acceleration at the stenosis but rather at the narrowed regions of the EIA (white arrowheads), which was also in agreement with corresponding Doppler US investigations. The magnification of the dilatation reveals complex helical and vortical flow patterns (white arrows), which were not seen in Doppler US. For future investigations, however, a spatial resolution of at least 1 mm is required to obtain or derive reliable flow information, e. g., WSS and pressure differences, for these comparably small vessels [119, 221].

### 3.6 BIOMEDICAL RESEARCH APPLICATIONS OF SIMULATED HEMODYNAMICS

Technical advances in patient-specific vessel surface reconstruction and CFD simulations, as well as increased computational power, enable biomedical engineers to model hemodynamic information in the human vascular system. Based on this evolution, several applications have emerged, such as the validation of patient-specific flow modeling, the influence of hemodynamic parameters on vessel wall mechanics and on disease initiation, and the flow prediction after a virtual treatment procedure. Here the domain experts try to test hypotheses related to the role of hemodynamics in CVDs by investigating the leading questions **BD<sub>1</sub> - BD<sub>4</sub>** that were mentioned in Section 3.2.3. Although some limitations still exist and are mostly found in simplified boundary conditions, patient-specific CFD modeling has the potential to support the concept of personalized medicine to aid therapeutic decision making [180]. In the following, we present prominent biomedical applications with a focus on cerebral aneurysms.

### 3.6.1 Verification and Validation

Early research in CFD blood flow simulations tried to mimic experimental studies by using idealized vessel geometries and boundary conditions. With the capabilities to simulate patient-specific hemodynamics, new studies are feasible that offer a significant advantage over simulations with idealized model assumptions. It is now possible to identify common hemodynamic flow behavior across a range of subjects, examine inter-subject variability and draw meaningful conclusions about quantitative and qualitative hemodynamic parameters in a particular CVD. The reliability of these studies, however, has to be proven by verification and validation of the CFD simulations, which relies on answering question **BD**<sub>1</sub>. However, *verification studies* of the CFD models, e. g., the comparison between numerical and analytical solutions, have received very little attention up to now [321].

Most of the work focuses on the validation aspect by comparing CFD simulations with *in vitro* and *in vivo* measurements. The main problem, however, consists in the lacking ground truth of the real flow. As stated in Section 2.5, flow measuring modalities, such as 4D PC-MRI, Doppler US or PIV, are also not capable of capturing it. Nevertheless, as long as no ground truth can be obtained, the comparison between CFD simulations and flow measurement seems to be well accepted in the community. This is motivated by the assumption that the measured flow depicts the underlying hemodynamics most reliably [322]. Note, this assumption relies more on *in vitro* than on *in vivo* experiments. The latter are difficult to control and exhibit a more limited spatiotemporal resolution than *in vitro* experiments.

Ford et al. [107] demonstrated a good agreement between clinical image data of a giant aneurysm and *virtual angiograms* as well as *residence time maps* that were derived from CFD simulation results. For the virtual angiograms, they simulated the attenuation of X-rays through the computed 3D contrast-agent flow dynamics. They extended their work with a comparison between CFD velocity profiles and *in vitro* PIV data of patient-specific carotid and cerebral aneurysms [106]. The study showed an overall good agreement between measured and simulated velocity values for both magnitudes and spatial distributions. Large vortex structures correlated in both modalities throughout the cardiac cycle. For some spatial locations, however, CFD simulations overestimated the speed values and showed discrepancies compared to PIV with respect to complex flow patterns.

Similar results were obtained by Buchmann et al. [45], who compared flow speed, vorticity and WSS distributions obtained from CFD simulations with PIV measurements at selected cross-sections of a carotid artery model. The simulated flow speed results demonstrated a very good agreement with the PIV results with a maximum and average flow speed error of  $\approx 11\%$  and  $\approx 6\%$ , respectively. The vorticity profiles have shown very similar flow behavior in terms of size and location of vortical flow structures as well as in vorticity distributions, with a maximum error of  $\approx 10\%$ . The WSS error ranges from 1% to  $\approx 30\%$  depending on the location of the cross-sections. In each case, the simulated results exhibit larger magnitude values.

In Ku et al. [196], a study is presented that reports a very strong correlation between predicted CFD velocity patterns and experimental data obtained using 2D PC-MRI in an *in vitro* large artery bypass model. The comparison revealed a maximum difference of 6% in terms of the volumetric flow rate, a very good



agreement regarding speed profiles but a slight to strong discrepancy of the flow rates and flow directions. The greater the distance of the cross-section planes from the inlet, the greater the differences in the results.

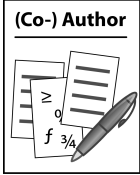
This was also observed in a work that was carried out by the author of the thesis to investigate the agreement between CFD simulation and *in vitro* 4D PC-MRI measuring (7 T) of flow in a cerebral aneurysm model [124]. The aneurysm silicone model is shown in Figure 25a, and the reconstructed surface mesh from a TOF-MRA image dataset is presented in Figure 25b together with an illustration of the flow direction. Furthermore, two cross-section planes  $P_1$  and  $P_2$  are indicated, which were used to sample the measured and simulated flow data. Plane  $P_1$  is placed near to the inlet with a cross-section diameter of about 6 mm and plane  $P_2$  is placed near to the outlet with a diameter of about 3 mm. The acquired 4D PC-MRI dataset was post-processed as described in Section 3.3.1 and exhibits a spatial resolution of  $1.0 \times 1.0 \times 1.0$  mm with a temporal resolution of 94.4 ms.

For the CFD simulation, the vessel surface and volume grid was generated according to the processing steps that were described in Section 3.4. Subsequently, the blood flow was modeled as incompressible Newtonian fluid with the time-dependent volumetric flow rate profiles from the measurement as boundary conditions. The measurement and simulation comprised a whole cardiac cycle of about 1 sec., from which 10 time steps were extracted for the investigation. Before the comparison was performed, the measured data was linearly interpolated on the CFD volume grid. The comparison at  $P_1$  and  $P_2$  comprised a qualitative analysis with respect to flow patterns and a quantitative analysis with respect to the average volumetric flow rate and flow speed.

The qualitative comparison is performed with a color-coded arrow glyph plot of the probed velocity values shown in Figure 25b and Figure 25c for  $P_1$ , and in Figure 25f and Figure 25g for  $P_2$ . The glyphs are color-coded according to the speed. For plane  $P_1$ , the flow pattern and flow speed distribution show a good agreement but for plane  $P_2$  they exhibit strong discrepancies. Furthermore, the measured flow tends to be more complex than the simulated flow, especially at  $P_2$ . In Figure 25e the quantitative comparison for  $P_1$  is shown and reveals a very good agreement between the two modalities. By contrast, there is only a moderate agreement between the two quantities at  $P_2$  although the profile development for the cardiac cycle is similar, as shown in Figure 25h. We conclude that the defined boundary conditions for the simulation retained near to the inlet and diverged with increased distance to the inlet. For both planes, the quantitative comparison shows higher flow rate and magnitude values in the case of the CFD simulation, which confirms observations from other groups [45, 196].

We identified two main reasons for the observed discrepancies:

- (1) On the one hand, the qualitative discrepancy with respect to the flow complexity may result from the simplified simulation model. It is possible that this model was not able to describe the complex flow behavior that was observed in the measured flow. On the other hand, the measured and post-processed flow still contains some noise and inaccuracy, which may lead to the disturbed flow patterns. This becomes more relevant for plane  $P_2$ , where at most only three voxels captured the flow at the vessel cross-section.



Gasteiger et al. [124]

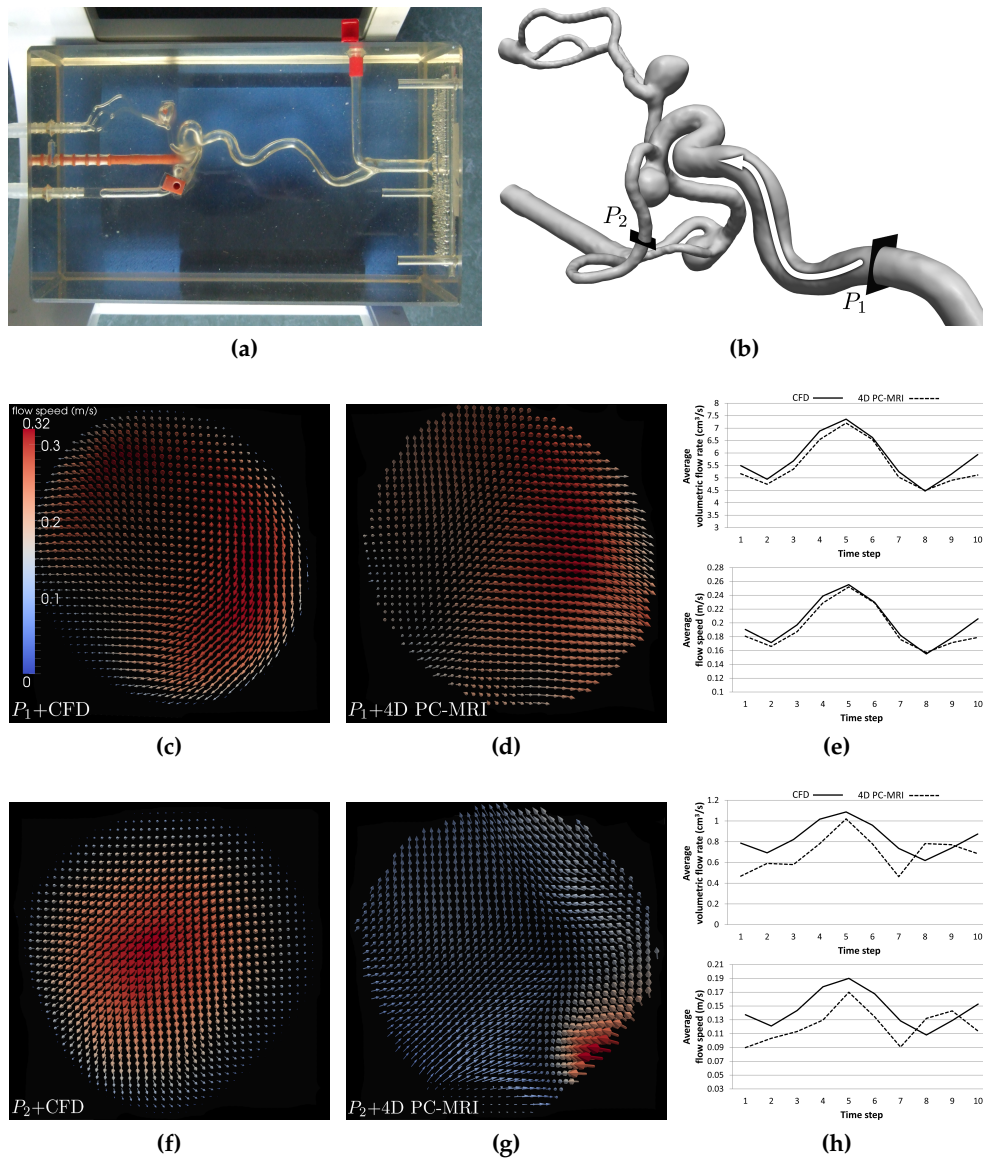


**Figure 25:** Comparison of flow hemodynamics between CFD simulation and *in vitro* 7 Tesla 4D PC-MRI measuring. Measuring and simulation are based on a cerebral aneurysm silicon model (a) and its reconstructed surface (b). A qualitative (color-coded arrow glyphs) and quantitative (average flow speed and flow rate) comparison at two cross-section planes near to the inlet ( $P_1$ ) and near to an outlet ( $P_2$ ) is performed. The comparison at  $P_1$  demonstrates strong correlations but for  $P_2$  the correlation is weak. Although the profiles of the quantitative values are similar, the CFD values are always higher than measured values for the cardiac cycle.

- (2) The quantitative discrepancies between  $P_1$  and  $P_2$  result from different flow medium properties that are used in the measurement and the simulation. The viscosity and density of the simulated flow medium were lower than those of the medium for the measurement. As a result, the spatiotemporal flow quantities developed faster in the simulation than in the measurement.

In addition to *in vitro* validations, *in vivo* comparisons between CFD and PC-MRI are also made. Boussel et al. [41] investigated the correlation between 4D PC-MRI (1.5 Tesla) and CFD simulation of blood flow in three patients with cerebral aneu-

rysms. They observed a strong correlation of the flow patterns and a moderate correlation in terms of flow speed, WSS and MWSS. Although the locations of high and low values show good agreement, the absolute magnitudes of these quantities reveal greater discrepancies, e.g., significantly larger WSS and lower MWSS values for 4D PC-MRI. Similar results were obtained by Isoda et al. [167] and Cebal et al. [66], who observed high agreement in flow patterns and moderate correlation regarding quantitative parameters, such as WSS, MWSS and OSI. The absolute flow speed values are also higher in CFD simulations compared to the measured values with a difference of 5-50%, depending on the selected location. In general, as the vessel diameters become smaller, larger differences are observed between CFD and PC-MRI flow quantities. It turns out that the limited spatial and temporal resolution of 4D PC-MRI is an important factor for the discrepancies (see Sec. 2.5.2). For small vessel diameters, only a few voxel cover the vessel and the measured velocity information is averaged due to the partial volume effect, which introduces errors in the calculation of quantitative parameters.

In a recent work by Berg et al. [23], a flow comparison between CFD and 7 T 4D PC-MRI in a healthy *Circle of Willis* (CoW) and two cerebral aneurysms was performed. The author of the thesis was involved in the vessel segmentation and surface reconstruction of the CoW. Due to the higher magnetic field strength, an increased SNR was achieved compared to 1.5 or 3 Tesla measurements. Additionally, the spatial resolution was increased to  $0.8 \times 0.8 \times 0.8$  mm instead of the common  $1.0 \times 1.0 \times 1.6$  mm at the expense of longer scan times and smaller measured volumes. The qualitative comparison also shows a very good agreement for flow patterns and flow speed profiles with slightly larger values for the CFD simulation. Because of the higher SNR and larger spatial resolution, the quantitative comparison reveals an average discrepancy of  $\approx 20\%$ . This is significantly smaller than the previous works and leads to the conclusion that CFD is able to accurately predict intracranial velocity information when realistic geometries and boundary conditions are provided.

### 3.6.2 Hemodynamics and Vessel Wall Biomechanics

Experimental observations have shown the influence of hemodynamics on the histological structures of the vessel wall and vice versa. Moreover, there is widely accepted evidence that wall modifications by means of hemodynamic parameters play a critical role on the development and outcome of CVDs [53, 81, 323]. Thus, in addition to modeling patient-specific hemodynamics, CFD simulations are also exploited to investigate the role of biomechanical aspects in cardiovascular health, diseases and treatment, such as the correlation between coated stents and thrombus formation or restenosis. Considerable attention is being paid to the impact of hemodynamic parameters on the three arterial wall layers: *intima*, *media* and *adventia* [53]. Among these layers, the *intima* with its endothelial cells is of special interest since it responds directly to the chemical and mechanical stimuli of the flowing blood. This process of adaption is called *cell remodeling* and investigations to understand these processes are related to question **BD**<sub>2</sub>. Numerous studies have indicated that the endothelial cells respond differently to various hemodynamic parameters.

Two of the most studied parameters are the WSS and OSI, which are suggested as important factors for the pathogenesis of vascular diseases such as atherosclerosis and aneurysms [72]. A uniform and laminar shear stress field tends to stretch and align the cells in the direction of the flow. This is thought to be *atheroprotective*, which means a protection against the formation of atherosclerosis [81, 373]. A low WSS with a high OSI, however, causes a vessel wall thickening with irregular cell shape modeling. Although the induced wall thickness is protective for aneurysm formation, this process also switches the cells from *atheroprotective* to *atherogenic*, which promotes atherosclerosis. Related to the processes of atherosclerosis development, there is also a need for ongoing research for a better understanding of plaque development and its rupture, which can cause strokes, pulmonary embolisms or heart attacks [72, 323].

Furthermore, the influence of WSS and OSI on aneurysm formation and its progression is not well understood. It is known that the local vessel wall dilatation arises from degeneration of *elastin* and the smooth muscles, with an associated increase in collagen production. For the initiation of this process, high WSS combined with increased flow speed and pressure has been demonstrated in recent studies [68, 234]. A disagreement, however, exists regarding the aneurysm growth and rupture due to a progressive wall weakening, with two schools of thought: *high-shear stress* and *low-shear stress* [42, 233, 301]. Proponents of the low-shear stress theory claim that low WSS and high OSI cause intimal damage and inflammation due to aggregation or blood components. This leads to the progressive degeneration of the wall.

The high-shear stress theory explains the wall weakening as being due to an increased production of *nitric oxide* (NO) caused by abnormally high WSS. The overexpression of NO results in a lower arterial tone owing to the scarcity and apoptosis, i. e., cell death, of smooth muscle cells and pathological wall remodeling. Moreover, an excessive level of WSS leads to a dysfunction and finally to a destruction of the endothelial cells. Because of this disagreement, further investigations are necessary to obtain a coherent understanding of the correlation between shear stresses and the aneurysm progression.

### 3.6.3 Hemodynamics and Risk Assessment of Cerebral Aneurysms

In addition to investigations about the role of hemodynamics in the initiation of a CVD, there is also considerable interest in its application for cardiovascular risk assessment, which refers to research question **BD<sub>3</sub>**. A prominent application here is the assessment of cerebral aneurysm rupture risk. As stated in Section 2.3, each aneurysm bears a high risk of rupture with fatal consequences for the patient. A reliable assessment of the rupture risk is desired mainly for the following two reasons:

- As soon as an aneurysm is detected, preventive interventions are commonly considered because of the poor prognosis of an SAH. Each treatment, however, bears a certain risk, which can exceed the natural risk of rupture. Thus, the treatment of an aneurysm has to be balanced against its rupture risk. Providing a precise risk assessment would be very valuable for the clinicians and patients in their decision process.



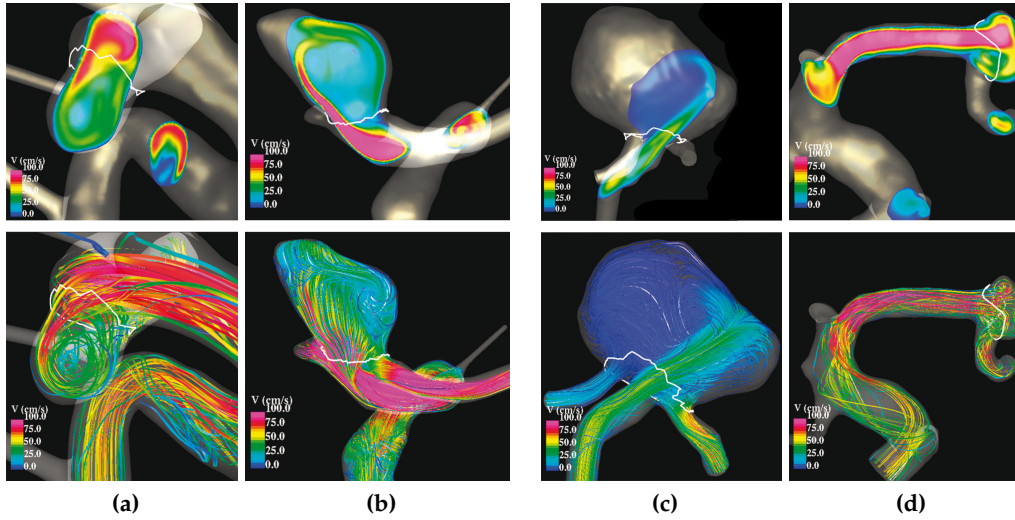


**Figure 26:** Qualitative hemodynamic parameters that seem to be correlated with an aneurysm rupture: (a) simple vs. (b) complex flow pattern and (c) concentrated inflow jet with small impingement zone vs. (d) diffuse inflow jet with large impingement zone. (Images reprinted from Cebal et al. [63] © ASNR 2011 with kind permission of the American Society of Neuroradiology.)

- In cases of multiple aneurysms, which one is most likely to rupture and should be treated first?

As indicated in the previous section, the mechanisms that promote the progression of an aneurysm, including its rupture, are not well understood. They involve a complex interplay between hemodynamics, biomechanical wall properties, aneurysm morphology and interaction with structures around the aneurysm, so-called *peri-aneurysmal environment* [12, 301]. Currently, the strongest clinical predictor for rupture and for treatment decisions is the aneurysm size, which is the maximum aneurysm diameter. Larger cerebral aneurysms are more likely to rupture than smaller aneurysms [363]. However, small aneurysms do rupture and morphological information alone may not be sufficient to assess the rupture risk [108]. Thus, several studies propose and demonstrate that hemodynamic parameters are important indicators for an increased risk of cerebral aneurysm rupture.

One of the most relevant research efforts has been performed by Juan Cebal (George Mason University, Fairfax, USA) and colleagues in recent years. In two consecutive studies, they propose a flow classification system consisting of four qualitative hemodynamic parameters that exhibit an association with aneurysm rupture: *flow complexity*, *flow stability*, *inflow jet concentration* and *size of the impingement zone* with respect to the aneurysm sac surface (see Sec. 3.2.2) [62, 63]. In Figure 26, examples of a simple vs. a complex flow pattern as well as a concentrated inflow jet with a small impingement zone vs. a diffuse jet with a large impingement zone are presented. Based on a total of 272 aneurysm datasets, the authors have shown that ruptured aneurysms were statistically more likely to have complex and unstable flow patterns (over 70%) or a concentrated inflow jet with a small impingement zone (over 65%). This confirms recent findings by other researchers like Xiang et al. who identify significant morphological and hemodynamic parameters that discriminate intracranial aneurysm rupture [370]. In a pop-

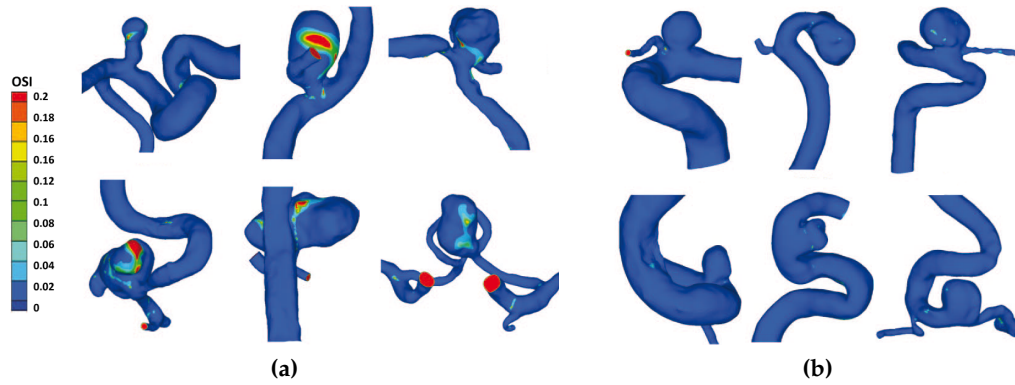


**Figure 27:** Association between high OSI values for ruptured aneurysms (a) compared to low OSI values for unruptured aneurysms (b). However, the location of high OSI does not correlate to the location of rupture. (Images reprinted from Xiang et al. [370] © Wolters Kluwer Health 2010 with kind permission from Wolters Kluwer Health.)

ulation of 119 aneurysms (38 ruptured, 81 unruptured) they observed a complex flow pattern with multiple vortices in over 60% of the ruptured cases and simple flow patterns with a single vortex in over 75% of all unruptured aneurysms.

One limitation of these studies, as with most previous studies, consists of the reconstructed surface models of the ruptured aneurysms. All models are derived from image data that were acquired *after* the event of rupture. The studies are performed with the assumption that the aneurysm geometry with its simulated hemodynamic parameters is not substantially affected by the rupture. A ruptured aneurysm, however, can undergo a variety of structural and hemodynamical changes during or after an SAH, such as a thrombus formation or daughter bleb formation [67]. Therefore, it may be necessary to obtain the aneurysm geometry based on the image data shortly before the rupture occurs to compare the ruptured and unruptured cases.

Two of these very rare cases are presented by Cebal et al.[57] and Sforza et al. [300], who each separately performed a hemodynamic study of a cerebral aneurysm that was imaged a few hours before an SAH occurred. Both studies found that the aneurysms exhibited a concentrated inflow jet that hit a small region of the aneurysm sac and created a complex intra-aneurysmal flow structure. Thus, these insights are consistent with the results of the aforementioned studies.

By contrast to these qualitative flow parameters, however, insights about quantitative parameters are less consistent. As mentioned in the previous section about low and high shear theories, related studies showed different observations with respect to WSS. Xiang et al. demonstrated that ruptured aneurysms had lower WSS magnitudes and larger areas of low WSS than unruptured aneurysms [370]. Cebal et al. [64] performed a similar study with 210 datasets that indicates higher WSS and MWSS values for ruptured aneurysms. In the aforementioned case investigated by Cebal et al.[57] for the aneurysm just before it ruptured, elevated WSS was only observed near to the impingement zone while the rest of the aneurysm surface exhibited low WSS. This was also observed in the case studied by Sforza et al. [300]. With respect to the OSI, consistent observations were made that in most cases high OSI values were observed for ruptured aneurysms compared to the unruptured cases shown in Figure 27a and Figure 27b, respectively [370].

### 3.6.4 Virtual Treatment Planning for Cerebral Aneurysms

In Section 3.4 we explained the concept of *personalized medicine* to tailor the prevention, management and treatment of a patient-specific disease, which refers to research question **BD**<sub>4</sub>. The virtual treatment planning of cerebral aneurysms fits into this concept by focusing on a *personalized endovascular procedure* due to coiling and stenting (see Sec. 2.3.2). Both procedures are being performed more and more because they have several advantages over a surgical clipping, e.g., a decreased treatment risk and shorter hospital stay. Currently, relevant treatment decisions, such as the type of coils, stents or flow diverter as well as their placement, depend mainly on the experiences of the neuroradiologist. Additionally, the outcome of the procedures in terms of aneurysm embolization and changed hemodynamics is less predictable.

In order to support and optimize therapeutic decisions, considerable research is performed to promote a patient-specific pretreatment simulation of coiling and stenting [10, 86]. In this context, the following section focuses on *virtual stenting* because of the increased confidence in multiple stents or specialized flow diverters alone being capable of inducing an embolization by re-establishing the physiological blood flow. Recent advances in *virtual coiling* can be found in the work of Wei et al. [355] and Morales et al. [241].

The overall goal of virtual stenting is to predict which stenting options are most appropriate for a given patient-specific aneurysm. For this, four aspects are of primary interest:

- development of a specific stent design and constraints,
- a reliable deployment of the stent,
- a robust CFD grid generation and
- the alteration of hemodynamics in terms of stent design and placement.

An efficient method for deploying stents with an arbitrary shape has recently been proposed by Larrabide et al. [204]. This method is based on a *simplex deformable*

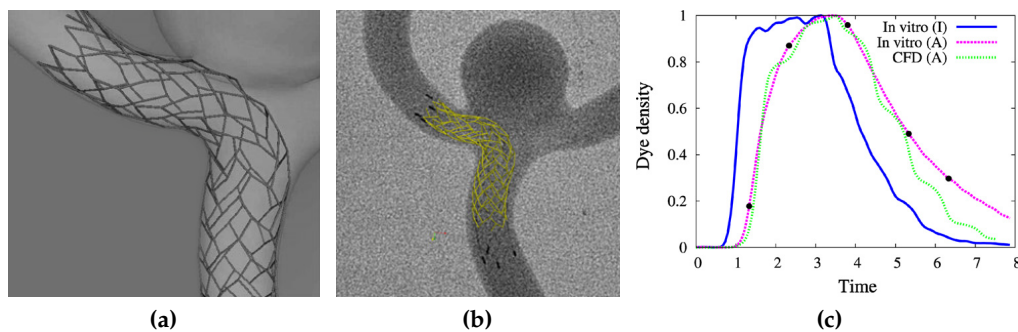


**Figure 28:** Comparison between virtual stent deployment and in vitro experiments. In (a) the virtual released stent geometry is presented and overlaid over the in vitro result (b). The time-density curves from the in vitro experiment in the inlet (I, blue) and in the aneurysm (A, pink) as well as in the aneurysm for the CFD simulation (A, green) is shown in (c). (Images reprinted from Larrabide et al. [204] © Elsevier 2012 with kind permission from Elsevier.)

*model*, which incorporates constraints of the stent geometry, such as strut pattern and the angle between struts. An *in vitro* evaluation with two real stents released in a silicone phantom shows good qualitative and quantitative agreement. The two stents were previously reconstructed from micro-CT image data and deployed virtually in the phantom model. For the evaluation, a comparison was made of the time curves of the contrast agent density, the fill-in/wash-out behavior by means of CFD-simulated virtual angiograms and the overlays between *in vitro* and virtual releases are. In Figure 28, the comparison for one stent type is shown with the final released virtual stent geometry (Fig. 28a, the overlay with the *in vitro* result (Fig. 28b) and the time-density curves from the *in vitro* experiment in the inlet (I), in the aneurysm (A) and in the aneurysm for the CFD simulation (A) (Fig. 28c). The comparison shows good agreement between the virtual and *in vitro* stent released geometry as well as between the wash-in phases. Stronger differences occur in the wash-out phases, where the contrast is transported away from the aneurysm faster in the CFD than in the *in vitro* experiment.

Once a stent has been deployed, a valid numerical grid, i. e., "watertight", of the stent and vessel geometry must be generated, which can be tedious and challenging to create. Appanaboyina et al. [10] presented an effective automatic approach to accomplishing this task by means of adaptive Boolean and mesh refinement operations. Based on the resulting CFD grid, they performed several pre- and post-stenting simulations to investigate the alteration of the hemodynamics in terms of different stent strut shapes, stent-parent vessel configurations and positions. Their results demonstrated an overall reduced inflow rate and maximum flow speed as well as a disturbed and redirected inflow jet, shown in Figure 29. Depending on the stent configurations, the intra-aneurysmal flow circulation can be changed, e. g., from counter clockwise to clockwise and the magnitude of WSS can increase or decrease.

These findings are confirmed in other related studies, which also reveal additional insights into flow diverter performance and rupture risk [60, 182, 243, 319]: First, the performance of flow diverters in modifying intra-aneurysmal flow can be substantially reduced by increasing the porosity of the mesh. This observation may help in selecting appropriate flow diverter diameters and mesh design adjustments. Second, flow diverters can lead to a rupture after their deployment due to increased intra-aneurysmal pressure and flow changes in the parent vessels, especially in giant aneurysms. These adverse effects, however, are still not well understood and should be considered for further investigations.

**VIRTUAL INTRACRANIAL STENTING CHALLENGE:** In the context of virtual stenting, the annual *Virtual Intracranial Stenting Challenge* (VISC) was launched and is becoming a standard test case in computational minimally-invasive cerebrovascular intervention [12, 56]. The objective of this challenge is to assess the ability of academic groups to provide clinical partners with valuable pre-treatment hemodynamic information for a given patient-specific cerebral aneurysm and flow diverter design. Depending on the given case, the groups have to partly or completely perform the data acquisition pipeline proposed in Section 3.4. The used methodology, simulation parameters and computation times, software and hardware choices as well as stent performances are compared between the participants. The members of the MoBeStAn project (see Sec. 1.4) have successfully participated in the VISC



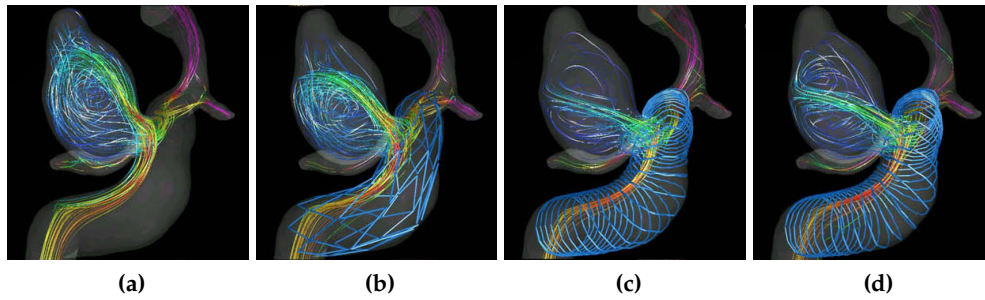


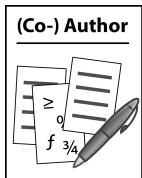
**Figure 29:** Qualitative comparison of different virtual stent types on the altering of the intra-aneurysmal flow behavior depicted with color-coded streamlines: (a) without stent, with (b) Neuroform stent, (c) left helical stent and (d) right helical stent. The most effective stent in terms of a reduced inflow is the left helical stent. (Images reprinted from Appanaboyina et al. [10] © Elsevier 2009 with kind permission from Elsevier.)

several times, where the author of this thesis was involved in the aneurysm surface reconstruction and geometric processing [168, 169]. Without going into details, only one complex case from VISC 2010 will be briefly discussed. Further details are described in Janiga et al. [169].

A 3D-RA dataset, several DSA images of a wide-necked giant aneurysm and the geometry of two common commercial flow diverters were provided by the VISC organizers. The flow diverters were a *SILK* (Balt International, Montmorency, France) and a *Neuroform* (Boston Scientific Neurovascular, Fremont, Canada) stent, both presented in Figure 30a. The tasks consisted in:

- (1) a reliable aneurysm surface reconstruction,
- (2) the selection of an appropriate stent configuration in terms of stent type, position and deployment,
- (3) a reliable blood flow modeling and CFD simulation,
- (4) a meaningful blood flow analysis to provide information about the most appropriate configuration for that case.

A volume rendering of the cerebral aneurysm was already presented in Figure 16d and exhibits a weakly defined vessel boundary and blending artifacts. Due to the image artifacts, only a manual image segmentation was applicable and the reconstructed surface was validated by our clinical corporation partner with the help of the DSA images. For each configuration a hybrid volume grid (prisms and tetrahedrons) was generated and the blood flow was modeled as Newtonian flow with rigid vessel walls. With respect to the individual stent deployment, a free-form deformation scheme by Botsch and Kobbelt [37] was applied. For the deployment, the clinical partner was also involved to discuss and validate the final stent positions. In Figure 30b, the reconstructed surface, the resulting color-coded streamlines without stent and the labeled inlet *A* and outlets *B* to *F* are shown. In order to identify the most appropriate stent configuration, the authors considered the flow stasis in the aneurysm and the degree of parent vessel occlusion. The flow stasis can be computed with the turnover time (see Eq. 9) and is an indicator of thrombus formations. The prevention of parent vessel occlusion is crucial to ensure a sufficient blood supply to subsequent brain regions and can be estimated by



Janiga et al. [168]

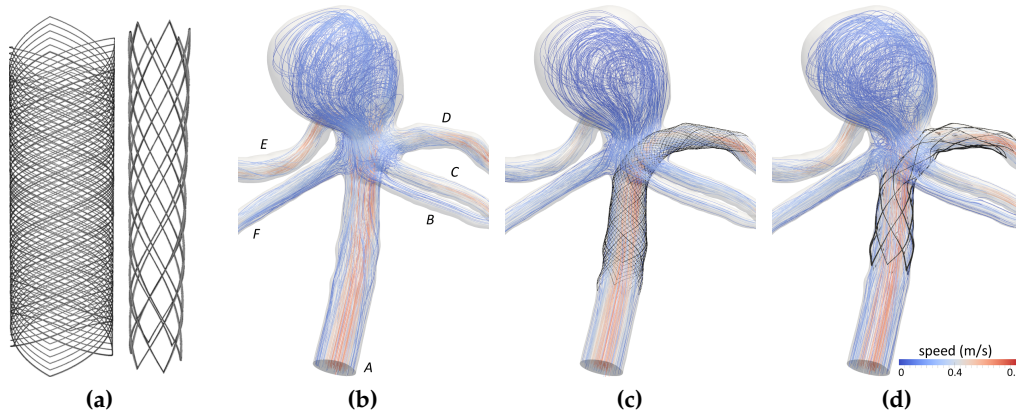


**Figure 30:** Different stent configurations and resulting intra-aneurysmal flow behavior for the VISC 2010 challenge. The SILK and Neuroform stent geometries are shown in (a, left) and (a, right). Each stent type was deployed in various parent vessel configurations, which are indicated in (b). The SILK stent (c) achieved the best performance compared to the Neuroform stent (d) in terms of decreased inflow rate and increased turnover time. For both stents the best results were obtained for the parent vessel configuration A-to-D. (Stent data is courtesy of the VISC committee. Flow data is courtesy of Gábor Janiga.)

considering the flow rate at each outlet. Among all stent configurations, the SILK stent within the parent vessel *A-to-D* was identified as the best solution, presented in Figure 30c. In comparison to the configuration without a stent, the inflow rate into the aneurysm was reduced by 57%, the turnover time was increased by 77% while sufficient blood supply to the other outlets was ensured. The best results for the Neuroform stent were also achieved within the parent vessel *A-to-D* but with a lower stent performance compared to the SILK stent.

The Neuroform stent only achieved an inflow rate reduction of 21% and a turnover time increase of 24%. Figure 30d shows the changed flow behavior that demonstrates a higher inflow speed compared to the SILK stent. This results from the higher porosity of the Neuroform stent. Thus, the performance of a flow diverter depends on both its mesh design and its deployed position. These findings demonstrate that virtual stenting is capable of supporting clinical treatment decisions. However, without knowledge of the material properties of the vessel wall and a reliable thrombus model, the accuracy of results are limited. This should be considered for incorporating the results in an intervention planning.

### 3.7 SOFTWARE TOOLS AND FRAMEWORKS

In the previous sections, we presented several processing steps and techniques for the data acquisition and data analysis of cardiovascular hemodynamics. A workflow-driven and integrated solution is necessary to support studies on large multicenter and multi-population datasets for providing clinically pertinent information as stated in the introduction of this chapter. Currently, no all-in-one software solution exists that is able to carry out all steps. Domain experts in both domains use different scientific software tools and packages that range from in-house implementations and academic solutions to commercial products. However, there is also ongoing research and development with a focus on the integration

of several processing steps into one software solution. In this section, we present a brief overview of some software tools, packages and frameworks, which are grouped into:

- data acquisition for simulated data,
- post-processing of 4D PC-MRI datasets,
- techniques for hemodynamic data analysis and
- integrated software tools.

Here we do not intend to provide an exhaustive list but a representation of established solutions in these domains and tools that we have identified as being efficient in daily practice. Some of the tools and frameworks can be used for several purposes, e. g., image and geometric processing as well as data analysis. Hence we refer to them in the corresponding subsection.

### 3.7.1 *Data Acquisition Simulated Datasets*

The data acquisition for simulated datasets comprises the highest number of processing steps, ranging from vessel segmentation to surface reconstruction and volume grid generation to the CFD simulation itself (see Sec. 3.4). We present freely available and commercial tools that can be utilized to accomplish these processing steps. Some of them can also be used for the post-processing of the 4D PC-MRI datasets.

#### 3.7.1.1 *Segmentation and Surface Reconstruction*

Similar to the large amount of image segmentation algorithms that have been proposed, there are also various tools that implement most of them. We focus on those tools that include the methods presented in Section 3.4.2. Furthermore, we present some tools that provide algorithms for the subsequent surface extraction.

**ITK and VTK.** The *Insight Segmentation and Registration Toolkit (ITK)* and *Visualization Toolkit (VTK)* (Kitware Inc., Clifton Park, New York, USA) are very popular open-source and cross-platform libraries written in C++ for image processing and visualization methods. Both libraries can be easily extended and integrated into customized frameworks and they work on various data types as well as dimensions. ITK here focuses on medical image data and provides an extensive list of segmentation methods including the approaches mentioned in Section 3.4.2, such as thresholding, region growing and level set. Since ITK does not address visualization tasks it can be complemented with VTK to accomplish the surface reconstruction by means of the Marching Cubes algorithm. Moreover, VTK offers methods for surface smoothing and geometric processing, such as Laplacian smoothing and cutting. It also provides various visualization algorithms for scalar, vector, tensor and volumetric datasets supported by 2D and 3D interaction widgets.

**MeVisLab.** A comprehensive and modular framework for medical image processing and visualization is found in the cross-platform system **MeVisLab** (Fraunhofer MEVIS, Bremen, Germany). It supports rapid prototyping developments by assembling various processing modules into data-driven, hierarchical networks

(see Fig. 31a). These modules comprise basic and advanced image processing and visualization modules including methods for segmentation and registration, volume and surface rendering as well as for quantitative morphological and functional analysis. For example, it implements the MPUI approach of Schumann et al. [296] to achieve smooth vessel surfaces from a binary segmentation mask. MeVisLab also integrates the aforementioned ITK and VTK libraries, which extend the functional features of the framework significantly. Each module is expandable with C++ and the framework offers a flexible graphical user interface (GUI) definition controlled by scripting functionalities (Python and JavaScript). Thus, the framework is useful for users with both advanced and less advanced programming experience to perform complex segmentation, geometry and visualization tasks. For academic research the platform is freely available but not fully open-source.

### 3.7.1.2 Geometric Processing

For software tools regarding geometric processing, we rely mainly on capabilities to prepare the vessel surface for the subsequent volume grid generation. This involves surface artifact removal, cutting and remeshing. We refer to the integrated software tools in Section 3.7.4, which provide further geometric methods such as centerline extraction and branch splitting.

**Blender and 3D Studio Max.** For geometric editing, established modeling tools such as the freely available **Blender** (Stichting Blender Foundation, Amsterdam, The Netherlands) or the commercial **3D Studio Max** (Autodesk GmbH., Munich, Germany) (see Fig. 31b) are useful due to their graphical interaction schemes and modeling capabilities. Both cross-platform tools work on various surface mesh formats and provide graphical modeling tools such as surface cutting and extrusion, mesh refinement and deformation as well as primitive editing, such as vertices or triangles. Thus, they are more flexible and adaptive to geometric processing than MeVisLab or VTK. No programming skills are necessary but for a particular vessel processing pipeline they can be customized by means of scripting functionalities.

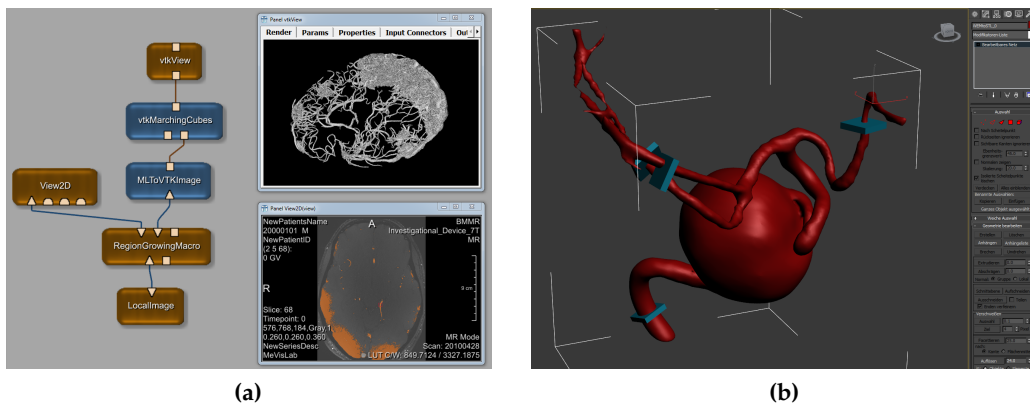


**Figure 31:** (a) Example network in the rapid prototyping framework **MeVisLab** for image segmentation and surface reconstruction. The integration of **ITK** and **VTK** modules extends the capabilities of this framework. (b) Scene setup of **3D Studio Max** for trimming the inlets and outlets of cerebral aneurysms after surface reconstruction.

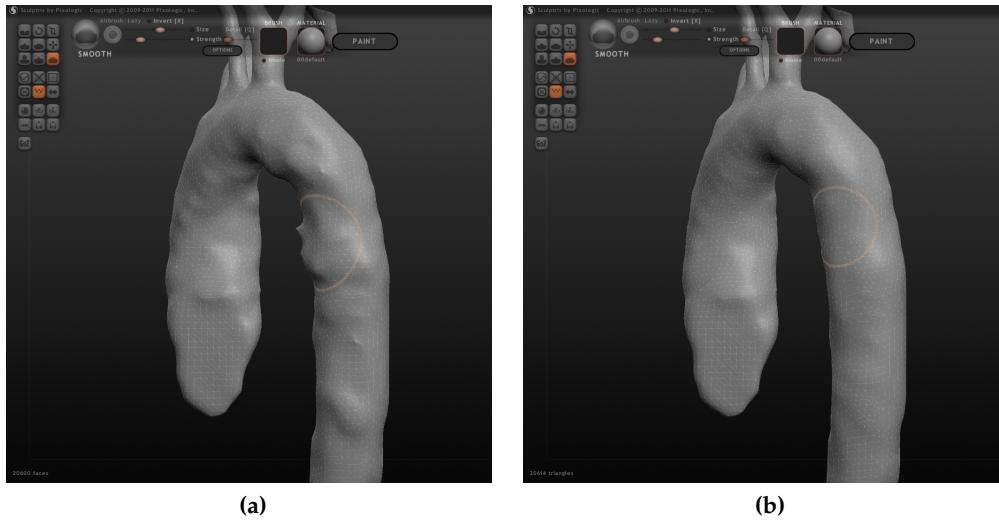


**Figure 32:** Example of surface smoothing in **Sculptris** for an aorta surface: (a) application of the smooth brush (red circle) on noisy regions results in smoothed surface regions (b).

In terms of usability Blender requires a longer training period compared to 3D Studio Max due to its complex GUI and interaction design.

**Sculptris.** An interesting tool that complements classical modeling tools is the cross-platform and freely available sculpting software **Sculptris** (Pixologic Inc., Los Angeles, USA). It focuses on an intuitive virtual sculpting procedure by considering the underlying mesh as *virtual clay*. Sculptris provides intuitive sculpting *brushes* such as drawing, flattening and smoothing as well as an advanced local tessellation approach of the mesh. The tool constantly analyzes the surface curvature and dynamically increases or decreases the mesh resolution depending on the detail created by the brush. With respect to vessel geometry processing, it can be used to facilitate surface smoothing and vessel remodeling. This is shown in Figure 32a where a smoothing brush (reddish) is placed over a noisy vessel part of a reconstructed aorta. In Figure 32b, the surface noise has been removed after several applications of the smoothing and drawing brush.

**NetGen.** For surface remeshing, the freely available and open-source tool **NetGen** (Johannes Kepler University Linz, Austria) can be utilized to obtain high-quality surface triangulations. It implements an advancing front algorithm based on abstract rules that control new vertex placements and edge connections starting from certain feature edges. Feature edges are identified either when the angle between the two normals of adjacent triangles is larger than a given threshold or by user-defined selections. After the initial mesh is generated, the quality of the triangulation is improved by applying several local operations, such as edge flipping or vertex movement, according to an error functional. Settings for the mesh granularity and quality can be adjusted by the user or are encapsulated in templates. Further information about the underlying approach can be found in Schöberl et al. [295]. It is important to note that NetGen only works on two-manifold input meshes. This prerequisite is not always given and manual effort is necessary to correct these meshes, e. g., with Blender or 3D Studio Max.



### 3.7.1.3 Volume Grid Generation

The generation of volume grids is supported by many open-source and commercial tools. The application depends mainly on the specific finite element problem, the spatial domain (2D/3D), and the type of finite elements, e. g., triangular, tetrahedral or hybrid. We refer to three established tools and software packages that are able to automatically generate high-quality grids with an adaptive grid refinement.

**NetGen and TetGen.** **TetGen** (Weierstrass Institute, Berlin, Germany) or the aforementioned NetGen can be utilized as freely available and open-source tools for the volume grid generation. Both grid generators enable an adaptive tetrahedralization of an input mesh but they are conceptually different. NetGen employs its advancing front algorithm to fill the interior with tetrahedral elements starting from the optimized surface mesh. The grid density depends on a user-defined element size and curvature radius, which ensures adaptive grid density in small vessel branches.

The approach of TetGen is based on the Delaunay tetrahedralization and its refinement [303]. Here the mesh quality is controlled by a user-defined quality measurement that is defined as the ratio of the circumradius of an element to its shortest edge. In comparison to NetGen, the TetGen approach achieves better distributions and size adaption of the tetrahedral element, e. g., a higher element density at the vessel wall. This results from the Delaunay tetrahedralization, which is able to insert new vertices at arbitrary locations on the surface during the refinement. A detailed comparison and evaluation can be found in Fedorov et al. [103]. In neither tools, however, are prism elements used to model the vessel boundary layers (see Sec. 3.4.4). Thus, an increased number of elements is necessary to cover the boundary layers with an appropriate density, leading to an increased computation time in the subsequent CFD simulation.

**ANSYS ICEM CFD™.** The generation of hybrid grids, e. g., tetrahedrons and prisms, can be achieved with the commercial software **ANSYS ICEM CFD™** (ANSYS Inc., Berkeley, CA, USA). It also integrates several geometric processing steps in one workflow by providing a complete meshing suite including surface remeshing, surface and grid repair as well as mesh simplification. Furthermore, it is robust in terms of non-two-manifold surface meshes that can contain holes, T-junctions and overlaps.

### 3.7.1.4 CFD Simulation

In general, CFD simulations are complex and several requirements should be fulfilled, such as robust convergence behavior, flexible parametrization of the flow model and the capability to deal with huge volume grids. We present two established and validated tools that provide appropriate solvers to fulfill these requirements in most cases.

**ANSYS Fluent®.** For CFD simulations the commercial software **ANSYS Fluent®** (ANSYS Inc., Berkeley, CA, USA) is widely used and well validated by academic researchers. It is often combined with its complemented tool ANSYS ICEM CFD™ for remeshing and volume grid generation. Among others things, it includes solvers for steady and unsteady Newtonian and non-Newtonian fluids as well as capabilities for fluid-structure interactions. ANSYS Fluent® is numerically robust

in terms of boundary conditions and high-resolution volume grids, which is necessary to reliably model complex blood flow in various morphology vessel configurations. It provides a user-friendly GUI and well-balanced parallel scalability in terms of network computations. Some of the functionalities, however, act as *black boxes* and provide no direct control by the user. Additionally, a great financial investment is necessary to purchase the software system with a restrictive license policy for multicore usage.

**OpenFOAM®.** Due to some limitations of commercial CFD tools, such as *black box* behavior, license restrictions and high costs, the development of freely available and open-source CFD software packages has been increasing in recent years. Here, **OpenFOAM®** (OpenCFD Ltd., Bracknell, UK) is one of the most relevant CFD tools that is being used more and more frequently as an alternative in academic research and companies. Similar to equivalent commercial products, it offers flexible solver capabilities to model complex blood flow or other engineering applications, such as chemical reactions or combustion processes. Being open-source, OpenFOAM® provides users with complete control to customize and extend its existing functionality and solvers for a particular case. Additionally, the tool integrates volume grid generation and its manipulation as well as post-processing tools, e. g., VTK, to analyze the simulated datasets. In comparison to ANSYS Fluent®, however, it is less robust in terms of high-resolution volume grids and convergence behavior.

### 3.7.2 Post-Processing 4D PC-MRI Datasets

The post-processing of 4D PC-MRI datasets includes image artifact reduction, vessel segmentation to mask the velocity information in the vessel lumen from the static tissue and the generation of a vessel surface mesh to provide anatomical context information (see Sec. 3.3).

**Velomap-Tool.** The Velomap-Tool is an in-house implementation proposed by Bock et al. [28] that was developed in the research group of Michael Markl. It is implemented in **Matlab** (MathWorks Inc., Natick, Massachusetts, USA) and focuses on the reduction of all relevant image artifacts in 4D PC-MRI datasets, such as the correction of background phase distortions, the removal of phase wraps and the reduction of noise. The tool provides a user-friendly GUI and a tailored workflow to accomplish each artifact reduction. Additionally, it supports the computation of the PC-MRA image, which can be utilized for a subsequent segmentation of the vessel lumen.

**MeVisLab.** The prototyping platform MeVisLab has already been presented as a software framework to accomplish segmentation and surface reconstruction tasks for the data acquisition of simulated datasets. Due to its medical image processing capabilities and expandability, MeVisLab can also be utilized to accomplish all relevant post-processing steps for measured flow datasets. Standard noise reduction filters can be applied and the framework can be extended with customized modules that implement the algorithms to carry out further artifact reduction, PC-MRA and TMIP image computation. The subsequent vessel lumen segmentation, static tissue masking and vessel surface extraction can also be performed by the image processing and visualization modules provided. Here MeVisLab benefits from the



integration of ITK and VTK as well as other third-party libraries and interfaces, such as Lapack and a Matlab interface.

### 3.7.3 Data Analysis

In Section 3.2.4 we presented several established techniques for the qualitative and quantitative data analysis of hemodynamic information. Domain experts utilize either in-house software developments or available tools that are applicable to investigate multidimensional datasets. Most of these tools, however, are tailored to the engineering domain and their usability varies greatly. In the following, we present three tools and frameworks that combine a qualitative and quantitative analysis.

**EnSight.** The most utilized software system for data analysis in both domains is the commercial scientific visualization software **EnSight** (CEI Inc., Apex, North Carolina, USA). EnSight provides a rich set of several interaction and visualization techniques for qualitative analysis such as 2D contour drawing, interactive MPR views, isosurface rendering, pathlines and vortex core line extraction. It also offers standard quantification capabilities such as data curve plotting, WSS computation for measured flow data and volumetric flow rate estimation. More advanced quantifications can be achieved by exporting the sampled velocity information into external software packages such as Matlab or **Microsoft Excel**<sup>®</sup> (Microsoft Inc., Redmond, Washington, USA). The software is able to handle large, unsteady datasets and supports various structured and unstructured data grid types and data formats. An example of data analysis with EnSight is presented in Figure 33a for flow analysis in the aorta. In the middle view, the aorta surface is shown with four color-coded cross-section planes to quantify the flow at these locations according to the mean WSS vector and the mean volumetric flow volume. Corresponding plots and time curves are presented on the left and right side for two planes. However, discussions with our domain experts reveal that the utilization of EnSight for large-scale studies is limited. It is not tailored to a user-driven flow analysis in complex blood vessels, which often leads to a high user interaction effort for standard analysis tasks such as the placement and alignment of cross-section planes.

**QFlow.** The commercial software package **QFlow** (Medis, Leiden, The Netherlands) aims for a highly accurate quantification of 4D PC-MRI flow data and is designed for utilization by clinicians. The software can be embedded in a clinical environment, provides data post-processing in terms of background phase distortions and phase wraps, and offers a (semi-)automatic detection of vessel borders. Furthermore, it provides an automatic calculation of certain flow quantities like volumetric flow rates and the regurgitant fraction. An example of these analysis methods is shown in Figure 33b for the quantification of the mean flow speed in the aorta and the pulmonary artery. Due to its tailored workflow, quantitative analysis on large-scale studies is feasible. The capabilities for a qualitative analysis, however, are very limited and only comprise the color-coding of flow speed values in the 2D vessel contour.

**ParaView:** A freely available and well-known open-source data analysis tool is **ParaView** (Kitware Inc., Clifton Park, New York, USA), which is based mainly on VTK. Similar to EnSight, it offers qualitative and quantitative techniques for

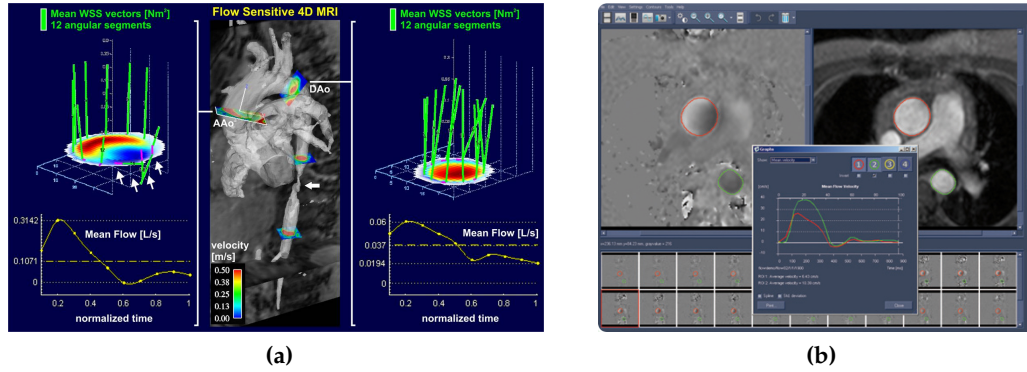


**Figure 33:** Software tools and packages for qualitative and quantitative analysis of hemodynamics in clinical research applications: (a) placement and alignment of probing planes with calculation and visualization of WSS in **EnSight**, (b) depiction of flow volume profiles over the cardiac cycle in **QFlow**.

large datasets and supports various data formats and grid types. Among other things, ParaView provides curve plots, streamlines, pathlines and 3D widgets for cross-section planes and seed point placement. Its capabilities can be extended by integrating your own functionalities thanks to its open-source interface and VTK integration. Since ParaView aims for a generic scientific data visualization, it is not tailored to the analysis of blood flow in vascular systems. As a consequence, it exhibits the same limited applicability for large-scale studies due to a time-consuming and tedious interaction effort, especially for non-experienced users.

**MeVisLab** In the context of data analysis, the already presented prototyping platform MeVisLab can be utilized. The various qualitative and quantitative analysis methods offered, the capability to implement tailored analysis methods and the generation of a flexible GUI facilitate the development of a customized data analysis tool. However, the modular-based concept of MeVisLab requires programming skills and considerable time to develop such an analysis tool.

### 3.7.4 Integrated Software Tools

In the previous sections, we presented available software tools, packages and frameworks to perform the data acquisition, processing and analysis of simulated and measured datasets. For the data acquisition and analysis of simulated datasets, several tools are necessary that are not adapted to the cardiovascular domain. This results in time-consuming interaction efforts, data exchanges and conversions. Tools that are adapted to the post-processing and quantitative analysis of measured flow datasets require additional tools for the qualitative analysis. Integrated software solutions that provide an adaptive workflow for measured and simulated flow ensure faster data acquisition, processing and analysis. This would provide the basis for large-scale and multicenter studies to extract clinically pertinent and reproducible results. In the following, we present some of these tools grouped into solutions for measured and simulated hemodynamics.

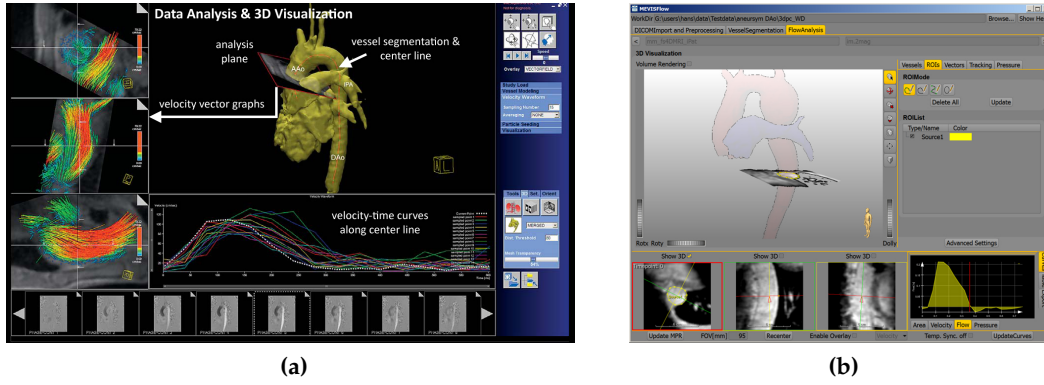


**Figure 34:** Examples of integrated software tools for standard qualitative and quantitative analysis of 4D PC-MRI datasets: (a) **SIEMENS 4D flow** and (b) **MEVISFlow**. Among other things, both tools enable workflow-driven and semiautomatic dataset post-processing (e. g., artifact reduction and vessel segmentation), flow quantification and visualization by means of probing planes, integral lines and particles. (Image (a) is from Barker et al. [20]).

#### 3.7.4.1 Integrated Solutions for 4D PC-MRI Datasets

The subsequent two solutions for 4D PC-MRI datasets integrate all relevant post-processing steps as well as a qualitative and quantitative data analysis. They are either freely available or exist as preliminary implementations in clinical workstations.

**SIEMENS 4D Flow.** As a manufacturer of MRI scanners, the engineering and electronics company Siemens also equips its associated workstations with several clinical applications for 2D PC-MRI blood flow analysis. With **SIEMENS 4D Flow** (Siemens Healthcare, Siemens AG, Erlangen, Germany) the vendor presents its first software prototype that is fully embedded in a clinical workstation for 4D PC-MRI data analysis [20]. Although it is still under development and evaluation, the tool allows a straightforward and time-efficient analysis of quantitative and qualitative hemodynamic parameters directly after data acquisition. It starts with a semi-automatic artifact reduction, vessel segmentation and surface extraction. Subsequently, various data analysis and visualization methods are provided, supported by intuitive interaction schemes. Among other things, the tool offers an interactive *point-and-click* definition of cross-section planes, emitter planes and vessel center line calculations, as well as profiles for volumetric flow rates, mean flow speed and flow visualizations with color-coded pathlines and vector glyphs as presented in Figure 34a.

**MEVISFlow.** A similar but academic software solution is called **MEVISFlow** (Fraunhofer MEVIS, Bremen, Germany) [96, 152] shown in Figure 34b. In comparison to the SIEMENS 4D flow tool, MEVISFlow offers the calculation and visualization of pressure difference maps [222] and a connectivity analysis considering uncertainty caused by image noise. Furthermore, pathlines can also be color-coded according to curvature, direction and their emitter region. MEVISFlow is based on MeVisLab and can be obtained free of charge for academic usage and clinical evaluation.

### 3.7.4.2 Integrated Solutions for Simulated Flow Datasets

Software solutions for simulated hemodynamic datasets integrate most of the necessary data acquisition steps and provide several data analysis methods. Similar to integrated software solutions for 4D PC-MRI datasets, they aim for a streamlined workflow and intuitive interaction schemes tailored to the domain experts. In the following, we present three tools that are mostly freely available. None of the presented tools, however, integrate the CFD simulation part due to its complexity and requirements regarding robustness and convergence behavior. Thus, available CFD simulation packages, such as OpenFOAM® or ANSYS Fluent®, are still required as an intermediate processing step.

**AngioLab.** The most relevant tool is the **AngioLab** (Universitat Pompeu Fabra, Barcelona, Spain), which is based on the **GIMIAS** platform (graphical interface for medical image analysis and simulation) [205]. GIMIAS is a freely available and open-source framework dedicated to developing software prototypes for biomedical image computing and simulations in research and clinical usage. The AngioLab suite focuses on cerebral aneurysms and provides a workflow from automatic image segmentation to morphological vessel characterization, virtual treatment and visualization of CFD results (see Fig. 35a). It includes advanced geometric processing tools, e. g., correction of fused vessel sections, centerline extraction [7] and aneurysm decomposition (see Fig. 35b).

The morphological characterization comprises the derivation of shape descriptors and standard quantifications, such as aspect ratios and aneurysm volume. The descriptors are based on invariant Zernike moments [236], which allow shape matching independent of the orientation or scale of the geometry. They are used to compare the new patient's aneurysm and its nearby vessels with other aneurysms that were treated previously and are stored in a database. Thus, it supports the clinician in the therapeutic decision making. The virtual treatment planning fo-

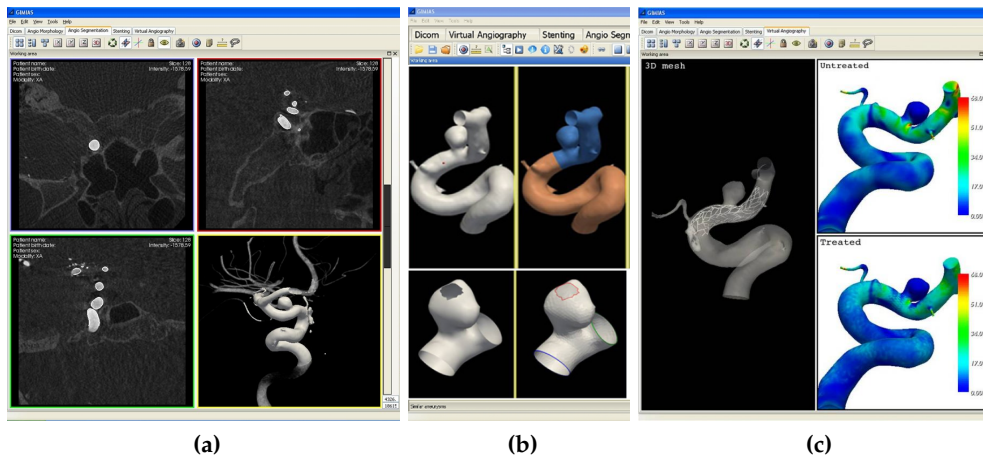


**Figure 35:** Screenshots from the **AngioLab** suite as an example of an integrated and workflow-oriented software system for simulated flow datasets. The workflow consists of (a) vessel and aneurysm segmentation, (b) surface generation and geometric processing (e. g., inlet and outlet cutting) as well as (c) virtual stent deployment and qualitative data analysis of the resulting hemodynamic information. (Images from project website of the **GIMIAS** platform.)

cuses on virtual stenting [204] and coiling [241] consisting of flow diverter and coil type selection, placing and deployment. After virtual treatment, the CFD simulation can be performed in external software packages and the resulting datasets can be compared with the untreated case. The comparison consists of qualitative data analysis methods, such as surface color-coding and streamlines (see Fig. 35c). Additionally, AngioLab is capable of creating and to reviewing clinical reports containing all the information that is obtained during the anamnesis and data analysis. However, the suite does not support the generation of a numerical volume grid.

**Mimics® Innovation Suite.** A similar tool to AngioLab but with a slightly different focus of application is the commercial software package **Mimics® Innovation Suite** (Materialise, Leuven, Belgium). Among other things, the tool is developed for cardiovascular engineering on patient-specific anatomy to support the treatment planning of CVDs. Here it focuses more on surface reconstruction, accurate patient-specific implant planning and the rapid prototyping of these implants, such as aortic aneurysm devices, flow diverters and heart replacements, for physical experiments or education. The capabilities of the suite range from (semi-)automatic image segmentation and quantification, e.g., grade of aortic calcification and 2D/3D measuring, classification of the pathology based on statistical models, access root planning and geometric processing methods. These methods include surface cutting, centerline extraction, remeshing and the generation of a volume grid, which can subsequently be delivered to an external CFD simulation package.

In contrast to AngioLab, however, image and surface artifacts, such as under segmentations and vessel fusions, cannot be corrected. Furthermore, the capabilities of a quantitative and qualitative analysis of the CFD results are very limited. They only comprise standard surface coloring of scalar values and provide no additional exploration methods such as probing or streamlines.

**VMTK.** A fairly well known tool in the bioengineering community is the *Vascular Modeling Toolkit* **VMTK** (Orobix, Bergamo, Italy). This open-source toolkit represents the framework of Antiga et al. [8], which we already mentioned in Section 3.4.2 for the vessel segmentation. VMTK focuses mainly on vessel segmentation, 3D reconstruction, geometric analysis, numerical grid generation and surface data analysis of blood flow vessels. It provides an interactive guided level set segmentation, centerline extraction based on embedded Voronoi diagrams, surface cutting and remeshing, as well as the generation of numerical volume grids that consist of prisms and tetrahedrons. Furthermore, VMTK offers automatic methods for splitting a vascular tree into its constituent branches and robustly mapping these branches to a rectangular parametric space [9]. This mapping facilitates investigations and comparisons of surface-based quantities, e.g., WSS or OSI, between a population of different vessel models or datasets. Besides this surface data analysis, no further visual exploration approaches for the hemodynamic information are provided. All segmentation and geometric processing techniques are based on ITK and VTK as well as other libraries such as NetGen and TetGen. By means of a limited user interface, each technique can be applied and composed via a simple scripting language. A workflow-driven GUI support, however, is not available and can only be accomplished by integrating the VMTK capabilities into a separate application.



### 3.8 FURTHER READING

In Section 3.2.1 and Section 3.2.2, we presented relevant quantitative and qualitative hemodynamic parameters that are investigated in relation to the presence, evolution and outcome of CVDs. Further parameters have surfaced and been the focus of several studies in recent years. Cebal et al. [64] propose several quantitative parameters that are also seen as indicators for cerebral aneurysm ruptures, such as a high *inflow concentration index*, a large *shear concentration index* and a low *viscous dissipation ratio*. This is complemented by Baharoglu et al. [17] who identified an obtuse *inflow angle* between flow in the parent vessel and the aneurysm dome axis as corresponding to an increased risk of rupture. The severity of valvular and vascular stenoses can be assessed by *pressure difference maps*, which can be simulated or derived from 4D PC-MRI datasets [96, 98]. Improved PC-MRI acquisition has led to reliable *turbulence* quantifications that are used to assess pressure drops over stenoses, thrombus formations and in the development of atherosclerosis [97]. Turbulence and *flow separation* are investigated qualitatively by Markl et al. [222] in 4D PC-MRI of the heart and great vessels in healthy subjects and pathological cases. For example, increased turbulence behavior was observed in the descending aorta after an aortic coarctation. This correlates to reports about higher turbulence values in stenoses [97].

An interesting work was recently proposed by Meng et al. [233] in terms of the high and low WSS controversy for the growth and rupture of cerebral aneurysms (see Sec. 3.6.2 and Sec. 3.6.3). They hypothesized that this controversy is a manifestation of the complexity of three different aneurysm phenotypes: *small thin-walled*, *mostly thin-walled* and *entirely thick-walled*. Depending on the phenotype, high or low WSS can promote cerebral aneurysm growth and rupture.

First experiences of incorporating 4D PC-MRI flow acquisition and processing into the clinical workflow were recently proposed by Allen et al. [1]. A radiologist requested 4D PC-MRI for several pathological and post-surgical cases, e. g., aortic aneurysms and aortic valve repair, as additional flow information to standard 2D PC-MRI acquisition. In some cases the clinical impression changed and in most cases quantitative information was added due to 4D PC-MRI. The capability to investigate the time-resolved and volumetric flow may reduce dependence on time-intensive 2D PC-MRI acquisitions. However, the average percent difference in quantitative data was  $35 \pm 28\%$  and the average processing time for the 4D PC-MRI datasets was  $88.5 \pm 22.5$  min. Nevertheless, the authors conclude that the incorporation is feasible and has the potential to impact clinical assessment in multiple cardiovascular pathologies and post-treatment situations. This was also confirmed by Ansari et al. [6], who presented a study to determine whether 4D PC-MRI flow acquisition could provide insights into intracranial arteriovenous malformation hemodynamics and to report the changes in flow observed during induced embolization.

An intensive discussion about the validation and verification of simulated hemodynamics as well as uncertainty throughout the data processing pipeline from image acquisition to the final simulation is given by Garbey and Davies [122]. Among other things, they emphasize the importance of accurate and reproducible vessel surface reconstructions since vessel geometry has the greatest influence on the subsequent simulated hemodynamic parameters such as velocity and WSS.

In this context, Hong et al. [155] proposed a new vascular reconstruction approach based on *implicit generalized cylinders*. For this model-free method, a set of locally constructed general cylinders with arbitrary cross-sections are smoothly blended along a given vessel skeleton. The cylinders are implicitly generated by means of summed up 2D piecewise algebraic splines that represent individual vessel cross-sections along the skeleton. Compared to the MPUI approach of Schumann et al [296] (see Sec. 3.4.3), the proposed method achieves a higher geometric smoothness and is more robust in terms of noise. However, the approach depends on a reliable vessel segmentation and a comparison to the improved MPUI method by Wu et al. [369] was not performed. A comparative study of the latest surface reconstruction methods for vascular structures was recently conducted by Wu et al. [368]. The authors evaluated the strengths and weaknesses of these methods and investigated the applicability of each method for several specific applications.

In the discussion about uncertainty in simulated hemodynamics by Garbey and Davies [122], the authors suggest establishing a large database of patient-specific simulations that not only cover one heartbeat but also the various conditions of the patient during daily life. Along with clinical trials, this database would lead to a more realistic flow impression of a patient and may provide statistically valid hemodynamic indicators for vascular diseases. Effective data mining and statistical analysis methods on a large number of patient studies would be challenging but is vital to derive clinically pertinent information. Further open problems in computational hemodynamics and artery wall mechanics are discussed in Taylor and Humphrey [323]. Among other things, they emphasize the need for research that synthesizes complementary advances in related research domains such as molecular biology, biomechanics and computational methods for purposes of increasing the understanding of vascular physiology and pathophysiology as well as improving the design of medical devices and clinical interventions.

### 3.9 SUMMARY AND IMPLICATIONS FOR THE THESIS

Quantitative and qualitative hemodynamic parameters play an important role for the understanding of the initiation and evolution of CVDs. These parameters are investigated in two areas of application: the *clinical research domain*, which uses mainly 4D PC-MRI flow data, and the *biomedical research domain* for which simulated flow data is mainly utilized. The goals for the clinical research are to obtain a better understanding of normal flow behavior in healthy subjects and how abnormal flow may promote or worsen CVDs. This knowledge is complemented by biomedical researchers who focus on a more detailed view of correlations between hemodynamic parameters and the underlying mechanisms for the initiation and outcome of CVDs. Moreover, due to advances in CFD simulations, biomedical researchers are able to support the concept of *personalized medicine* regarding personal risk assessment and therapeutic decision making for certain CVDs.

Depending on the area of application, the analysis of hemodynamic parameters involves several stages, which are summarized in Figure 36. For the clinical research domain, patient-specific 4D PC-MRI flow datasets are acquired and processed. The processing stage consists of image artifact reduction, vessel segmentation to mask static tissue and surface extraction for anatomical context visualizations. In the case of the biomedical research domain, patient-specific vas-



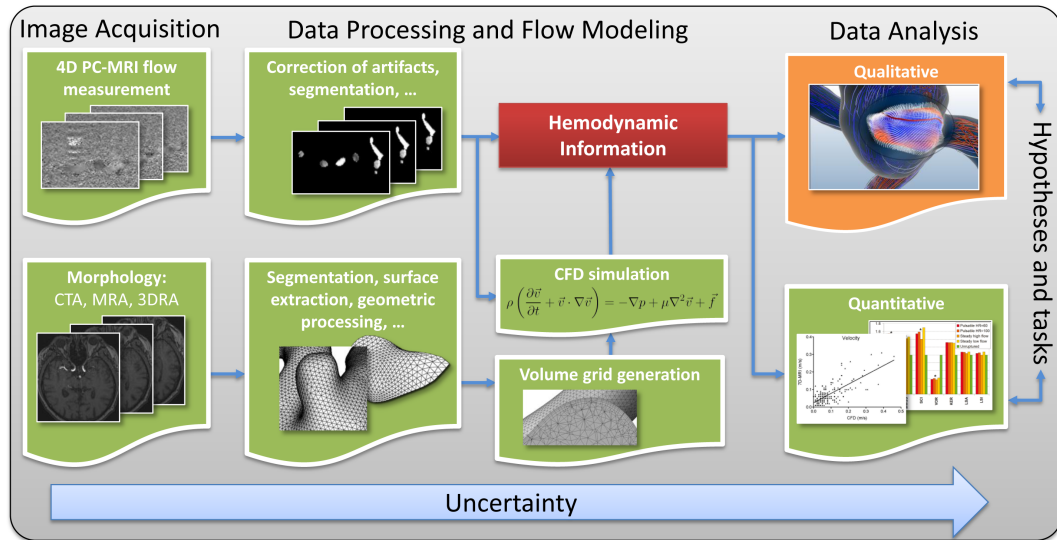


**Figure 36:** Summary of the workflow pipeline for measured and simulated hemodynamic information. The workflow primarily consists of four stages: image data acquisition, data processing and flow modeling as well as data analysis. The contributions of this thesis focus on qualitative analysis by means of visual exploration approaches. Each stage of the pipeline is accompanied by uncertainty due to various error sources, such as data discretization, filtering and mapping to graphical primitives.

cular image data are acquired by means of CTA, CE-MRA or 3D-RA. In order to obtain simulated flow datasets, the image data need to be processed in terms of vessel segmentation, surface extraction and geometric processing, an optional deployment of flow diverters, volume grid generation and blood flow modeling. The blood flow modeling is carried out by CFD simulations with patient-specific boundary conditions that are derived from the 4D PC-MRI datasets such as flow speed and pressure profiles. Finally, the hemodynamic parameters obtained are analyzed qualitatively and quantitatively to evaluate hypotheses or to conduct certain tasks.

For both domains, it is important to emphasize that *no ground truth* about the real underlying flow is available yet and the accuracy of the acquired hemodynamics is limited. CFD simulations are very sensitive to the reconstructed vascular geometry and are often based on simplified boundary conditions such as no fluid-structure interaction due to missing properties of the vessel wall. Flow measuring with 4D PC-MRI suffers from a limited spatial and temporal resolution as well as from image artifacts during the acquisition process. Several studies, however, have demonstrated a moderate to strong agreement between simulated and measured hemodynamic parameters. Comparisons with other flow measurement methods, such as Doppler US and PIV, can be used to further validate the accuracy of both modalities. The reliability of the hemodynamic information is also influenced by the data analysis. The data filtering, discretization and interpolation as well as data mapping to graphical representations such as streamlines or pathlines introduce errors that have to be considered for the final flow interpretation. Thus, at each stage of the flow data acquisition, processing and analysis *uncertainty* is involved, which is challenging to quantify.

Despite these limitations, the aforementioned workflow pipeline is well accepted in both domains and provides the foundation for further improvements. In this

context, this thesis focuses on improved visual exploration approaches in qualitative data analysis for both the hemodynamic parameters and their enclosing vessel anatomy (highlighted in Fig. 36). Semi-automatic, reproducible and expressive visualization methods are necessary to obtain clinically pertinent and consistent information based on large-scale and multicenter datasets. Based on the previous sections and the literature review, several implications for the visual exploration can be made, which motivate the major goals of this thesis and are briefly summarized:

**Goal 1:** There is a verifiable association between the vascular blood flow and its enclosing vessel geometry. The hemodynamics are influenced by the surrounding vessel morphology and vice versa. Pathological vessel wall modifications can lead to a particular CVD. Thus, for an appropriate investigation of the hemodynamics, both types of information, flow and morphology, should be visualized together. However, this leads to an *embedded surface problem* where an expressive depiction of morphological features and visibility of the embedded flow information must be guaranteed. Classical approaches of clipping or semi-transparency do not fulfill this requirement appropriately. The thesis aims for more advanced approaches that will support domain experts in the visual perception of both kinds of information.

**Goal 2:** There are several hemodynamic parameters that seem to have a strong influence on the outcome of a certain CVD. Some of these parameters are extracted in a time-consuming and non-standardized way combined with a non-expressive visualization. For large-scale patient studies on multicenter datasets, these kinds of procedures are not appropriate because they do not ensure reproducibility and comparability. Furthermore, they do not support a user-friendly and streamlined investigation of the parameters. Two particular examples are the *inflow jet* and *impingement zone* for cerebral aneurysms [63]. Thus, the thesis aims for an automatic detection and expressive visualization of both qualitative parameters to support domain experts in their corresponding investigations.

**Goal 3:** Domain experts are often interested in the correlation between multiple hemodynamic parameters, such as flow speed, pressure and WSS. For a detailed investigation, they often group them into focus and context parameters, e. g., WSS (focus) and the underlying flow (context) [75]. Additionally, they investigate changes or differences in these parameters, which can result from different time steps or acquisition modalities, virtual treatment procedures or altered morphology. Domain experts need effective visual exploration approaches to obtain insights into these complex multiparameter datasets. Existing approaches present these data either in a multiparameter visualization or in a side-by-side view. Both approaches, however, can lead to visual clutter and occlusions or require increased mental effort in terms of the spatial correlation between individual parameters. The thesis aims for a way to overcome these disadvantages by developing a *focus-and-context approach* that provides spatial correlation and flexible visual filtering.

Before we go into details, a general overview of related flow visualization and

exploration techniques is presented. Some of these techniques and approaches provide the foundations to achieve the goals of this thesis.

#### 4.1 INTRODUCTION

With the advent of hemodynamic data acquisition, visual exploration techniques are an essential part of the data analysis process. The complex nature of these datasets requires an effective visual depiction and exploration of their multivariate and multidimensional characteristics. In its basic form, however, the hemodynamic data consists solely of the steady or unsteady flow velocity information, in particular flow direction and speed. Thus, classical vector field visualization techniques, which were proposed not explicitly for the clinical or biomedical research domain but more for a broader branch of applications, e. g., engineering and the modeling of weather systems) can be applied. Due to the increased relevance and complexity of hemodynamics, it emerged that these established methods were often not adapted to the needs and requirements of the domain experts. Therefore, the visualization community has identified an exciting new research area in recent years. Newly adapted and efficient approaches are being developed, which aim for both expressive visualizations and effective exploration schemes.

This chapter summarizes most of the related works in this area and complements both the existent qualitative data analysis methods presented in Section 3.2.4 and the theoretical background for further contributions made by this thesis. Contributions, in which the author of the thesis participated as co-author, are also incorporated here. The chapter starts with a general overview of flow visualization techniques, which aim for a more expressive depiction of flow information (Sec. 4.2). Based on these methods, more adaptive approaches are presented that focus on hemodynamic data (Sec. 4.3), in particular on cardiac and aortic flow as well as on cerebral hemodynamics. Great potential lies in the incorporation of illustrative visualization methods. Thanks to their capability of simplification and increased visual perception, they support domain experts in flow exploration and interpretation. Finally, the chapter concludes with a discussion about the presented methods and how some of the concepts may be suitable for subsequent contributions of the thesis (Sec. 4.4).

#### 4.2 GENERAL FLOW VISUALIZATION

Flow visualization is one of the classic branches of scientific visualization. Over the last two decades, a considerable amount of techniques have been proposed that have been designed for different types of data and information the users want to extract. Since a comprehensive survey of this variety of techniques is out of the scope of this thesis, only a brief introduction, categorization, and recent developments are given. The interested reader is referred to the more elaborated state-of-the-art surveys by McLoughlin et al. [230] (geometric-based), Salzbrunn et al. [288] (partition-based) and Laramée et al. [202] (topology-based).

#### 4.2.1 Challenges

Advances in flow modeling and increased computational power lead to a large and complex amount of flow data that needs to be processed and visualized appropriately. The acquired multiparameter datasets consist of multivariate data with more than one dependent variable, such as velocity and temperature, as well as multi-dimensional data with more than one independent variable, such as 3D and 4D. Thus, the selection of appropriate visualization techniques is a challenging task and depends on the characteristics of the flow dataset, field of application and information that is to be extracted. There are a number of challenges that visualization scientists have to tackle [230]:

**Large datasets, computation times and irregular grids.** From a technical point of view, the handling of large amounts of data with its spatiotemporal distribution on regular and irregular (also called unstructured) grids is one of the main issues that need to be resolved. For example, some visualization techniques compute integrated geometry that is tangential to the velocity field, such as streamlines or pathline particles. The data processing and presentation of these visualization results should ideally be achieved at interactive frame rates to provide an efficient exploration. Thus, a lot of research has been devoted to these topics and a tremendous performance improvement has been achieved with the advent of modern graphics processing unit (GPU) hardware in recent years. However, the possibility of transferring the data processing and visualization from the central processing unit (CPU) to the GPU depends mainly on the grid type and the visualization technique [47]. While for regular grids appropriate approaches exist, data processing on irregular grids is still challenging and non-trivial [230, 291]. Furthermore, the portability is restricted to the limited amount of GPU memory in current hardware, which often leads to a performance bottleneck.

**Seeding and interaction.** All geometric-based methods require a seeding location within the data domain from which discrete geometry is integrated tangentially to the velocity field. Also for some direct flow visualization techniques certain seeding or placement locations are necessary. The location, shape, orientation, and size of the resulting geometry ultimately represents the underlying flow behavior. As a consequence, capturing all the relevant flow features, such as vortices, critical points or laminar flow, depends mainly on the position and spatial frequency of the seeding locations. This is even more challenging for 3D than for 2D due to the balance between coverage, occlusion and visual complexity. In the case of time-dependent datasets the temporal location of the seeding also becomes important. Thus, effective seeding strategies are necessary to support domain experts in placing and distributing seeding objects. Among other things, these should include interaction schemes for 3D localization, geometry filtering and (semi-)automatic identification of semantically relevant seeding regions.

**Visual perception.** As for other visualization domains, a particular challenge in flow visualization is the visual depiction of the extracted information. The visualization methods should ensure an appropriate perception of the spatiotemporal and multivariate flow characteristic. This primarily involves a balance between coverage and filtering, appropriate color scales, resolving occlusions and visual clutter, and enhancement depth perception and spatial correlation. In terms of visual complexity, appropriate simplification techniques are necessary, which still

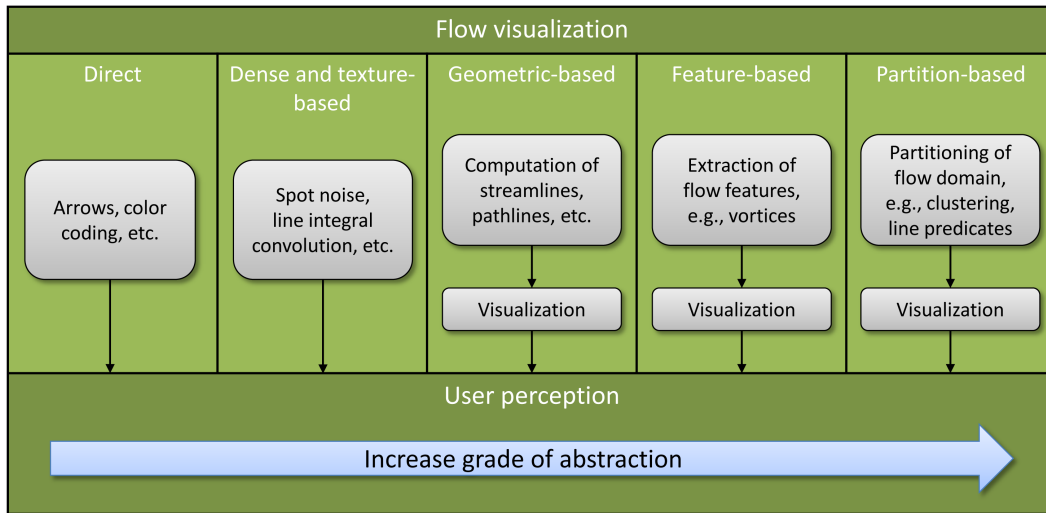


**Figure 37:** Overview about the categorization of flow visualization methods. For geometric-, feature- and partition-based methods some preprocessing steps are necessary before the final visualization can be applied. From direct to partition-based techniques the grade of flow abstraction is increasing. (Image adapted and reprinted from Salzbrunn et al. [288].)

convey all the relevant flow information to support decision-making and scientific discovery. These considerations also play an important role in the usage of animation to depict time-dependent flow behavior, especially in 3D. Depending on how much experience the domain experts have, moving particles or animated surface deformations may not be intuitive or comprehensible for them. Thus, visualization researchers discovered the potential of illustration techniques and are motivated by both the extensive history and the success of these techniques, e.g., arrow glyphs or fanning in time [316, 347].

#### 4.2.2 Categorization

With the emergence of different types of datasets, fields of application and needs of the domain experts, more and more flow visualization techniques have been developed. Post et al. [266] proposed one of the first categorizations of these techniques, which was later partly extended by Laramée et al. [202, 203], Salzbrunn et al. [288], and McLoughlin et al. [230]. Based on these state-of-the-art reports, a categorization of existent flow visualization techniques is presented, which is summarized in Figure 37. With each of the subsequent five categories the grade of abstraction to depict the flow information is increasing.

##### 4.2.2.1 Direct Flow Visualization

Direct flow visualization techniques are the simplest approaches to depict flow behavior. They are applied directly to the sample points of the velocity field and consist mainly of color coding and glyph primitives. A common example is the placement of arrow glyphs where flow direction and speed are mapped to arrow direction, size and color. This is shown in Figure 38a for a synthetic 2D flow that passes a cylinder. The 2D domain is embedded as context information and



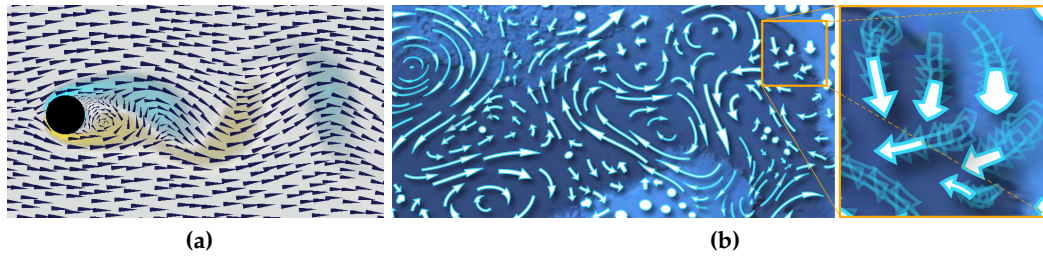


**Figure 38:** Examples of direct flow visualization methods. In (a) 2D arrowheads at each grid point indicate the direction and magnitude of flow with an embedded cylinder. The background is color-coded according to the clockwise (blue) and counter clockwise (yellow) flow vorticity. Arrow glyphs are also utilized in (b) for the visualization of ocean currents. Additionally, the glyphs are filtered to better capture local vortices. The close-up shows the arrow trajectories and the morphing of their glyph shape. (Image (a) reprinted from Kirby et al. [187] © IEEE 1999 with kind permission from IEEE, (b) reprinted from Jobard et al. [173] with kind permission from the Cornell University Library.)

color-coded according to the clockwise (blue) and counterclockwise (yellow) flow vorticity. A comprehensive overview of classic direct flow visualization techniques can be found in Hauser et al. [148].

Direct techniques are simple to implement, computationally inexpensive, and can be applied to time-dependent datasets. However, they may suffer from several disadvantages, such as visual clutter and occlusions (especially for 3D data domains) or distracting patterns in the case of uniform grids. Additionally, glyph primitives may lead to confused popping artifacts for time-dependent datasets during animations. As a result, considerable research effort has been made to minimize these problems, including appropriate glyph filtering, selective and adaptive glyph seeding strategies as well as smooth glyph transitions during animations. This is demonstrated in a recent work by Jobard et al. [173] and shown in Figure 38b. For a 2D ocean dataset dynamic arrow glyphs indicate the time-dependent flow where the trajectories and the morphing of the glyphs are additionally highlighted. These examples show also the possible combination of flow clustering and direct flow visualization to reduce occlusion and visual clutter. The arrow density in Figure 38b can be controlled by a custom 2D map to better capture local vortical structures.

#### 4.2.2.2 Dense and Texture-based Flow Visualization

Another category of flow visualization techniques is based on intensity functions or randomized noise textures that are stretched and smeared according to local flow properties. They can be applied to the whole data domain or to a subdomain, e.g., to a probing plane, and provide a dense representation of the underlying flow field including flow features, such as vortices and critical points. Existent techniques can be assigned to three main classes: *spot noises* [342], *line integral convolutions* (LIC) [52] and *texture advections* [226]. Spot noise techniques operate on unity intensity functions, so-called *spots* (e.g., ellipse-shaped), that are distributed over the data domain and warped over time to reflect the underlying flow field (see Fig. 39a). The widely used LIC techniques are based on a 2D or 3D noise texture where the texels are convolved along the path of streamlines using a filter



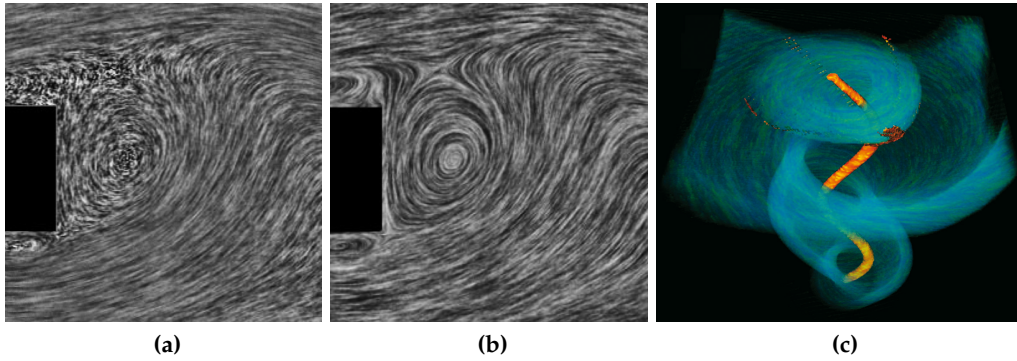


**Figure 39:** Examples of dense and texture-based flow visualization methods. The spot noise visualization in (a) of a 2D flow field with an obstacle does not capture small details in the flow field compared to the LIC visualization in (b) with its higher spatial resolution. A flow speed masking is applied to the 3D LIC visualization of a tornado dataset to reduce occlusions to the vortex core line (yellow-red tube). (Images (a) and (b) reprinted from Laramée et al. [203] © John Wiley and Sons 2004 with kind permission from John Wiley and Sons, (c) reprinted from Weiskopf et al. [360] © IEEE 2007 with kind permission from IEEE.)

kernel. Due to their higher spatial resolution, LICs reflect regions of high flow speed more accurately compared to spot noise techniques (see Fig. 39b). Texture advection methods achieve similar visual results to LICs but operate on *texels* (coinage of texture elements) or groups of texels that are moved according to local flow vectors. A detailed investigation of dense and texture-based techniques can be found in Laramée et al. [203].

Over the last decade, representatives of each class have been improved with respect to computation time, indication of flow orientation (upstream or downstream), capturing of high local change of speed and application on arbitrary surfaces [203]. The dense flow visualization for steady and unsteady 2D flow including surface flow is close to being solved. For 3D flow fields, however, the dense representation is still challenging, mainly due to perceptual issues, such as occlusions and visual complexity. For a reliable flow interpretation, appropriate spatial selection and visual filtering approaches are necessary that ensure both the visibility of and the context information about the 3D flow dynamic. Similar to volume rendering of scalar fields, established procedures for spatial selection are interactive volume clipping and mapping of flow properties to optical properties, respectively [359]. In Weiskopf et al. [360] the visual filtering of dense texture-based flow visualizations is accomplished by volumetric importance functions that map flow features, such as vortex core regions and flow speed to opacity, as shown in Figure 39c. As a result, features are enhanced and visual complexity in less interesting regions is reduced, while context information is still provided.

#### 4.2.2.3 Geometric-based Flow Visualization

An established category of flow visualization techniques is based on the extraction of geometric objects for which the shape is directly related to the underlying flow behavior. These geometric- or integration-based techniques define a set of seeding locations from which trajectories are computed that are used to construct the geometric objects. Common examples are (illuminated) streamlines (see Fig. 40a),

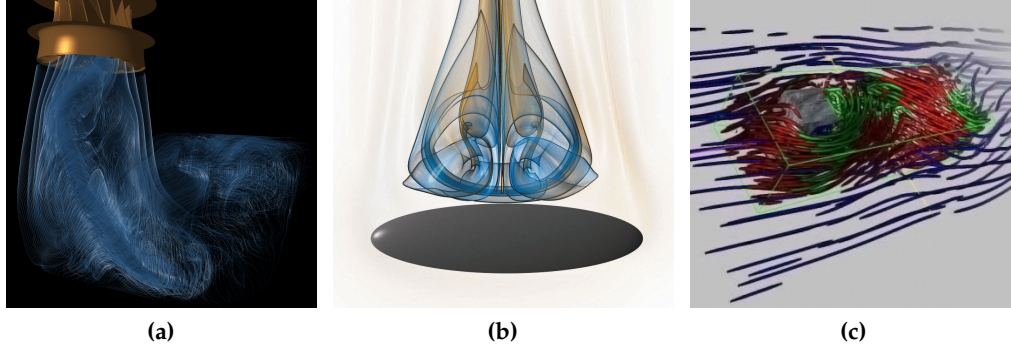


**Figure 40:** Examples of geometric-based flow visualization and exploration methods. Illuminated streamlines for simulated flow from a drafttube are shown in (a) and stream surfaces with enhanced surface shape is presented in (b). A magic volume widget is utilized in (c) to enable an interactive focus-and-context visualization of streamlines. The streamline density outside the focus region (outline) is reduced and different material properties are applied to streamlines inside the focus region. (Image (a) reprinted from Mallo et al. [219] and (b) reprinted from Hummel et al. [161] © IEEE 2005 and 2010 with kind permission from IEEE, (c) reprinted from Mattausch et al. [225] © ACM 2003 with kind permission from ACM.)

pathlines and stream surfaces (see Fig. 40b). Streamlines are seeded at point locations and are tangent to the velocity field for *one* particular point in time. Thus, a streamline  $\mathbf{c}$  represents the trajectory of a massless particle in a steady flow field or for a fix time point  $t_i$  in an unsteady flow field  $\mathbf{V}$ . Formally, it can be expressed as:

$$\begin{aligned} \frac{\partial}{\partial s} \mathbf{c} &= \mathbf{V}(t_i, \mathbf{c}(s)) \\ \mathbf{c}(0) &= \mathbf{x}_0 \end{aligned} \quad (23)$$

with  $s$  as the line parameter of  $\mathbf{c}$  seeded at point position  $\mathbf{x}_0$ . A stream surface is constructed from a set of adjacent streamlines seeded at a seeding curve. Pathlines are used for unsteady flow fields and they are tangent to the velocity field at *any* point in time  $t$ :

$$\begin{aligned} \frac{\partial}{\partial t} \mathbf{c} &= \mathbf{V}(t, \mathbf{c}(t)) \\ \mathbf{c}(0) &= \mathbf{x}_0. \end{aligned} \quad (24)$$

The line integration is approximated by using numerical integration methods, such as the *Euler* or *Runge-Kutta schemes* [325]

Two challenges for geometric-based methods are the *seeding placement* and *visual depiction* of the geometric objects. For example, too many streamlines may lead to visual clutter and too few streamlines may lead to missed flow features. Furthermore, integral objects in 3D data domain increase visual complexity and introduce occlusion issues. Thus, a lot of research work has been done to tackle these challenges, including:

- uniformly dense seeding schemes [172, 211],
- line seeding on surfaces and stream surface filtering [224, 307],

- increased depth perception by means of illustrative visualizations [35, 101, 161] (see Fig. 40b) and
- exploration schemes, e. g., the *magic volumes* [225] (see Fig. 40c).

Based on these previous works, issues with respect to seeding and visual depiction in steady and unsteady 2D data domains are considered to be solved. The same can be said for seeding in unsteady, structured 3D flow domains from a performance point of view due to efficient GPU implementations. However, for the steady and unsteady 3D data domain some challenges still remain and are currently an active area of research that includes: (semi-)automatic seeding strategies, performance improvements for unstructured grids, simplification and perception, as well as uncertainty and comparative visualization. A comprehensive overview of both geometric-based flow visualization techniques and unsolved problems is presented in McLoughlin et al. [230].

#### 4.2.2.4 Feature-based Flow Visualization

Representatives of the first three flow visualization categories focus on the depiction of basic flow properties, such as flow direction and speed. In contrast to them, feature-based flow visualization techniques aim to depict meaningful flow patterns, in particular flow features and flow topology. Examples of important flow features are:

- vortices (regions of swirling behavior),
- vortex core lines (connected swirling centers),
- critical points (isolated points where vector magnitude is zero) and
- shock waves (discontinuities in a physical flow quantity like pressure).

In general, a two-step procedure is performed, which consists of feature extraction and visualization of these features. The definition, extraction and the way these features are visualized depend on the dataset, the application and the research question [266]. A fundamental flow quantity for the extraction process is the Jacobian matrix of the vector field  $\mathbf{V}$ . For a particular point  $\mathbf{x}$  in a 3D Cartesian space its Jacobian  $\mathbf{J}$  consists of the first partial derivatives of the underlying vector field:

$$\mathbf{J}_{\mathbf{V}}(\mathbf{x}) = \begin{bmatrix} \frac{\partial \mathbf{V}_1}{\partial x}(\mathbf{x}) & \frac{\partial \mathbf{V}_1}{\partial y}(\mathbf{x}) & \frac{\partial \mathbf{V}_1}{\partial z}(\mathbf{x}) \\ \frac{\partial \mathbf{V}_2}{\partial x}(\mathbf{x}) & \frac{\partial \mathbf{V}_2}{\partial y}(\mathbf{x}) & \frac{\partial \mathbf{V}_2}{\partial z}(\mathbf{x}) \\ \frac{\partial \mathbf{V}_3}{\partial x}(\mathbf{x}) & \frac{\partial \mathbf{V}_3}{\partial y}(\mathbf{x}) & \frac{\partial \mathbf{V}_3}{\partial z}(\mathbf{x}) \end{bmatrix}. \quad (25)$$

Based on the Jacobian, critical points can be classified by means of their eigenanalysis into: attracting (also called sinks) or repelling (also called sources) points or foci as well as saddle points and centers [266]. Furthermore, several derived local vector field properties can be obtained, such as the *divergence* or the *curl* [82]. The divergence is a signed scalar measure that can be used to localize sources (divergence  $> 0$ ) or sinks (divergence  $< 0$ ) in a vector field. The curl characterizes the rotation of the vector field by means of a vector where the direction is the axis of

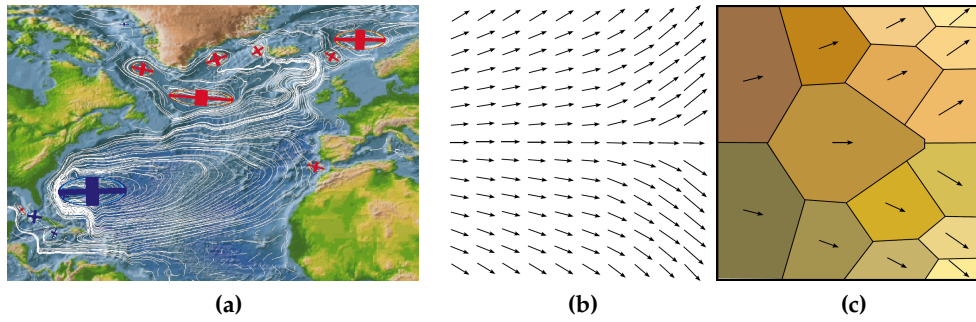


**Figure 41:** Example of feature-based and partition-based flow visualization methods. In an ocean dataset the vortex structures and their surrounding flow are approximated by ellipsoids and streamlines (a), respectively. Color coding indicates the rotation direction of the vortices as clockwise (red) and counter clockwise (blue). The flow field in (b) has been clustered in (c) by means of flow averaging (i.e., a similarity-based approach) and depicted with arrow glyphs. (Image (a) reprinted from Sadarjoen and Post [283] © Elsevier 2000 with kind permission from Elsevier, (b) and (c) reprinted from Salzbrunn et al. [288].)

rotation and the vector length represents the magnitude of rotation. This property can be used to identify vortical flow regions. Finally, the acceleration describes the change of speed over time and position. For steady vector fields, the acceleration is only with respect to the position.

After the flow features are extracted they can be directly visualized, e.g., with glyphs or by means of geometric objects, e.g., streamlines or pathlines seeded at the features (see Fig. 41a). This procedure raises the visualization to a higher level of abstraction, which reduces the amount of visual data considerably. Further developments in this ongoing research field consider *feature tracking*, i.e., the trajectories or movement of features, and *event detection*, i.e., the detection of feature merging, splitting and vanishing. For a comprehensive collection of techniques and references, the interested reader is referred to the surveys by Laramée et al. [202] and Pobitzer et al. [264]. Despite all of these efforts there are still challenges and open questions that need further work, including interaction schemes to support feature extraction, performance issues and identification of other flow features.

#### 4.2.2.5 Partition-based Flow Visualization

The last category of flow visualization techniques is called partition-based and was proposed by Salzbrunn et al. [288]. They define it as an approach that "...partitions the whole domain according to certain characteristics which are based on vector values, integral curve properties of contained features. The resulting partition defines the structure with respect to the flow's behavior and serves as a basis for further visualizations."

Thus, in contrast to the feature-based approach, partition-based methods do not classify the domain into features and no features but try to communicate a description of the flow in its entirety. They aggregate several flow regions into clusters that represent the flow field more coarsely and often hierarchically with different levels of data aggregation. Similar to feature-based methods, a two-step procedure is utilized: the computation of a similarity measure and the visualization of the aggregation result. Here the main challenge is to establish an appropriate similar-

ity measure on which the aggregation is based. According to the aforementioned definition, two different aggregation schemes exist in practice: *cluster-based* and *integral line-based*.

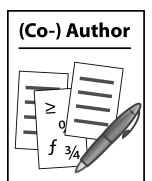
Cluster-based methods group flow regions into sub-regions, so-called clusters, with respect to local or global similarity measures, such as position and divergence of the vectors [326]. In addition to this similarity-based concept, other concepts exist, such as flow topology-based concepts or simulations of physical processes like anisotropic diffusion [123], to define the clusters. In general, cluster-based methods rely on flow information at each voxel or cell in the dataset. After the flow region is partitioned, each cluster can be represented with simple coloring or by means of an icon, e.g., an arrow glyph that depicts the average flow direction, illustrated in Figure 41b and Figure 41c.

Integral line-based methods cluster the flow field according to similar behavior of streamlines and pathlines. Related techniques can be grouped into *topology-based* and *general integral line-based* approaches. Topology-based methods are related to feature-based methods since they employ flow features, e.g., critical points, boundary switch points and separatrices. They use these features to portray the flow topology, which describes the entire flow field in a concise and compact manner (see Fig. 42a) [290, 328]. The topological structure separates the flow domain into parts with similar flow behavior. Topological information can also be used to compress and to compare different vector fields as well as to construct new vector fields in a more consistent way.

General integral line-based methods utilize properties of particle traces that are defined according to a user-defined behavior to structure the flow. In Salzbrunn and Scheuermann [289], streamline predicates are introduced, which are Boolean functions that return true if a streamline fulfills a particular property, e.g., passing a vortex. All streamlines that fulfill a particular predicate or combination of predicates are part of the same disjunct characteristic set, which is considered as a flow structure. Salzbrunn et al. [287] extend this approach to 3D time-dependent flow fields with pathline predicates. In another approach Rössl et al. [281] form a parameter space by means of geometric line properties, e.g., the Hausdorff distance. The clustering is done in the parameter space and back-projected onto streamlines to group them.

A hierarchical vector field clustering based on the computation of a characteristic scalar field was proposed by Kuhn et al. [197] in which the author of this thesis was involved. The scalar field is defined by means of the bending energy of each streamline and a density function that describes the probability of occurrence of a certain bending energy value. Clusters are extracted by identifying local minima of the density function and merged according to a user-defined number of clusters. The local minima indicate the boundaries between neighbored clusters. Additionally, the clusters are classified in terms of the complex three eigenvalues of the Jacobian matrix of all representative cluster elements. In general, the imaginary parts of the eigenvalues give information about the rotational flow behavior and the real part about the translational behavior. Thus, the following three cluster classifications are derived:

- A cluster is assumed to be *turbulent* if the standard deviation of the imaginary and real parts are large, i.e., high fluctuations of flow movement and rotation.



Kuhn et al. [197]



See video no. 1  
on DVD



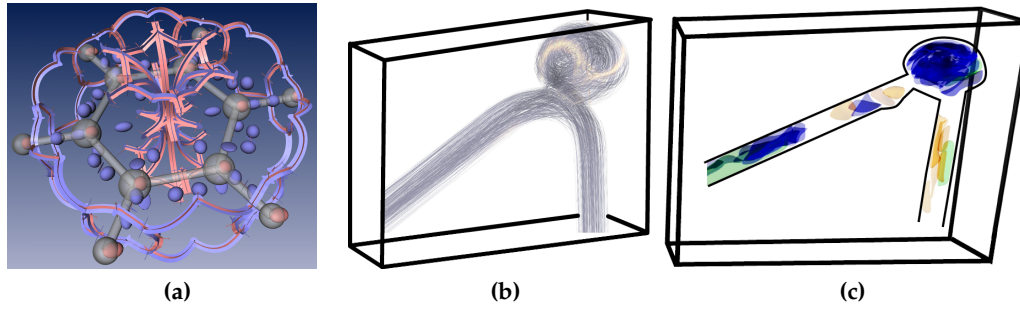


**Figure 42:** Examples of integral line-based partitioning of complex 3D flow fields. In (a) the topological skeleton of the benzene dataset with several critical points is shown. The partitioning of the flow field in an artificial aneurysm dataset (b) is presented in (c). The flow was clustered into regions of vortical (blue), turbulent (orange) and laminar (green) flow. (Image (a) reprinted from Theisel et al. [328] © IEEE 2003 with kind permission from IEEE, (b) and (c) reproduced from Kuhn et al. [197] © Eurographics Association 2011 with kind permission of the Eurographics Association.)

- If a cluster exhibits only a high standard deviation of the imaginary parts it is classified as *vortex*.
- In all other cases the cluster is classified as *laminar*.

Note that this kind of classification indicates a "trend" and represents the major flow behavior. For instance, a "laminar" cluster is dominated by laminar flow behavior. However, different flow behaviors can be part of this cluster, too. An example of the cluster identification and classification is presented in Figure 42b, where streamlines show the flow behavior in an artificial aneurysm dataset. The resulting cluster classification is presented in Figure 42c) and indicates regions of high vortical flow (blue) in the aneurysm sac as well as increased turbulent flow behavior (orange) in the outflow region. This identified flow behavior has also often been observed in patient-specific aneurysm datasets with laminar inflow, vortex structures in the aneurysm and helical outflow regions.

Despite the potential of partition-based methods to represent vector fields in an abstract manner, the following open challenges exist: a validation of how accurate the boundaries of the partitioning are, the identification of an appropriate scale level for hierarchical clustering methods and more intuitive visual depictions of topological information. Most of the current abstract topological representation schemes may be less comprehensible for non-experienced users compared to direct or geometric-based visualization techniques. A detailed presentation of partition-based flow visualization techniques can be found in the survey by Salzbrunn et al. [288].

### 4.3 VISUALIZATION OF HEMODYNAMIC DATA

Visualization approaches that focus explicitly on hemodynamic data are a relatively recent research area. Currently, domain experts mostly use established flow visualization techniques as presented in Section 3.7. These techniques and tools, however, primarily originate from the engineering domain and are not adapted to explore flow in the vascular anatomy (e.g., irregular vessel shapes and noisy



datasets). Additionally, they are not tailored to the needs and habits of the domain experts, especially physicians. As a consequence, visualization scientists are proposing new and adaptive approaches that aim for a supportive hemodynamic exploration. This section presents relevant challenges and existent approaches that mainly focus on measured *cardiac* and *aortic flow* (clinical research domain) as well as on simulated *hemodynamics in cerebral aneurysms* (biomedical research domain).

#### 4.3.1 Challenges

Visualization and exploration methods for hemodynamic data have to cope with certain challenges to ensure acceptance by and applicability to the domain experts. This can only be achieved if the proposed methods are able to provide a more expressive and efficient exploration than current methods. Fortunately, domain experts are aware of the limitations and restrictions of these methods, e. g., time consuming interaction and high visual complexity, which means they have an open attitude to novel approaches. To exploit this situation, the following challenges and requirements have to be considered in addition to those that are discussed for general flow visualization methods in Section 4.2.1. In fact, the following challenges represent refinements of the former, which have been adapted to vessel structures and users with little experience in flow exploration.

**Robustness.** Depending on the flow acquisition modality, the methods have to cope with data noise and artifacts, in particular for 4D PC-MRI. Thus, robust integration schemes for integral lines are necessary to achieve long and smooth line or stream surface geometries. The limited data quality also influences visualization methods, which are based on derivatives, e. g., for feature extraction. This requires appropriate smoothing approaches for the scalar and vectorial data values as well as robust data derivation approximations.

**Expressive depictions.** In contrast to technical users and engineers, most of the physicians are not experienced in the interpretation of complex flow visualizations, such as abstract flow topology, cluster or scalar field renditions. Even bundles of 3D integral lines are often perceived as visually complex and hard to understand, e. g., in terms of flow direction and spatial relationship. Additionally, most domain experts, particularly physicians, are not familiar with the meaning and implications of all parameter settings involved, such as integration step size or the  $\lambda_2$  threshold. Parameter settings and flow interpretation are also crucial for the amount of time required when it comes to large-scale studies. As a consequence, the visualization methods should provide simple but expressive and reliable depictions of the (time-dependent) flow behavior. This involves (semi-)automatic data aggregation, perceptual color scales, visual filtering of noisy and irrelevant flow renditions, e. g., short integral lines, as well as feature extraction with comprehensible depictions. Furthermore, the required parameter settings should be reasonable and robust in terms of small changes.

**Intuitive interaction schemes.** The exploration of the spatiotemporal hemodynamics requires interaction in the 3D space to capture the 3D vector- and scalar-valued data over time, e. g., seeding and probing. Analyzing the data *only* on a 2D domain would prove to be tedious and reduce both the spatial relationship to the vascular structure and the mental "reconstruction" of the flow behavior. Interaction in 3D, however, is challenging for inexperienced users. It requires intuitive

and guided approaches that prevent the user from getting lost. Moreover, the interaction and the subsequent expressive visualization should be accomplished in real time to provide an efficient analysis.

**Task-driven analysis.** Currently, the qualitative analysis of cardiovascular hemodynamics consists mainly of a visual exploration to obtain new insights about certain CVDs and the flow behavior. However, increased knowledge of relevant hemodynamic indicators along with advances in flow acquisition and modeling result in some distinct tasks that domain experts want to perform. This includes, for instance, the comparison between simulated and measured flow or between pre- and post-treatment as well as the identification of vortical flow regions. The challenge is to adapt the visualization and interaction methods to accomplish these tasks efficiently. This also involves validations of the methods and incorporating feedback from the domain experts.

#### 4.3.2 Cardiac and Aortic Flow

Substantial work has been performed by Roy van Pelt [336] who has focused on both expressive visualizations and effective exploration schemes. In one of the first works related to this, Van Pelt et al. [337] propose a stylistic flow visualization based on an intuitive seed plane placing. The placing is accomplished by a single mouse-click interaction at the vessel region of interest, which extracts a vessel-aligned cross-section. The extraction is based on the TMIP (see Sec. 3.3.2) and an eigen-decomposition of the structured tensor at the clicked position. Subsequently, the cross-section is used to seed streamlines and pathlines for local flow inspection (see Fig. 43a). Illustrative visualization methods are utilized to depict time-dependent flow rates by means of *arrow trails* (see Fig. 43b), through-plane regurgitate flow by means of *exploded planar reformations* and the anatomical context with toon shading and line rendering. The informal user feedback reveals an overall acceptance, improved seeding strategy and expressive flow inspection based on the proposed techniques. It emerges that integral lines are evaluated as the most effective way to inspect the flow behavior and that physicians are also interested in a correlation between a visual depiction of flow properties *and* their quantitative numbers. Furthermore, domain experts point out a need to interactively modify the seeding plane, e. g., moving and scaling, after the automatic alignment for an adaptive flow inspection.

In Van Pelt et al. [338] they extend their work for blood flow in the heart and propose improved seeding and visualization approaches. They introduce an interactive virtual seeding probe, which is automatically aligned to the local averaged flow field. In contrast to the previously introduced cross-section plane, the probe alignment can also be applied to non-tubular structures, e. g., the heart valves. The averaged flow field is computed by a *temporal mean orientation projection* (TMOP) volume, which describes a voxel-wise mean distribution of the blood-flow orientations for a full cardiac cycle. The final orientation of the probe is accomplished by fitting the long axis of the probe to the TMOP orientation tensor by means of the eigenvalue coherence measure. Based on this automatic alignment the probe's interactive movement is restricted to the view-aligned 2D plane to simplify the interaction for the user. Similar to the above-mentioned work of Van Pelt et al. [337], the probe serves as a seeding location for various expressive flow visualization

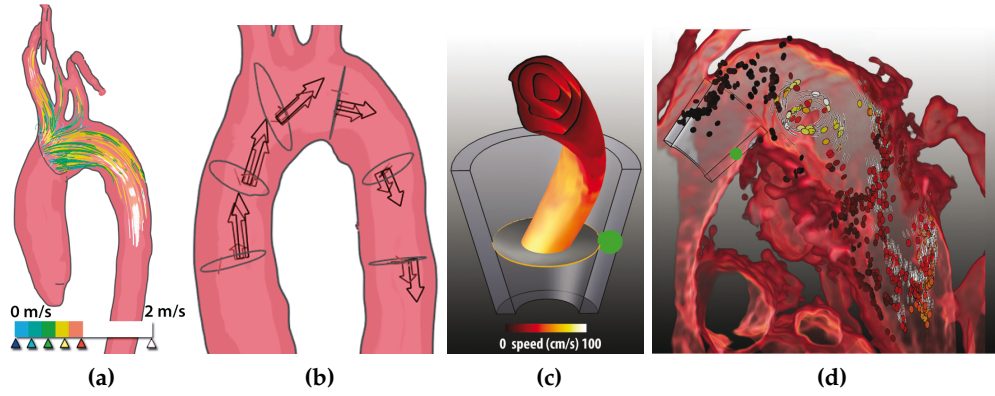


**Figure 43:** Interactive flow exploration approaches for aortic flow datasets. Based on semi-automatic placed cross-section planes pathlines can be seeded (a) to investigate local flow patterns or arrow trails are used to depict temporal flow rates (b). The seeding can also be accomplished interactively by means of a flow-aligned probe for path surfaces (c) and particles (d). In (d) the volume dataset is also clipped along the probe to reveal the particles. (Images reprinted from Van Pelt et al. [337, 338] © IEEE 2010 and 2011 with kind permission from IEEE.)

techniques including illustrative particle traces, halo enhanced pathlines and path-tubes as well as path surfaces (see Fig. 43c). The blood flow visualization techniques were embedded in a volume rendering of the anatomical context using the TMIP volume dataset, which could be clipped in alignment with the probe or with one of the world axis (see Fig. 43d).

The domain experts appreciated the automatic probe alignment but express the need for a local adaption of the probe. Thus, the restrictive 2D movement was positively valued. In terms of the flow visualization, the participants responded positively to most of the presented techniques and they considered the real-time capability of each technique as an important feature. The illustrative particles were rated as a meaningful visualization to depict the blood-flow recirculation and they represent the analogy of contrast agent injections. They regarded the integrated halos for the integral lines as having improved depth perception and preferred the wider path tubes over the thinner pathlines. Depending on the domain experts and anatomical region, the path surface visualization was more or less accepted. For cardiac-oriented physicians, the surface does not always convey a reliable flow behavior, especially in the heart chamber.

Important recent work has also been contributed by Born et al. [33, 34], who utilize the concept of streamline and pathline predicates (see partition-based flow visualization techniques in Sec. 4.2.2) to structure cardiac and aortic flow. Depending on the type of integral line, they define several user-defined predicates to capture flow structures with interesting or abnormal steady and unsteady flow behavior. For example, predicates for streamlines evaluate to true if they exhibit a certain mean or maximum speed, pass vortices (see Fig. 44a) or pass certain anatomical ROIs. In order to achieve a reliable vortex detection on the noisy datasets, they combine standard vortex core and vortex region measurements into a point predicate as follows:

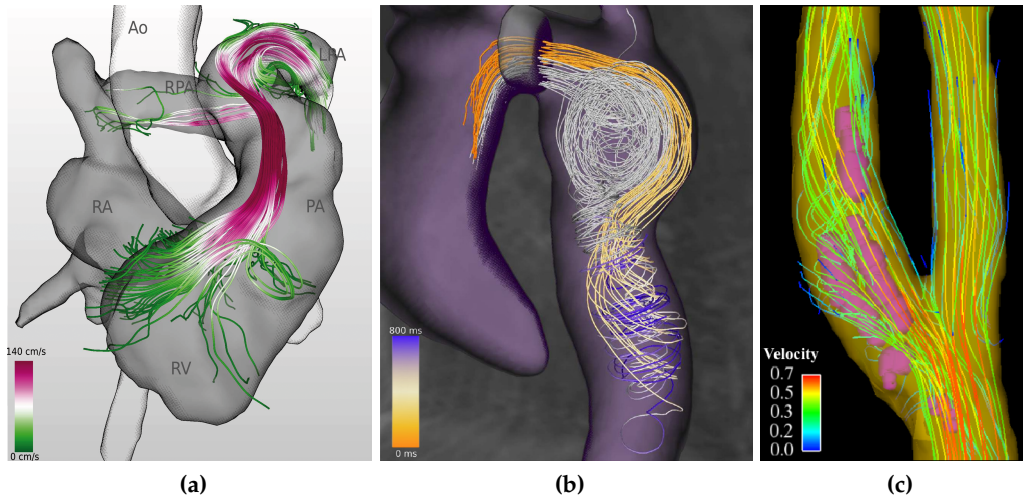


**Figure 44:** Examples of the application of the line predicates concept to depict (a) vortex structures in the left pulmonary artery (LPA) and to extract pathlines with (b) long residence times in an aortic aneurysm. The depiction of vortex core regions (pink spheres) in the right carotid bifurcation is shown in (c). (Images (a) and (b) reprinted from Born et al. [33, 34] © IEEE 2012 and 2013 with kind permission from IEEE, (c) reprinted from Stalder et al. [309] © ISMRM 2010 with kind permission from ISMRM.)

1. Vortex core lines are computed according to the reduced flow speed criterion of Sujudi and Haines [312] and filtered out if they are below a certain length.
2. Vortex regions are detected based on the  $\lambda_2$  criterion by Jeong and Hussain [170].
3. A vortex is detected if a streamline point evaluates to true when at the same position a vortex core line is present and the  $\lambda_2$  criterion is fulfilled.

Examples for pathline predicates are the residence time of particles in a user-defined ROI (see Fig. 44b) or passing a ROI in a certain time step. Given these predicates, the resulting integral lines can be used to analyze the flow in several ways, such as through identification of retrograde flow or flow with high speed, the depiction of flow distribution into the right and the left lung, the evolution of vortices and the evaluation of congestive heart failure. Domain experts appreciated the global view of the flow data, which depicts large-scale features. The individual line predicates are assessed as being useful to investigate correlations between flow behavior and certain diseases. For example, flow with high speed may indicate stenosis, flow regions with a high residence time indicate blood clot generation or lower heart efficiency and vortices may indicate aneurysm formation. Overall, the participants suggested using the proposed flow structure method for a more standardized flow analysis due to the potential of predefined predicates. Despite performance issues and certain artifacts due to the spatial resolution of the 4D PC-MRI datasets, the domain experts demanded additional quantitative values to obtain more reliable conclusions or for comparison purposes. For instance, they are interested in the blood pressure and flow volume rate at some user-defined vessel sections or along the flow features. Stalder et al. [309] also focus on the automatic extraction and visualization of regions with vortical and helical flow in 4D PC-MRI datasets. Unlike Born et al. [34], however, they utilize only the reduced

flow speed criterion of Sujudi and Haimes [312] to detect vortex cores. These cores are depicted with overlapping spheres scaled according to the local vorticity (see Fig. 44c). Due to the usage of only one vortex measure, this approach is more sensitive to noise in the 4D PC-MRI datasets and leads to an increased detection of false positive vortex core regions (see white arrow in Fig. 44c). The approach was applied to an aorta of a healthy subject, an aortic aneurysm as well as carotid and intracranial arteries. In the pathological aorta case, certain vortical and helical flow regions occur, which were not present in the healthy case.

A flow structuring and visualization approach was also proposed by Krishnan et al. [194] that is based on the *finite time Lyapunov exponent* (FTLE) fields. FTLE has recently gained popularity in flow visualization and is a non-negative, scalar measure of coherence in terms of the trajectories of closely seeded particles [143, 302]. Lower values correspond to less coherent flow structures and higher values represent structures that have a low separation behavior (see also Sec. 4.4.2 for a discussion of FTLE).

In the context of 4D PC-MRI aortic flow analysis, Krishnan et al. utilize this measure for both on-the-fly restricting integration-based visualization methods and flow structuring. Based on the velocity data, they compute a scalar field consisting of the FTLE measure and the average speed to detect the vessel boundary automatically during particle integration. This is in contrast to existent and (semi-)automatic approaches that use a segmentation mask based on the anatomical image data, the PC-MRA image or TMIP (see Sec. 3.3.2). The flow structuring is accomplished by computing a flow map on a user-defined 2D seeding plane based on the FTLE measure. This flow map indicates the final position of a particle after advection as a function of its seed point and can be clustered into regions of similar flow behavior. Each cluster represents one flow structure and is visualized by integral surfaces, such as stream or path surfaces, to provide a simplified depiction of flow bifurcations and recirculations (see Fig. 45a). Therefore, the boundaries of each clustered region on the seeding plane are extracted and used as seeding curves for the integral surfaces. Although integral lines and integral surfaces represent flowing particles in an intuitive way, they may lead to visual clutter and occlusions, in particular for non-experienced users. Thus, adapted flow simplification schemes are needed that identify important flow regions and visualize them in an expressive and reliable way.

A recent work by Van Pelt et al. [339] focuses on a sparse representation of the flow field based on a spatiotemporal hierarchical flow clustering. The individual cluster hierarchy is represented with illustrative glyph visualization, so-called *path arrows*. The clustering employs a bottom-up approach starting at each grid cell and merges cells to one cluster with respect to two dissimilarity measures. The first measure merges cells based on an elliptical dissimilarity measure that compares the velocity and position of the current vector with the corresponding averaged values of adjacent clusters [326]. The second measure utilizes a local linear expansion that describes the difference between the current cell velocity vector and a modeled velocity vector in a potentially similar cluster [55]. To ensure fast computation times, the merging process is implemented with a coarse hierarchical clustering scheme that merges multiple clusters in one iteration. The level of detail is adjusted by the



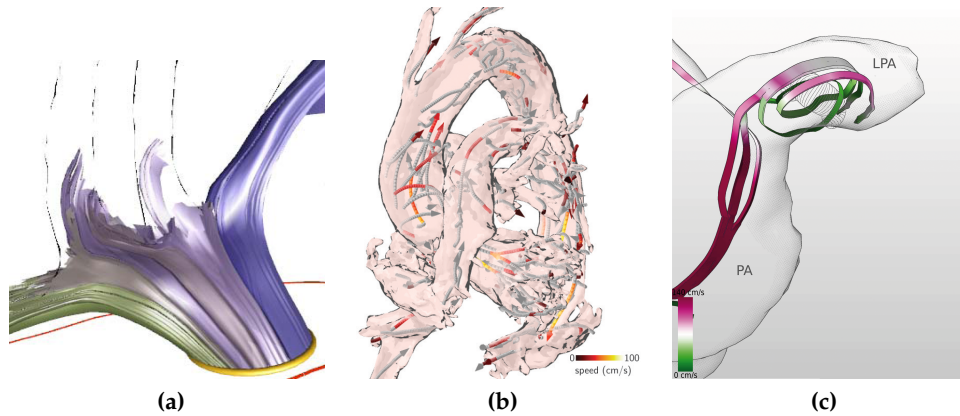


**Figure 45:** Examples of flow clustering in 4D PC-MRI datasets of the aorta. In (b) the application of FTLE fields is used to segment the flow into diverging parts for each vessel. The segmentation is represented by means of integral surfaces seeded from the ring-like region (yellow). A spatiotemporal clustering is shown in (b) by means of path arrows that depict similar flow behavior over a certain time window (gray). In (c) a more abstract flow depiction of Figure 44a is shown where illustrative streamtapes simplify the more complex streamline bundles. Additionally, the vortex core region is depicted as hatching surface. (Image (a) reprinted from Krishnan et al. [194] and (c) reprinted from Born et al. [32] © IEEE 2012 and 2013 with kind permission from IEEE, (b) reprinted from Van Pelt et al. [339] © John Wiley and Sons 2012 with kind permission from John Wiley and Sons.)

user and results in 3D clusters that reside in the space-time domain. For a given hierarchy level, a pathline is seeded either at the center point of each cluster for a fixed time point or at the temporal center point of each cluster.

Based on these pathlines, illustrative path arrows are used to convey the flow behavior statically or as an animation (see Fig. 45b). The qualitative and quantitative evaluation reveals that both dissimilarity measures are compact but the elliptical measure is more aligned to the flow field and more robust in terms of noise compared to the local linear expansion measure. For a comprehensive visualization, the level of detail is crucial and pathlines seeded at the temporal center point of each cluster provide the most sparse representation.

Born et al. [32] have also recently proposed an approach for flow simplification and illustrative depiction. They extend their work of applied line predicates to structure the flow based on user-defined predicates. Additionally, vortex core lines with a measure of the vortex extension are computed. A flow structure is a characteristic set of streamline bundles for which representative streamlines are extracted. The extraction is accomplished in three steps:

1. Each bundle is voxelized with respect to the original grid resolution and subsequently smoothed by a Gaussian filter.
2. From the resulting voxel mask, a topological incorrect skeleton is computed that still preserves the overall shape of the characteristic streamline set.
3. Representative streamlines are identified, which cross the skeleton voxels by a certain amount of crossings.



Inspired by hand drawings each of the representative streamlines for each bundle are depicted by *illustrative streamtapes* with arrow heads and color coding with respect to the flow speed. The vortex core lines are visualized with ellipsoid-like tube hatching (see Fig. 45c) and represent a more expressive depiction than in the approach of Stalder et al. [309] (see Fig. 44c). The approach is applied to three 4D PC-MRI datasets including a healthy human heart, a heart after the surgical repair of a tetralogy of Fallot and an aorta with an aneurysm (see Sec. 2.2). Based on these datasets, three domain-experts (two radiologists and one medical physicist) were asked to compare the illustrative flow visualization with the original line bundle depiction regarding usefulness, comprehensibility and limitations. Overall, the simplified visualization was rated as more intuitive and easier to understand. They appreciate the comprehensive overview of the pre-defined flow features, which can be used for comparison purposes (e.g., flow measurements before and after treatment) and as basis for further flow analysis, e.g., for the WSS. However, for some visualizations the flow directions did not become clear.

Besides an expressive and simplified flow representation, domain experts are also interested in a comparison of flow aspects, e.g., the evolution of flow characteristics over time. Angelelli et al. [4] present a comparative visualization approach for flow through tubular structures, e.g., blood flow in the aorta. Inspired by curved planar reformation techniques, the authors straighten the tubular flow grid along the centerline and present the reformation in a side-by-side view. Subsequently, several flow visualization techniques, such as pathlines and glyphs, are used to visualize the deformed flow in a juxtaposed screen-aligned view at interactive frame rates. Depending on the accuracy of the centerline, the deformation may introduce numerical inaccuracies regarding the resulting vector data. Thus, the approach also provides the capability of applying the flow visualization techniques to the original vector field and deforms the visualization afterwards. This avoids the numerical errors but does not ensure interactivity and is therefore optional. The side-by-side view offers a comparison of several flow visualization aspects, including flow at different time points, flow from different view angles, different visualization techniques applied to the same data and seeding at different locations. An informal evaluation with domain experts for 4D PC-MRI analysis of aortic flow rated the approach as a potentially useful and comprehensive comparison method for hemodynamic data. However, the experts conclude that the usage requires some training because they are used inspecting the flow within the original flow grid. Furthermore, they are unsure if the approach is applicable for pathological vessel structures that are not tubular, e.g., aneurysms. In these cases, the centerline computation and reformation become challenging.

#### 4.3.3 Hemodynamics in Cerebral Aneurysms

Since flow analysis in cerebral aneurysms is becoming relevant due to technical developments in recent years, the visualization community discovered it for the development of adaptive visual exploration methods to support or complement the analysis. In contrast to the cardiac and aortic domain, hemodynamic data for cerebral aneurysms are more commonly obtained from CFD simulation due to the limited spatial resolution of 4D PC-MRI measuring. In general, most of the

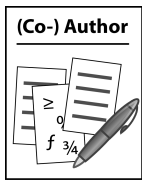
visualization methods and flow simplification schemes presented in the former section are applicable to flow in cerebral aneurysms, such as illustrative particles and depth-enhanced integral lines. Moreover, due to the higher spatial resolution and less data noise of CFD hemodynamics, these methods often result in less distracting visualizations, e. g., longer and smoother line integrations. Nevertheless, flow in cerebral aneurysms differs from cardiac and aortic flow in terms of the enclosing morphology and certain flow aspects that are relevant for the aneurysms initiation and outcome.

Considerable contributions are made by the works by Mathias Neugebauer [245], who focuses on effective exploration schemes to investigate wall, near-wall and embedded hemodynamics. Wall hemodynamics, such as WSS and OSI, play an important role for risk assessment of cerebral aneurysms. Here the morphology of the aneurysm surface can be very complex and it offers a few landmarks, e. g., the ostium, centerlines and aneurysm axes. Greater mental effort for a non-experienced user is necessary for both the navigation to surface parts with salient wall hemodynamics and putting the obtained information into the context of already visited surface parts.

Neugebauer et al. [247] tackle this problem and present an overview visualization that simultaneously depicts all surface data in a combination of a 2D map display with a 3D visualization of the aneurysm surface (see Fig. 46a). The author of this thesis was partly involved in this approach. The map layout is arranged around the 3D surface and consists of five segments textured with orthogonal projections from the aneurysm, which are not visible to the user, i. e., left, right, above, below and back. The projections are generated by a cube mapping with the cube center located at the center of the aneurysm. Due to the distortions of the projection, the map serves as a contextual and interactive overview and the 3D visualization as a focus region. Salient wall features that are located on hidden parts are visible in the overview visualization and can be dragged into the focus region. During interaction the map display is updated with the new projection views, and surface parts that are hidden by the map are indicated by a pen-and-ink rendering. To support user interaction and correlations between the 2D map and 3D visualization, the map provides a pictogram-based overlay and a correlation tool. The tool marks a selected map point and its opposing map point as well as the corresponding locations on the surface. In addition to this overview visualization, the authors investigate established color maps, such as a linear gray map, optimized color map and heated object map, to depict scalar information with high scalar frequency [210].

The informal user feedback from five radiologists reveals that of all the presented maps the optimized and heated object maps depict the scalar information best in terms of scalar value estimation. However, the participants criticized the fact that the maps do not provide a more defined distinction between high and low values. Based on this feedback, a split color map for high and low values is presented consisting of two maps that link scalar distributions to luminance values with red as an established signal color for high values (see Fig. 46a).

When it comes to the overview map, the participants need some time of training to get familiar with the orientation and interaction of the map layout. Here the pictogram-based overlay and the correlation tool were considered helpful in understanding the different projected views. The domain experts consider the vi-



Neugebauer et al. [247]



See video no. 2 on DVD

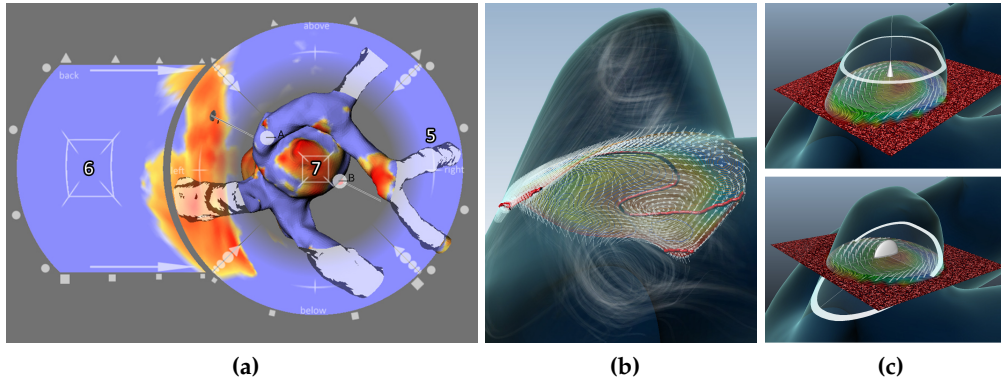


**Figure 46:** Flow exploration approaches for cerebral blood flow. In (a) an interactive 2D map display layout is shown to investigate scalar surface data. Surface regions that are not visible to the viewer are mapped on the map sections. Two examples of an anatomy-guided exploration are shown in (b) for the ostium scope and in (c) for the aneurysm scope. Each scope provides different visualization templates and widgets, such as contextual streamlines, arrow glyphs and interactive LIC planes that can be oriented along anatomical axes. (Image (a) and (b) reprinted from Neugebauer et al. [247, 248] © John Wiley and Sons with kind permission from John Wiley and Sons.)

visualization as comprehensible and appreciate the overview for efficiently locating surface regions with salient wall hemodynamics. The approach is limited with respect to the shape of the aneurysm sac. For non-convex shapes, the cube mapping projection results in overlapping parts that can occlude important surface regions.

A flattening approach is also proposed by Goubergrits et al. [134] to generate WSS maps of ruptured and unruptured aneurysms. The aneurysm sac is projected on a plane by means of a spherical proxy geometry to facilitate a statistical analysis and comparison of WSS distributions between ruptured and unruptured aneurysms. For non-convex aneurysm shapes, however, this projection may also lead to degenerated and occluded surface parts.

Beside this wall hemodynamics, domain experts are also interested in embedded hemodynamic data at certain anatomical landmarks of the aneurysm. Inspired by the visual information-seeking principle "*overview first, details on demand*", Neugebauer et al. [248] propose an anatomy-guided flow exploration approach that provides three scopes of the embedded hemodynamic data: a *global scope*, an *ostium scope* and a *local scope*. Each scope provides visualization templates and a guided interaction that facilitates exploration for non-experienced users. The global scope enhances fast and slow flow in the aneurysm as well as the inflow and outflow behavior of the aneurysm by means of streamlines with adaptive color maps. The ostium scope depicts certain flow characteristics on and close to the ostium, such as signed flow rate, speed and surrounding flow. To minimize visual clutter, different levels of detail are provided that hide or show the different characteristics with glyphs, contour lines or streamlines (see Fig. 46b). The local scope enables the user to investigate flow characteristics in the parent vessel and the aneurysm in detail by means of exploration widgets, which are oriented to parent vessel centerlines or to aneurysm axes.

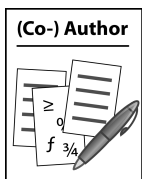
Each widget is used as sampling plane and depicts flow speed and direction as well as the degree of vorticity with established visualization techniques, such as glyphs and color-coded LICs (see Fig. 46c). The proposed approach was evaluated in a qualitative user study with two radiologists who appreciate the separation into three scopes from a global to a local view. Combined with the concept of visualization templates and guided interaction, they are able to focus on the flow exploration at regions of interest and are not preoccupied with adjusting visualization parameters. For some cases, however, the participants suggested providing an additional unconstrained interaction. Furthermore, some visualization templates are perceived as visually complex and should be only embedded on demand ("*less is more*").

For the risk assessment of cerebral aneurysms, the inspection of near-wall flow with integral lines is a common procedure, especially at locations with bleb formations (see Sec. 3.7). Standard seeding strategies would require a manual placement of seeding objects, such as planes or spheres, which is tedious and may not cover the seeding region sufficiently. Even with the guided exploration widgets proposed by Neugebauer et al. [248], the seeding planes are restricted to certain axes and require a complex anatomical analysis as a prerequisite.

In Köhler et al. [191] an effective surface seeding strategy is presented that enables a near-wall seeding at certain surface regions. The author of this thesis was partly involved in developing this approach. Starting from a particular surface location, a user-defined area is selected and extruded into the vessel. Between each original triangle and its extruded version, a prism is constructed with randomized positions of seeding points within. The individual extrusion vectors result from the directions between the original mesh vertices and their shrunken positions after a Laplacian smoothing is applied. The user is able to interactively adjust the radius of the extruded surface area and the extrusion depth as well as the definition of a ring-shaped surface selection. Based on this seeding approach, the density of integral lines at near-wall locations of salient surface features can be easily increased and used for a detailed flow inspection. Furthermore, this approach is not restricted to cerebral aneurysms but can be used on any kind of blood vessels.

The inspection of near-wall hemodynamics was further investigated by a work of Neugebauer et al. [249], who introduce the *AmniVis-Explorer*. This system enables the selection of cap-shaped surface features that might be of interest for the domain experts or resemble bleb formations. These surface regions are identified either automatically by the *shape index* and *curvedness measure* or manually by the user. Based on these ROIs, circular seeding regions are defined with seed points uniformly distributed underneath for a subsequent streamline integration (see Fig. 47a). The integration length is restricted and the resulting streamlines are unrolled into a 2D representation for comparison and classification purposes. For each seeding location, such a 2D representation is generated and aligned contextually next to the 3D focus visualization (see Fig. 47b). A particular 2D representation widget provides several interaction and visualization schemes, such as the depiction of the mean flow direction, slicing through different time steps and a binary classification that moves the widget to the opposite side, for further investigations.

Furthermore, the system supports the 3D navigation of the inspected flow pattern by automatically moving the camera from its current point of view to a se-



Köhler et al. [191]

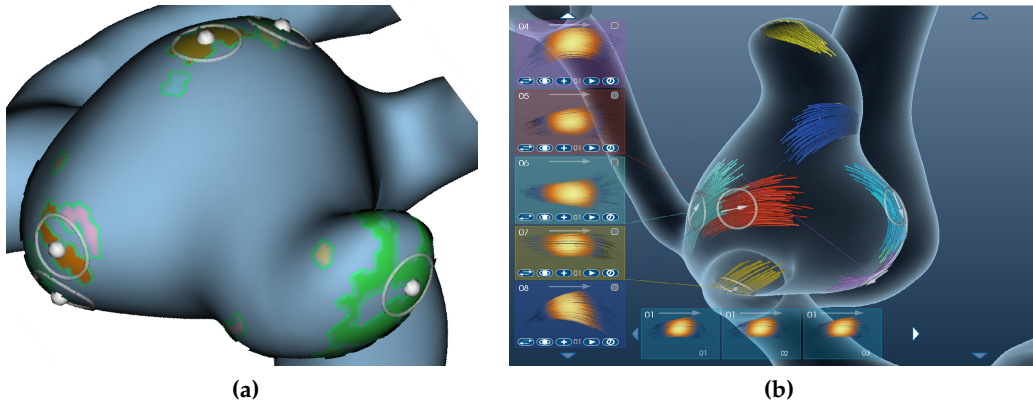


**Figure 47:** Selection of cap-shaped surface regions (a) as seeding locations for near-wall flow investigations by means of the AmniVis-Explorer. Each seeded streamline bundle is aligned at 2D representation next to the focus region (b) and can be investigated separately over time. (Images reprinted from Neugebauer et al. [249] © John Wiley and Sons 2013 with kind permission from John Wiley and Sons.)

lected flow pattern along a comprehensible path. The informal user feedback with two radiologists and one biomedical researcher demonstrated that the AmniVis-Explorer enables a consistent workflow of selection, exploration, classification and comparison for near-wall flow. The separation into focus and context regions and most of the interaction schemes were appreciated by the participants. Depending on the participant's expertise in 3D navigation, they employ the 2D representation more than the 3D visualization, or vice versa. Further evaluations with a larger group of participants and more datasets are necessary to get a deeper understanding of user's preferences and the kind of flow classes that are of interest to the domain experts. The resulting feedback and insights should be incorporated into the AmniVis-Explorer to enable a qualitative study of large-scale and multicenter datasets.

#### 4.4 DISCUSSION

The last two sections presented a variety of visualization and exploration approaches for general flow data and for cardiovascular hemodynamics, respectively. With the challenges described (see Sec. 4.2.1 and Sec. 4.3.1) and the implications of the thesis (see Sec. 3.9) in mind, we discuss some of these approaches in more detail. We also consider particular characteristics of hemodynamic datasets. Depending on the acquisition modality, hemodynamic datasets consist of structured (4D PC-MRI) or unstructured (CFD simulation) volumetric grids. Furthermore, they exhibit a certain amount of noise, especially in the case of measured flow data and they have in common that the vectorial flow data inherently exhibit no sinks or sources, i.e., they are *divergence free*. Cases where measured flow vanishes or appears result from the limited spatiotemporal resolution, low signal intensity and data noise.



#### 4.4.1 *Structured vs. Unstructured Grids*

Dense and texture-based flow visualization methods rely mostly on structured grids to achieve interactive frame rates by exploiting GPU texture capabilities. This is also the case for all integration schemes in interactive, geometric-based methods as well as for feature- and partition-based methods that are based on them. As a consequence, some of the exploration methods of cardiac and aortic flow also require structured grids [152, 194, 336]. Through modifications to these approaches, they can be applied to unstructured grids but they will not exhibit interactive frame rates. A remedy would be to convert the unstructured grids to structured grids by means of certain interpolation schemes.

This procedure, however, has two limitations. First, the conversion would introduce inaccuracies, whereby some flow features may get lost. Second, unstructured grids consist of a high grid cell density of about 0.02 to 0.08 mm. To setup a structured grid with a similar spatial resolution to minimize interpolation errors would result in an enormous amount of memory, especially in the case of multiple time steps. This memory consumption exceeds most of the current GPU texture memory capacities and thus requires an asynchronous data streaming [343].

#### 4.4.2 *Flow Reduction and Depiction*

In addition to a fast visual feedback, the domain experts are interested in an overall understanding of the flow dynamics and behavior. Direct- and geometric-based methods are intuitive but lead to occlusions and tend to be confusing when applied to the volumetric datasets. Furthermore, the placement and seeding at each grid point result in a lot of redundant flow information. This requires a reduction to relevant flow information and intuitive interaction schemes to define regions of interest and seeding regions.

With respect to flow reduction or simplification, an established procedure is to extract flow features or line representatives based on integral lines. The assumption is that integral lines capture the whole spatiotemporal flow dynamic, in particular pathlines. After relevant features and representatives are extracted they can be visualized in a different manner. However, the application of general feature extraction methods that achieve appropriate results on artificial (mostly high-resolution with a low amount of noise) or analytical flow fields would be limited. Since these methods rely on the Jacobian matrix, they assume either a continuous derivation at each sample point or little noise in the flow datasets to minimize discretization errors. Neither of these are true of measured flow. Even for simulated flow data, the inherent data noise and discretization error are not negligible and would lead to error-prone results.

Despite these limitations, the visual depiction of most general feature- and partition-based depictions are not suitable for non-experts in flow analysis, even for CFD and biomedical engineers. From our own experiences with domain experts, representations of topology and clusters, as proposed by Theisel et al. [328] or Kuhn et al. [197], are hard to interpret. Although these representations describe the flow in a concise and compact manner, the final renditions are too abstract and not comprehensible enough for non-experienced users.



Flow reduction methods for cardiac and aortic flow also incorporate feature- and partition-based approaches but tackle the problem with noise and depiction in a more suitable manner. The *concept of line predicates* [287, 289], which is utilized by Born et al. [33], seems to be a flexible and robust approach of structuring the flow into bundles based on user-defined or data-driven features. In combination with the subsequently proposed illustrative visualization approach for the bundle's representative and the vortex core regions, an expressive and reliable flow reduction could be achieved [32]. Existent topology-based methods (see Fig. 42a) focus only on derived flow features and are not able to incorporate user-defined features, e. g., high-speed flow that runs through an anatomical region.

However, some aspects have to be considered when using the line predicates concept and the illustrative depiction of the bundle's representative, as proposed by Born et al. [32, 33]. Some of these aspects are also mentioned by the authors. The flow structuring by means of line predicates utilizes solely integral lines that fulfill specific *line-based properties* and *derived properties*. Line-based properties rely on the integral line geometry and probed flow quantities, such as line curvature and speed. Derived properties are based on the underlying velocity field or anatomical vessel information, such as vortex regions and vessel sections. As a consequence, the complete spatiotemporal flow domain has to be covered with integral lines to ensure that anatomical or time-dependent flow features are not missed.

The quality of the extracted line-based features strongly depends on the quality of the line geometry. Thus, the integration scheme used should achieve long and smooth integral lines with low integration errors even on measured flow data. Furthermore, because of data noise and long integration times, the accumulated error can be quite large. The derived properties require a robust extraction scheme to identify reliable flow features. For instance, in Born et al. [33], vortex regions are detected by combining two predicates for the detection of vortex core lines and vortex regions. In terms of the identification of the bundle's representative, the skeletonization procedure in Born et al. [32] assumes no spherically shaped flow regions to extract a reliable skeleton. These cases, however, are likely to happen in sphere-like anatomy, such as saccular aneurysms or heart chambers, which might restrict the approach to tubular structures only.

The application of the FTLE measure by Krishnan et al. [194] for restricting integration-based visualizations and flow structuring of 4D PC-MRI datasets also requires some consideration. By definition, the FTLE measure is a scalar value that characterizes the separation between neighboring trajectories over a finite time interval. These separations indicate *Lagrangian Coherent Structures* (LCS), which separate dynamically distinct regions in time-dependent flow fields. In the context of blood flow, an LCS represents, for example, the transition region between the interior and exterior of a blood vessel. In general, the computation of the FTLE measure involves an eigenanalysis of the *Cauchy-Green deformation tensor* that is composed by the Jacobian matrix.

To identify LCS reliably, the computation of an FTLE scalar field is computationally intensive, as it requires a large number of integration steps and resampling of the original structured grid. This computation can be performed on the GPU in a pre-processing step [79] but there are several dataset- and operator-dependent parameters including the integration time, the amount of resampling and the threshold for the FTLE magnitude that indicate a LCS. These parameters, however, have

a crucial effect both on the integration termination at the vessel border and for the "detail" of flow structuring. For example, there is no inherent FTLE threshold value that ensures a separation of vortical flow from other flow regions. In comparison to the aforementioned line predicate concept, this is less reproducible and flexible because it does not enable the definition of user-defined (or task-driven) requests, e. g., vortical flow that runs through a particular vessel section. Furthermore, Krishnan et al. [194] compute the average FTLE measure over time to be more robust in terms of data noise at the vessel border. This would lead to erroneous terminations in regions of strong anatomical movement, which is likely for heart chambers or some CVDs at the aorta, e.g., aneurysms.

To overcome this limitation, the authors suggest a combination of the FTLE measure with an explicit vessel segmentation mask. However, this would require a reliable time-dependent segmentation of the (pathological) anatomy, which is challenging and still an open issue.

For flow reduction in cerebral aneurysms little work has been done yet. In Neugebauer et al. [248], streamlines outside a certain flow speed range are omitted by means of an opacity transfer function. Depending on the dataset, however, the remaining streamlines can still be very complex and hard to interpret, especially the spatial relationship of the lines. An aggregation of these bundles to certain representatives as presented in Born et al. [32] would lead to a more clear flow depiction.

This is partly solved by the hierarchical flow clustering approach of Van Pelt et al. [339], which was also applied to aortic flow datasets. The aggregation of similar and neighbored flow vectors to clusters with a subsequent illustrative and representative path arrow visualization, reduce the amount of integral lines considerably. Here the path arrows communicate the space time flow behavior in one representation. For regions of complex flow behavior, however, we assume that the final visualization may still lead to a considerable cognitive load for the domain experts, especially in the case of animated path arrows (see Fig. 45b). On the one hand, the complexity can be reduced by choosing a higher level of detail that results in larger clusters and fewer path arrows as representatives. On the other hand, relevant flow features could be missed because the integration of the representative path arrow starts at the center of a cluster. Since a larger cluster may contain multiple features, it is likely that the path arrow will not capture them, e. g., vortical regions surrounded by helical flow.

Beside these approaches, it would be worthwhile to apply other flow reduction and visualization approaches for cardiac and aortic flow to cerebral blood flow. Because of the higher spatiotemporal resolution and lower data noise in the simulated datasets, we assume more reliable and robust results as for the measured datasets. For example, the evaluation of line predicates would rely on longer and smoother integral lines and a resampling for the FTLE measure could be omitted. Moreover, an interesting application of the FTLE concept would be the extraction of the inflow jet in cerebral aneurysms. This flow structure enters the aneurysm as parallel inflow with higher speed than its surrounding flow and disperses after it hits the vessel wall. This characteristic separation corresponds to an LCS that should be indicated by the FTLE measure.

#### 4.4.3 Seeding and Interaction

In the domain of general flow visualizations, there exist a limited amount of interaction schemes that support seeding, probing and visual filtering in the 3D space. The *magic volume* approach by Mattausch et al. [225] (see Fig. 40c) utilizes a 3D volume that can be arranged freely in 3D to define a 3D seeding region. As mentioned in Section 4.3.1, a freely available interaction in 3D is challenging for non-experienced users and would result in a time-consuming and tedious task. Other approaches that focus on a uniform seeding [211] or the identification of meaningful seeding structures [224] over the whole flow domain do not provide the required flexibility of a user-driven flow exploration. They also do not ensure the capturing of all relevant flow features. However, they can be used as an overview and starting point for further and local investigations.

In contrast to the general flow visualization domain, several flow visualization approaches for hemodynamic data are accompanied by intuitive interaction schemes including seeding, probing and viewpoint selection. All of them have in common a restricted degree of freedom and an anatomy- or flow-guided alignment, which were appreciated by the domain experts in their feedback. The two cross-sectional plane approaches proposed by Van Pelt et al. [337] and Hennemuth et al. [152], respectively, reduced the interaction effort of probing and seeding in tubular structures to one click (see Fig. 43a). The parent vessel exploration widget for cerebral aneurysms presented by Neugebauer et al. [248] is also restricted to tubular structures because it requires a reliable, pre-computed centerline.

The virtual probe approach of Van Pelt et al. [338] is capable of aligning automatically in non-tubular structures, such as heart chambers or aneurysms (see Fig. 43d). Combined with the illustrative particle visualization, it resembles the injection of contrast agent. The fitting approach of the virtual probe utilizes a structure tensor that is based on an averaging of the underlying velocity directions. Thus, it is robust in terms of data noise and artifacts of the measured flow data within the vessel but may lead to a mistaken positioning at the vessel border to the higher level of noise.

The *AmniVis-Explorer* by Neugebauer et al. [249] facilitates a categorization, a (semi-)automatic seeding and viewpoint selection of near-wall flow (see Fig. 47b). It provides a well-organized overview of the 2D representation of the seeded near-wall streamlines, their spatial relationship to the 3D flow domain and temporal changes to their flow dynamics. A limitation of this approach consists of the current 2D unfolding scheme of the seeded streamlines. The unrolling of the streamlines into a plane results in strong distortions for vortical, near-wall flow or streamlines that integrate nearly perpendicular to the seeding region into the aneurysm. Vortical flow near the vessel wall is a relevant flow feature that might be interesting for the risk of rupture assessment.

#### 4.4.4 Conclusion

The approaches and discussions have shown that general flow visualization techniques are incorporated into visual exploration methods that are tailored to cardiovascular hemodynamics. An adaptation is necessary because common flow visualization approaches do not consider the needs and habits of the domain ex-

perts, e. g., high visual complexity and challenging 3D interaction, as well as the characteristics of the datasets and vessel anatomy, e. g., data noise and anatomical movement. An interesting observation is that more adaptive methods for measured cardiac and aortic flow exist than for simulated hemodynamics in cerebral aneurysms. There are several possible reasons. Measured flow requires less processing effort compared to simulated flow data, e. g., no or at least a simplified vessel segmentation, no vessel mesh processing and no computationally intensive simulations. Additionally, the measured flow accuracy in large vessels is higher than in small vessels. For practical and performance reasons, the structured grids are easier to handle and more efficient to process than the unstructured grids. From the domain expert point of view, some physicians tend to have more confidence in 4D PC-MRI measuring than in CFD simulations due to the simplified boundary conditions of the CFD models. Furthermore, they assess 4D PC-MRI as a step closer to use in clinical trials because of its increasing application in clinical research and they promote the quantitative and qualitative analysis.

Nevertheless, the proposed visual exploration methods for hemodynamic datasets support a qualitative analysis but their application is partly restricted to a certain vessel anatomy or shape and require a robust pre-processing. Most of the methods depict the flow expressively and provide intuitive exploration schemes. Here, established concepts are *flow aggregation*, *illustrative depiction* and *guided interactions*. In most cases the methods focus rather on a flow exploration than on a task-driven analysis. For example, comparison approaches are still missing and not tackled yet. In this context, the importance of flow speed and regurgitant blood flow (i.e., backward flow) for the physicians should be considered. Unusual speed values and high regurgitant fractions may indicate certain CVDs and should be enhanced in a qualitative task-driven analysis.

In terms of the summarized implications of the thesis in Section 3.9, we also conclude that no existent method focuses on *embedded surface problems* (research **goal 1**), the extraction and visualization of the inflow jet and impingement zone (research **goal 2**) or on *focus-and-context approaches* for multiparameter visualizations of hemodynamic datasets (research **goal 3**). In this context, however, the line predicate concept and FTLE fields are the inspiration for the inflow jet extraction procedure we propose in Chapter 6.

#### 4.5 FURTHER READING

The seeding and occlusion problem of integral lines and surfaces in 3D has been tackled by visualization scientists in recent years. Li and Shen [211] present the first view-dependent 3D seeding approach for streamlines based on the 2D evenly-spaced streamline approach by Jobard et al. [172]. Streamline seed positions are carefully spaced out in image space and projected back to 3D to reduce visual clutter and to minimize depth ambiguity caused by overlapping streamlines in the final 2D image. With this approach a variety of effects are possible, such as level of detail, depth peeling and stylized rendering to enhance the perception of 3D streamlines. However, temporal coherence is not always ensured, which may introduce distracting popping artifacts.

In Günther et al. [141], the first approach of view-dependent integral line selection is proposed that fulfills dense covering of the flow domain, avoidance of

visual clutter due to occlusion and temporal coherence. Integral lines are smoothly faded out based on their screen contribution to the image space. An existent order-independent transparency technique is utilized and modified to ensure both decreased perception load and interactive frame-rates. For local flow inspection, an interactive brushing tool is presented that enables the selection of a representative integral line in image space and enhances similar lines in a user-defined neighborhood.

A method for automatically finding the globally most representative stream surface is proposed by Martinez Esturo et al. [224]. They introduce a surface-based quality measure that prefers surfaces where the flow is aligned with the principal curvature directions. Among other things, they apply it to a CFD flow dataset of a cerebral aneurysm and are able to extract a stream surface that covers the main vortical flow in the aneurysm.

In Tao et al. [317], an information-theoretic framework is presented that enables an automatic identification of expressive streamline representatives and viewpoint selection. The streamline representatives capture flow features by passing through the vicinity of critical points or interesting regions. The viewpoint selection ensures that most of the representatives and their characteristic shape can be seen. Thus, it would be worthwhile to investigate how this approach can be applied to extract relevant blood flow features and to support the exploration with preselected viewpoints.

Given the variety of flow visualization techniques and the increased complexity of datasets, there is a need for comparative and uncertainty flow visualization as well as for evaluation of visualization techniques. These related research fields, however, have not been sufficiently addressed by the visualization community yet. There are several motivations for flow comparison, such as different flow acquisition techniques, different grid resolutions and differences in flow visualization algorithms. Fundamental discussions and possible solutions are presented by Verma and Pang [344].

A general overview and discussion about visualization of uncertain data is presented by Griethe and Schumann [138] as well as by Boukhelifa and Duke [40]. For example, Boukhelifa and Duke conclude that the value of uncertainty visualization is severely limited by the quality and scope of uncertainty data, by the limited confidence in the data itself, and by the perceptual and cognitive confusion that the depiction of this data can generate. Glyph-based visualizations of uncertainty in vector fields and different algorithms are presented in Wittenbrink et al. [365] and Hlawatsch et al. [153]. Contributions to the visualization of uncertain flow data are made by Otto [260]. The evaluation of visualization techniques regarding dataset type, user task and research questions is necessary for several reasons, such as the identification of most suited techniques or which adaptations are necessary.

Since statistical user studies for flow visualization techniques are challenging and tedious, most visualization scientists rely on a qualitative and informal user study. In Laidlaw et al. [199], one of the few works focusing on a quantitative user study for 2D vector field visualization techniques, e.g., LICs and streamlines, is presented. They present a task and testing framework to evaluate which technique is most suited to identify and characterize critical points as well as to predict particle movement. Moreover, the discussion and framework provide a basis for com-

paring other visualization methods, for creating more effective methods and for defining additional tasks to further understand the tradeoffs among the methods.

In recent years, interactive visual analysis methods of multivariate datasets have shown a great potential to reduce the visual amount of data and to support a flexible data exploration. An important concept here is *linking&brushing* that is introduced by Gresh et al. [136] and extended in Doleisch et al. [92]. The dataset is presented in different linked views consisting of the *physical space*, e. g., a 2D slice or a volume rendering, and the *parameter space* where each parameter is mapped to classical information visualization techniques, such as scatterplots, parallel coordinates and histograms. The user is able to visualize focus regions in the dataset by *brushing* or selecting regions of interest in the parameter space. The physical space is *linked* with the brushing and the selected regions are emphasized with standard visualization techniques, such as coloring and glyph representations. By means of Boolean combinations applied to different parameter selections, several features can be discovered. This concept is applied by Zachow et al. [374] and Pobitzer et al. [263] for analyzing nasal airflow data and for pathline filtering, respectively. For an overview of interactive visual analysis methods we refer to Doleisch and Hauser [93] and to Section 7.2.

In terms of blood flow visualization, Van Pelt and Vilanova [340] present a complementary discussion and outlook on key challenges for blood-flow research. Furthermore, they demonstrate to what extent the challenges have been met in the state of the art in this field.



## Part II

### MAIN CONTRIBUTIONS

From where does my help come?  
My help comes from the Lord, who made heaven and earth.  
*(The Bible, Psalm 121, Verses 1-2)*



## VISUALIZATION OF BLOOD FLOW VESSELS WITH EMBEDDED FLOW INFORMATION

This chapter is based on:

"Adapted Surface Visualization of Cerebral Aneurysms with Embedded Blood Flow Information". Rocco Gasteiger, Mathias Neugebauer, Christoph Kubisch and Bernhard Preim. In *Eurographics Workshop on Visual Computing for Biology and Medicine (VCBM)*, pp. 25-32, 2010.

"Perceptual Evaluation of Ghosted View Techniques for the Exploration of Vascular Structures and Embedded Flow". Alexandra Baer, Rocco Gasteiger, Douglas W. Cunningham and Bernhard Preim. In *Computer Graphics Forum (EuroVis)*, 30(3), pp. 811-820, 2011.

### 5.1 INTRODUCTION

One of the basic statements from Chapter 3 is the complex interplay between hemodynamics and its surrounding vessel morphology. Thus, both information have to be visualized simultaneously to establish a spatial relationship during the visual exploration. Wall flow characteristics can be displayed with adaptive map-to-surface approaches, which provide both an overview about the hemodynamic characteristics and the morphological context (see Neugebauer et al. [247]). However, when visualizing the internal 3D flow information, a projection to 2D maps is not suitable because it would lead to strong flow distortions, occlusions, and does not ensure spatial correlation to the morphology. Therefore, domain experts are used to investigate embedded flow information combined with its enclosed vessel anatomy.

Since the flow is spatially embedded in the surrounding vessel surface, occlusion problems have to be resolved that include a meaningful visual reduction of the vessel surface but still provides important anatomical features. In this chapter, we focus on research **goal 1** of the thesis at hand (see Sec. 3.9) and present an adapted vessel surface visualization, which depicts important anatomical and surface features, whilst simultaneously gaining appropriate visibility of the embedded flow visualization. While the originally published approach in Gasteiger et al. [127] was developed primarily for surfaces of cerebral aneurysms, we show that it can be applied to general blood vessels as well.

The most common approach to tackle this *embedded surface* or *nested surface* problem is to render the enclosing surface semitransparently as shown in Figure 48a. More transparency increases the visibility of the internal flow visualization, but strongly decreases the depiction of important surface shape features (see Fig. 48b). Additionally, regions of several semitransparent surface parts lying in front of each other, can cause a misleading interpretation of the spatial relationship. For example, it is difficult to verify which parts of the vessel are in front to or behind each other if transparency is high, especially for static images. Additionally, flow

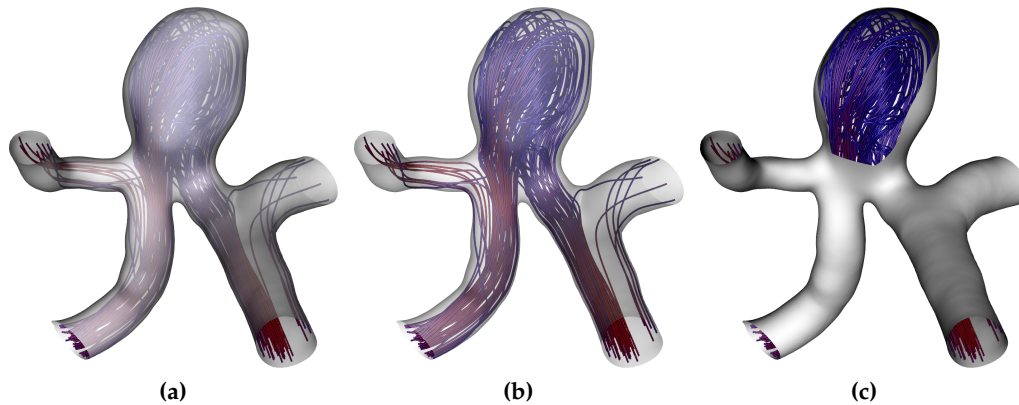


**Figure 48:** Standard visualization techniques for vessels with embedded flow information. A semitransparent surface rendering is used in (a) to reveal internal flow information that are depicted with illustrative streamlines. An increased transparency in (b) leads to an increased flow visibility, but strongly decreases the depiction of surface shape. Clipping is shown in (c) that excludes all surface information outside the clipping range.

quantities are often mapped on visual attributes like color or texture. A semitransparent layer in front of the flow visualization can mislead the interpretation of these flow quantities. Both problems, less surface shape depiction and ambiguities of the spatial relationship decrease the observer's ability to mentally link the aneurysm morphology with the internal flow visualization. Another approach is surface clipping based on a user-defined clipping plane or front-face clipping. This ensures maximum visibility to the embedded flow visualization, but all surface information excluded by the clipping is lost, shown in Figure 48c.

Our approach is inspired by illustrative visualization techniques like smart visibility methods and line rendering. These techniques are used in traditional illustrations for conveying shape and surface features as well as preserving visibility of embedded structures. Additionally, we employ atmospheric attenuation and shadow casting to increase both perception of depth and spatial relationship. The presented design decisions are also motivated by means of other medical visualization applications, which deal with embedded structures, such as liver surgery and neck dissection [269, 331].

Based on the proposed adapted vessel surface visualization, we conducted an initial qualitative user study with 40 participants (domain experts and non-domain experts). We presented visualizations of different surface types of cerebral aneurysms with embedded flow information depicted as streamlines. The participants had to evaluate our approach against a semitransparent surface rendering in terms of shape, depth, and flow perception. Based on this study, we improved our approach and conducted a controlled perceptual user study with a total of 86 participants. The experiments in these studies revealed a more accurate perception of the vessel surface in both depth and shape perception compared to the semitransparent rendering. Additionally, our questionnaire analysis demonstrated a qualitatively overwhelming preference for the adaptive surface visualization.

In summary, the contributions of this chapter are:

- A perceptually enhanced vessel surface visualization to preserve both important surface and anatomical features as well as an appropriate visibility

of the embedded flow visualization. The requirements of our adapted surface visualization were derived from discussions with medical experts and biomedical engineers as well as from the literature.

- We present a multi-pass rendering framework that composes several visualization layers of the surface and flow data. Thereby, we incorporate illustrative and depth enhancing rendering styles including ghosted view, line rendering, shadow, and depth attenuation to accomplish the visualization requirements. For the flow visualization we consider established techniques, such as integral lines and glyphs. Our framework, however, provides the flexibility to adapt each layer with other visualization or renderings techniques, e. g., more advanced flow depictions.
- To evaluate our approach with respect to a traditional semitransparent surface rendering, we design and conduct a qualitative and a perceptual user study. The perceptual study comprises three controlled experiments to analyze the perception of the vessel surface shape and its spatial relationship as well as the embedded flow. Both techniques are evaluated with respect to the participants' accuracy, response time, and their personal preferences.

## 5.2 RELATED WORK

Effective embedded surface (also called *nested surface*) visualizations are relevant in several domains like engineering, vector field analysis, medical research, and treatment planning. Examples of the engineering domain are technical illustrations of various objects, such as buildings, cars and mechanical devices. The depiction and analysis of complex integral surfaces with self-occlusions and subjacent layers is an example of the vector field domain. Finally, radiation therapy planning [163], liver surgery planning [269], or biomedical problems like visual exploration of nasal airflow [374] are applications of embedded surface scenarios in medical research and treatment planning. However, similar to the visual exploration of hemodynamic data in blood vessels each scenario is faced with occlusions and the same challenges regarding perception of shape, depth, and spatial relationships of all layers. Several visualization and perception-based research domains are involved to cope with these challenges.

**ILLUSTRATIVE SHAPE VISUALIZATION.** Illustrative shape visualizations aim at reproducing artistic drawings to convey surface shape details by means of shading, texturing, and pen-and-ink techniques [286]. Existent approaches are mainly based on local geometry and illumination information, such as normals, curvature measures and changes of luminance. Inspired by hand-drawn illustrations, Gooch et al. [133] present a non-photorealistic shading model that exploits the human sensitivity for cool and warm colors to convey shape and depth. Kindlmann et al. [186] incorporate this shading model in curvature-based transfer function design to convey depth and shape of volume datasets.

Based on classical bump mapping approaches Cignoni et al. [76] enhance surface details by incorporating a sharpened normal field into the traditional diffuse shading model. This normal enhancement emphasizes corners and edges resulting in an increased shape perception. An exaggerated shading approach is proposed

by Rusinkiewicz et al. [282] based on dynamically adjusting the effective light position for different areas of the surface. They also incorporate multiple scales of smoothed normal fields to convey details at a user-defined frequency. For an overview of standard shading approaches and a new shading model, which is driven by experimentally-founded statistical models we refer to recent contributions of Veronika Soltészová [304].

Fundamental questions concerning shape perception based on texture patterns were investigated by Interrante et al. [164] and Kim et al. [183]. Their findings reveal a more accurate shape perception for anisotropic texture patterns when the direction(s) of the texture anisotropy were aligned with one or both of the principal directions of curvature over the surface, as opposed to being aligned with an arbitrary direction. While all of these shading- and texture-based approaches certainly enhance the surface shape, they rely on an opaque surface rendering, which is not applicable for enclosing vessel surface rendering. However, we incorporate information about the local normal orientation in our approach to convey local surface orientation, such as concave and convex regions.

A reduced 3D surface description with visually pleasant results is the focus of illustrative line renderings, which are originated from traditional pen-and-ink illustrations. The main representatives are silhouettes [165], feature lines [84, 174, 371], stippling [16], and hatching [207, 267]. Each technique is capable to convey certain surface information, such as object boundaries, contours, curvature and illumination with a reduced amount of visual information. Because of their general application they can be combined and incorporated into several visualization domains, such as architecture, engineering and medical visualization [128, 269] (see also next paragraphs). For our application, however, we only consider silhouettes as suitable for surface rendering of vascular structures with internal flow. Depending on the flow visualization technique the generated lines and stripes on the surface may cause visual clutter in a combined visualization. For example, this is the case if integral lines are used as flow visualization.

**VISUALIZATION OF HIDDEN AND EMBEDDED STRUCTURES.** Essential works to convey hidden structures of multi-layered objects are inspired by traditional hand-drawn illustrations and artistic design principles. In Appel et al. [11] a haloed line effect is introduced and discussed to enhance hidden lines and the spatial relationship between crossing line segments. Dooley et al. [95] present the definition of illustration rules that are used to automatically adjust line and surface rendering parameters, such as line width, transparency and style, depending on occlusion, importance and endpoint conditions. Some of these design decisions, e. g., hidden line depiction, are also used in our approach. Examples of line renderings in interactive technical illustrations are presented by Nienhaus and Döller [252] as well as by Fischer et al. [105]. They utilize multi-pass renderings to extract several layers of hidden structures with a subsequent illustrative visualization of each layer, such as halftoning, silhouettes and contours. In a composing step they combine each layer to the final image. Thereby, the methods by Kaplan et. al [179] can be incorporated to accomplish an efficient identification of hidden line segment ordering.

A multi-pass framework for illustrative rendering of complex and self-occluded integral surfaces is proposed by Hummel et al. [161] and Born et al. [35]. They incorporate several rendering techniques, such as transparency modulations, hatch-



ing textures, halftoning and illustrative streamlines, to reveal subjacent layers and to enhance shape and depth perception of each layer. Our approach is also based on the concept of multi-pass rendering and individual layer visualizations.

Fundamental research in conveying both enclosing surface shape and embedded structures was accomplished by Interrante et al. [163] who investigated how sparsely-distributed opaque texturing can be used to depict the shape of transparent isointensity surfaces of radiation dose. They apply principle direction texture stripes on the enclosing surface and show that its 3D shape and relative depth to the embedded object can be more easily and accurately perceived compared to isotropic texture patterns and arbitrarily aligned texture stripes. Similar experiments and findings are demonstrated by House et al. [160]. An interactive view-dependent transparency model is proposed by Diepstraten et al. [90] to improve shape perception of embedded structures. Based on traditional manual illustrations they extract an effective set of design rules to adjust color-shaded, semitransparent surface renderings of embedded objects. As a result, the transparency and visibility of objects are adjusted according to the camera view and spatial relationship between opaque and semitransparent objects. This kind of visualization is an example of ghosted views and belongs to the group of *smart visibility techniques*.

Smart visibility techniques focus on exposing the most important visual information in the resulting images and originate from technical illustration. Other examples are cut-away views, section views, and exploded views. Viola and Gröller [347] discuss these techniques, which are also applicable for medical application and intervention planning [49, 330]. The basic strategy of these "smart" techniques is to emphasize the most relevant visual information of an object by means of local modifications of visual representations or changes in spatial arrangement according to importance values of the multi-layered objects. For our application the internal flow visualization is assumed to be the most important visual information and the enclosing vessels as spatial context. Thereby, we utilize the concept of ghosted views, which modify locally visual attributes, such as color and transparency to reveal embedded structures as presented in Diepstraten et al. [90]. Color and transparency modifications are also common in illustrative volume rendering for flow, science, and medicine by means of "smart" transfer functions [316, 131]. Exploded views are not suitable because they decrease the observer's ability to mentally link the vessel morphology with the internal flow visualization. Similar problems occur for masking techniques, such as cut-away and section views [91, 212]. Since they perform a view-aligned local clipping of enclosing surface parts, all morphological vessel information related to local internal structures, e. g., flow or treatment devices, are lost.

**CONVEYING DEPTH AND SPATIAL RELATIONSHIP.** Our application is also related to conveying information of depth and spatial relationship. Two important cues for depth and spatial arrangement are shadowing and shading [353]. A survey about existent shadow rendering approaches can be found in Liu and Pang [213]. The already mentioned non-photorealistic shading model by Gooch et al. [133] can also be considered to convey depth in such a sense that cool colors recede while warm colors advance. In Luft et al. [217] an image-based method is presented to efficiently integrate depth cues into complex scenes based on the differences between the depth buffer and its low-pass filtered copy. Further depth cues are atmospheric

attenuation, depth blurring and line fading, which are discussed in Rheingans and Ebert [275] and Svakhine et al. [315].

Shadow-like depth indicators by means of an adaptive hatching method are proposed by Ritter et al. [276] to enable reliable comparisons of spatial distances in complex vascular structures. The distances between intersected vessel parts are encoded with a modulated hatching width and brightness at these intersections. We incorporate shadow and atmospheric attenuation into our framework because of their general usage and well-established perception. A weighted combination of illustrative rendering techniques is utilized by Tietjen et al. [331] for depth- and shape-enhanced medical surface visualizations inspired by medical textbook illustrations. The weighting is controlled by a so called *shading map*, which combines several illumination and surface information, such as plateau and raking light, atmospheric attenuation, and curvature. The final shading map describes the intensity at each surface location, which is used as lookup table for various techniques including silhouettes, features lines, stippling and hatching. Except from silhouettes, however, pen-and-ink techniques are not suitable for our application, as discussed in the above paragraph about illustrative shape visualizations.

**PERCEPTUAL EXPERIMENTS.** In computer graphics and visualization, findings from psychophysical studies are increasingly used for both to evaluate and compare existent methods as well as to improve their effectiveness [21]. For the work at hand we consider evaluations with respect to the perception of shape, depth, and spatial relationship as well as to smart visibility techniques, which include also methods for embedded surface visualizations. Several researchers have examined the 3D shape perception of structures by asking the participants to orient prepositioned gauges to coincide with the perceived surface normal at several positions on the object's surface [18, 78, 183]. The normal estimates of the participants were compared with ground truth data provided by a registered 3D surface model to analyze the participants' accuracy. The visualization techniques were evaluated according to the recorded average angle errors in normal estimation. This gauge technique was pioneered by Koendrink et al. [189]. We consider this technique as very effective and incorporate it in the design of our study.

Studies concerning depth and spatial perception focus mainly on tasks for depth ordering and spatial relationships. In the already mentioned work on shadow-like hatching methods by Ritter et al. [276] the participants either had to specify the correct depth order of marks on complex vascular structures or to determine the depth distance order between vascular segments. Similarly, Weigle et al. [356] presented complex filamentous structures using various shadowing methods and asked participants to identify which one of several overlapping structures was in front. Kuß et al. [198] presented a complex scene consisting of three volumetric objects and one transparent filamentous structure for a few seconds and then asked their participants whether a filament runs through a transparent structure. The different visualization techniques were evaluated with respect to both accuracy and response time. In the context of embedded flow information we are not faced with complex vascular structures and consider tasks for depth ordering as the most effective way to assess depth and spatial relationship.

To the best of our knowledge, no comprehensive and rigorous evaluation of smart visibility techniques has been performed; only some informal studies exist.

Li et al. [212] demonstrated their system for authoring and viewing interactive cutaway illustrations to medical educators, illustrators, and architects to gather informal feedback. Similarly, Tietjen et al. [329] presented anatomical visualizations to medical experts and analyzed the subjective preference of the participants in a questionnaire-based form. One of the most rigorous studies to date is from Chan et al. [70], who asked participants to rank the degree of perceived transparency and quality of the generated images. These findings, however, are strictly bound to particular applications and it is difficult to generalize from them. There is considerable evidence that performance on such preference or meta-tasks – where one's beliefs and opinions are surveyed – does not always correlate well with actual task performance [351]. Controlled perceptual experiments can be performed such that the results are more general and enable a quantitative analysis of specific visualization techniques. Baer et al. [14] presented experimental studies, where participants were asked to examine the focus parts of focus-context illustrations. Accuracy and response time were measured to evaluate different visualization techniques.

### 5.3 REQUIREMENT ANALYSIS AND DATA INPUT

As mentioned in the introduction of this chapter we focus on an expressive visualization of pathological and non-pathological vessel morphology with embedded flow visualizations. According to the literature and discussions with domain experts it turns out that for the qualitative analysis of these two information the flow visualization is of major interest. However, the inspection of the flow is strongly related to its surrounding vessel anatomy, as stated in descriptions like:

*"Typical normal flow patterns, such as flow acceleration near the aortic valve or mild right-handed helical systolic flow in the ascending aorta, can be appreciated."* [222] or  
*"...flow patterns showing the bleb at the flow impaction region"* [67].

Given this strong reference to the anatomical context, a detailed visual description of it would lead to an increased occlusion of the embedded flow information. Thus, an adaptive vessel visualization is needed that conveys the most important anatomical features whilst simultaneously gaining appropriate visibility of the embedded flow visualization. Based on observations in the literature and discussions with our domain experts we address the following requirements:

**Visibility of internal flow visualization:** An appropriate visibility of the internal flow visualization is required during the visual exploration and qualitative evaluation process. With "appropriate", we mean as few as possible occlusions of the flow visualization and reliable perception of its encoded information, e.g., color-coded speed. This supports the viewer in interpreting and tracing the flow. Thereby, we observe that the focus of attention is mostly centered to the camera, which implies a maximum visibility of the flow towards the viewer.

**Conveying of anatomical features:** An adaptive vessel visualization should convey important anatomical features consisting of general morphological information and morphological features relevant for pathological cases. General morphological information are the vessel boundaries that convey branches and diameters

as well as regions with high curvature. Morphological features for pathologies are anatomical landmarks, which are taken into account during flow inspection. Since we focus on cerebral aneurysms, we consider the inlets and outlets, the ostium as well as blebs as most important landmarks (recall Sec. 2.3.1). For other CVDs, however, there are also relevant landmarks, such as valves and aortic dissection areas for inspection of heart failures and Marfan syndrom. Another important requirement is the general usability of the anatomical feature visualization. For a general adaptive vessel visualization, the feature representation should be perceivable and not distracting, regardless of the embedded flow visualization technique.

**Conveying of spatial relationships and depth:** Occluded morphological surface features and flow information have to be distinguished from visible parts of the surface and flow. Additionally, depth cues according to overlapped vessel parts and surface distances to the viewer have to be provided. These hints increase the perception of spatial relationships between different vessel parts and tracing of the embedded flow. Furthermore, attenuation of distant information supports focusing on relevant information close to the viewer.

In the following, we describe the details of our approach to fulfill these requirements based on the data input that results from the data acquisition pipeline presented in Section 3.3 and Section 3.4 for measured and simulated hemodynamic datasets, respectively. In particular, we consider the surface mesh of the vessel, the structured or unstructured vector field as well as the meshes of the inlets, outlets and the ostium in the case of a cerebral aneurysm. The usage of the vessel surface mesh as morphological context is suitable since it is a common result from the post-processing of clinical image data even for the measured datasets. Moreover, for the simulated flow datasets the computational domain is fitted to the vessel surface and ensures a well-defined spatial coverage of the final flow visualization techniques. A volume rendering on the original image datasets may lead to an over- or under-represented vessel boundary, which does not cover the spatial extension of the flow visualization. Additionally, the adjustment of the transfer function may be challenging due to noise, partial volume effects or contrast bolus dynamics in the image datasets (see Sec. 3.4.2).

#### 5.4 ADAPTIVE SURFACE VISUALIZATION

We achieve an adaptive vessel surface visualization by composing several illustrative rendering styles of the data input, shown in Figure 49. The data input consists of the vessel surface, the anatomical features and the flow information, in particular flow velocity. The subsequent workflow consists of two stages: the *layer stage* where several offscreen renderings of the data input are generated and the *composing stage* where the layers are composed to the final visualization. A ghosted view rendering is applied to the vessel surface and silhouette rendering is used to depict both the vessel boundary shape and anatomical features. The flow field data is represented with established flow visualization techniques, such as arrow glyphs or (illustrative) streamlines and pathlines.

Note that we do not focus on proposing new flow visualization techniques but on a combination of existent techniques with the adaptive surface visualization. These three layers and their depth information are delivered as input to the composite stage. In this stage, we compose each layer depending on its depth informa-

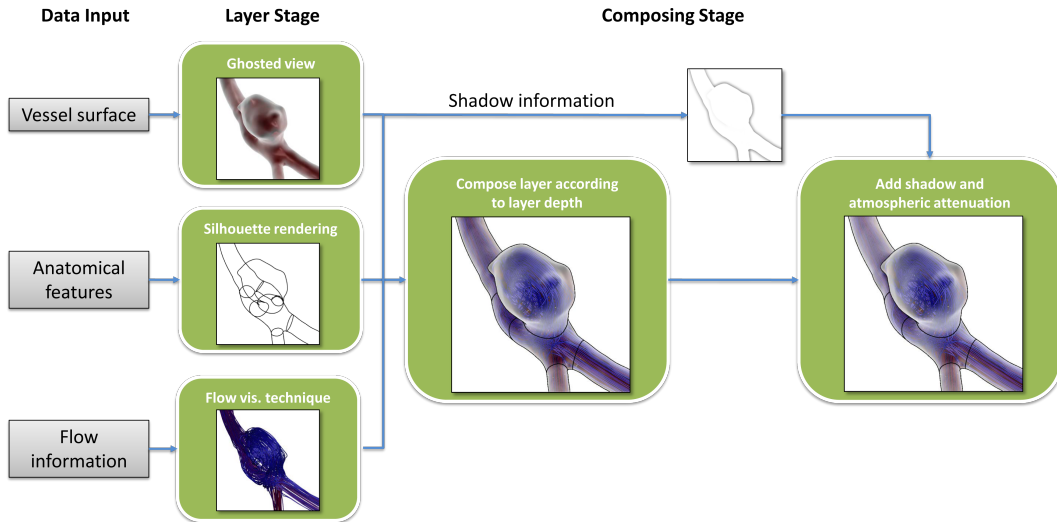


**Figure 49:** Overview of our adaptive surface visualization approach that consists of two stages. In the layer stage we generate several offscreen renderings of the data input including a ghosted view for the vessel surface, silhouette rendering for anatomical features and the vessel boundary as well as established flow visualization techniques for the flow velocity. Additionally, a shadow information layer is derived from the vessel surface. In the composing stage all layers are put together with atmospheric attenuation to the final visualization.

tion. Additionally, we apply shadowing and atmospheric attenuation to the composed result derived from the vessel surface. In the following, we give a detailed description of each stage with implementation details.

#### 5.4.1 Ghosted View Rendering

For the visibility of the embedded flow visualization a certain kind of transparency rendering of the vessel surface is necessary. Inspired by smart visibility techniques, we utilize a ghosted view approach of the vessel surface and consider rules regarding transparency rendering that are proposed by Diepstraten et al. [90]. These rules are derived from hand-drawn ghosted views, which can be found in technical or medical illustrations. They are expressed as follows:

- Faces of transparent objects never shine through.
- Opaque objects which are occluded by two or more transparent objects do not shine through.
- Transparency falls off close to the borders of transparent objects and increases with the distance to the borders.

We incorporate these rules by applying a ghosted view on the front faces and an opaque rendering of the back faces. The ghosted view is achieved by means of a view-dependent transparency in such a way that the surface regions are more transparent the more the regions are orientated to the viewer. For the surface orientation we compute the angle between the view direction and the surface normal. In particular, we employ an approximation of the Fresnel reflection model<sup>1</sup> that

<sup>1</sup> Named after the French engineer and physicist Augustin-Jean Fresnel.



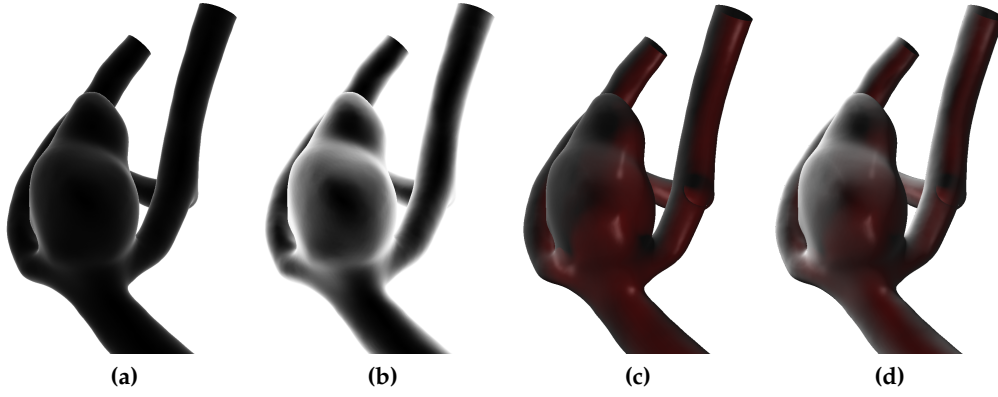


**Figure 50:** Encoding of the Fresnel transparency with different edge fall-off values  $r$ . A value of  $r = 3.0$  is used in (a) and  $r = 1.0$  in (b) that emphasizes more the surface shape. Darker values relates to lower transparency. For each value the resulting ghosted view rendering with the opaque backfaces are shown in (c) and (d), respectively.

describes the amount of reflected and refracted light when it moves between two media of differing refractive indices [292]. More light is reflected with increasing incident angles to the surface, whereas for small incident angles more light is refracted and penetrates the interface between the two media. We replace "reflection" with the inverted "transparency" to achieve more front face opacity at regions facing away from the viewer and more visibility to the back faces at regions facing towards the viewer. This enhances regions with high surface curvature, which are located around regions towards the viewer. The Fresnel transparency  $\alpha_{\text{fresnel}}$  can be expressed as:

$$\alpha_{\text{fresnel}} = 1.0 - (|\hat{n} \cdot \hat{v}|)^r, \quad (26)$$

where  $\hat{n}$  and  $\hat{v}$  are the normalized surface normal and view vector, respectively. The parameter  $r \geq 0$  controls the strength of the opacity edge fall-off and is user-defined. A value of  $r = 0$  corresponds to full transparency of the edge fall-off color and with increased  $r$  the edge fall-off color becomes more opaque. In Figure 50a and Figure 50b the Fresnel transparency with  $r = 3.0$  and  $r = 1.0$  are shown applied to a cerebral aneurysm dataset. Darker values correspond to higher transparency and brighter values represent higher opacity of the edge fall-off color. A linear blending between edge fall-off color and back face color controlled by  $\alpha_{\text{fresnel}} \in [0, 1]$  is depicted in Figure 50c and Figure 50d, respectively. Initially, we define white as edge fall-off color because of the later neutral color blending with the embedded flow visualization.

**Implementation.** We implement the ghosted view rendering by means of a two-pass offscreen rendering using the frame buffer object (FBO) capability of OpenGL. In the first pass we render the Phong-shaded back faces color and its depth information into two textures. In the second pass we assign the edge fall-off color to the front faces and set its alpha value to the computed Fresnel transparency. The final color and depth information are also stored into two textures.



### 5.4.2 Silhouette Rendering

Pen-and-ink methods like line drawings, hatching and stippling are effective illustrative techniques to sparsely convey the shape, material and illumination of an object [78, 286]. However, for the usage as enclosing surface depiction with embedded structures some of these methods are less expressive and may introduce visual clutter depending on the enclosed visualization. We observed this for feature line methods, hatching and stippling, which result in distracting overlaid information when inspecting embedded flow visualizations, especially for line-based flow visualization techniques, e. g., integral lines.

This is demonstrated in Figure 51a and Figure 51b for a suggestive contour [84] and hatching rendering [207] over a streamline visualization in a cerebral aneurysm dataset. The streamlines are color-coded according to local speed. In Figure 51c the same aneurysm dataset is shown only with silhouette rendering for the vessel boundary, the inlets and outlets as well as the ostium, which leads to a more clear visualization. Although the hatching visualization indicates the bulge on the aneurysm sac it may lead to occlusion at the vessel border due to the dense line representation. Such bulge or bleb formations are also indicated by our ghosted view rendering as shown in the right image of Figure 49.

As a consequence, we utilize only silhouette rendering to the vessel boundary and its anatomical features because we want to provide a flexible shape description, which is applicable to various flow visualization techniques. Furthermore, simple silhouette rendering seem to be an intuitive way to communicate vessel shape and feature information with embedded flow dynamics. This has not only been shown in medical textbooks but also in discussions with our domain experts.

**Implementation.** We implement an object-based silhouette rendering on the GPU to ensure individual line stylization, e. g., stippling patterns or texturing. Image-based approaches are less flexible concerning the control over resulting line attributes [165]. Silhouette edges are either identified where an edge connects a front and back face or where an edge has only one adjacent face. We use the triangle adjacency information of OpenGL to detect these edges in the geometry shader and construct a view-aligned quad for each edge in the same shader. The four vertices of the quad are shifted along a vector, which is the cross-product between the edge and viewing direction. For the two "inside" vertices the displacement vector

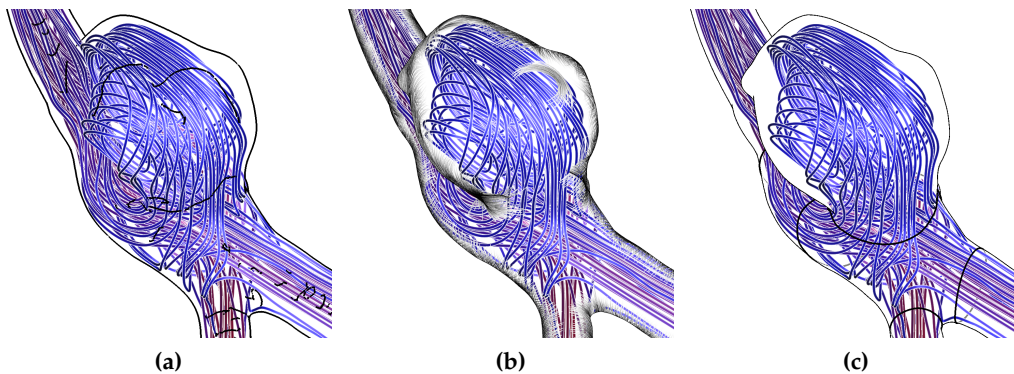


**Figure 51:** In comparison to suggestive contours (a) and hatching (b), a simple silhouette and contour rendering of the anatomical features (c) leads to a more clear visualization.

is flipped. Additionally, we assign texture coordinates to each quad vertex that enable a flexible line stylization. We perform two line rendering FBO passes, one for the vessel boundary and one for the anatomical features. For each pass we apply two different line styles in the fragment shader to distinguish between visible and hidden lines, later. The four resulting colors and the depth information are stored in four textures for the final composite stage. The hardware-accelerated silhouette detection was originally proposed by McGuire and Hughes [228], but they did not have access to the geometry shader stage. Therefore, they generated a degenerated quad geometry for each edge with its adjacency information on the CPU and had to upload it to the GPU at the expense of increased GPU memory load. In the vertex shader, they detected the silhouette edges and expanded the corresponding quads.

### 5.4.3 Flow Visualization

The input flow field consists of vector and scalar information at each grid point, such as direction, speed and pressure. As shown in Chapter 4, a large variety of established and adaptive techniques exist to visualize these or derived information. Since we do not focus on new flow visualization techniques, we consider only techniques that are frequently used for visualizing hemodynamic characteristics, such as streamlines, glyphs, stream surfaces and isosurfaces [61, 194, 336]. For a better perception of spatial relationships in cases of dense streamline and glyph representations we incorporate depth-dependent halos proposed by Everts et al. [102]. These halos convey the spatial depth between overlaid lines and glyphs by adapting the size of the halo depending on the depth between two crossing segments. The halo rendering and texture mapping are provided optionally to the user.

**Implementation.** For the streamline and glyph visualization we utilize a combination of the method presented in Everts et al. [102] and the aforementioned silhouette rendering. In a preprocessing step we integrate the flow field with the adaptive Runge-Kutta scheme [325] to generate streamline linestrips starting at user-defined seed locations. Together with line adjacency information we pass them to the geometry shader and generate view-aligned and connected quads combined with texture coordinates. This is in contrast to Everts et al. [102], who generate all quad geometry on the CPU at the expense of increased GPU memory load. Once the view-aligned quads are passed to the fragment shader, we apply depth-dependent halos and line illumination. The glyphs are based on line segments, which are located at each flow grid point and aligned according to the local velocity vectors. The segment lengths are scaled to the magnitude of the flow vectors. For each line segment we generate a view-aligned quad with texture coordinates and compute the depth dependent halos by means of the quad's texture coordinates. Stream surfaces are based on multiple seeded streamlines at user-defined seeding curves with subsequent triangulations. Integral lines, glyphs, and stream surfaces can be color-coded according to several scalar attributes, such as speed or pressure. Again, the color and depth information of the chosen flow visualization are rendered in two separated FBO textures for the final composing.

#### 5.4.4 Shadow and Atmospheric Attenuation

It is well known that shadow and atmospheric attenuation are important depth cues. Therefore, we integrate both cues into our final visual rendition to increase depth perception and spatial relationship between overlapped vessel parts as well as to support the viewer in tracing the flow and focusing on close visual information. We approximate shadow casting in a non-physically correct but computationally efficient way by applying the method of Luft et al. [217]. They compute a *spatial importance function*  $\Delta D$  from the depth buffer and its low-pass filtered version by

$$\Delta D = G * D - D,$$

with  $G * D$  being the convolution of a normalized Gaussian filter kernel and the depth buffer  $D$ . Thereby, a negative spatial importance value  $\Delta D^-$  with  $\Delta D < 0$  represents areas of background objects that are close to other occluding objects. The shadow casting is approximated by adding  $\Delta D^-$  to the original color, which causes a local darkening depending on the magnitude of  $\Delta D^-$  scaled with a user-defined parameter  $\lambda$ . We apply this approach to the vessel front faces based on modified depth buffer information of them to ensure a consistent darkening independent of the view point transformation.

By default, depth values correspond to object distances related to the camera's near and far clipping plane in a mostly logarithmic scaling. If these planes will change, e.g., due to zooming (perspective camera) or translation (orthographic camera), the resulting depth values also change. This is demonstrated in Figure 52c, where for two camera distances the depth values for an aneurysm surface are shown. For a vessel section, the two resulting spatial importance values  $\Delta D$  are presented in the corresponding insets where dark regions indicate  $\Delta D < 0$ . It can be seen that for the two camera distances the importance values change. This will cause a non-constant appearance of the shadow casting, which may result in a misinterpreting of spatial distances. Since view point transformations are

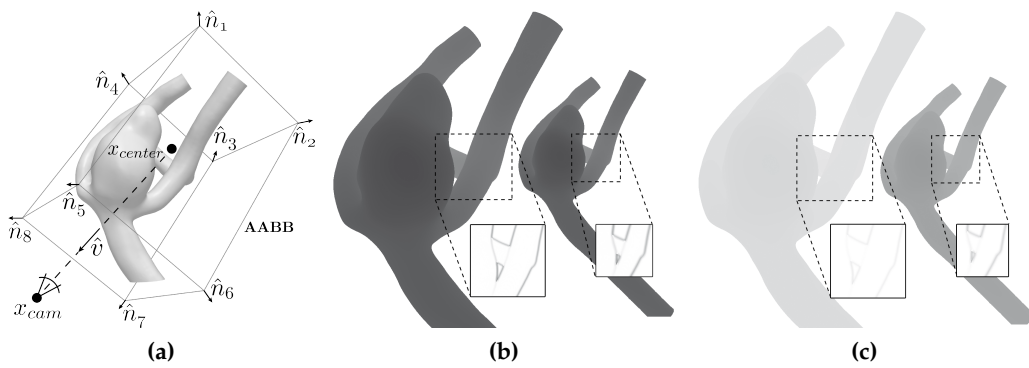


**Figure 52:** Illustration of pseudo depth value computation and its effect on the spatial importance function  $\Delta D^-$ . The depth values are related to the current closest and farthest point of the bounding box shown in (a). This results in constant  $\Delta D^-$  values in (b) independently from the current viewing transformation. On the contrary, standard depth values change during viewing transformation that results also to changed  $\Delta D^-$  in (c).

**Algorithm 1** Computation of the pseudod depth values.**Require:****AABB** Axis-Aligned Bounding Box of the vessel $\mathbf{x}_{\text{center}}$  Center of **AABB** $\mathbf{x}_{\text{cam}}$  Camera position**Ensure:** Linear depth value  $d(\mathbf{p})$  for each vertex  $\mathbf{p}$  relative to **AABB**

```

1: for Each Frame do
2:    $\hat{\mathbf{v}}$  = normalized view vector between  $\mathbf{x}_{\text{cam}}$  and  $\mathbf{x}_{\text{AABB}}$ 
3:    $\alpha_{\min} = \infty$ 
4:   for Each Bounding Box Point  $\mathbf{x}_i$  do
5:      $\hat{\mathbf{n}}_i$  = normal at  $\mathbf{x}_i$  of AABB
6:      $\alpha_i$  = angle between  $\hat{\mathbf{v}}$  and  $\hat{\mathbf{n}}_i$ 
7:     if  $\alpha_i < \alpha_{\min}$  then
8:        $\mathbf{x}_{\text{near}} = \mathbf{x}_i$ 
9:        $\alpha_{\min} = \alpha_i$ 
10:    end if
11:  end for
12:   $\mathbf{x}_{\text{far}}$  = diagonal corner point of  $\mathbf{x}_{\text{near}} \in \mathbf{x}_{\text{AABB}}$ 
13:   $d(\mathbf{x}_{\text{near}}) = d(\mathbf{x}_{\text{cam}}, \mathbf{x}_{\text{near}})$ 
14:   $d(\mathbf{x}_{\text{far}}) = d(\mathbf{x}_{\text{cam}}, \mathbf{x}_{\text{far}})$ 
15:  Compute  $d(\mathbf{p})$  according to Equation 27
16: end for

```

important interaction schemes during the visual exploration process, a consistent shadow appearance is necessary.

Thus, we generate additional pseudo depth values for the vessel front faces, which are related to the vessel bounding box and are used for the shadow casting computation. The algorithm for computing the modified depth values is presented in Algorithm 1 and illustrated in Fig. 52a. The input for the algorithm are the axis-aligned bounding box (**AABB**) of the vessel and the current camera position  $\mathbf{x}_{\text{cam}}$ . The output is a linear depth value  $d(\mathbf{p})$  for each vertex position  $\mathbf{p}$  that is relative to the extent of the **AABB**.

For each frame, we compute the normalized view vector  $\hat{\mathbf{v}}$  between the  $\mathbf{x}_{\text{cam}}$  and the center point  $\mathbf{x}_{\text{center}}$  of the **AABB**. The view vector is utilized to identify the closest and farthest corner point of the **AABB** to the camera position by computing the angles between  $\hat{\mathbf{v}}$  and each of the eight **AABB** vertex normals  $\hat{\mathbf{n}}_i$  with  $i \in [1, 8]$ . The closest corner point  $\mathbf{x}_{\text{near}}$  is identified with the smallest angle, and the farthest point  $\mathbf{x}_{\text{far}}$  is its diagonal corner point. Based on  $\mathbf{x}_{\text{near}}$  and  $\mathbf{x}_{\text{far}}$  pseudo depth near  $d(\mathbf{x}_{\text{near}})$  and far  $d(\mathbf{x}_{\text{far}})$  values are computed as Euclidean distances to the camera position. The normalized depth value  $d(\mathbf{p}) \in [0, 1]$  of a vertex  $\mathbf{p}$  is then computed as

$$d(\mathbf{p}) = \frac{d_{\text{far}}(\mathbf{x}_{\text{cam}}, \mathbf{x}_j) - \mathbf{p}_z}{d_{\text{far}}(\mathbf{x}_{\text{cam}}, \mathbf{x}_j) - d_{\text{near}}(\mathbf{x}_{\text{cam}}, \mathbf{x}_i)} \quad (27)$$

with  $\mathbf{p}_z$  as Euclidean distance between  $\mathbf{p}$  and the camera position in eye space. This ensures a linear scaling of depth values between vessel sections with consistent values of  $\Delta D$  independent of the camera transformation, shown in Figure 52b.

Atmospheric attenuation as second depth cue is introduced by applying a fog effect to the final composition, which makes the vessel and its embedded flow fade into the distance  $d(\mathbf{p})$  from Equation 27. The fog effect is accomplished by a linear blending between the composed color and the background color in the composite stage, later. Because most of the flow visualization techniques employ color-coding for hemodynamic quantities, such as speed and pressure, the fog effect would modify this coloring and may distort the interpretation of the coded attribute. Therefore, we apply the linear fog blending only to these vessel parts where  $d(\mathbf{p}) \geq d(\mathbf{x}_{\text{cam}}, \mathbf{x}_{\text{center}})$ , i. e., behind the center of the **AABB**. Formally, we define the atmospheric attenuation value  $a(\mathbf{p})$  as follows:

$$a(\mathbf{p}) = \max \left( \frac{d(\mathbf{x}_{\text{cam}}, \mathbf{p}) - d(\mathbf{x}_{\text{cam}}, \mathbf{x}_{\text{center}})}{d_{\text{far}} - d(\mathbf{x}_{\text{cam}}, \mathbf{x}_{\text{center}})}, 0 \right). \quad (28)$$

**Implementation.** The shadow casting and atmospheric attenuation are applied in the composite stage based on an FBO texture that contains the pseudo depth values and attenuation values of the front vessel faces. We generate this texture in the render pass for the Fresnel transparency of the vessel front faces. Therefor, we pass  $d(\mathbf{x}_{\text{near}})$  and  $d(\mathbf{x}_{\text{far}})$  from lines 13 and 14 of Algorithm 1 to the vertex shader and compute  $d(\mathbf{p})$  there. In the associated fragment shader, the interpolated depth and attenuation values are stored in the red and green channel, respectively, of the aforementioned FBO texture. The convolution of this texture with the Gaussian filter, the computation of the spatial importance function  $\Delta D$ , and the application of the fog effect are entirely accomplished in the composite stage on the GPU.

#### 5.4.5 Compositing

The previous sections generated several offscreen rendered textures, which represent information and visualization layer of the vessel and embedded flow. Overall, we pass nine textures to the composite stage where they are composed to the final adaptive vessel visualization, including the shadow casting and atmospheric attenuation. Furthermore, there are four user-defined parameters, which are required for the texture generation and compositing: the edge fall-off value  $r$  for the Fresnel transparency (see Sec. 5.4.1), the kernel size and standard deviation of the Gauss filtering as well as the scaling parameter  $\lambda$  for the computation of the spatial importance function (see Sec. 5.4.4).

For each parameter, however, we identified empirically suitable default values, which are independent of the vessel size and screen resolution. We set the edge fall-off value  $r$  to 2.0 for an appropriate trade-off between visibility of the embedded flow and contextual vessel shape representation. For the convolution of the pseudo depth texture we parametrize it with a standard deviation value of 20 and a kernel size of 2% of the screen diagonal, as proposed by Luft et al. [217]. Combined with a value of 5.0 for  $\lambda$  this ensures a recognizable but not distracting shadow casting at the edges of crossing vessel sections. Note that each flow visualization technique may be accompanied by further parameter adjustments, but this is not related to our approach.

The composition performs an ordered accumulation of each texture layer to ensure a correct final blending. Additionally, parts of vessel sections, anatomical

---

**Algorithm 2** Compositing of all offscreen rendered layers to the final adaptive surface visualization. Depth values are in the range between 0 (near plane) and 1 (far plane).

---

**Require:**

$C_{\text{front}}, D_{\text{front}}$  : Color, depth texture front faces  
 $C_{\text{back}}, D_{\text{back}}$  : Color, depth texture back faces  
 $C_{\text{silhouette-visible}}, D_{\text{silhouette-visible}}$  : Color, depth texture visible silhouette lines  
 $C_{\text{silhouette-hidden}}, D_{\text{silhouette-hidden}}$  : Color, depth texture hidden silhouette lines  
 $C_{\text{features-visible}}, D_{\text{features-visible}}$  : Color, depth texture visible anatomical feature lines  
 $C_{\text{features-hidden}}, D_{\text{features-hidden}}$  : Color, depth texture hidden anatomical feature lines  
 $C_{\text{flow}}, D_{\text{flow}}$  : Color, depth texture flow visualization  
 $D_{\text{pseudo}}$  : Pseudo depth texture of vessel front faces  
 $\lambda$  : User defined weighting for  $\Delta D^-$

**Ensure:** Composite output color

```

1:  $\alpha_{\text{fresnel}}$  = alpha channel of  $C_{\text{front}}$ 
2:  $\alpha_{\text{flow}}$  = alpha channel of  $C_{\text{flow}}$ 
3:  $d(\mathbf{p})$  = red channel of  $D_{\text{pseudo}}$ 
4:  $a(\mathbf{p})$  = green channel of  $D_{\text{pseudo}}$ 
5:  $\Delta D^- = \min(\text{gaussFilter}(d(\mathbf{p})) - D_{\text{front}}, 0)$ 
6: color =  $C_{\text{back}}$ 
7: if  $D_{\text{features-hidden}} < 1$  and  $D_{\text{features-hidden}} < D_{\text{back}}$  then color =  $C_{\text{feature-hidden}}$ 
8: if  $D_{\text{flow}} < D_{\text{back}}$  then color = mix(color,  $C_{\text{flow}}, \alpha_{\text{flow}}$ )
9: color = mix( $C_{\text{front}}$ , color,  $\alpha_{\text{fresnel}}$ )
10: if  $D_{\text{front}} < 1$  then color = color +  $\lambda \Delta D^-$ 
11: color = mix(color,  $C_{\text{background}}, a(\mathbf{p})$ )
12: if  $D_{\text{front}} \geq 1$  then color =  $C_{\text{background}}$ 
13: if  $D_{\text{silhouette-visible}} < D_{\text{front}}$  then color =  $C_{\text{silhouette-visible}}$ 
14: if  $D_{\text{silhouette-hidden}} < 1$  and  $D_{\text{silhouette-hidden}} > D_{\text{back}}$  then color =  $C_{\text{silhouette-hidden}}$ 
15: if  $D_{\text{features-visible}} < 1$  and  $D_{\text{features-visible}} < D_{\text{front}}$  then color =  $C_{\text{feature-visible}}$ 

```

---

features and the visualized flow can be enhanced separately. All steps are summarized in Algorithm 2, which takes the 15 offscreen rendered textures and the default parameters for the computation of  $\Delta D$ . The function `gaussFilter(texture)` in line 5 of Algorithm 2 performs the low pass filtering of the pseudo depth values with the parametrized Gauss convolution. The compositing starts with the backface color, which is replaced or mixed with the color of subsequent layers, depending on their depth values. The multiple `mix( $C_a, C_b, r$ )` function in Algorithm 2 represents a linear blending between two colors depending on  $r \in [0, 1]$  with  $(1.0 - r) \cdot C_a + r \cdot C_b$ . Note that the user has the opportunity to enable and disable some visualization styles, such as hidden parts rendering, shadow casting and atmospheric attenuation. For a simplified illustration of the compositing steps, however, we omit these statements in Algorithm 2.



**Implementation.** The implementation of Algorithm 2 is straightforward and applied to a full screen render pass with a screen-aligned quad. The quad and its texture coordinates are generated in a geometry shader and passed to the fragment shader with the accompanied textures and parameters. The access to the individual textures is performed by means of the quad's texture coordinates.

## 5.5 RESULTS AND INFORMAL USER FEEDBACK

We applied our approach to several pathological and non-pathological clinical vessel datasets consisting of cerebral vessels and aneurysms as well as aortas and aorta ectasias. The cases of cerebral aneurysms include standard types, i. e., saccular and fusiform, as well as special malformations, such as presence of blebs and giant aneurysms. The flow fields for the aortic datasets are acquired by 4D PC-MRI, and for the cerebral datasets CFD simulations are performed. The vessel surfaces with their flow grids are generated and preprocessed according to the acquisition pipeline in Section 3.4. The spatial resolutions of the measured datasets range from  $150 \times 150 \times 50$  to  $144 \times 256 \times 128$  voxels with a voxel size of  $1 \times 1 \times 1$  to  $2 \times 2 \times 2.5$  mm and the temporal resolution comprises 20 to 25 time steps with about 50 to 70 ms between each time step. The simulated flow grids are composed of 181,000 to 3,321,525 volume elements (tetrahedra and prisms) with a volume diagonal of 0.02 to 0.08 mm. The number of triangles for the vessel surfaces range from 19,234 to 380,914.

The presented approach is embedded in the prototyping environment MeVis-LAB and implemented in C++, supported by OpenGL, GLSL and VTK. On a standard PC (3.2 GHz Core Duo, 4GB RAM) using an Nvidia GeForce 9800 GT, we achieve interactive frame rates for a screen resolution of  $1280 \times 1024$ . Because we provide empirical default values for the ghosted view and shadow casting parameters, user interaction is only necessary to enable and disable individual render layers, such as hidden flow parts or depth attenuation.

In Figure 53, we present a comparison between a semitransparent visualization and our approach applied to a cerebral aneurysm with a bleb formation. The embedded flow is visualized with illustrative streamlines and color-coded according to the local speed. The semitransparent rendering in Figure 53a provides a clear view onto the embedded flow visualization but conveys vessel shape and depth poorly. Vessel shape and depth depiction is increased by our ghosted view rendering with atmospheric attenuation and shadow casting, respectively, shown in Figure 53b. Additionally, the ostium as anatomical feature is emphasized by a contour rendering and hidden flow parts are indicated in gray to track the flow more comprehensibly. However, the bright edge fall-off color of the ghosted view rendering might lead to a misinterpretation of the enclosing surface orientation. This was reflected in the results of the informal user feedback presented in the subsequent section. As a consequence we changed the bright edge fall-off shading to standard Phong shading, as presented in Figure 53c. In Figure 53d, the atmospheric attenuation and shadow casting is turned off for comparison.

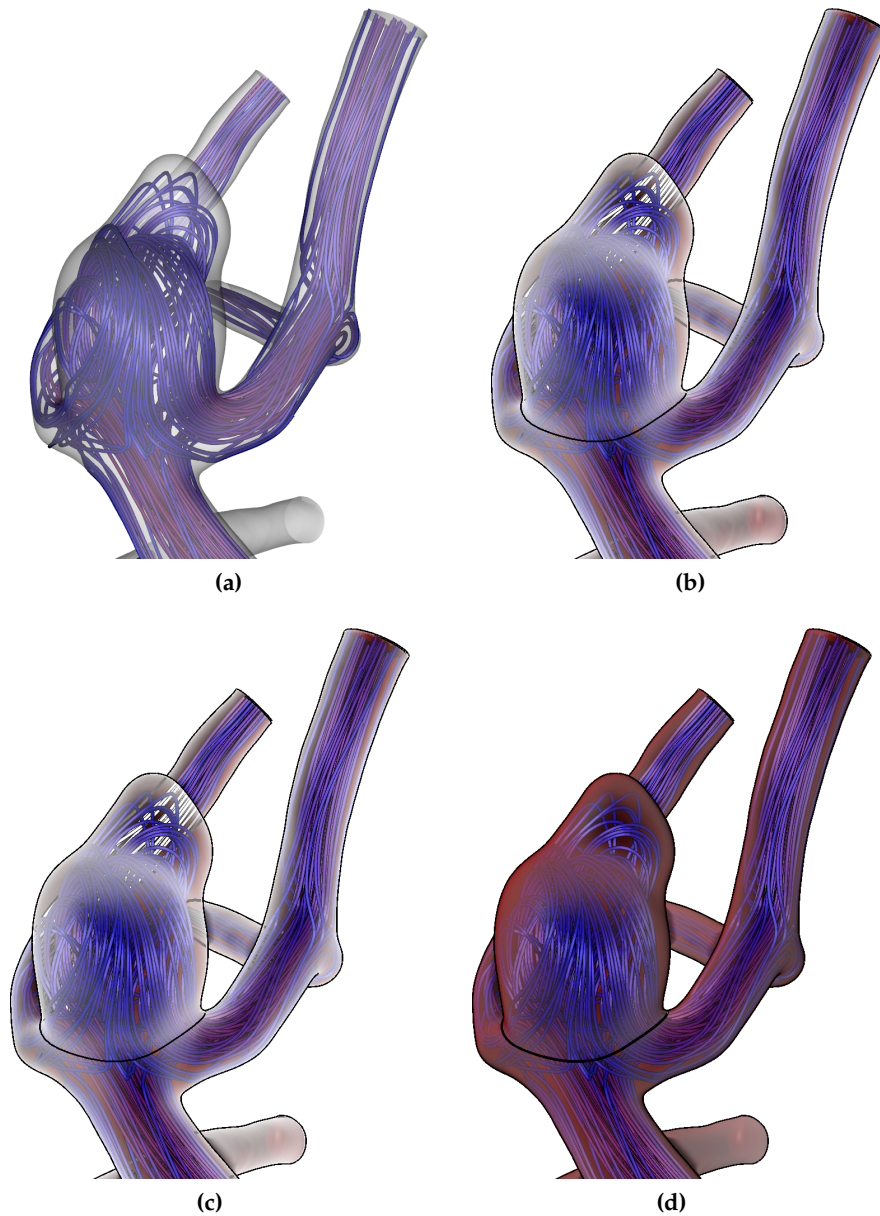


**Figure 53:** Comparison between (a) the semitransparent and (b) our adaptive surface visualization approach applied to a cerebral aneurysm with embedded illustrative streamlines. Anatomical features are indicated with silhouette rendering and gray lines depict hidden flow or vessel parts. In (c) shadow casting and atmospheric attenuation are added to improve depth perception. The modified version of our approach based on the informal user feedback is shown in (d) with a Phong-shaded non-white front face color, increased line width for the anatomical features as well as removed hidden flow and vessel parts.

### 5.5.1 Informal User Feedback

Since we aim for an effective vessel surface depiction with embedded flow visualization that overcomes limitations of standard semitransparent surface rendering we collected an initial feedback from domain experts and visualization scientists. Based on this feedback and resulting improvements we conducted a controlled perceptual user study to quantify the efficiency of our approach. The informal user feedback was accomplished by means of a domain expert survey with 40 participants (13 of which were medical experts). In the following we present the survey design and its important results, which we used to improve our approach for the subsequent perceptual user study.

#### 5.5.1.1 Survey Design

We designed a web-based questionnaire, which contains 30 randomized image pairs – one web page for each image pair. Each pair consists of one of three cerebral aneurysm surface renderings: one depicting the aneurysm semitransparently (50% transparency) and one with our approach. The camera settings are identical for each individual pair but changed between two pairs. The light conditions are constant and set to a white light located top left of the camera. For each dataset the embedded flow is depicted with color-coded streamlines based on the flow speed. We asked the participants to evaluate our approach according to the following four criteria:

- **Depth Perception:** *"Which figure conveys more information about depth?"*
- **Spatial Relationships:** *"In which figure can you recognize more overlapping surface parts?"*
- **Flow Perception:** *"In which figure can you better perceive the flow?"*
- **Surface Shape:** *"In which figure can you recognize the surface shape better?"*

For each question, the participant was prompted to decide between one of the two images. Additionally, each subject was asked to rate his or her medical experience and had the opportunity to provide a comment at the end of the questionnaire.

#### 5.5.1.2 Survey Results

For each criterion, we evaluated the participant's grade of satisfaction, which is shown in Figure 54. If a participant favored our approach for each of the 30 presented image pairs, his or her grade of satisfaction would be 100%, whereas a complete rejection results in a grade of 0%. In contrast to our expectations, most of the participants assessed our approach poorly regarding perception of depth (Fig. 54a), spatial relationship (Fig. 54b) and surface shape (Fig. 54d). Especially in the case of shape perception, 36 participants (90%) preferred our adapted visualization only to 20%. However, about 56% of the participants favored our approach to 80-100% according to the perception of internal flow, compared to the semitransparent visualization (Fig. 54c).

In addition to these preliminary results, half of the participants stated comments at the end of the questionnaire. In most comments, atmospheric attenuation and

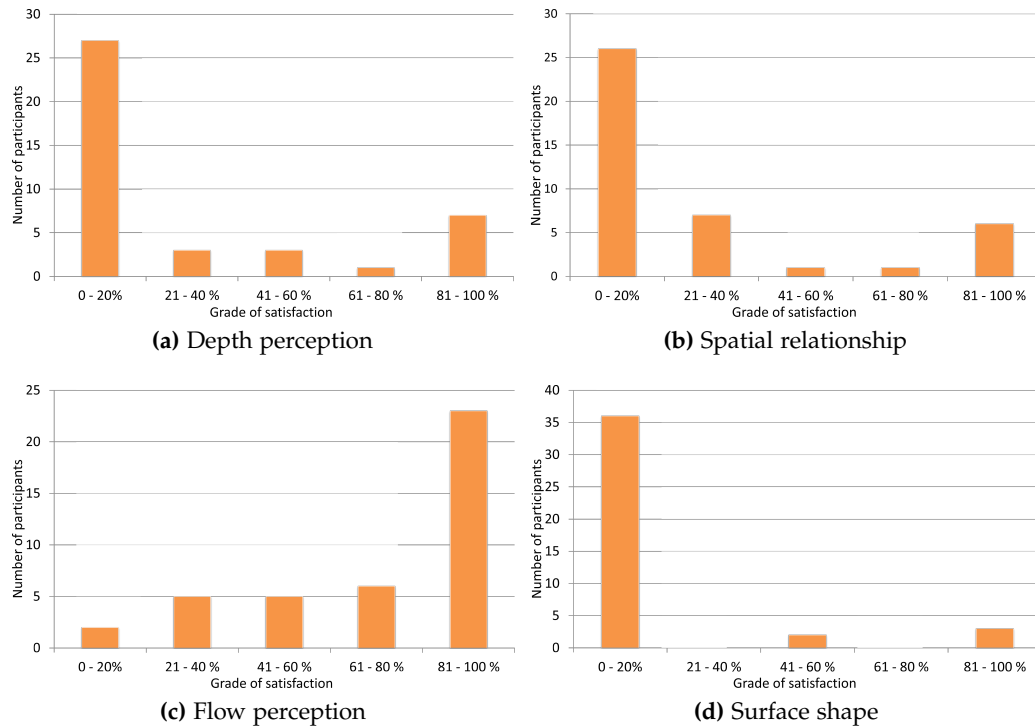


**Figure 54:** Survey results from the informal feedback according to the grade of satisfaction related to the perception of: (a) depth, (b) spatial relationships, (c) flow and (d) shape. (Images reproduced from Gasteiger et al. [127] © Eurographics Association 2010 with kind permission from the Eurographics Association.)

shadow casting were assessed helpful. Most of the criticisms, however, were related to the white edge fall-off color, which was rated as an "unnatural" shading of areas facing away from the viewer that led to an inverted interpretation of the surface orientation. This confusion was increased by the white background and atmospheric attenuation color. To obtain more insights about this issue, some of the participants were asked to interact with our visualization approach rather than looking at static images. As a result, the shading was now interpreted in a correct manner and the feedback was much more positive. Other comments criticized the undifferentiated thickness of the visible and hidden silhouettes as well as the visualization of hidden flow information. Especially in the combination with streamlines, the hidden flow parts were assessed confusing and disturbing in some cases.

### 5.5.2 Consequences and Improvements

We incorporated the insights of the informal user feedback into our approach to improve the shape and depth perception. Although the white edge fall-off shading seems to be appropriate in combination with camera interaction, it is probably not suitable for static depictions. Therefore, we modified our approach by using a diffuse shaded edge fall-off color based on the Phong-shaded front face color. This resulted in a more natural edge fall-off coloring that increased the shape description at these edges. We responded to the criticisms regarding the silhouette rendering and hidden flow parts in two ways. First, we increased the line width for

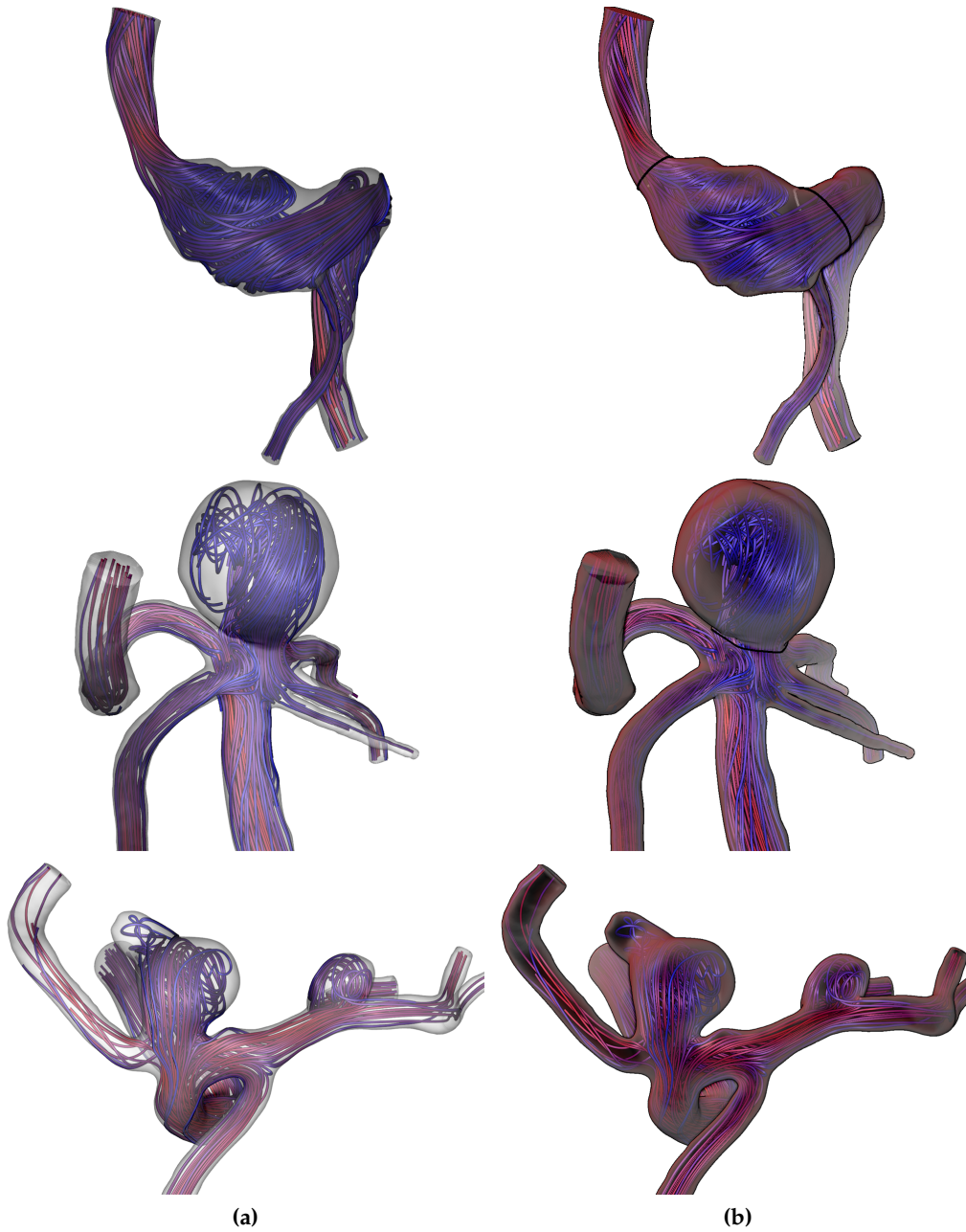


**Figure 55:** Application of our modified adaptive surface visualization approach on different cerebral aneurysm datasets as a result of our initial informal user feedback. In (a) the semitransparent and in (b) the adaptive surface visualizations are shown, respectively. The datasets represent a fusiform aneurysm (upper row), a giant aneurysm (middle row) and a case of two saccular aneurysms (lower row).



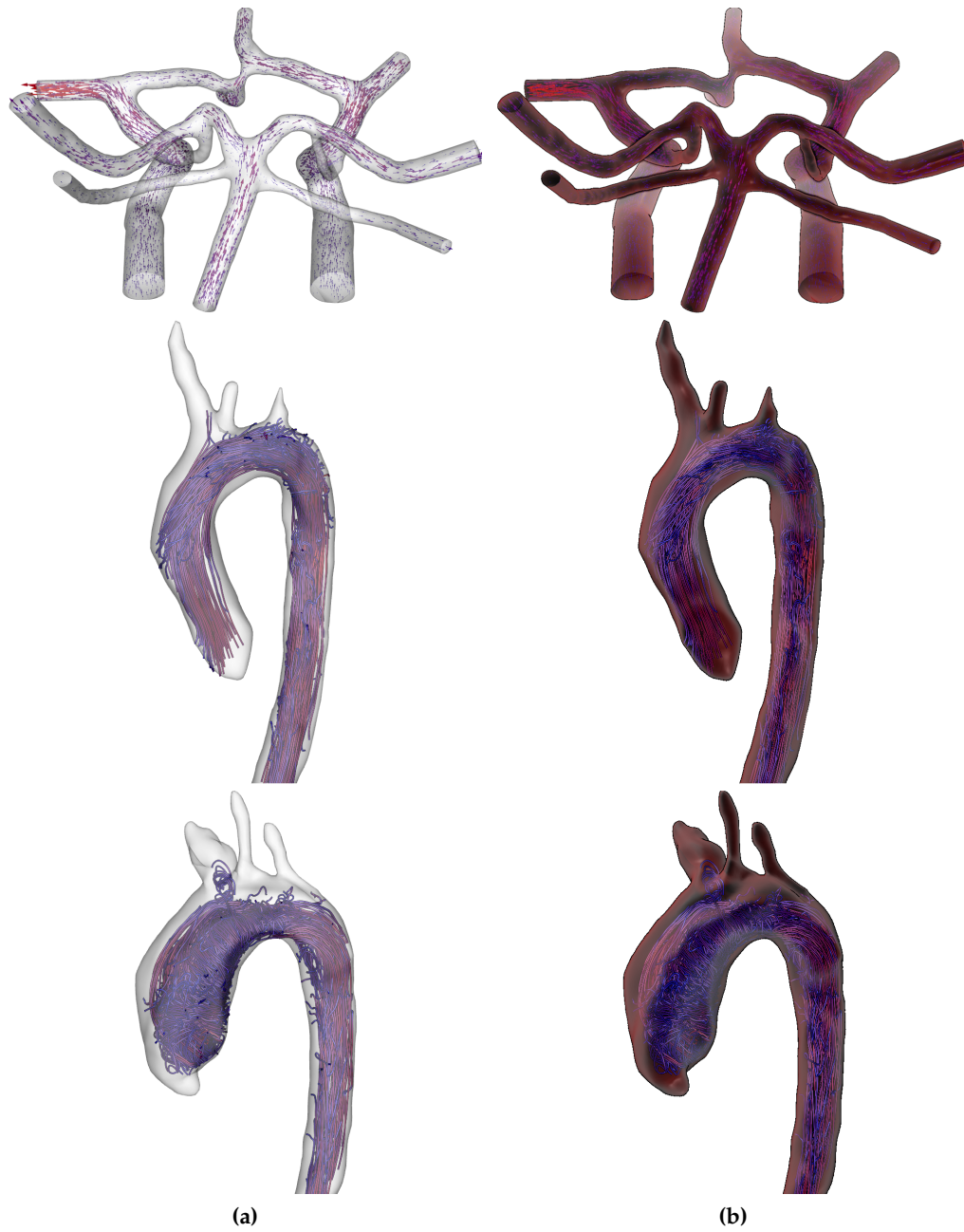


**Figure 56:** Further results of our visualization approach applied to a healthy Circle of Willis (upper row) and an aorta dataset (middle row) as well as a case of an aorta ectasia (lower row). Flow velocity for the Circle of Willis is depicted with scaled and color-coded glyphs and for the two aorta datasets with pathlines. The scaling and coloring is according to the local speed.



anatomical features and decreased the line width for visible and hidden contour lines. Second, we removed the visualization of hidden flow by default and provide it only on demand. As mentioned earlier, the final result of our modified approach is shown in Figure 53c applied to the same aneurysm dataset.

Based on these modifications, further results are shown in Figure 55 and Figure 56 for several vascular datasets. For each figure and dataset the left column represents the semitransparent rendering compared to our adaptive surface rendering in the right column. In the upper row of Figure 55 a fusiform cerebral aneurysm is presented with indication of the inflow and outflow regions as anatomical features. The middle row of Figure 55 shows a giant cerebral aneurysm with the ostium as anatomical feature. A dataset of two saccular cerebral aneurysms with an additional bleb formation on one aneurysm is shown in the lower row of Figure 55. For this dataset, no anatomical landmarks are emphasized.

The Circle of Willis from a volunteer is shown in the upper row of Figure 56. For this dataset the flow velocity is visualized with arrow glyphs, which are scaled and color-coded according to the local speed. The middle row of Figure 56 represents an aorta of a healthy subject and the lower row an aorta ectasia (recall Sec. 2.2) of a patient, respectively. The flow velocity of both aorta datasets is depicted with pathlines and color-coded according to the local speed.



See video no. 3  
on DVD

## 5.6 CONTROLLED PERCEPTIONAL STUDY

Our initial survey is primarily informal and questionnaire-based, and thus reflects more the personal beliefs and preferences of the participants than the actual objective measurement of task performances. Thus, after adopting our approach according to the informal user feedback we are interested in a more detailed user study about its effectiveness by means of controlled task-driven experiments. This study was primarily designed by Alexandra Baer and the author of the thesis provided the software framework to conduct the study. For this study, we also had a strong collaboration with a psychologist (Douglas W. Cunningham), who has a fundamental background in computer graphics and visualization. In the following, only the main aspects and findings of the study are presented. Further details can be found in the work of Baer et al. [15].

We designed and conducted three perceptual experiments to evaluate three visualization techniques: semi-transparency (S) and our ghosted view approach without (G) and with depth enhancement (GD) that includes shadow casting and atmospheric attenuation. For all three techniques we depict the flow information with color-coded streamlines where the color represents the local speed. An optimized color scale is used to enhance the quantitative character of the speed data [210]. We evaluate the three techniques in the context of the visualization of cerebral aneurysms, but we are convinced that the experiments and outcomes are also applicable on other vessel flow domains, such as aortic or cardiac flow.

The aim of this study is to measure whether and how the techniques G and GD facilitate the assessment process of cerebral aneurysms and the internal blood flow compared to S. Thus, we evaluate the techniques with respect to their ability for:

### 1. Perceptually effective shape representation

## 2. Showing embedded flow

### 3. Perceptually effective spatial representation of the aneurysm's parent vessels

Since these three criteria are effectively independent of each other, we separated the evaluation and design into three individual experiments concerning shape perception, smart visibility and spatial relation. After intensive discussions with the psychologist, we selected the following hypotheses (H) to define the parameters that have to be measured.

**Shape-H1:** G and GD facilitate the vascular structure's shape perception - as measured by **accuracy** - better than S.

**Shape-H2:** G and GD facilitate the vascular structure's shape perception - as measured by **response time** - better than S.

**Smart-H1:** G and GD facilitate the assessment of embedded flow - as measured by **accuracy** - better than S.

**Smart-H2:** G and GD facilitate the assessment of embedded flow - as measured by **response time** - better than S.

**Spatial-H1:** G and GD facilitate the vascular structure's spatial perception (depth ordering) - as measured by **accuracy** - better than S.

**Spatial-H2:** G and GD facilitate the vascular structure's spatial perception (depth ordering) - as measured by **response time** - better than S.

**H-GD:** GD will be more effective in each category than G and S.

To test these hypotheses, statistical significance tests were run on the results of the experiments [104]. In the following, we present in short the experimental setup, the conduction of each experiment, their analysis and the final results. For a more detailed description we refer to the work of Baer et al. [15].

#### 5.6.1 Experimental Setup

In order to investigate accuracy and response time, the participants were asked to fulfill different tasks referring to the appropriate experiment type. We perform the experiments on five representative, patient-individual 3D aneurysm models (see Fig. 57), which are visualized with each of the three techniques. The resulting renderings are called *stimuli* in the following and are presented to the participants. Except for the shape perception experiment all participants were shown only static

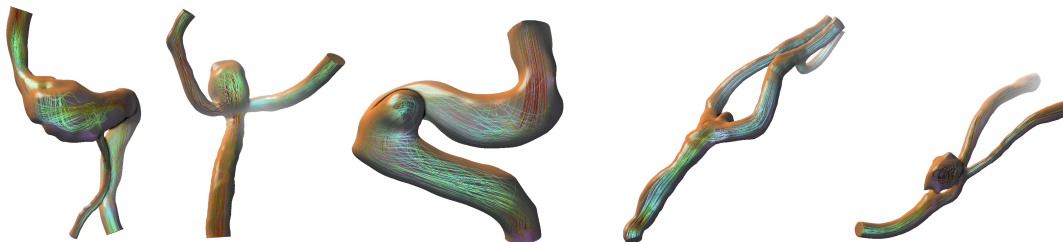


**Figure 57:** The five cerebral aneurysm datasets on which the visualization techniques are evaluated. The aneurysm models are visualized with our ghosted view approach, including depth enhancement. (Image adapted and reprinted from Baer et al. [15] © John Wiley and Sons 2011 with kind permission from John Wiley and Sons.)

stimuli to investigate a so-called *within-participant factor* (visualization technique) with three levels (S, G, and GD). For the shape perception experiment a *between-participant factor* (interaction) was investigated by dividing the participants into two groups: one saw only static stimuli and one could rotate the aneurysm model. We recruited a total of 86 participants from various parts of the university, each participating in only one experiment. The participants consisted of visualization scientists, medical doctors, engineers and students. The exact number of the participants for each experiment can be found in the corresponding experiment sections.

All participants were tested under the same environment conditions and were instructed in written form before each experimental session started. One practice trial followed the instruction, to familiarize each participant with the specific task. Each experiment consisted of stimuli images being shown one at a time on a white background and the participants were asked to perform a task according to the experiment type. Each stimulus was presented until the participants finished the task explicitly to move on to the next stimulus. The individual response time for each task was captured automatically and the participants could comment their decisions to obtain more insights in the final result analysis. All techniques and aneurysm models were presented in random order to avoid expectation effects. At the end of each experiment, the participants were asked to evaluate the techniques using a bipolar 5 point Likert scale (very good, good and neutral), with each pole representing the performance of one technique compared to the other. This allows us to subjectively compare specific technique properties.

### 5.6.2 Shape Perception Experiment

For measuring the reaction time and accuracy of shape perception we employed the gauge figure technique from visual psychophysics to obtain local estimates of surface orientation and thus to analyze the perceived surface shape [189].

**Gauge methodology:** Participants were shown the 3D aneurysm models with a gauge figure placed on the front side of the model's surface. Each gauge was drawn as a small ellipse representing a disc and a single line indicating the normal of the disc (see Fig. 58a). Participants were asked to orient the gauges to coincide with the apparent surface normal at that specific surface point. The orientation of the gauge was controlled by the mouse and the gauge geometry did not penetrate or interact with the 3D model to avoid an indication of the surface shape to the participants.

**Stimuli:** For the stimuli images, we choose viewpoints corresponding to preferred views of neuroradiologists. Each stimulus consists of a single gauge placed on a single surface model, visualized with either G, GD, or S. The gauge figures were located at opaque, semitransparent, and fully transparent surface regions to enable an analysis of each technique and each characteristic regions. To increase the number of aneurysm models we are changing the viewpoints for four models, which results in nine models instead of the original five datasets. This may help to reduce the ability to recognize an object as being identical to one already seen. We also define a perceptual "gold standard" for the gauge figures by presenting a full opaque and shaded stimulus of each dataset at the end of the experiment, since we expect the participants to perform most accurately on shaded models. Overall,

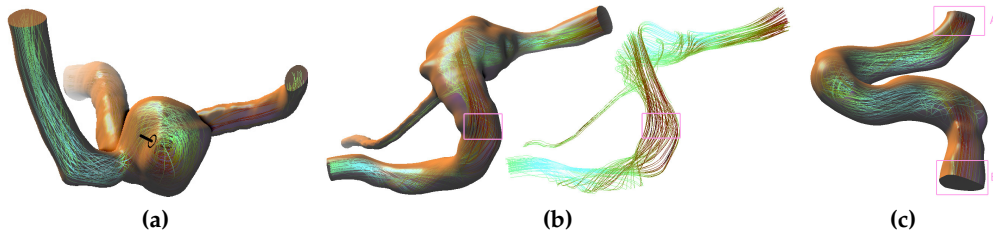


**Figure 58:** Examples of the stimuli for the three kind of experiments: (a) the shape stimulus with the gauge widget, (b) stimuli for the smart visibility experiment with the highlighted vessel and flow region (pink), respectively, and (c) stimulus for the spatial relation experiment with labeled vessel sections (pink). (Image adapted and reprinted from Baer et al. [15] © John Wiley and Sons 2011 with kind permission from John Wiley and Sons.)

we have 36 stimuli consisting of nine models with three techniques and the nine models in fully shaded renderings.

**Between-participant design:** It is well known that camera interaction facilitates the shape perception of 3D surfaces, which was also demonstrated in our informal user feedback survey. Thus, we are interested in how static and dynamic stimuli have influence on the shape perception with respect to the gauge alignment. This between-participant factor was investigated by two equal-sized groups of 17 participants each. While the gauge interaction was the same for both groups, one group received static 3D renderings of the aneurysm models (group -RO) and one had the opportunity to rotate the scene (group +RO). Since we wanted to evaluate the perception for the given view (which is the preferred view for specialists) and not the perfect surface normal vector, we decided to restrict the range of possible rotations to  $15^\circ$ .

### 5.6.3 Smart Visibility Experiment

This experiment is conducted to assesses the techniques' ability and effectiveness to show the embedded flow visualization. We refer to this as the techniques' smart visibility characteristics, but we do not evaluate the flow visualization.

**Visibility methodology:** Participants were asked to define the average flow color at different highlighted vessel regions (see Fig. 58b (left)) using the *CColor-Dialog* of the Microsoft Foundation Class. These individual color results are used to determine the average color error compared to a perceptual color "gold standard", which is represented by the flow at that specific region. Therefore, we used stimuli images illustrating only the flow visualization on a white background (see Fig. 58b, right) and present them at the end of the experiment.

**Stimuli:** Each static stimulus is overlaid with a pink rectangle selecting a certain surface and the corresponding flow region. We chose only semitransparent and fully transparent surface regions because opaque regions will fully occlude the embedded flow. We used eight models, whereas four models were overlaid with a rectangle positioned in transparent and four models with a rectangle positioned in semitransparent regions. Similar to the spatial experiment we changed the view-point of three aneurysm models to obtain eight models. Combined with the three visualization techniques S, G, and GD as well as the eight gold standard stimuli this results in 32 stimuli. We recruited 27 participants for this experiment.

#### 5.6.4 Spatial Relation Experiment

A common strategy to analyze spatial perception is to ask the participants to determine the perceived depth ordering [276, 356]. We employ this depth judgment strategy and use the vessel branches of the aneurysm models to investigate the techniques' accuracy according to the hypothesis SPATIAL-H1.

**Depth methodology:** For each stimulus, the participants had to determine which branch is closer to the viewer. Possible answers were branch *A*, branch *B* or *None*, if both branches have the same distance to the viewer.

**Stimuli:** We generated stimuli images illustrating the aneurysm models with two branches vertically aligned. Furthermore, the models were rotated around the aneurysms' x-axis clock- or counterclockwise by 0, 10 or 20 degrees (see Fig. 58c). The specific vessel branches were marked with pink rectangles labeled with *A* and *B* to focus the participants on these vessel regions. In total we have 36 stimuli consisting of four models, each rotated with three different angles and visualized with S, G, and GD. We left out stimuli images of the fourth model shown in Figure 57, since its two branches were too close to separate them. The experiment was conducted with 25 participants.

#### 5.6.5 Experiment Analysis and Results

We analyzed the accuracy, the response times, and the subjective technique evaluation. Accuracy for shape perception was determined by analyzing the perceived surface normal vectors, for smart visibility by analyzing the perceived blood flow color, and for the spatial experiment by determining the correct and false answers of the depth judgment task. Initially, we tested all data for a normal distribution with the *Shapiro Wilk test*, since this is a major requirement for choosing an appropriate significance test and consequently achieving valid results. According to these results, we applied standard statistical methods to analyze significances for each factor level. We applied the *non-parametric Friedman* combined with the *Wilcoxon signed rank test* for the pairwise comparison, since our results are not normally distributed. Moreover, for the shape experiment we used the *Wilcoxon-Mann-Whitney test* to compare group -RO and group +RO, since this non-parametric test assesses whether there is a significant difference between two independent samples.

##### 5.6.5.1 Shape Analysis

We stored the xyz-components of the adjusted gauge surface normal vector as well as the response time for each participant and each gauge figure task. Accuracy was quantitatively analyzed by comparing the gauge vectors with the corresponding estimated perceptual "gold standard" vectors (gs-vectors).

**Accuracy:** The average angle deviation of the normal estimates compared to the gs-vectors for group -RO was between  $28.7^\circ$  and  $30^\circ$  as well as for group +RO between  $21.2^\circ$  and  $26.3^\circ$ . Participants of group -RO were more precise with GD and of group +RO with G (see Fig. 59a). The *Wilcoxon-Mann-Whitney test* confirmed significantly more precise results for group +RO and no significant difference for group -RO. Participants of group +RO were more precise with G than with S.



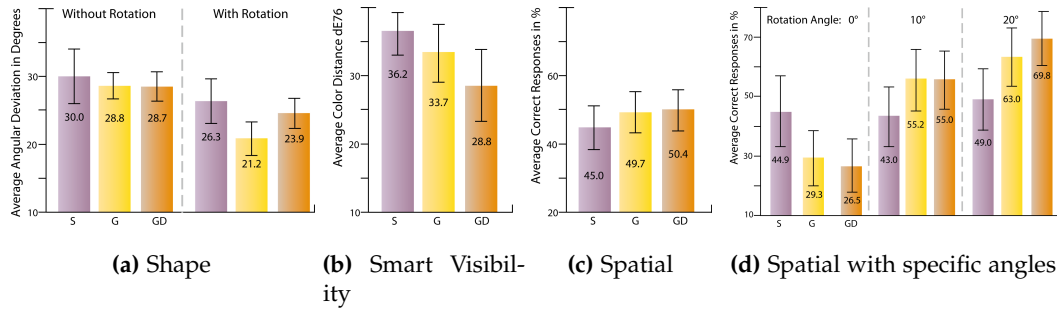


**Figure 59:** The average results and error bars (95% confidence intervals) for (a) the shape experiment (group -RO and group +RO), (b) the color distance of the smart visibility experiment, (c) all correct responses for the spatial experiment and (d) separated for each rotation angle. (Images reprinted from Baer et al. [15] © John Wiley and Sons 2011 with kind permission from John Wiley and Sons.)

Thus, SHAPE-H1 can be confirmed. Moreover, G enables significantly more accurate shape perception than GD. However, the results also show that SHAPE-H1 can only be confirmed as long as the participant could rotate the model and the gauge is not set at fully transparent regions. For group -RO no significant difference between S, G, GD was found and **Shape-H1** has to be rejected.

**Response time:** The average response times for group -RO are 15s for S, 15.8s for G, and 16.2s for GD. Group +RO required 22.8s for S, 28.5s for G and 25.6s for GD. It can be seen that participants of group +RO required more time orienting the gauges but they had smaller angular errors. Both groups performed significantly faster with S than with G and GD, even though participants performed more accurate with the ghosting techniques. Nevertheless, we had to reject SHAPE-H2. In summary, group +RO was significantly more accurate but slower than group -RO.

#### 5.6.5.2 Smart Visibility Analysis

The accuracy of flow perception indicates the smart visibility characteristics of the illustration techniques. All three techniques were evaluated by the perceptual difference between the estimated color and the perceptual "gold standard" color (gs-color). Representing the gs-color and the participants' color choices in Lab color space allows to compute color differences as Euclidean distances ( $\Delta E$ ), since this color space is perceptually linearized. A difference of 1.0  $\Delta E$  means that the color difference between two colors is perceptually distinguishable.

**Accuracy:** Participants' estimated colors more precisely in terms of smaller distances  $\Delta E$  to the gs-colors, for G and GD (see Fig. 59b). The participants performed significantly better with GD than with S and G. No significant difference was confirmed between S and G. One reason might be that the participants defined the flow color for S, which they expected to be the right one and not the color they really saw. When the participants were asked to explain their adjusted colors during the experiment, they confirmed that assumption. This happened especially after they saw the first G stimulus. This might be eliminated by designing a between-participant design for this experiment similar to the shape experiment. Therefore,



we have to reject SMART-H1, but we are able to confirm that GD enables a more accurate assessment of embedded flow than S.

**Response time:** The average response times are very close to each other. However, a significant difference exists between S and GD, whereas GD achieved faster results. Even though G is better than S and a significant difference may occur with further results, SMART-H2 has to be rejected, too. We are only able to confirm that GD accelerates the assessment of embedded flow compared to S.

#### 5.6.5.3 *Spatial Analysis*

The knowledge of each stimulus and the recorded answers enable the analysis of correct and false responses with respect to the depth order. Additionally, we evaluate S, G, and GD referring to the minimal perceived rotation angle.

**Accuracy:** A statistically significant correlation exists between the techniques and the number of correct responses. The correct responses with S were 45%, with G 49.7%, and with GD 50.4% (see Fig. 59c). The paired test confirmed significantly more correct answers for G and for GD compared to S. Both ghosting techniques exhibited no significant difference. We can, however, confirm SPATIAL-H1. A detailed view on the individual rotation angles reveals interesting insights (see Fig. 59d). For the 0° angle, a significant difference exists for S and G as well as for S and GD with more correct answers for S. This difference may reflect a bias towards a response of "no separation in depth" for S. In such a case, lower performance for the two larger rotations is to be expected, which is precisely what we find. Stimuli showing a rotation angle of 10° and 20° were significantly more often correctly perceived with G and GD than with S. The larger the rotation angle, the higher the significant difference and the larger the difference of correct responses between G (63%) and GD (69.8%). Thus, SPATIAL-H1 can be confirmed for 10° and 20° but has to be rejected for 0°.

**Response time:** The average response times are 8 s for S, 7.5 s for G, and 7.2 s for GD. Overall, the response times in this experiment showed no significant effects and we have to reject SPATIAL-H2.

#### 5.6.5.4 *Questionnaire Results*

Our questionnaire analysis measures participants' attitude towards a technique based on the selected items on the bipolar 1-5 Likert scale. The results of each pairwise technique comparison for each experiment (colored bars) are illustrated in Figure 60 for all 86 participants. As illustrated in Figure 60b, 34 participants (39.5%) rated G compared to S with very good and 41 (47.7%) with good. Thus, 75 participants (87.2%) preferred G over S. The comparison of GD and S in Figure 60b showed that 73 participants (84.9%) rated GD as very good or good, and thus, preferred this technique over S, too. Finally, Figure 60c shows the comparison results for G and GD with a small preference for GD. A total of 19 participants (22.1%) rated G with either very good or good, 29 participants (33.7%) preferred GD and chose very good or good, and 38 participants (44.2%) liked both kinds of visualization techniques and chose neutral. In summary, the majority of all participants preferred G and GD over S with an attitude towards GD.

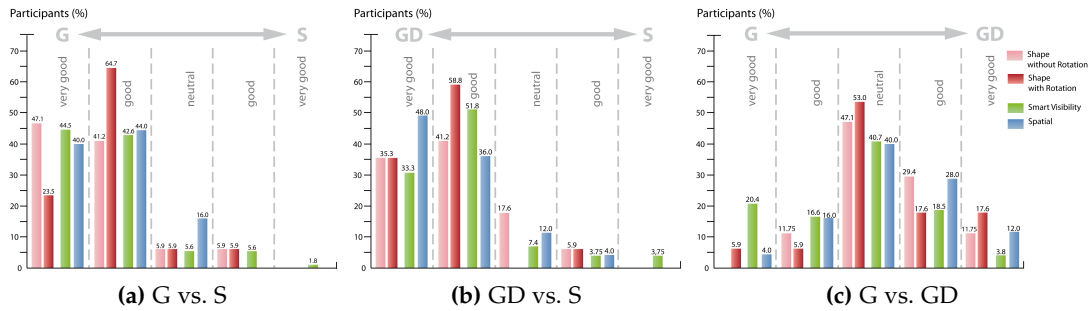


**Figure 60:** Result of the questionnaire in terms of the participants' attitude towards one of the three technique. The bar chars in (a) and (b) show a clear preference for the ghosted view technique compared to the semitransparent visualization. A small trend towards a preference of the ghosted view with depth enhancement over the ghosted view can be seen in (c). (Image adapted and reprinted from Baer et al. [15] © John Wiley and Sons 2011 with kind permission from John Wiley and Sons.)

## 5.7 CONCLUSION AND FUTURE WORK

We described an adaptive surface visualization for blood vessels to expose embedded flow information. We employed a ghosted view approach to ensure both contextual shape description and visibility of the enclosed flow information. Furthermore, silhouette rendering was used to depict anatomical features, and depth enhancement was achieved by means of shadow casting and atmospheric attenuation. We have shown that our approach is applicable to several clinical datasets, such as aortas and cerebral aneurysms with different grades of complexity. Moreover, we are convinced that our approach can be applied to other tubular (and non-medical) structures with embedded information.

Our initial survey with 40 participants demonstrated a better perception of the embedded flow in comparison to a common semitransparent surface visualization. Additionally, valuable improvements could be derived, such as a more natural edge fall-off coloring for the ghosted view and restriction in terms of hidden flow visualizations. Based on the altered version, we conducted a controlled perceptual user study with task-based experiments. The quantitative analysis revealed the advantage of our approach and clearly showed that it supports a more accurate analysis of blood vessels with embedded flow than the traditional semitransparent technique. Additionally, we found an overwhelming preference for our approach. However, we could not identify statistically significant improvements in terms of accuracy and response time for every task. An example is the shape experiment with restricted camera rotation. As a standard speed accuracy trade-off, the participants required more time using our approach, since they perceived the surface shape better, and thus, aimed at orienting the gauge vector as close as possible to the gold standard vector.

For future work we consider a (semi-) automatic extraction of morphological features, such as inlets and outlets, to reduce manual effort and preprocessing time. Therefore, we consider information about the vessel centerlines and their local distances to the surrounding surface. A promising approach would be the aneurysm decomposition method based on harmonic functions recently proposed by Jiang and Strother [171] (recall Sec. 3.4.3).

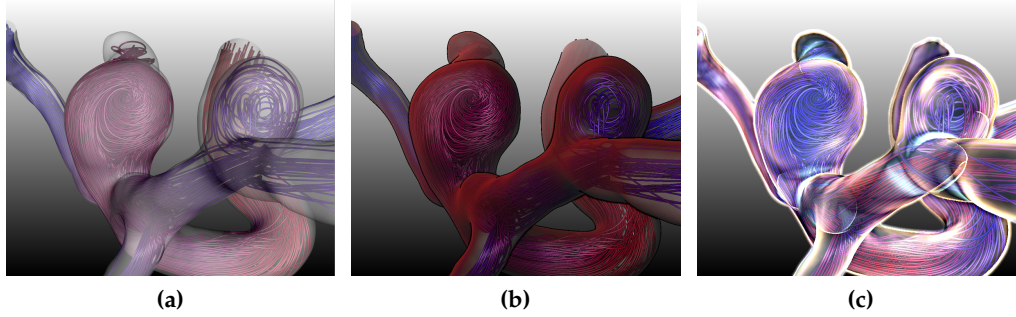


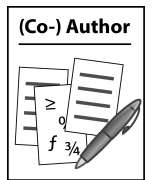
**Figure 61:** Comparison between the semitransparent rendering (a), our adaptive vessel surface approach (b) and the improved ghosted view shading by Lawonn et al. [206] (c) of a cerebral aneurysm dataset with two saccular aneurysms. Compared to our approach the improved ghosted view reveals more embedded flow information at vessel regions that are oriented away from the viewer and convey more expressively concave and convex surface shape information. (Images reprinted from Lawonn et al. [206] © Eurographics Association 2013 with kind permission of the Eurographics Association.)

Further investigations are also needed regarding other depth enhancement methods, e.g., depth of field, and an improved view-dependent transparency of the current ghosted view technique. A limitation of our method lies in opaque regions, which are oriented away from the viewer and occlude the embedded flow visualization. For example, the flow visualization in the two large carotid arteries of the Circle of Willis dataset in Figure 56 (upper row) are hardly visible. This results from the vessel direction that is nearly perpendicular to the view direction. Although we assume an orientation of the focus region towards the viewer, it may be also relevant for some cases to reveal the embedded flow in vessel regions turned away.

In a recent work of Lawonn et al. [206], in which the author of the thesis was involved, an improved ghosted view shading was proposed. The current Fresnel transparency was exchanged with a view-dependent curvature transparency inspired by the *suggestive contour measure* [84]. For each vertex  $i$  a scalar measure  $s_i = \vec{w}_i \cdot \vec{l}_i$  is computed with  $\vec{w}_i$  as the projection of the view vector on the tangent plane of  $i$  and  $\vec{l}_i$  as the light gradient at  $i$ .

By definition, the zero-crossings of  $s_i$  represent the locations of the suggestive contours and represent surface regions with a transition between concave and convex regions based on the current view direction. These regions are visualized with increased opacity and highlighted expressively with two antipodal colors from the CIE Lab color space. As an additional effect, depth blurring was applied instead of atmospheric attenuation to convey depth information. Figure 61 shows a comparison between a semitransparent rendering (see Fig. 61a), our adaptive surface visualization approach (see Fig. 61b) and the improved ghosted view by Lawonn et al. [206] (see Fig. 61c) for the cerebral aneurysm dataset with the two saccular aneurysms. In comparison to the current ghosted view approach it can be seen that the improved ghosted view reveals more embedded flow information in regions that are oriented away from the viewer but conveys still important surface shape details.

This was also confirmed in an informal evaluation with one physician and two CFD engineers that are involved in hemodynamic analysis as well as six



Lawonn et al. [206]



See video no. 4 on DVD

researchers with background of medical visualization. Based on three tasks the participants stated an improved shape and embedded flow perception. Depth blurring and atmospheric attenuation were evaluated equally expressive with slightly more preference for blurring because of its more natural adaption to the human depth perception. As a consequence, it would be worthwhile to repeat the controlled perceptual user study from Section 5.6 with the additional improved ghosted view shading method to obtain quantitative evaluation results. In addition to the suggestive contour measure other transparent rendering styles might also be worthwhile to investigate, such as normal-variation and window transparency, as presented in Hummel et al. [161].

Finally, the perceptual user study focused on the general evaluation regarding shape and depth depiction as well as flow visibility. For a more detailed investigation how well our and the improved ghosted view approach by Lawonn et al. [206] can be applied for the analysis of certain flow behavior, a user study that incorporates specific flow questions, such as the number and location of vortices, is worthwhile. The design of this study could be oriented to the work of Laidlaw et al. [199] who propose a framework of a quantitative user study for 2D vector field visualization techniques.

## DETECTION AND VISUALIZATION OF QUALITATIVE FLOW PARAMETERS

---

This chapter is based on:

"Automatic Detection and Visualization of Qualitative Hemodynamic Characteristics in Cerebral Aneurysms". Rocco Gasteiger, Dirk J. Lehmann, Roy van Pelt, Gabor Janiga, Oliver Beuing, Anna Vilanova, Holger Theisel, and Bernhard Preim. In *IEEE Transactions on Visualization and Computer Graphics* (TVCG), 18(12), pp. 2178-2187, 2012.

### 6.1 INTRODUCTION

In the previous chapter, we dealt with research **goal 1** of this thesis, an expressive vessel surface visualization that facilitates both perception of the vessel shape and the embedded flow depiction. Thereby, the flow depiction comprises quantitative measures, such as direction, speed and pressure. As mentioned in Section 3.2, there are also qualitative parameters, such as flow complexity and recirculation. In addition to quantitative characteristics they are indicators for certain CVDs and have also influence on their initiation and progression. However, the individual "extraction" is based more on a visual flow inspection than on a mathematical definition, which is in contrast to quantitative characteristics. Moreover, some of the qualitative parameters are extracted in a time-consuming and non-standardized way combined with a non-expressive visualization. For large patient studies on multicenter datasets this kind of procedure is not appropriate because they do not ensure reproducibility and comparability.

In this chapter we focus on research **goal 2** (see Sec. 3.9) and propose an approach to automatically detect and visualize two qualitative parameters. Thereby, we consider the *inflow jet* and *impingement zone* of blood flow in cerebral aneurysms, in particular saccular aneurysms. Fusiform-shaped aneurysms do not exhibit these two hemodynamic characteristics. In recent studies, it has been shown that the shape of the inflow jet and its impingement zone are associated with the risk of rupture [17, 63, 64].

The inflow jet consists of parallel inflow with high speed compared to other parts in the aneurysm. The impingement zone is the region on the aneurysm wall where the inflow jet is seen to impact the wall for the first time with high speed. A concentrated inflow jet with a small impingement zone increases the risk of a rupture. Two other identified qualitative characteristics are the flow complexity and flow stability, which are defined as the number and movement of vortices over time. Complex and unstable flow have shown a higher correlation to aneurysm rupture compared to a simple and stable flow pattern. As a consequence, these in-

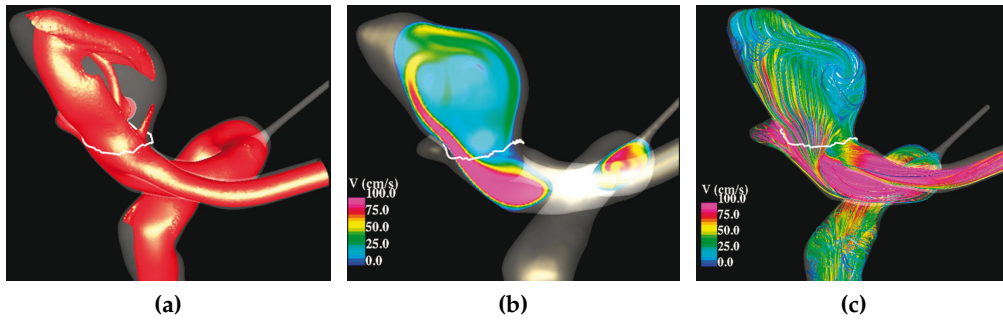


**Figure 62:** Current procedure to extract and assess the inflow jet and impingement zone, respectively. In (a) an isosurface is extracted based on a user-defined iso-value to identify the region of high inflow speed. A subsequent cross-section plane is placed and aligned manually in (b) at the "core" of the inflow jet and color-coded. For further investigations of the inflow jet behavior color-coded streamlines are used in (c). The coloring encodes the flow speed. (Images reprinted from Cebal et al. [63] © ASNR 2011 with kind permission of the American Society of Neuroradiology.)

dicators are considered as relevant for the rupture risk assessment in unruptured aneurysms. A risk assessment is important for two main reasons. First, every surgical and endovascular treatment carries a risk of complication. The decision to treat an aneurysm has to be balanced against the risk of rupture. Second, in cases of multiple aneurysms the question arises which of them should be treated first, i. e., which one is more likely to rupture [71].

The investigation of the inflow jet and impingement zone is currently accomplished by the visual inspection of isosurfaces of the speed as well as color-coded cross-section planes and streamlines, shown in Figure 62. Based on an adjusted isospeed value the region of the inflow jet is defined by the domain expert (see Fig. 62a). Subsequently, a cross-section plane is placed and aligned that roughly cuts the inflow jet region in half. The sampled speed values are then color-coded according to an adjusted color scalar range to emphasize a high inflow speed region (see Fig. 62b). The same color scale is applied to streamlines seeded at the ostium into the aneurysm to depict the inflow behavior (see Fig. 62c). Finally, the impingement zone is identified at the aneurysm surface region where the manually extracted inflow jet impacts the wall for the first time. This procedure, however, has the following drawbacks, which exhibit a high interpersonal variation and a time-consuming manual extraction for each dataset:

- The domain expert has to decide, which isospeed value corresponds to an appropriate inflow jet speed.
- The cross-section plane has to be adjusted manually and requires a reliable alignment that cuts the jet in half. This is challenging since the jet is a 3D flow structure that has to be captured with a 2D, linear probing plane.
- The domain expert has to adjust a suitable scalar range to map the probed speed values to a noticeable color coding, which does lead to an over- or underestimation of an inflow jet.



- The size of the impingement zone is purely estimated on the perceived impact region at the aneurysm wall based on the aforementioned extracted inflow jet structure.

These drawbacks make it difficult to achieve a reproducibility and comparability between domain expert studies, especially for large patient studies. This includes also investigations of the two hemodynamic parameters regarding comparisons of pre- and post-stenting as well as changes over time. A reliable, standardized, and (semi-)automatic approach would ensure a user-friendly and less operator-dependent analysis procedure. Thus, we focus in this chapter on an automatic detection and visualization of the inflow jet with its impingement zone. In particular, we derive a formal description of the inflow jet by utilizing local streamline properties and automatically extracting a characteristic inflow jet seeding curve. Based on this seeding curve, we integrate an inflow jet boundary contour and identify its impingement zone on the aneurysm wall.

In summary, the contributions of this chapter are:

- An approach to automatically detect and extract a characteristic seeding curve, on which we construct an inflow jet boundary contour for steady flow datasets. Our approach utilizes local streamline properties to formalize the inflow jet and impingement zone detection. Based on the extracted inflow jet boundary contour, our approach localizes the impingement zone. To the best of our knowledge we present the first formal description of an inflow jet.
- Expressive visualization techniques for the inflow jet and the impingement zone along with the relevant anatomical context. The specific design of the visualization aims at two goals: to convey the reliability of the two detected parameters and to provide an easy to understand visualization with a minimum of visual clutter.
- An evaluation of our approach with six domain experts to qualitatively compare the two automatically and manually extracted hemodynamic parameters.

## 6.2 RELATED WORK

The investigation of qualitative hemodynamic characteristics is relevant for different vessel flow domains, such as cardiac, aortic and cerebral flow. Through the years, however, their detection still remained on a purely visual inspection of established flow visualization methods, such as color-coded cross-section planes, glyphs and streamlines [17, 62, 222, 311]. The cumbersome extraction procedure from Section 6.1 is derived from the corresponding literature and discussions with domain experts. This procedure seems to be appropriate for the limited number of processed datasets, which were used in most of the studies so far. Large patient studies on multicenter datasets are necessary though to derive clinically pertinent information that will improve clinical practice (see Sec. 3.9).

A considerable progress in this direction was accomplished by Cebal et al. [63], who proposed the identification of the inflow jet and impingement zone as strong indicators for estimating the risk of rupture of cerebral aneurysms based on 210

datasets. In a subsequent work, they identified quantitative parameters, such as the inflow concentration index and MWSS, that also correlate to an increased risk of rupture. However, for studies with ever-growing numbers of datasets a standardized and (semi-)automatic data analysis is mandatory that involves both robust data extraction and expressive visualization.

**FEATURE-BASED AND PARTITION-BASED FLOW VISUALIZATION.** The detection and visualization of qualitative hemodynamic parameters, is related to feature-based and partition-based flow visualization methods (see Sec. 4.2.2). For qualitative parameters that are based on the detection of vortices, such as flow stability and flow complexity, established vortex (core line) extraction methods can be used [170, 312, 358]. Salzbrunn et al. [289, 287] incorporate methods for vortex detection into their line predicates approach to identify integral lines, which run through vortex regions. In contrast to the detection of flow structures by using analytical definitions, Heidberg et al. [149] proposed an automatic pattern matching approach. They employed a set of idealized flow patterns, such as swirling flow or vortices, and computed a similarity of these patterns to the underlying vector field region. Among other things, they applied their approach to measured cardiac and aortic flow to identify vortex regions as well as right-handed and left-handed swirls.

Cluster-based methods group flow regions into characteristic sub-regions with respect to local or global similarity measures like the bending energy of integral lines. The resulting clusters can be represented in a multiscale visualization approach [123, 197, 326]. Most of the aforementioned methods, however, need a formal description of the flow structures, which is not available for the inflow jet and impingement zone, yet. Furthermore, methods that are based on similarity measurements require the adjustment of an appropriate threshold level to extract the interesting flow structure. This is still mainly left to the user. Nevertheless, our approach is inspired by line predicates that analyze local properties of the integral lines. This concept provides a flexible method to identify a large variety of flow structures. Instead of evaluating Boolean functions we employ these properties to compute scalar fields on which we extract the inflow jet and impingement zone.

**VISUAL EXPLORATION OF CARDIOVASCULAR HEMODYNAMICS.** Methods for the visual exploration of cardiovascular hemodynamics focus on expressive depictions of flow behavior combined with user-friendly interaction schemes (see Sec. 4.3.2 and Sec. 4.3.3). Thereby, most of the existent techniques consider quantitative parameters, such as velocity and WSS. Qualitative parameters are described indirectly by using geometric-based methods, such as integral lines and path surfaces [194, 338] or texture-based methods, e. g., LICs [248]. Although the proposed methods enable both an expressive visualization of flow behavior and guided seeding strategies the interpretation of certain flow structures remains by the user. However, the detection of vortex regions in cardiac and aortic flow, plays an important role in the identification of abnormal flow behavior that indicates the presence of vascular diseases, e. g., the formation of atherosclerosis and the development of thrombogenesis.

In the works of Born et al. [33, 34], the line predicate concept is applied to cardiac and aortic 4D PC-MRI flow data to depict streamlines that indicate vortex

regions. In a subsequent work, Born et al. [32] visualize the corresponding vortex core regions by means of a tube-like structure that resembles the rotational flow behavior. Vortex core detection and visualization on measured aortic flow data is also performed by Stalder et al. [309], but with a less expressive depiction.

The spatiotemporal hierarchical flow clustering proposed by Van Pelt et al. [339], focuses on an aggregation of flow regions according to certain dissimilarity measures with a subsequent simplified glyph representation. Although it is also applied to cerebral aneurysms, the dissimilarity measurements do not take qualitative parameters, e.g., the inflow jet, into account. Nevertheless, we are inspired by the illustrative visualization methods utilized in these approaches, such as the glyph representations and illustrative path surfaces. Furthermore, the application of the line predicate concept for measured blood flow data seems to be robust regarding data noise.

### 6.3 REQUIREMENT ANALYSIS AND DATA INPUT

Our approach focuses on the detection and visualization of the inflow jet and its impingement zone. Thereby, the localization of the impingement zone is directly related to the pathway and extension of the inflow jet that has to be detected first. Currently, a formal definition of both qualitative parameters does not exist, but the following informal description can be derived based on Cebal et al. [63, 64]:

- The **inflow jet** (also called inflow stream) is a flow structure that consists of parallel inflow with high speed compared to other parts in the aneurysm. The jet is evaluated as "concentrated" or "diffuse", depending on its thickness and penetration depth into the aneurysm sac. A concentrated inflow jet penetrates relatively deep into the aneurysm sac and is thin or narrow in the main flow direction. A diffuse inflow jet is thick compared with the aneurysm neck and disperses quickly once it penetrates into the aneurysm sac.
- The **impingement zone** is the region on the aneurysm wall where the inflow jet is seen to impact the wall for the first time and to change its direction and/or to disperse. The size of that region is either evaluated as "small" or "large" depending on the ratio between the area of the impingement region and the area of the aneurysm sac. The zone is considered as small if the area is smaller than 50% of the aneurysm sac area, and large otherwise.

This description, however, is not precise enough to enable a reproducible and consistent extraction that would be necessary for interpersonal or large patient studies. This includes also reliable comparisons of the inflow jet and impingement zone regarding pre- and (virtual) post-stenting as well as changes over time. Therefore, we subsequently define requirements that are derived from the aforementioned informal description and from discussions with our domain experts.

**Formalization:** A formalization of the target flow structures, namely the inflow jet and the impingement zone, is required. The formal characterization should reliably discriminate the target flow structures from any other structures. The formalization has to be exclusive in terms of a reliable detection of the inflow jet.

**Automatic and Robust Detection:** Based on the formalization, an automatic and robust detection approach is necessary to facilitate a reproducible detection. The

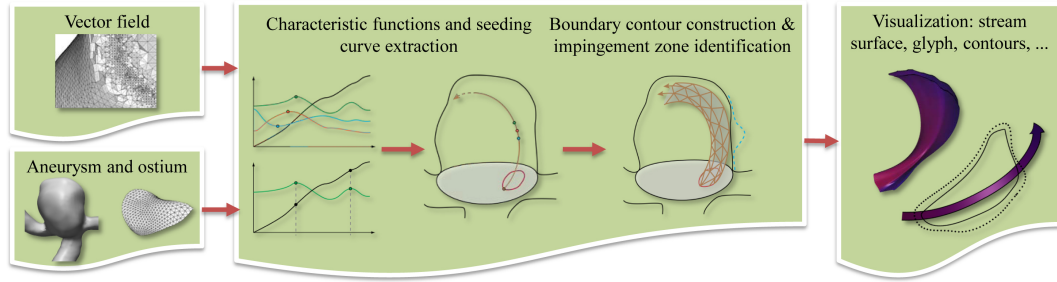


**Figure 63:** Overview of the extraction approach: Based on the vector field we seed streamlines at the ostium into the aneurysm. We identify several local line properties on the streamlines to compute a quality scalar field on the ostium. Given this scalar field we extract a seeding curve on the ostium, which is used to construct the boundary contour of the inflow jet. A second scalar field is computed on the aneurysm surface to indicate the impingement zone. Finally, we visualize both information expressively. (Image adapted and reprinted from Gasteiger et al. [125] © IEEE 2012 with kind permission from IEEE.)

approach should be free of parameters and robust with respect to noise, sampling, and discretization artifacts.

**Expressive Visualization:** A set of expressive visualization techniques is needed that conveys the location and character of the inflow jet and the impingement zone. The target structures must not be obscured and should be clearly recognizable. In order to reduce manual effort, carefully chosen default values should be provided.

In the following, we describe the details of our approach to fulfill these requirements based on the data input that results from the biomedical research data acquisition pipeline presented in Section 3.4 for simulated hemodynamic datasets of cerebral aneurysms. We consider only simulated blood flow data because cerebral 4D PC-MRI flow measurement is restricted to rare and expensive 7 T MR scanners that provide the necessary spatial resolution to represent at least major cerebral arteries (see Sec. 3.5).

CFD simulations of the blood flow are based on approximations with many assumptions that are difficult to verify. However, studies have shown that image-based patient-specific CFD models are capable of reproducing the flow structures observed *in vivo* during angiographic examinations [65] and compared to measured or experimental flow data (see Sec. 3.6.1). Furthermore, simulations enable to study the hemodynamics in different vessel geometries and to assess treatment options. Thus, we focus on simulated blood flow data and utilize the aneurysm surface mesh, the unstructured vector field as well as the ostium mesh as data input for our approach.

#### 6.4 DETECTION OF THE INFLOW JET AND IMPINGEMENT ZONE

In Figure 63 the overview of our approach is shown. Based on the vector field, we seed streamlines at the ostium into the aneurysm and compute several characteristic functions, such as curvature and acceleration, for each streamline. These functions are derived from our inflow jet description and are used to formalize a quality function for each streamline that computes a scalar field on the ostium. This scalar field represents a measurement how likely a streamline belongs to the inflow jet structure. Given this scalar field, we extract a seeding curve on the

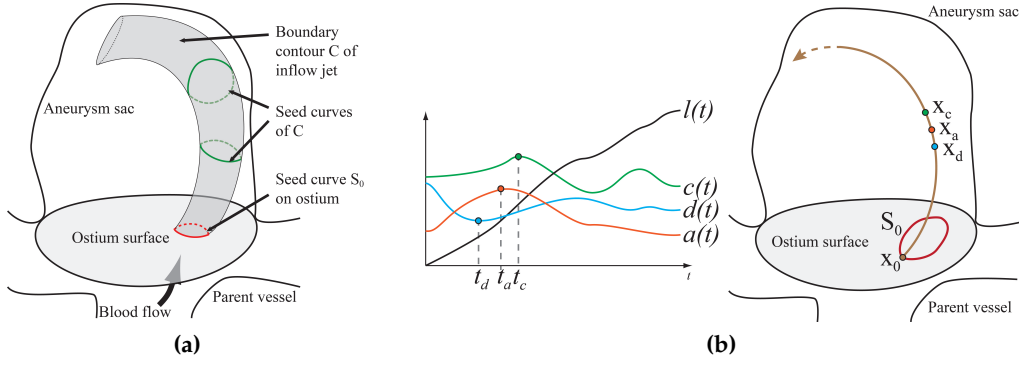


**Figure 64:** Setup for computing the inflow jet: it is bounded by a contour surface  $C$ , which is a stream surface given by a closed seeding curve  $S$ . Different seed curves define the same stream surface. We focus on the seeding curve  $S_0$  on the ostium. (b) The four characteristic functions (acceleration, curvature, distance to surface and arc length) of a streamline (left), together with their first extrema, (right) the corresponding points of the streamline. (Images adapted and reprinted from Gasteiger et al. [125] © IEEE 2012 with kind permission from IEEE.)

ostium, which is used to construct the boundary contour of the inflow jet. Subsequently, the boundary contour is utilized to formalize a second quality function that defines a scalar field on the aneurysm surface to indicate the impingement zone. Finally, the boundary contour and the impingement zone are expressively visualized by means of standard and illustrative rendering techniques. In the following, we present the details for each of the two qualitative parameters.

#### 6.4.1 Formalization of the Inflow Jet

Our approach to detect the inflow jet is based on the assumption that the inflow jet is a *stream object* that is bounded by a boundary contour  $C$ . This means that the boundary contour is a stream surface, which can be described by a closed seeding curve  $S$ . Here  $C$  is obtained by applying a numerical stream surface integration starting from  $S$ . To find the boundary contour  $C$ , we have to solve two problems. First, we have to define conditions for streamlines to be part of  $C$ . Second, we have to find a closed seeding curve  $S$  for starting the integration. Note that this problem does not have a unique solution: there are several seeding curves producing the same stream surface. To overcome this, we restrict ourselves to seeding curves on the inflow part of the ostium surface. This setup is illustrated in Figure 64a.

For the first problem, we collect local properties of a streamline to be part of the inflow jet. To define them, we use the relation between inflow jet and impingement zone. In fact, we assume that a certain point of an inflow jet streamline comes close to the impingement zone. This means that a streamline of the inflow jet should contain locations where three properties are simultaneously fulfilled:

- A:** The point of the streamline should have a locally minimum distance to the aneurysm surface.
- B:** There should be a rapid change of flow direction.

**C:** There should be a strong change of flow speed, i.e., a strong magnitude of the acceleration of the velocity field.

Clearly, in general there is no streamline consisting of a point fulfilling **A-C** simultaneously. Thus, we have to come up with an approach to search for streamlines fulfilling **A-C** as much as possible.

Given is a point  $\mathbf{x}_0$  on the ostium surface. From  $\mathbf{x}_0$  we integrate the streamline  $\mathbf{x}(t)$  with  $\mathbf{x}(0) = \mathbf{x}_0$  and compute the following characteristic functions of  $\mathbf{x}(t)$ :

- $d(t)$  is the minimum distance of  $\mathbf{x}(t)$  to the aneurysm surface,
- $a(t) = \|\mathbf{a}(t)\|$ , where  $\mathbf{a}(t) = \frac{\partial^2 \mathbf{x}}{\partial t^2}$  is the acceleration of the streamline,
- $c(t) = \frac{\|\dot{\mathbf{x}} \times \mathbf{a}\|}{\|\dot{\mathbf{x}}\|^3}$  is the curvature of the streamline, where  $\dot{\mathbf{x}} = \frac{\partial \mathbf{x}}{\partial t}$  is the tangent vector of  $\mathbf{x}$ , and
- $l(t) = \int_0^t \|\dot{\mathbf{x}}(s)\| ds$  is the arc length of the streamline from  $\mathbf{x}_0$ .

Technically, the functions  $d, a, c$  are computed by precomputing the 3D scalar fields  $d(\mathbf{y})$ ,  $a(\mathbf{y})$ ,  $c(\mathbf{y})$  as

- $d(\mathbf{y})$  is the distance of a 3D point  $\mathbf{y}$  to the aneurysm surface.
- $a(\mathbf{y}) = \|\mathbf{J}(\mathbf{y}) \mathbf{V}(\mathbf{y})\|$ , where  $\mathbf{V}$  and  $\mathbf{J}$  are velocity field and Jacobian at  $\mathbf{y}$ , respectively, and
- $c(\mathbf{y}) = \frac{\|\mathbf{V} \times \mathbf{a}\|}{\|\mathbf{V}\|^3}$  is the local streamline curvature at  $\mathbf{y}$ .

Then, we get  $d(t) = d(\mathbf{x}(t))$ ,  $a(t) = a(\mathbf{x}(t))$ , and  $c(t) = c(\mathbf{x}(t))$ . Furthermore,  $l(t)$  is computed by using the polygonal approximation of  $\mathbf{x}(t)$  resulting from the numerical integration. From the functions  $d, a, c$  we compute the following parameter values:

- $t_d$  is the smallest positive  $t$  where  $d(t)$  has a local minimum,
- $t_a$  is the smallest positive  $t$  where  $a(t)$  has a local maximum,
- $t_c$  is the smallest positive  $t$  where  $c(t)$  has a local maximum.

Before computing them, we employ a Gaussian smoothing on the streamline data values  $d(t)$ ,  $a(t)$ , and  $c(t)$  to reduce noise due to resampling artifacts. The parameter values  $t_d$ ,  $t_a$ , and  $t_c$  define the following characteristic points of the streamline:  $\mathbf{x}_d = \mathbf{x}(t_d)$ ,  $\mathbf{x}_a = \mathbf{x}(t_a)$ , and  $\mathbf{x}_c = \mathbf{x}(t_c)$ . Figure 64b gives an illustration of the parameter values and their corresponding points on a streamline.

Now, we can characterize the inflow jet in the following informal way: The streamline  $\mathbf{x}(t)$  is part of the inflow jet if the points  $\mathbf{x}_d, \mathbf{x}_a, \mathbf{x}_c$  are close to each other (in arc length distance), and the points  $\mathbf{x}_d, \mathbf{x}_a, \mathbf{x}_c$  are not too far away from the seeding point  $\mathbf{x}_0$  (in arc length distance). We formalize this by the following quality function  $q(\mathbf{x}_0)$ :

$$q(\mathbf{x}_0) = l_{a,c,d} \cdot (|l(t_a) - l(t_c)| + |l(t_c) - l(t_d)| + |l(t_a) - l(t_d)|), \quad (29)$$

with

$$l_{a,c,d} = \frac{1}{3} \cdot (l(t_a) + l(t_c) + l(t_d)).$$



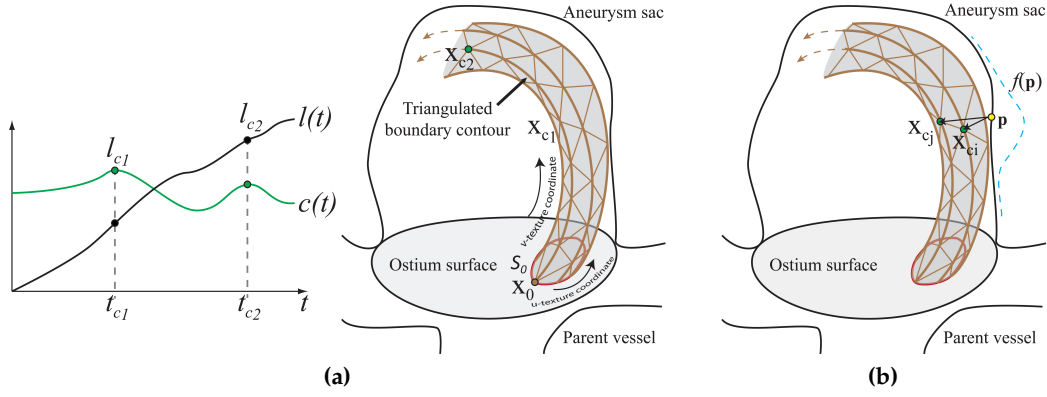


**Figure 65:** (a, left) Integration stop criteria: the arc length and curvature functions of a streamline, together with the second maximum of the curvature, (a, right) the corresponding points of the streamline. (b) Illustration for the quality function  $f(p)$  that is used to indicate the impingement zone. (Images reprinted from Gasteiger et al. [125] © IEEE 2012 with kind permission from IEEE.)

Computing  $q$  on every point of the ostium surface gives a scalar field on the ostium. Note that isoline  $q = 0$  would give the ideal seeding curve, but it does not generally exist because no streamline needs to exist consisting of a point fulfilling **A-C** at the same position. Thus, setting a small threshold  $q = q_0$  gives the seeding curves  $S_0$  for the boundary contour. Throughout this chapter we have chosen  $q_0 = q_{0.05}$ , with  $q_{0.05}$  as the five percent quantile of all values in  $q$ .

#### 6.4.2 Construction of the Inflow Jet Boundary Contour

The construction of the boundary contour is accomplished by numerical integration of the inflow jet seeding curve  $S_0$  in forward direction along the flow. For this, a criterion is required that indicates an appropriate stop of integration. The inflow jet disperses shortly after the impingement zone, associated with a rapid change of curvature (see Sec. 6.3). From there, the jet disperses in the rest of the aneurysm blood flow. Since the first local maximum of the curvature is assumed to be close to the impingement zone, we employ the second local maximum as stop criterion. This facilitates a sufficient length after the impingement zone.

We formalize this as follows: first, the arc length  $l_{c2} = l_{x_0, x_{c2}}(x(t))$  along each streamline  $x(t)$  of the boundary contour is measured from the seeding point  $x_0 \in S_0$  to the point  $x_{c2}$  being the second local maximum  $t_{c2}$  of the curvature  $c(t)$ , illustrated in Figure 65a. Second, the arc length of each streamline  $x(t)$  of the boundary contour is restricted to the median  $l_s$  of the arc length values  $l_{c2}$ , which yields the desired stop criteria:  $l_s = \text{median}(l_{c2})$ . Finally, the numerical representation of the boundary contour is given by a triangulation of neighbored streamlines (see Fig. 65a). Furthermore, for each contour vertex a pair of  $(u, v)$ -texture coordinates is assigned with  $u$  and  $v$  increasing around the boundary contour and along the streamline, respectively.

### 6.4.3 Indication of the Impingement Zone

With regard to the literature, the impingement zone depends on the inflow jet where it is seen to impact the aneurysm wall for the first time, and where it is associated with a change of the flow direction (see Sec. 6.3). Hence, our approach uses property **B** again in order to compute a scalar field  $f$  for each point  $\mathbf{p}$  on the aneurysm surface that indicates the impingement zone, given by the following quality function  $f(\mathbf{p})$ :

$$f(\mathbf{p}) = \frac{1}{n} \sum_{i=1}^n \|\mathbf{p} - \mathbf{x}_{c_i}\|, \quad (30)$$

with  $n$  being the number of available points  $\mathbf{x}_{c_i}$ ,  $i = 1, \dots, n$  of the inflow jet surface (see Fig. 65b). Formally speaking, the smaller  $f(\mathbf{p})$  is, the larger is the probability that the aneurysm surface point  $\mathbf{p}$  is part of the impingement zone. In Section 6.5.3, this scalar field is applied for a comprehensible impingement zone visualization.

## 6.5 VISUALIZATION OF HEMODYNAMIC CHARACTERISTICS

In this section, we provide several visualization techniques of the inflow jet boundary contour and the impingement zone. Additionally, the surface of the aneurysm and its parent vessel are illustrated as anatomical context in order to further support the interpretation of the presented visualization approaches. Our approach applies a ghosted view on the vessel surface to enhance the enclosing vessel surface while ensuring a maximum visibility of the embedded visualizations. The ghosted view is similar to the method presented in Gasteiger et al. [127], but without depth enhancement.

### 6.5.1 Visualization of the Inflow Jet Boundary Contour

The result of the inflow jet boundary contour construction is a stream surface based on the seeding curve  $S_0$ , given by the quality function  $q(\mathbf{x}_0)$  (see Eq. 29) and threshold  $q_0$ . Our approach depicts this surface with standard Phong shading and a color coding of the speed of the underlying blood flow field. A blue-to-red color mapping is used, since this is a familiar slow-to-fast color scale for physicians (see Fig. 66a). Inspired by illustrative integral surface renderings [161, 338] and hatching, our approach optionally provides surface stripes to enhance the surface shape and bending behavior of the inflow jet boundary (see Figure 66b). The stripes are procedurally generated in the fragment shader using the assigned  $(u, v)$ -texture coordinates from Section 6.4.2. Additionally, we ensure a uniform stripe density in screen space [114].

Since the inflow jet disperses after the impingement zone, the flow behavior becomes less predictable. To convey this, our technique provides a fade-out effect of the surface after it reaches the impingement zone. Thus, the start location corresponds to  $\mathbf{x}_{c_1}$  (property **B**), and we convert  $\mathbf{x}_{c_1}$  to the  $v$ -texture space. The opacity is linearly decreased for each surface point larger than the corresponding  $v$ -texture coordinate until it reaches the end of the surface. The fade-out effect can be seen

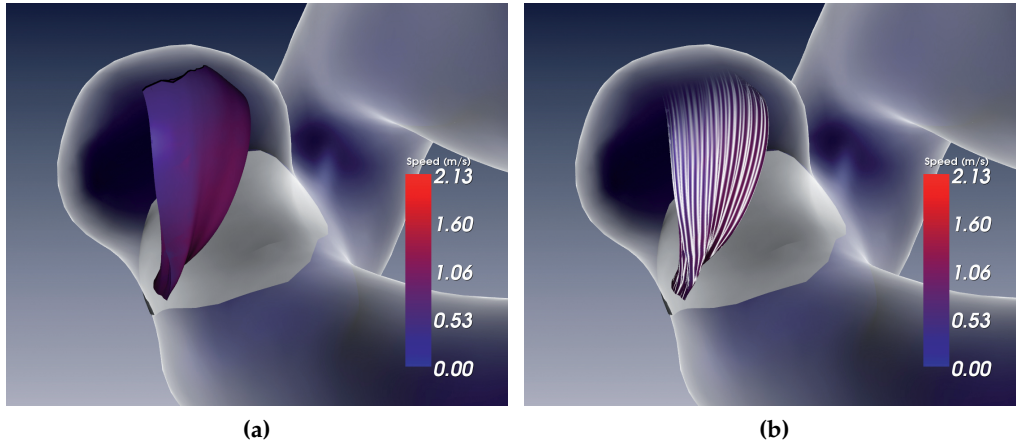


**Figure 66:** Two visualization styles of the inflow jet boundary surface: (a) color-coded surface shading, which is in (b) enhanced with surface stripes to convey surface shape. (Image reprinted from Gasteiger et al. [125] © IEEE 2012 with kind permission from IEEE.)

in Figure 66b, where it was added to the surface stripes visualization. To avoid misleading interpretations of this sharp boundary contour depiction, we provide a *safety margin* as second boundary contour around it. This boundary contour corresponds to  $q_0 = q_{0.1}$  with  $q_{0.1}$  as the ten percentile of all values in  $q$ . We visualize this boundary contour with a fuzzy-like surface rendering by modulating the surface transparency according to the Fresnel transparency from Section 5.4.1 and depicted in Figure 67a.

### 6.5.2 Visualization of the Inflow Jet as Glyph

In addition to a solid visualization of the inflow jet boundary contour our technique provides a more simplified description of it. Inspired by illustrative flow drawings in anatomical textbooks, we use an arrow glyph to depict the jet. The glyph geometry is view-aligned and points along the average direction of the inflow jet boundary surface. Additionally, we use a halo rendering at the glyph borders to highlight the glyph geometry from its background. The entire glyph is shown in Figure 67b and corresponds to the inflow jet presented in Figure 67a. The glyph geometry itself is based on the geometric centerline generated by averaging the boundary contour streamlines. The resulting line is depicted with view-aligned quads similar to the illustrative line rendering approach presented in Everts et al. [102]. We optionally provide the same speed color encoding as for the boundary surface.

### 6.5.3 Visualization of the Impingement Zone

For the depiction of the impingement zone we employ the scalar field on the aneurysm surface computed by the quality function  $f(\mathbf{p})$ , defined in Equation 30. A trivial visualization technique would be to highlight such surface points which consist of the minimum value  $f(\mathbf{p})$ . Since only a few points would fulfill this condition, this kind of technique poorly conveys the spatial extension of the impinge-

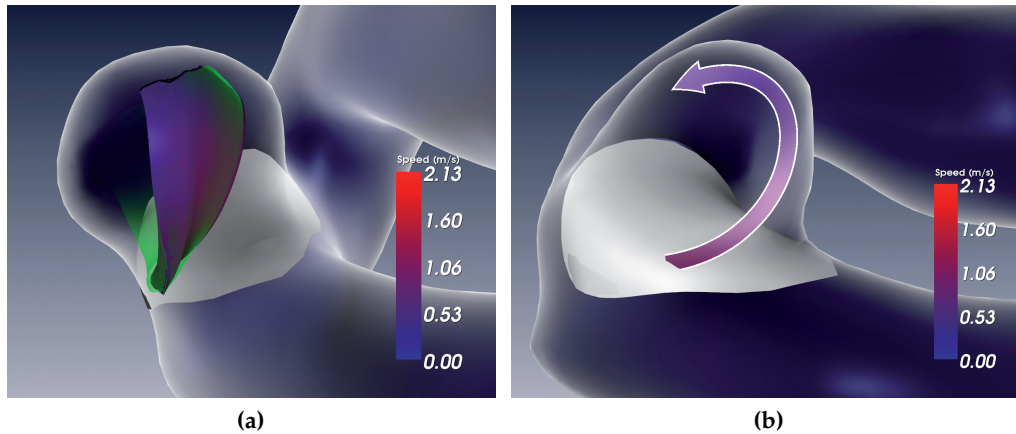


**Figure 67:** (a) Indication of a safety margin by means of a second boundary visualized with Fresnel transparency. (b) Depiction of the inflow jet by an arrow glyph. (Images reprinted from Gasteiger et al. [125] © IEEE 2012 with kind permission from IEEE.)

ment zone. Therefore, we propose two more expressive visualization techniques of the impingement zone.

First, we use an isocontouring on the scalar field similar to the extraction of the seeding curve  $C$  by choosing a threshold lower than  $f = f_{0.05}$ . Additionally, we also provide a *safety margin* contour line by using  $f = f_{0.1}$  and depict it with a stippling pattern. Note that  $f_b$ ,  $b \in \mathbb{R}$  is the  $b$  percentile of all values of  $f$ . The final result can be seen in Figure 68a, where the contour lines were smoothed with a spline interpolation to reduce sampling artifacts due to the linear interpolation of the isocontouring. Furthermore, this sparse representation can be later used as an overlay for several hemodynamic surface parameters, e.g., WSS and pressure, to support the correlation between these attributes and the impingement zone.

The second visualization technique for the impingement zone consists of an opacity mapping of the scalar field. We map the maximum scalar value to fully opaque and the scalar value corresponding to  $f = f_{0.1}$  to fully transparent. We blend a surface color linearly between both values. This is shown in Figure 68a with a yellow surface color. In contrast to the contour rendering, the opacity mapping conveys different levels of closeness to the underlying relevant inflow jet regions. Note that this can also be accomplished by multiple contour lines lower than  $f = f_{0.05}$ .

## 6.6 RESULTS AND EVALUATION

In order to evaluate our approach, we employed five patient-specific aneurysm datasets, each consisting of its ostium and surface as well as the steady CFD flow dataset. The volume grids of the vector field are composed of 181,000 to 2,308,785 volume elements (tetrahedrons and prisms) with a volume diagonal of 0.02 to 0.08 mm. The number of triangles for the vessel surfaces range from 19,234 to 380,914. On our prototype system, the pre-processing time of the datasets ranges from 20 to 120 sec on a mid-class desktop computer (Core 2 Duo 3.16GHz, 8GB RAM, Nvidia GeForce 9800 GT), depending on the resolution of the dataset. The pre-processing includes dataset loading, tracing the inflow streamlines and com-



See video no. 5  
on DVD

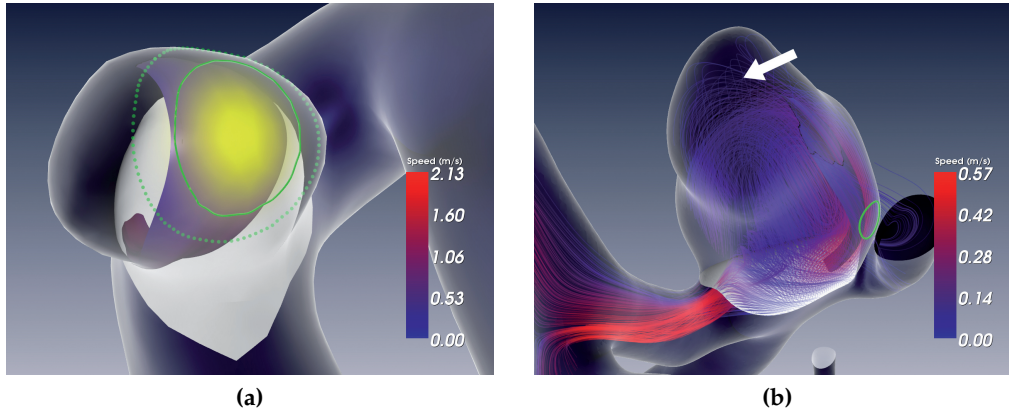


**Figure 68:** (a) Contour rendering of the impingement zone and its safety margin. Within the contour the quality function is mapped to opacity (yellow). (b) Depiction of an inflow jet and its impingement zone for a pre-ruptured aneurysm. The color-coded inflow jet boundary contour is enclosed by the inflow streamlines. The white arrow points to the known rupture location, which is apart from the indicated impingement zone (green). (Images reprinted from Gasteiger et al. [125] © IEEE 2012 with kind permission from IEEE.)

puting the scalar fields  $d(\mathbf{y})$ ,  $\alpha(\mathbf{y})$ , and  $c(\mathbf{y})$ . The computation of  $q(\mathbf{x}_0)$  and  $f(\mathbf{p})$  (see Eq. 29 and Eq. 30), the extraction of the seeding curve, the construction of the inflow jet boundary contour and glyph as well as the generation of the contour lines are accomplished in 7 to 20 seconds for each dataset. The visualization techniques described in Section 6.5 and their adjustments can be performed at interactive rates. The approach is embedded in the prototyping environment MEVisLAB and implemented in C++, supported by OpenGL, GLSL, and VTK.

The whole extraction process of the inflow jet and impingement zone is accomplished automatically. The relevant parameters consist of the isovalues for extracting the inflow jet boundary contour  $C$  (see Sec. 6.4) and for extracting the impingement zone (see Sec. 6.4.3). Since we derive these values statistically from the corresponding scalar fields, no user adjustments are necessary. In the following, we present some extracted inflow jets with their impingement zones.

The inflow jet in Figure 68b is depicted with the color-coded stream surface visualization enclosed by the inflow streamlines. The impingement zone is indicated by the green contour rendering. For this dataset, a former rupture location is known and highlighted with a white arrow by a domain expert. An interesting observation is the difference between the impingement zone and the rupture location. Even the manually adjusted impingement zones by the domain experts (see Sec. 6.6.1) show this difference. The correlation between impingement zone and the potential location of a rupture is still unclear and needs further investigation. However, the small size of the extracted impingement contour correlates to the observation of recent studies that small impingement zones are associated with an increased risk of rupture (see Sec. 6.1).

In Figure 69a the inflow jet is illustrated by the color-coded glyph geometry to depict the average direction and speed of the stream surface. The glyph indicates a straight inflow of the jet and a strong curvature at the aneurysm dome with low speed. Our approach indicates the impingement zone near to the ostium because



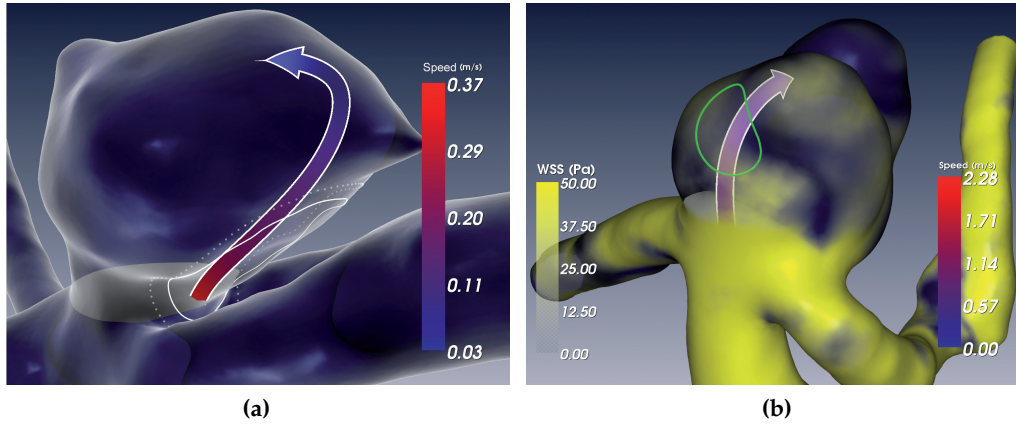


**Figure 69:** Depiction of extracted inflow jets and impingement zones for two different datasets. A color-coded inflow jet glyph is used in (a) with an impingement zone near to the ostium. A second zone could occur at the dome point. The correlation between inflow jet (glyph) and impingement zone (green contours) with WSS distribution is shown in (b). The magnitude of WSS is mapped to opacity. (Images reprinted from Gasteiger et al. [125] © IEEE 2012 with kind permission from IEEE.)

the first local curvature maxima of the boundary streamlines are located there. Furthermore, for this particular location the flow seems to hit the aneurysm surface with high speed. However, a second impingement zone could occur at the dome point of the aneurysm where the inflow jet consists of a high curvature.

To support the investigation of the correlation between WSS and impingement zone, the hemodynamic structures are shown in Figure 69b. The WSS is encoded on the front faces of the aneurysm with a yellow color map where the WSS magnitude is mapped to the opacity. The inflow jet is indicated by the glyph visualization and the impingement zone by the green contour rendering. The visualization shows an increased WSS distribution at the neck of the aneurysm but not within the impingement zone contour. Thus, the observation of Cebal et al. [63], who stated an increased WSS distribution at the impingement zone, could not be confirmed for this dataset.

#### 6.6.1 Evaluation

The evaluation of our approach considers quantitative and qualitative assessments of the five representative datasets  $D_1$  to  $D_5$ . Three biomedical researchers and three neuroradiologists participated as domain experts in the evaluation. Two of the three biomedical researchers are experts in CFD simulations and strongly involved in blood flow simulation for cerebral aneurysms. One biomedical researcher is specialized in 4D PC-MRI blood flow measuring and its evaluation with advanced flow tools like Ensight. The neuroradiologists treat cerebral aneurysms regularly. Additionally, two of the three physicians are involved in clinical research on the investigation of the risk of rupture or heart diseases due to pathological blood flow behavior. The evaluation comprises a robustness analysis of the inflow jet boundary surface extraction, a qualitative comparison between the automatically and manually extracted inflow jet and impingement zone as well as an



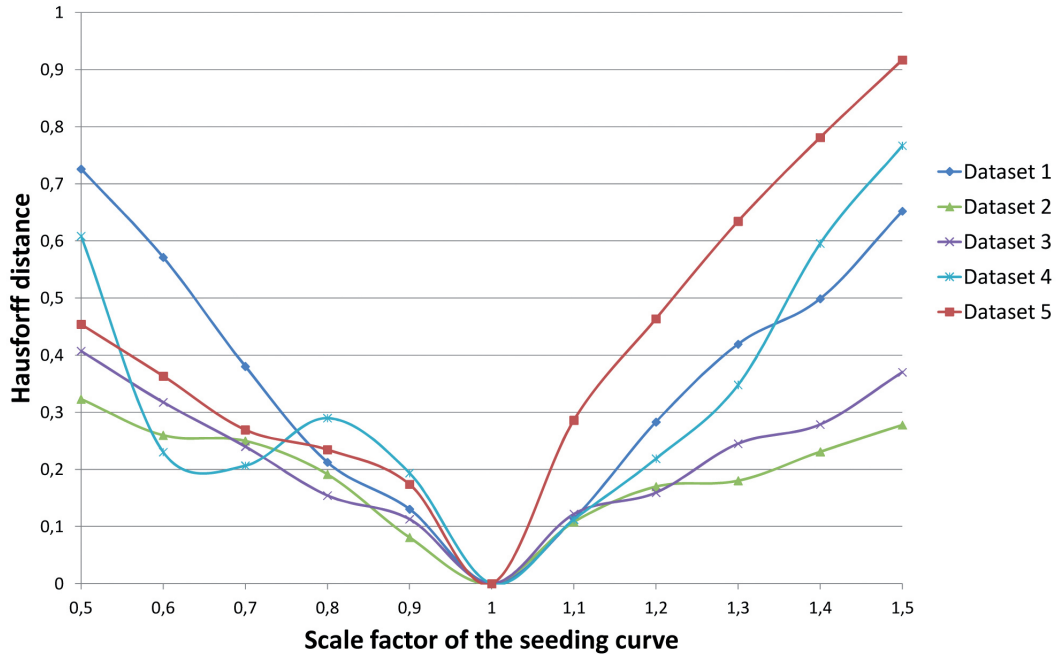


**Figure 70:** Robustness in terms of the seeding contour variation and the Hausdorff distances between the resulting boundary contours of the five datasets. (Image reprinted from Gasteiger et al. [125] © IEEE 2012 with kind permission from IEEE.)

informal user feedback of the employed visualization techniques for both hemodynamic characteristics.

#### 6.6.1.1 Robustness

The extracted inflow jet boundary surface is based on the boundary contour determined on the ostium's surface. Thus, we evaluate the robustness and sensitivity of the boundary surface extraction w.r.t. a variation of the boundary contour and the ostium's surface as seeding structure. In order to measure the robustness, we investigated the variation of the input: the boundary contour is linearly scaled to its double and half size. We measure the Hausdorff distances [261] from the original inflow jet boundary surface to the inflow jet boundary surface which is determined subsequently to the mentioned variation. This has been conducted for the five datasets.

The distance results are shown in Figure 70: A strong sensitivity would lead to rapid and large jumps within the Hausdorff distances caused by strong differences in the shape of the resulting inflow jet boundary surfaces. However, the diagram shows that the distances (approximately) grow linearly with the considered variation. This behavior corresponds to a low sensitivity and affirms the robustness of the approach.

#### 6.6.1.2 Qualitative Comparison of the Inflow Jet

Since there is no gold standard for a *real* inflow jet, we qualitatively compare the results of our automatic detection approach with the results that are adjusted by the domain experts. As a consequence, exploration methods are required, which enable the experts to interactively specify an inflow jet. In practice, however, the

investigation of the inflow jet is novel and no standard techniques exist to precisely extract the inflow jet. Thus, we provide a framework that consists of several visual exploration techniques including color-coded streamlines, cross-section planes, and speed isosurfaces. These techniques are also chosen by Cebal et al. [63, 64] and seem to be accepted in the domain-specific literature. The participants were asked to perform four tasks to specify an inflow jet in each dataset and to compare it to the automatically detected one. For each of the following tasks the aneurysm surface with its ostium was provided and the participants could fully interact (zoom and rotate) with the 3D scene:

**Task 1:** Specification of the inflow jet streamlines by filtering the inflow streamlines according to their color-coded speed. The streamlines are seeded on the ostium in forward direction and the filtering is performed by adjusting a speed threshold. Each streamline, which has at least one vertex above the threshold, is removed. For further comparison we extract a concave contour on the ostium's surface based on the adjusted inflow jet streamline bundle. This contour is considered as an approximated seeding curve of the manually adjusted inflow jet.

**Task 2:** Specification of a speed isosurface of the inflow jet, which starts at the ostium and ends up at the thought impingement zone. To generate the isosurface, participants are able to adjust an isovalue of the speed and get a visual feedback of the resulting isosurface.

**Task 3:** Alignment of a cross-section plane, which describes a *core* cross-section through the inflow jet. The plane is color-coded with the probed speed values and can be adjusted by a widget, which has handles to translate or rotate the plane in arbitrary directions. Additionally, the participants can turn on/off the inflow jet streamlines and speed isosurfaces they adjusted before to get hints about the spatial orientation of the jet.

**Task 4:** Evaluation of the manually specified and automatically extracted inflow jets by answering the following questions after **tasks 1-3** were finished:

Q1: *Did you overestimate or underestimate the adjusted inflow jet in **task 1** and **task 2**?*

Q2: *Which of the inflow jets do you judge to be more accurate, the automatically or manually extracted one, and why?* For this question, the participants were shown their adjusted inflow jet streamline bundle and the automatically extracted inflow jet stream surface for each dataset. Additionally, they could embed the adjusted cross-section plane and speed isosurface for further hints.

Q3: *Did you feel you have been limited by the provided framework to specify the inflow jet?*

For the qualitative comparison between the automatically detected and the manually adjusted inflow jets, we compare the following two results for each dataset: (1) The shape and location of the inflow jet seeding curves on the ostium resulting from **task 1** with the seeding curve  $S_0$  of Section 6.4, and (2) the location of the cross-section planes with respect to the inflow jet boundary contour  $C$  of Section 6.4.2. We expect for comparison (1) an intersection of the seeding curve  $S_0$  with the manually extracted seeding curves and for comparison (2) an intersection of the cross-section planes with the boundary contour. The more the intersections are equal in shape and location, the more the automatically and manually extracted inflow jets are correlated with each other.

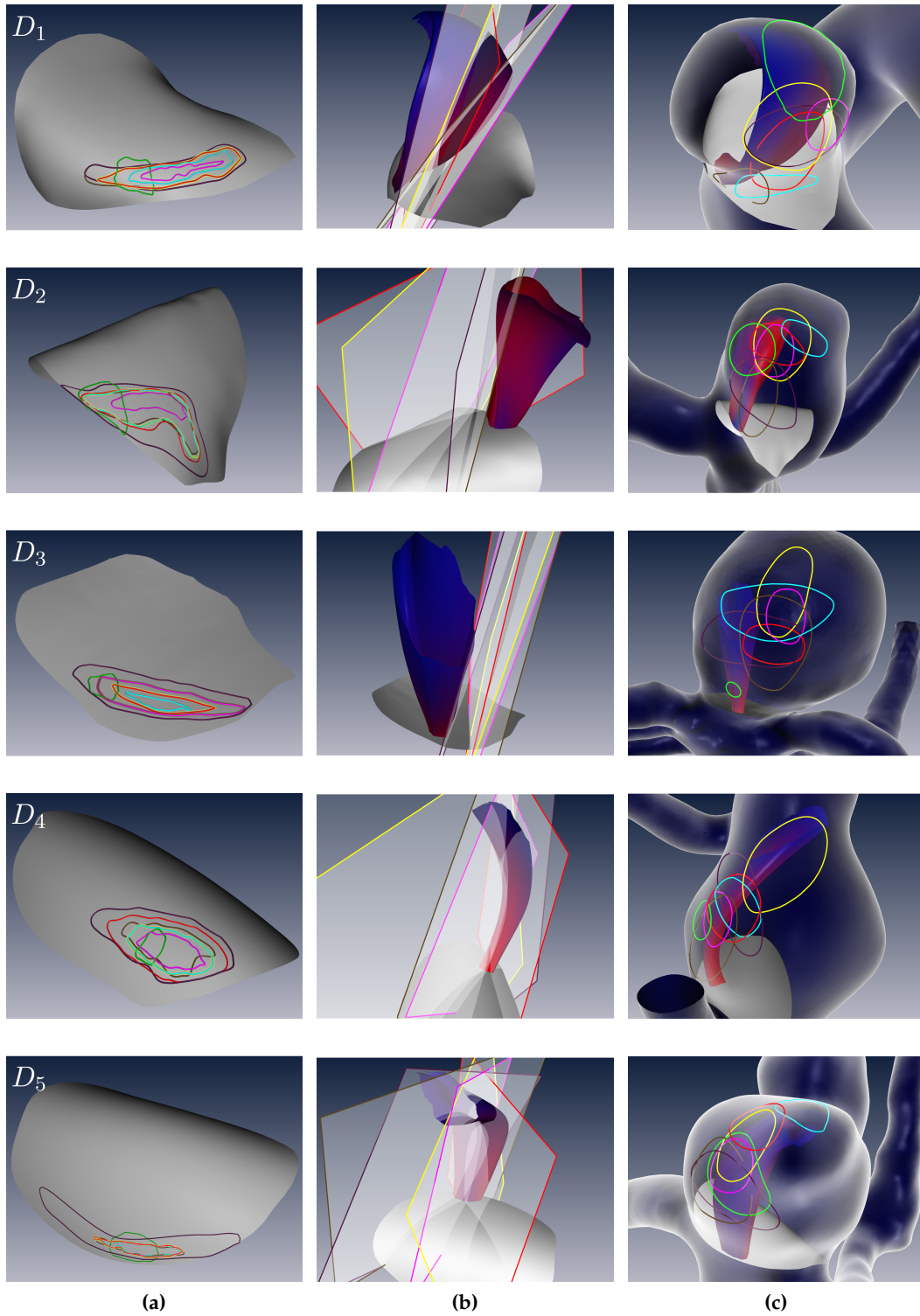


**Figure 71:** Qualitative comparison between the automatically (green) and manually (other colors) extracted inflow jet and impingement zone, respectively: (a) resulting seeding curves on the ostium, (b) cross-section planes related to the automatically extracted boundary contours and (c) resulting impingement zone contours. Each row represents one dataset. (Images reprinted from Gasteiger et al. [125] © IEEE 2012 with kind permission from IEEE.)

In Figure 71, the comparison is shown for the five datasets. The results of the participants and the automatic approach are labeled with different colors. In Figure 71b the seeding curves on the ostium are shown, where several observations can be made. There exists an intersection between the manually extracted seeding curves, but their individual sizes vary among the datasets. It follows that there is some significant overlap among the participants in terms of the inflow jet streamline bundle, but also that some of the participants seem to specify the inflow jet in varying degrees of *sharpness*. Furthermore, it can be seen that the automatically extracted seeding curve is embedded in the intersection of the manually extracted curves in each dataset. Thus, our approach detects the location of the inflow jet relatively close to the manually specified inflow jet streamline bundles. For two datasets ( $D_4$ ,  $D_5$ ) the automatically extracted curve is located at the center of intersections between the manual curves, which implies a strong correlation between the boundary contour and the *core* of the adjusted inflow jet streamline bundles. However, there are some differences in terms of the shape and location. First, in three datasets ( $D_1$ - $D_3$ ) the seeding curve is located more or less at the edge of the intersection, which corresponds to a moderate correlation to the manually specified inflow jet streamlines. Second, in almost each dataset the seeding curve is smaller and more circular compared to the manually extracted ones, which are more elongated. This implies that our approach underestimates the inflow jet.

The Figure 71b shows the comparison between the cross-section planes and the color-coded inflow jet boundary contour. Similar to the manually adjusted inflow jet streamline bundles, the differences of the planes' locations and alignments vary between the participants. Except for dataset  $D_2$ , however, the planes' intersections seem to be close to each other, which implies a moderate to strong correlation in terms of the inflow jet core direction. Based on these intersections, it can be seen that the boundary contour in datasets  $D_1$ ,  $D_4$ , and  $D_5$  is also part of the corresponding inflow jet core. For dataset  $D_2$  the boundary contour is close to the intersections and for dataset  $D_3$  the correlation to the inflow jet core seems to be weak.

#### 6.6.1.3 Qualitative Comparison of the Impingement Zone

The next part of the evaluation consists of a comparison of the automatically extracted impingement zone with the manually indicated impingement zones by the participants. Since an impingement zone is based on the underlying inflow jet, there is also no gold standard for such an aneurysm surface region. Thus, we compare the impingement zones qualitatively like the inflow jets before. We extended our framework by a surface drawing tool and asked the participants to perform the following tasks:

**Task 5:** Specification of the impingement zone by drawing a contour on the aneurysm surface where the inflow jet seems to hit the surface. For this task, the participants were shown their adjusted and color-coded inflow jet streamline bundles enclosed by the aneurysm surface visualization. Additionally, they were able to embed their cross-section planes as a further spatial hint of the inflow jet specification. Initially, a spline contour on the aneurysm surface was shown with four handles. The participants were able to move the handles on the surface, to insert

new handles or to remove them. During the interaction, the spline contour has been adapted and was located on the aneurysm surface.

**Task 6:** Evaluation of the manually specified and automatically extracted impingement zone by answering three questions (Q4-Q6) after task 5 was finished. The questions Q4 through Q6 were the same as questions Q1 through Q3 in task 4, but with "inflow jet" replaced by "impingement zone". For the qualitative comparison, we use the extracted impingement contour of our approach and compare its shape as well as its location with the manually indicated contours. We expect an intersection of both contour types. The more the intersections are equal in shape and location, the more the automatically and manually extracted impingement zone contours correlate to each other.

In Figure 71c, the qualitative comparison is shown where the results of the participants and the automatic approach are labeled with the same color as for the inflow jet comparison in Figure 71a. In addition to the impingement zone contours the automatically extracted inflow jet boundary contour is embedded as spatial hint for its corresponding impingement zone contour. Similar to the comparison of the inflow jet, several observations can be made. In terms of the intersection between the automatically and manually indicated impingement contours, a moderate to strong correlation can be seen for three datasets ( $D_2$ ,  $D_4$ , and  $D_5$ ). For the other two datasets, the intersection correlates weak in  $D_1$  and is empty in  $D_3$ . Contour size and shape are similar in three datasets ( $D_1$ ,  $D_2$ ,  $D_5$ ), but smaller and more circular in datasets  $D_3$  and  $D_4$ . However, an interesting observation is the relatively high interpersonal variance in terms of the contour size, shape, and location. It seems that the participants have different associations between inflow jet and impingement zone, which results in using different visual information to specify the impingement zone.

#### 6.6.1.4 Visualization Techniques

Besides the qualitative comparison, the participants were asked to evaluate the presented visualization techniques described in Section 6.5. For all techniques, the participants were able to interact with the scene. First, we considered the inflow jet surface depiction. All respondents stated that the visualization of the inflow jet as color-coded stream surface is comprehensible and that the color scale is reasonable. The additional safety margin was positively assessed, since it avoids a binary assessment of the inflow jet shape and extent. The stripe overlay supports the shape perception in general, but its value depends on the grade of the surface twisting and bending. For a more helical and bended surface shape, the stripes were assessed expressive as for a more laminar and even oriented inflow jet surface. Thus, the surface stripes should be provided optionally.

The fade-out effect of the stream surface after the impingement zone was rated as not necessary, since the sharp end of the inflow jet surface is assumed to be more reasonable in terms of the jet's spatial extent. The next part of visualization evaluation addressed the inflow jet glyph. All participants appreciated the simplicity of the glyph. One participant suggested to use that description as an overview visualization at the beginning of the inflow jet investigation. For a more detailed view, however, the boundary contour was preferred, especially with respect to the shape and spatial extent of the inflow jet. For this reason, one neuroradiologist

rated the glyph depiction as less suitable. In contrast to this, one biomedical expert valued the glyph as helpful to identify the main inflow jet behavior, but it should be enclosed with the safety margin visualization to get an impression of the spatial extension.

Finally, we evaluated the visualization of the impingement zone. All participants appreciated the contour line depiction. One participant suggested to provide an opaque rendering of the contour interior optionally to indicate the region more prominently. He agreed that this would lead to an occlusion of the underlying flow information. However, he considered this not as disadvantage if the investigation focus would be on the impingement zone. The additional safety margin contour was also evaluated positively and should always be provided with the original impingement zone contour. In terms of the opacity encoding of the scalar field  $f$  the participants rated this visualization as reasonable to identify aneurysm surface regions with different relevance to the impingement zone. Similar to opaque rendering of the contour interior mentioned above, a participant pointed out the caused occlusion problem and suggested to try multiple contour lines instead.

### 6.6.2 Discussion and Limitations

The qualitative comparison of the inflow jets and impingement zones allows us to draw some conclusions that are discussed in the following. For this discussion, we incorporate both the answers of the participants for the questions they were asked in **task 4** and **task 6** as well as their feedback during the evaluation. First, we address the comparison of the inflow jet.

Although the domain experts stated to have an intuitive understanding of an inflow jet, their manual adjustments show a significant degree of variation among each other. On the one side, they mostly agreed in adjusting the core of the inflow jet, but on the other side they defined the extension of the jet differently large. Five out of six domain experts stated that they probably overestimated the inflow jet streamline bundles and one expert declared to adjust the streamlines neither overestimated nor underestimated (**Q1**). Compared to the domain experts, our approach underestimated the inflow jet, since the shape of the underlying seeding curve  $S_0$  is always smaller than the seeding curves derived from the participants. However, the curve  $S_0$  is mostly placed in the intersection of all manually extracted seeding curves, and in three out of five datasets ( $D_1$ ,  $D_4$ , and  $D_5$ ) the resulting inflow jet boundary contour is located close to the manually defined inflow jet core.

This observation was also considered by the participants in terms of judging the accuracy (**Q2**). They stated that for two datasets ( $D_4$ ,  $D_5$ ) the automatically extracted inflow jet is more accurate since the boundary contours comprise the inflow jet core more *sharp* compared to their specified streamline bundles. Furthermore, the lengths of the two boundary contours were assessed as sufficiently long after the impingement zone. For one dataset ( $D_1$ ), the resulting boundary contour was rated as at least as accurate as the manually specified streamline bundles because of its closeness to the inflow jet core and its reasonable inflow behavior into the aneurysm.

For two datasets ( $D_2$ ,  $D_3$ ), the manually adjusted streamline bundles were rated to be more accurate for two reasons: First, the stream surfaces were apart from the



inflow jet core specification and more located at the edge of the streamline bundles. Second, the resulting boundary contour was assessed as too short and not reaching the impingement zone indicated by the adjusted streamline bundles. It seems that our stop criterion for the stream surface integration was too sensitive for these two datasets (see Sec. 6.4.2).

Finally, the provided framework to specify the inflow jet was considered flexible enough in general (Q3). An interesting feedback was that some participants assessed the cross-section plane as not appropriate in some datasets to locate the inflow jet core. Due to the complexity of the jet course indicated by the adjusted streamline bundle, only parts of the core could be covered with the plane. Instead, a more deformable surface was desired. Fortunately, our detection approach might provide such a complex shape of the inflow jet.

The underestimation of the inflow jet is caused by the quality threshold parameter  $q_0$ , which influences the size and shape of the seeding curve  $S_0$ . Since we use a threshold  $q_0$  less than the five percentile of all  $q$  as an established statistical measure, the resulting seeding curves were restricted to a small region of the ostium surface, which obviously leads to the underestimation. It follows that a less restrictive quality threshold  $q$  is more appropriate than the initial one.

The qualitative comparison of the impingement zone reveals several insights and conclusions. Four participants stated that they overestimated the impingement zones and two participants underestimated it (Q4), but all agreed about not being limited by adjusting the impingement zone (Q6). In terms of the accuracy between the automatically and manually specified impingement contour (Q5) an interesting discussion occurred. During the evaluation, the participants were aware that they have no clear definition of an impingement zone. Intuitively, they considered the magnitude of streamline curvature and the color-coded speed as visual hints to identify the impingement zone, but they preferred the curvature more.

For two datasets ( $D_1$ ,  $D_3$ ), they were unsure and would identify two impingement zones. One zone would be located at the aneurysm wall near to the ostium where the jet seems to hit the wall with high speed but low curvature. The other zone would be near the dome point where the curvature is obviously high but the speed is low, which is unlikely for an *impingement* behavior. Based on this experience and having in mind that the automatically extracted impingement zone contours rely on the streamline curvature, the participants rated four datasets ( $D_1$ ,  $D_2$ ,  $D_3$ ,  $D_5$ ) at least as good as their impingement zone.

The spatial correlation between contour size and location with the underlying streamline curvature was reasonable and appropriate. Dataset  $D_3$  could also be meaningful because the automatically detected impingement zone is located at a region where the decreasing of speed seems to be high. For that case, the first local curvature maximum correlates also with a high magnitude of acceleration. Thus, it could be worth to integrate the magnitude of acceleration into the impingement zone detection with different weighting. Later, multiple suggestions for the impingement zone can be provided depending on the weighting between curvature and acceleration.

Finally, it seems that for some cases, e.g.,  $D_3$  the first local maximum of the curvature is not sensitive enough to ensure an appropriate inflow jet length with a subsequent impingement zone indication. It is reasonable that noise might in-

fluence the topology of, e. g., the curvature property (or other line properties) and that is the reason why we apply a noise smoothing (see Sec. 6.4). Nevertheless, for strong noise in the data it might be necessary to apply more sophisticated noise handling strategies, such as persistence-based [357] or scale-space-based approaches [273], which are directly related to future work.

Despite the advantages and possibilities for improvements of our automatic detection approach, we also consider two limitations that may occur. First, for the evaluation of the characteristic functions it is assumed to have continuous streamlines with an appropriate integration length. Our approach would fail for noisy vector field data where a continuous line integration is not possible or results in short line segments. In particular, this is the case for measured cerebral flow datasets, which exhibit a very low spatial resolution. Even with advanced subvoxel interpolation schemes, the limited scan resolution results in an undersampling of the patient-specific flow behavior that would lead to an unreliable inflow jet and impingement zone extraction.

The second limitation is related to the visual depiction of the inflow jet. Currently, the surface and glyph visualization convey no possible dispersion of the inflow jet, which may occur after a virtual flow diverter treatment. A dispersion measurement, e. g., FTLE [302] (see Sec. 4.3.2), with an expressive visualization of it would be necessary. The magnitude of dispersion can be correlated with the performance of a certain flow diverter design.

## 6.7 CONCLUSIONS AND FUTURE WORK

Qualitative hemodynamic parameters like inflow jet and its impingement zone play an important role for the investigation of rupture risk in cerebral aneurysms. We presented an approach to automatically extract both characteristics. In contrast to a manual extraction, our approach is novel in this field of application and yields reproducible results. Based on the literature and discussions with domain experts, we derived local streamline properties and used them for a formalization of the extraction process. We provided several visualization techniques to depict the inflow jet and impingement zone.

The qualitative comparison with six domain experts showed reasonable results for both characteristics. It could be shown that for three out of five datasets the automatically extracted inflow jet was rated as more accurate compared to the manually specified one, and that for four out of five datasets the corresponding impingement zones were meaningful. However, the evaluation also showed a high interpersonal variance in the specification of both characteristics. The domain experts stated that their specification is often subjective and based on different associations between inflow jet and impingement zone. This confirms the need for an automatic detection approach to gain reproducibility.

We are convinced that it would be worthwhile to apply our approach to other vessel domains where inflow jets and impingement zones may be relevant, e. g., at the arch of the aorta. A pathological narrowing at this region increases speed and pressure to the vessel wall, which may promote aneurysm formations [221]. For these cases the user can utilize an anatomy-guided cross-section plane [338] as seeding structure instead of an ostium.

For future work, we consider several possibilities apart from the improved noise handling mentioned in Section 6.6.2. Our inflow jet formalization is suitable to incorporate additional characteristics functions, e. g., pressure or bending energy, or to individually weight existent functions, which may improve the detection performance. This involves further investigations of the manually extracted inflow jet streamlines and shared line characteristics. In this context, it would be worthwhile to investigate the application of FTLE fields as alternative extraction method (see Sec. 4.3.2 and Sec. 4.4.2). The inflow jet flow structure characterizes a *Lagrangian Coherent Structure* that might be indicated by the FTLE measure. This measure would also result in a scalar field on the ostium surface from which a stream surface can be integrated. As for all FTLE applications, the challenge is to identify a reliable FTLE threshold that indicates the inflow jet separation from the enclosed flow field.

Our approach provides also a basis for comparative visualizations, for instances, the changes of the inflow jet and its impingement zone after a virtual treatment planning or over the cardiac cycle. Therefore, comparative visualization methods are required like fanning in time visualizations as presented in Grimm et al. [139]. The applicability of our approach to measured flow data in terms of robustness and accuracy has to be investigated as well. Currently, high-resolution 4D PC-MRI measuring is restricted to clinical research. Its application in clinical routine, however, is conceivable and existent hemodynamic analysis methods have to cope with these datasets to provide physicians with clinically pertinent information.



## FOCUS-AND-CONTEXT VISUALIZATION OF MULTIPLE HEMODYNAMIC PARAMETERS

---

This chapter is based on:

"The FlowLens: A Focus-and-Context Visualization Approach for Exploration of Blood Flow in Cerebral Aneurysms". Rocco Gasteiger, Mathias Neugebauer, Oliver Beuing and Bernhard Preim. In *IEEE Transactions on Visualization and Computer Graphics (TVCG)*, 17(12), pp. 2183-2192, 2011.

### 7.1 INTRODUCTION

Throughout this thesis we have emphasized that relevant hemodynamic information consists of multiple quantitative and qualitative parameters. In most cases, quantitative parameters are obtained directly by CFD simulations or by 4D PC-MRI flow measurements with subsequent data processing. Qualitative parameters are either extracted visually or based on a formalization as presented in the previous chapter. Besides the inspection and evaluation of one parameter, domain experts are also interested in the correlation of *multiple* parameters to explore the flow dataset. Here the number and type of information may depend on spatial vessel locations.

An example is the correlation between embedded flow behavior and distributions of wall information, such as WSS or OSI. A visual exploration of these correlations results in a *multiparameter visualization problem* that requires a multivariate and multidimensional data visualization, which corresponds to research **goal 3** (see Sec. 3.9) of this thesis. Due to the complexity of the hemodynamic data, effective exploration approaches are necessary to ensure both spatial correlation and prevention of visual clutter.

Two common approaches are side-by-side views and embedded multiparameter visualizations to present the individual data information. In most cases, side-by-side views are used where the individual information is represented in separated views that minimizes visual clutter and occlusion. This is demonstrated in Figure 72 where the blood flow behavior in a cerebral aneurysm prior to its rupture is investigated. Among other things, this includes the WSS (see Fig. 72a), the velocity (see Fig. 72b) and the inflow jet (see Fig. 72a and Fig. 72d). All three hemodynamic parameters are depicted with established visualization techniques, such as color-coded surfaces, streamlines and cross-section planes. Such side-by-side views, however, may require high mental effort in terms of the spatial correlation between the hemodynamic information. The advantage of embedded visualiza-

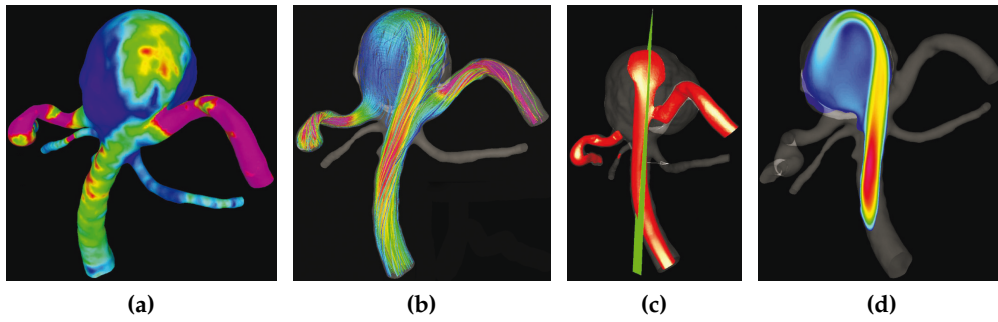


**Figure 72:** Visual exploration of hemodynamics in a cerebral aneurysm by means of side-by-side views. Three hemodynamic parameters are visualized at peak systole: (a) WSS as surface coloring, (b) speed as color-coded streamlines, (c) inflow jet as isosurface of a user-defined isospeed value and (d) a cross-section plane with speed color coding. (Images reprinted from Sforza et al. [300] © ASNR 2010 with kind permission of the American Society of Neuroradiology.)

tions consists in the direct spatial correlation between the data information but may lead to visual clutter and occlusions.

In this chapter, we present the FLOWLENS, a *focus-and-context* visual exploration scheme that combines advantages of the two aforementioned existent approaches to fulfill research **goal 3**. We identify relevant hemodynamic parameters based on the spatial vessel scope they are of interest. Subsequently, we organize these parameters into focus-and-context pairs and visualize both kinds of information by a picture-in-picture concept. Starting from the visual depiction of the context information, e. g., streamlines or pathlines, the user is able to define a 2D region-of-interest (ROI) with a subsequent embedding of the focus information, e. g., inflow jet, in the same spatial domain.

Since domain experts are not familiar with complex data visualizations, we define expressive visualization templates for the focus-and-context pairs and the spatial scopes to reflect the domain experts' needs and habits. Our approach ensures spatial correlation, reduced visual cluttering and a flexible definition of the ROI. As the field of application, we focus on simulated flow data in cerebral aneurysms because domain experts acquire and investigate most of the hemodynamic parameters for this particular CVD. However, we also demonstrate that our approach is also applicable for other vessel domains, e. g., aortic flow.

In summary, the contributions of this chapter are:

- We separate a cerebral aneurysm into the three anatomic scopes: global, wall, and aneurysm. For each scope we group relevant hemodynamic information into focus-and-context pairs, which are used as the basis for the visual exploration.
- We introduce the FLOWLENS as an interactive 2D widget to provide a flexible visual filtering for the visualization of the focus-and-context pairs. The exterior of the lens shape defines the region where the context information is depicted and the interior represents the region-of-interest where the focus information is embedded. Furthermore, the interior of the lens supports local probing and conveys changes over time for the focus information.



- For each focus-and-context pair, we propose different FLOWLENS visualization templates by employing existent flow and multiparameter visualization techniques. A template consists of the visualization of the focus parameter and the additional depiction of the context parameter inside the lens. Here we focus on a minimum of adjustable visualization parameters and minimum visual complexity as well as on an enhancement of spatial perception.
- Informal user interviews with three domain experts (two clinicians and one biomedical researcher) are conducted to assess the FLOWLENS visualization concept with respect to the visual exploration.

## 7.2 RELATED WORK

This section summarizes relevant work related to multiparameter visualization as well as focus-and-context techniques. Here we focus on techniques that visualize multivariate data with an explicit spatial context (2D or 3D). For datasets that do not generally have a spatial context, such as lists and tables of data, we refer to the overview presented in Ward et al. [354]. Additionally, a survey of general multiparameter and focus-and-context visualizations can be found in Chen et al. [73] and Cockburn et al. [77].

**MULTIPARAMETER VISUALIZATION.** Multiparameter visualizations associated with a spatial context aim for an integrated visualization of the multivariate datasets. The cognitive effort to detect and analyze structures or relationships between the individual data attributes is lower compared to that of scanning from back to front or left to right in side-by-side views. Moreover, for some cases, these insights may not be achieved by inspecting only individual parameters [210]. An integrated visualization, however, should exploit the visual perceptual capabilities as much as possible to avoid visual clutter. One of the basic techniques is mapping the parameter values to color, which was fundamentally investigated by Levkowitz et al. [210]. Due to the RGB model on display monitors, however, at most three parameters are able to be color-coded and perception-oriented color scales or spaces are necessary, such as heated-object color scale or the HSV color space. This ensures both that changes in quantitative values are perceived as uniform color changes and that the perceived ordering of the quantitative values is preserved. An extension of color mapping is texturing, which is discussed by Taylor [324].

Another established technique is a glyph-based representation. A glyph<sup>1</sup> is a geometric primitive that is positioned with respect to the spatial data points and whose attributes, such as shape, size and color, are modified according to some representative parameter values. Compared to color-coding and texturing, more parameter values can be encoded. General examples are *color icons* [210], cross-glyphs, stick figures, or *Chernoff faces* (see Ropinski et al. [279] for an overview). Glyph-based representations are also very common for multivariate medical datasets, such as the visualization of MRI diffusion tensors [94, 184], myocardial structures, perfusion and functions [256, 280, 327]. A comprehensive overview of glyph-based perfusion data visualization can be found in the work accomplished by Steffen Oeltze [254]. For a recent review of glyph-based visualization techniques in the

<sup>1</sup> In literature the term *glyph* is sometimes referred to as *icon* and can be used interchangeably.

medical domain, we refer to the survey of Ropinski et al. [279], who also propose specific glyph design guidelines. Although glyph-based visualization techniques are able to encode multiple parameters, they are most effective for 2D or surface datasets. For glyph placement in 3D, e. g., in volumetric grids, occlusion problems may occur. Furthermore, appropriate cluster and glyph-packing strategies are necessary to convey feature regions and to minimize visual clutter [185].

A combination of color, textures, glyphs, and isocontours for arbitrary multi-field datasets on surfaces is presented in Taylor [324] and Busking et al. [50] and for nested weather datasets in Treinish [332]. For a comprehensive overview of integrated multiparameter visualization techniques we refer to Bürger and Hauser [48]. Neugebauer et al. [248] utilize some of these techniques to visualize multiple hemodynamic parameters in cerebral aneurysms on cross-section planes and anatomical landmarks, e. g., the ostium, for an interactive exploration. Nevertheless, a careful selection and restriction of these techniques is required to minimize mental effort and distractions for the observers, especially for inexperienced users, such as cardiologists and neuroradiologists.

In the context of medical multiparameter visualization, the utilization of interactive visual analysis methods also becomes relevant. These methods merge visual exploration and data analysis techniques mainly by means of *linking&brushing* approaches (see Sec. 4.5). This approach was successfully applied to the analysis of cardiac data [136], fMRI data and material classification in virtual colonoscopy [25], nasal airflow data [374] as well as cerebral perfusion data [255]. Further applications can be found in the thesis of Steffen Oeltze [254].

Interactive visual analysis methods are effective in identifying correlations between parameter values and filtering of parameter values. Furthermore, values in the parameter space can be emphasized based on selections in the physical space or vice versa. Existent techniques, however, do not focus on an integrated multiparameter visualization and require some user interaction for the exploration. Our approach can complement these techniques by providing a more high-level multiparameter exploration in the physical space, which can then be used as a basis for a more detailed exploration in the parameter space with visual analysis methods.

**FOCUS-AND-CONTEXT VISUALIZATIONS.** In general, the amount of relevant information is often relatively small compared to the overall amount of acquired data. Hence, the focus-and-context (F+C) metaphor is frequently used to visually differentiate focus information from the spatial context. Data classification into focus and context information depends on the application and can be indicated interactively by the user or derived (semi-)automatically through data mining or knowledge discovery algorithms. According to Kosara et al. [192], the following four groups of F+C techniques exist:

**Distortion-oriented:** These techniques are based on a geometric distortion of the image to enable more space for the focus information. The total area of image space, however, remains the same. The classical approach is the *fish-eye view*, which magnifies the focus region within its surrounding context [120]. Distortion-oriented techniques have the drawback that they change the spatial relationship between parameter values and their spatial embedding, which may lead to misinterpretation.

**Overview + detail:** This group summarizes techniques that separate overview, i. e., context, and detail, i. e., focus, in different views or layers without a seamless transition. Common applications are magnification lenses and overview region vs. detail region in geographical mapping tools [77].

**Filtering:** A conceptual extension of overview + detail techniques consists in methods that show additional information in the focus and detail region, respectively. Fundamental work was accomplished by Bier et al. [24] who introduce the *magic lens*, which is a 2D widget with arbitrary shape rendered over the scene. The shape inside defines the focus region and the shape outside represents the context region. Within the focus region, visual filters may be incorporated to reveal hidden information, to enhance data of interest, or to suppress distracting information in a 2D or 3D scene. Applications can be found, for example, in (interactive) non-photorealistic renderings, line drawings [251], uncertainty visualization of DTI fiber pathways [43], embedding of context information in augmented reality [177] and context preserving volume renderings [195, 352]. Viega et al. [345] introduced volumetric lenses (3D magic lenses) and Mattausch et al. [225] employed these lenses to draw regions of 3D flow in greater detail. We are inspired by the *magic lenses* metaphor because of its flexible data filtering capability and its simple usability.

**In-place:** In-place techniques are similar to filtering methods but they do not require lenses and do not show additional information but rather point out information. Enhancement can be accomplished by using color, transparency, shape size or depth-of-field modulation [193]. Expressive F+C visualizations can also be achieved with *smart-visibility* [347] (see Sec. 5.2) and *importance-driven* visualization methods [348]. Focus information is revealed by attenuating or removing context information based on different *levels of sparseness* and is independent of the viewing direction. Here each level is represented by the modulation of optical properties, such as color and opacity, or by different rendering styles.

### 7.3 REQUIREMENT ANALYSIS AND DATA INPUT

In the field of medical research, several computational tools are being developed to help biomedical researchers and physicians in the investigation of CVD initiation and progression based on hemodynamic data. Without a visualization of these complex data it is not conceivable to understand the correlations between specific hemodynamic parameters and their influence on the CVD development. We intend to provide an effective visual exploration of multivariate hemodynamic information in blood vessels to support such investigation. Here, domain experts are interested in a high-level exploration of the hemodynamic behavior rather than of the data that can be obtained through quantitative analysis or visual analytics methods. Their exploration tasks involve getting an overview of the hemodynamic parameters as well as finding correlations, e. g., aneurysm formations based on certain WSS distributions or flow impact zones [67]. Hence, the goal of our approach is to provide a high level of usability, automation and expressive visualization of multiple hemodynamic parameters.

This goal is ambitious due to the complex nature of the data and the fact that the domain experts cannot be assumed to be familiar with advanced flow visualization techniques. Hence, from a series of interviews, observations and scenario discus-

sions, we derive several requirements regarding the habits and needs of domain experts. Here we focus on simulated data in cerebral aneurysms because they are currently the most relevant CVD for which multivariate hemodynamic information is acquired and investigated. Nevertheless, we also consider requirements that would enable an application of our approach to general vascular systems. The requirements are verified through the analysis of medical publications [63, 221, 301]. In addition to these requirements, we present the necessary data input for our approach.

**Hemodynamic information and spatial scopes:** To support domain experts in their visual exploration of the hemodynamics, we first have to identify relevant quantitative and qualitative hemodynamic parameters. These parameters may refer to different spatial scopes of the CVD, e. g., the WSS refers to the vessel wall scope while the inflow jet in a cerebral aneurysm is related to the aneurysm sac and wall. Hence, the definition of spatial scopes and the assignment of hemodynamic parameters to these scopes are important to steer the exploration process.

**Focus-and-context:** The visual representation of hemodynamic parameters for a given spatial scope corresponds to a multiparameter visualization. The simultaneous visualization of *all* parameters is not desired by the domain experts. Often, domain experts investigate correlations between a context parameter and a focus parameter within a specific spatial scope. For instance, they compare the flow with the WSS distribution on the surface to investigate the influence of the flow behavior, such as speed and direction, on the WSS. For such a visual filtering, a flexible and interactive focus-and-context approach with a simple interaction scheme is necessary. Here, multi-view approaches that consist of several side-by-side views each with a single visualization of a specific parameter may not be effective. Although a minimum of visual clutter is given, these approaches require increased mental effort in terms of spatial correlations for the viewer during the interaction. Thus, visualization approaches are required with a spatial embedding of the focus and context information to ensure this spatial correlation. For printed documentation purposes, however, side-by-side views are appropriate and established.

**Simplicity:** The visualization of the individual parameters must be as simple as possible to decrease mental effort and visual clutter. For each spatial scope, we shall represent the relevant hemodynamic parameters with established visualization techniques, such as color coding, streamlines and isosurfaces. Inspired by visualization template settings at medical workstations, e. g., for bone removal, this widespread concept is to be incorporated into our approach with appropriate default parameter settings. This supports the visual exploration in the sense that the domain experts are not distracted by the creation of the visualization but are able to focus on the exploration. For a comprehensible color mapping of scalar values, domain-specific habits and perception-oriented color scales should be considered. That involves linearized scales, which ensure a consistent perception of the ordering of and changes in the scalar values, e. g., warm colors to blue colors to convey high values to low values, respectively [210].

**Probing:** Domain experts are also interested in drawing certain hemodynamic parameters in detail at a particular vessel, e. g., the speed at a vessel cross-section. Probing meets this requirement by resampling the flow dataset with a probing object, e. g., a plane or a volume. It can be used to reduce data or to view data in a particular fashion. Care must be taken with respect to the sampling resolution to

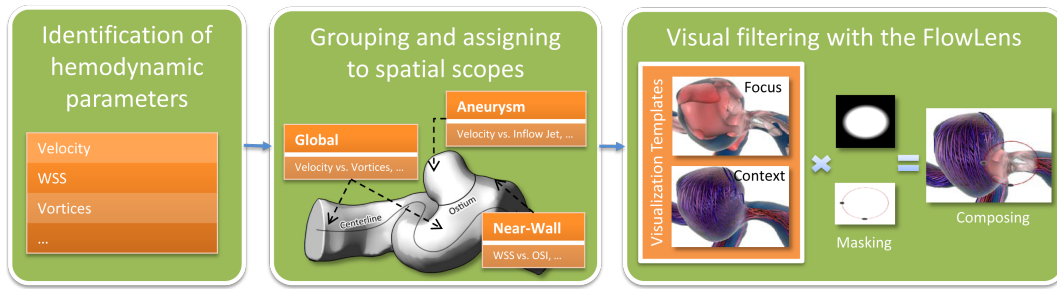


**Figure 73:** The workflow for our FLOWLENS concept consists of three steps. Left: identification of relevant hemodynamic parameters. Middle: grouping into focus-context pairs and assigning to spatial scopes. Right: visualization templates for focus-and-context pairs are composed in a picture-in-picture scheme by means of the lens shape masking.

avoid missing important high-frequency information or creating false confidence. Furthermore, a user-friendly placement must be provided to minimize interaction effort.

In the following, we describe the details of our so-called FLOWLENS approach to fulfill these requirements. Here we focus on simulated datasets for cerebral aneurysms because of the larger availability of multivariate hemodynamic information. However, our approach is also applicable to multiparameter information derived from measured 4D PC-MRI datasets, in particular aortic flow. In addition to the structured and unstructured flow grids, we also utilize the extracted vessel meshes, the ostium and parent centerline in the case of cerebral aneurysms as well as the segmentation mask in the case of measured datasets.

## 7.4 FLOWLENS CONCEPT

Our approach consists of three steps illustrated in Figure 73. In the first step we identify relevant hemodynamic parameters with a focus on cerebral aneurysms. Subsequently, these parameters are grouped into focus-and-context pairs and assigned to three spatial scopes. In the third step, we propose templates of focus-and-context visualizations for each scope to represent the involved pairs of hemodynamic parameters. We do not here focus on developing new flow visualization techniques but on representing each pair in an appropriate way based on existing techniques.

To avoid visual clutter and occlusions, we introduce the FLOWLENS as a flexible visual filtering approach that incorporates the visualization templates in a *picture-in-picture* scheme. During the visual exploration of a context parameter, the FLOWLENS can be placed over a spatial region where the correlation to its focus parameter is of interest. Within the lens, the visualization of the focus parameter is shown and the depiction of the context parameter is attenuated.

### 7.4.1 Identification of Hemodynamic Parameters

We have identified eight relevant parameters that have recently been used by biomedical researchers to investigate the aneurysm initiation, progression and



rupture. We recapitulate them briefly and refer to Section 3.2 for a more detailed description.

**Velocity:** The flow *velocity* described by the flow direction and speed is used to gain a first impression of the qualitative flow behavior, e. g., amount and speed distribution of aneurysm inflow. Low speed within the aneurysm sac also indicates a thrombus formation [272].

**Vortices:** An important hemodynamic parameter for several CVDs are flow *vortices*. A vortex is a flow structure that describes a region of swirling behavior and is seen as an indicator of certain pathologies and of a higher risk of aneurysm rupture. The number and spatiotemporal movement of vortices describe the flow complexity and stability (see Sec. 3.2.2). The flow complexity is considered as *simple* if only one recirculation or vortex structure occurs in a particular vessel region, otherwise the flow is considered as *complex*. The flow is considered as *stable* if vortices do not move or change. Studies have shown that aneurysms with complex and unstable flow patterns bear an increased risk of rupture [63, 301]. Furthermore, patients with an aorta ectasia exhibit an increased presence of abnormal vortical flow, which may promote this pathology further. A similar flow pattern in the ascending and descending aorta was observed in patients with the Marfan syndrome. This could explain the susceptibility to ectasia development in such patients [129].

**Inflow jet and impingement zone:** As indicated in the previous chapter, the *inflow jet* and its *impingement zone* also have an important influence on the risk of rupture. Ruptured aneurysms are more likely to have narrow inflow jets with a small impingement zone [63].

**WSS and OSI:** In Section 3.6.2 we discussed the role of WSS and OSI in the tissue structure modification of the vessel wall. The WSS represents the tangential force produced by blood moving across the vessel wall and the OSI describes the temporal changes of the WSS over the cardiac cycle. Although the influence of high and low WSS on the aneurysm progression and rupture risk is a subject of controversial debate, a consensus exists that high OSI promotes cerebral aneurysms and other CVDs, e. g., atherosclerosis [12, 72].

**Pressure:** Similar to WSS and OSI, the flow *pressure* is considered to be a promoter for the aneurysm initiation and progression because it affects the vessel wall weakening [12].

Note that this list of parameters represents the current state for cerebral aneurysms at the time of writing this thesis. Because the assessment of hemodynamics in cerebral aneurysms is an ongoing research field, additional parameters could be discovered or existent parameters might turn out to be less relevant. Furthermore, some of the aforementioned parameters also play an important role for other CVDs, e. g., a retrograde flow and a high flow complexity in the aorta during diastole may indicate heart failure diseases.

#### 7.4.2 Spatial Scopes and Hemodynamic Parameters

The identified hemodynamic parameters refer to three spatial scopes, which comprise the global vascular structure, the vessel wall, and the aneurysm sac. We assign the parameters to each scope and group them to hemodynamic focus-and-context pairs, summarized in Table 3:



Global Scope		Near-Wall Scope		Aneurysm Scope	
Focus	Context	Focus	Context	Focus	Context
Pressure, Vortices	Velocity	WSS, OSI, Pressure, Velocity	WSS, OSI, Pressure	Vortices, Pressure, In- and Outflow, Inflow Jet, Impingement Zone	Velocity

**Table 3:** Overview of the three spatial scopes with corresponding pairs of hemodynamic parameters that are relevant for the visual exploration.

**Global scope:** The global scope consists of the velocity information as the context parameter. It describes the overall flow behavior in the vessel, which can be the aorta or the parent vessels with the aneurysm sac. A more detailed view of the flow pattern can be achieved by incorporating flow pressure and vortex flow structures as focus parameters, e. g., to investigate the pressure distribution or vortices near to the vessel wall.

**Near-wall scope:** Investigations of near-wall information are relevant for aneurysm initiation and progression. As a consequence, WSS, OSI and surface pressure are considered as focus parameters. To depict the correlation of these parameters, we also define them as alternate context parameters. Domain experts are also interested in the underlying flow of vessel regions where values of high and low surface parameters occur. Hence, we define velocity information as an additional focus parameter.

**Aneurysm scope:** The flow behavior related to the interior of the aneurysm sac is relevant in assessing the risk of rupture. Therefore, we set vortices, pressure and inflow jet with its impingement zone as focus parameters and velocity as overall context parameter. With respect to the velocity in the aneurysm, domain experts also investigate the inflow and outflow behavior at the ostium. This is relevant, for instance, in assessing the outcome of a virtually performed treatment with flow diverters. Thus, we assign this information as an additional focus parameter.

#### 7.4.3 The FLOWLENS Design

We aim at an interactive focus-and-context approach with a simple interaction scheme and a flexible visual filtering of the aforementioned hemodynamic parameters. We present the FLOWLENS as a 2D focus-and-context approach that fulfills these requirements. Depending on the spatial scope, a context parameter is visualized outside the lens, and within the lens a corresponding focus parameter is embedded. The selection of the focus-and-context pair is user-defined and the visualization is accomplished by defining expressive visualization templates. Given this picture-in-picture concept, we achieve a high density of information in the lens region, where foveal vision occurs. In the following, we present the details.

#### 7.4.3.1 Dimensionality

Existing lens techniques can be categorized as 2D, 2.5D and 3D. The utilization of a 2D lens is based on the subsequent discussion of the advantages and disadvantages of each category with respect to the blood flow exploration and our requirements defined in Section 7.3.

**2D:** A 2D lens consists of a 2D shape that is placed in the image plane and based on the *magic lens* approach (see Bier et al. [24]). The lens transformation (movement, scaling, rotation) is restricted to the 2D image plane and can be easily manipulated by a 2D input device (mostly a mouse). Each visual style for the objects within the lens shape can be rendered in individual buffers and composed in a fragment shader. The manipulation of the lens content enables visual filtering of the flow by suppressing distracting information. However, probing a 3D flow field is not possible due to the missing spatial correlation between the 2D position of the lens and the 3D dataset.

**2.5D:** A 2.5D lens consists of a 2D shape which is placed and aligned in 3D, e.g., a cross-section plane. Its position has a spatial correlation to the 3D flow dataset and can be used as a seeding location for streamlines and pathlines as well as a sampling location for specific flow parameters. In contrast to a 2D lens, the movement and rotation of a 2.5D lens is extended to 3D. However, this leads to an increased interaction effort to place and align the lens within the 3D dataset. One-click strategies [337] or guidance strategies [248] based on centerlines or anatomical axes may be incorporated to support the placement. Additionally, the application of visual filters to flow subvolumes or their investigation are not useful due to the 2D restriction of the lens shape.

**3D:** A 3D volumetric lens (see Viega et al. [345]) is an extension of the 2.5D lens. In contrast to a 2.5D lens, a 3D lens consists of a 3D volume, such as a sphere or a box, on which visual or geometrical filters can be applied. The placement of a 3D lens has the same interaction effort as a 2.5D lens. Guidance strategies, such as snapping or advanced manipulation schemes [293], must be provided to support the placement.

Since simplicity is a major requirement, we decided to employ a 2D lens for the visual filtering. This is also motivated by the observation that medical experts are familiar with 2D tools, like magnifying lenses or rulers, on their clinical workstations. Additionally, we incorporate a 2.5D lens within the 2D lens to enable probing and slicing through the aneurysm flow. The probing plane is aligned perpendicular to the viewing direction and its 2D extension is restricted to the 2D lens shape. It can be moved interactively through the flow volume to ensure the spatial correlation.

#### 7.4.3.2 Lens Design

We provide two common lens shapes: a simple rectangular shape (see Fig. 74a) and an ellipsoidal shape (see Fig. 74b). The rectangular shape has a center  $\mathbf{C}$ , a width  $\mathbf{w}$  and a height  $\mathbf{h}$ . The shape of the ellipsoidal lens is defined by a center  $\mathbf{C}$  as well as by a major and minor radius  $\mathbf{a}$  and  $\mathbf{b}$ . The borders of both shapes are depicted by a single colored line or by a translucent transition zone defined by a rim width  $\mathbf{w}_{\text{rim}}$ . We define  $\mathbf{w}_{\text{rim}}$  as  $[0.95 \cdot d, d]$  with  $d$  as the Euclidean distance from the center to the borders. Furthermore, the ellipsoidal shape consists of two

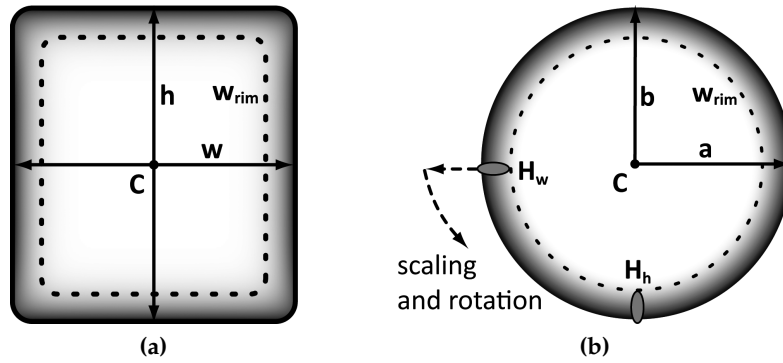


**Figure 74:** Illustration of the lens shape: (a) rectangular and (b) ellipsoidal. The transformation options are indicated by arrows. For the ellipsoidal shape, the handles are depicted with ellipses. (Images reprinted from Gasteiger et al. [126] © IEEE 2011 with kind permission from IEEE.)

handles (red) to indicate one of the possible interaction schemes described in the next subsection.

#### 7.4.3.3 Lens Interaction

The lens provides several interaction possibilities which consist of the lens transformation, manipulating the focal point of the camera, probing facilities as well as observing hemodynamic changes over time.

**Transformation:** Lens transformation is performed in a straightforward manner. The width and height of the rectangular shape can be adjusted by simply clicking and dragging one of the corresponding edges. Uniform scaling is performed by dragging one of the corners (see Fig. 74a). The major and minor radii of the ellipsoidal shape can be modified by clicking and dragging handles  $H_w$  and  $H_h$ . Furthermore, if the mouse translation also incorporates an up and down or left and right movement, a simultaneous rotation around  $C$  is possible. Uniform scaling is achieved by clicking and dragging the contour line (see Fig. 74b). For both shapes, translation is performed by clicking and dragging the inside of the lens.

**Center of camera rotation displacement:** If the lens is moved to a particular region of interest and a context parameter is shown, the user may rotate the camera around this region to investigate the current focus-and-context correlation from different views. In most cases, the center of the camera rotation, defined by the focal point, does not match with the center of the region of interest. Hence, we provide a displacement of the focal point to the current region of interest. The new focal point is located on the surface point of the focus parameter underneath the lens center. This point is determined by the first hit point of the intersection between a ray and the vessel surface. The ray is defined by the world position of the lens center and the camera position.

**Probing:** Probing is provided by placing a view-aligned 2.5D plane within the lens. The parts of the plane that are outside the lens are masked. The plane can be sliced by the user through the volume grid where specific hemodynamic parameters can be resampled, e. g., flow speed or pressure. The initial position of the plane corresponds to the intersection point of the ray and the vessel surface, as described for displacing the focal point. The plane normal is given by the normal-

ized ray direction. The spatial extension of the probe plane is restricted to the lens shape as well as to the inside of the cut contour.

**Observing changes over time:** Since we also deal with time-dependent flow data, a facility to explore hemodynamic changes over time is provided. Based on the current focus visualization within the lens, the progression of the focus parameter can be observed by slicing through the time steps. In each step, the focus visualization is updated to the current value of the focus parameter.

## 7.5 FLOWLENS VISUALIZATION TEMPLATES

We now present the visualization templates of the spatial scopes with their pairs of hemodynamic focus-and-context parameters (see Sec. 7.4.2). The FLOWLENS is utilized to achieve a visual distinction between the focus and context parameter. By default, the user-defined context parameter is visualized. For the visual correlation to that context parameter, the lens can be displayed and moved to the region of interest where the corresponding focus parameter is to be investigated. The visualization of the focus parameter is embedded into the lens and the context is either discarded or attenuated to avoid occlusions and visual clutter. The transition zone is used to blend smoothly between the focus and context visualization. We first describe the visualization of the context parameter and subsequently the combination with its focus parameter.

### 7.5.1 Global Flow Scope

For visualizing the flow velocity as the context parameter, we employ color-coded streamlines for steady flow and pathlines for unsteady flow. For the line propagation process we need to place seed points. These seed points implicitly influence which part of the flow will be visible. Since the flow at and near to the aneurysm is essential, we automatically place a seed sphere at a point  $\mathbf{x}_{\text{center}}$  on the parent vessel centerline. This sphere center point is located nearly at the middle of the centerline section below the ostium, illustrated in Figure 75a). The endpoints of this section result from the ostium extraction method described in Neugebauer et al. [246]. The radius of the seed sphere is defined by the maximum inscribed sphere radius at the sphere center. Information about maximum inscribed sphere radii results from the centerline extraction process presented in Section 3.4.3.

Within the seed sphere, we uniformly distribute seed points at which the line propagation starts in the forward and backward direction. In the case of measured aortic flow, we seed the integral lines at each voxel to cover the whole flow domain. For both cases, however, the number of seed points can be adjusted by the user. In terms of color coding, we employ a blue-to-red color mapping of the flow speed for low and high values, respectively. We also incorporate depth-dependent halos to increase the spatial perception of the generated lines [102] (see Sec. 4.2.2). Since the enclosing vessel surface as the spatial context is important for the exploration, we employ the ghosted view approach that was described in Chapter 5 [127] (see Fig. 75b).

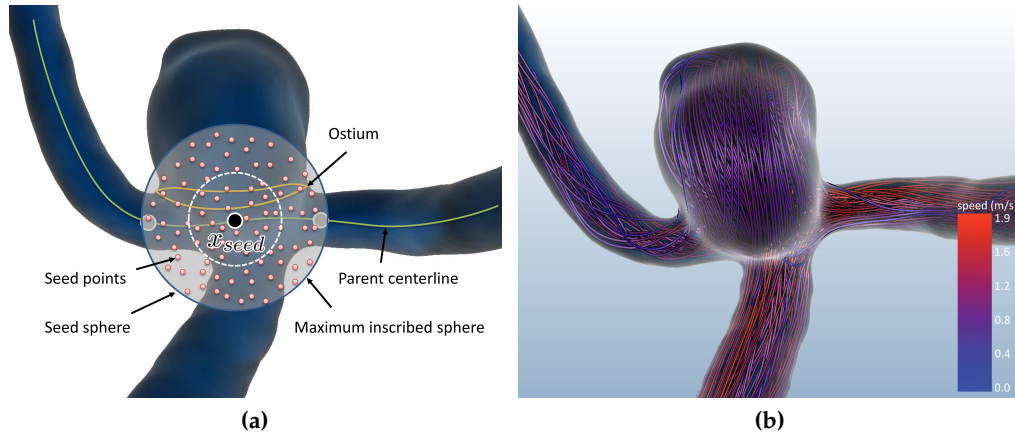


**Figure 75:** Depiction of the flow velocity as context visualization of the global scope: (a) seed point strategy for cerebral aneurysms with (b) resulting illustrative streamlines or pathlines. Color coding according to flow speed. (Image (a) reprinted from Gasteiger et al. [126] © IEEE 2011 with kind permission from IEEE.)

#### 7.5.1.1 Velocity vs. Pressure

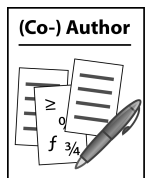
To provide information about flow pressure as a focus parameter, we employ an isosurface representation of the pressure values within the lens. Domain experts employ this kind of visualization method to extract structures from specific 3D scalar values, e.g., density values in medical image datasets. The isosurface extraction is based on a user-defined range of isovalues. We apply a white-to-red color map to distinguish low and high pressure surfaces. Linearized color maps are necessary to convey the uniform distance between these kind of hemodynamic scalar values. Within the lens, the visualization of the flow is attenuated by thin and semitransparent line renderings to avoid visual clutter (see Fig. 76a).

#### 7.5.1.2 Velocity vs. Vortex Structures

The depiction of vortices as a focus parameter within the lens requires the extraction of these flow structures. Vortex extraction is an essential goal in flow analysis and existing methods utilize either *local* or *global* criteria. In most cases, this results in integral lines that represent vortex cores or regions with swirling behavior. Local criteria are mainly based on an analysis of the Jacobian matrix and are fast to calculate, but may be sensitive to noise. Global criteria achieve more precise results at the cost of higher computation times.

In a recent work by Köhler et al. [190] in which the author of the thesis was involved, several existent local criteria in combination with line predicates (see Sec. 4.2.2) were compared for the extraction of vortices in 4D PC-MRI datasets. The following local criteria were compared: vorticity, torsion, normalized helicity, reduced speed, cores of swirling particle motion, Q-criterion and  $\lambda_2$ -criterion. For this comparison, a semiautomatic and efficient vortex extraction approach was proposed where each of the criteria could be flexibly integrated. Based on a post-processed 4D PC-MRI dataset (see Sec. 3.3), the procedure was as follows:

1. The whole dataset inside the segmentation mask was covered with pathlines starting at uniformly distributed seed points. Pathlines were integrated en-



Köhler et al. [190]

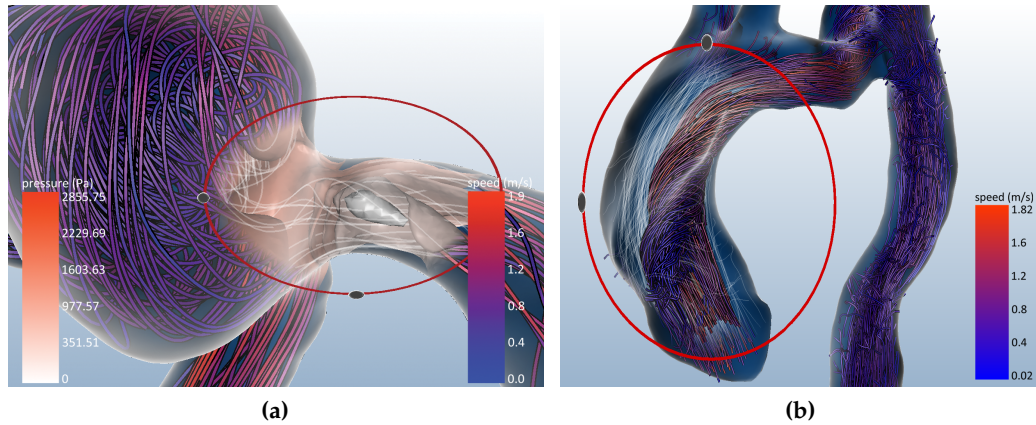


**Figure 76:** Application of the FLOWLENS in the global scope. The velocity is depicted with illustrative streamlines as context parameter. Within the FLOWLENS the flow pressure is depicted in (a) as focus parameter with isosurfaces. In (b) vortex structures are enhanced within the lens as focus parameter. In both images, the velocity is indicated as (semi-)transparent and thin streamlines within the lens. (Image (a) reprinted from Gasteiger et al. [126] © IEEE 2011 with kind permission from IEEE.)

tirely on the GPU using an adaptive Runge-Kutta-4 method as well as a hardware-accelerated quadrilinear interpolation for the vector information.

2. For each pathline point, the Jacobian matrix was computed based on the interpolated vectors at the point position.
3. Several line predicates were defined and applied to the resulting pathlines to extract vortex structures. This primarily involved the calculation and smoothing of a particular vortex criterion at each pathline point with a subsequent thresholding to distinguish between vortex and non-vortex structures. The thresholding was based on the mean value of the local criterion and the bending energy of the pathline to preserve long, curved pathlines.

Given this procedure, each criterion was evaluated as to how suitable it is for the identification of vortices in 4D PC-MRI datasets of the aorta and pulmonary artery. Since a quantitative evaluation is challenging due to the missing ground truth, the comparison relied on subjective impressions and key questions in co-operation with domain experts, in particular radiologists and cardiologists. The key questions referred to several quality criteria, such as the identification of an implicit vortex threshold to distinguish between vortex and non-vortex regions, correctness in terms of extracting at least every vortex that was discovered manually by the domain experts and pathline quality with respect to its length and smoothness.

The procedure was applied to ten pathological datasets of the aorta and pulmonary artery. In summary, the  $\lambda_2$ -criterion and the Q-criterion have shown the best results regarding the quality criteria.

We utilize the vortex extraction process proposed by Köhler et al. [190] with the  $\lambda_2$ -criterion and depict the resulting pathlines inside the lens. Context velocity information is visualized illustratively outside the lens and semitransparently inside the lens. This is shown in Figure 76b for 4D PC-MRI dataset of a patient with a former stenosis in the aortic arch, which was treated with bypass surgery. The lens



See video no. 6  
on DVD



exhibits an unusually strong vortical flow along the ascending aorta to the aortic arch, which may result from the altered vessel morphology.

### 7.5.2 Near-Wall Scope

The context parameters of near-wall information are WSS, OSI, and surface pressure as 2D scalar values onto the vessel surface. Here we consider only one surface parameter at once for the context visualization. As an established visualization method for 2D surface data, we use color coding for all three parameters. We apply a split color map to provide a distinction between normal and increased magnitude. Values below a user-defined threshold are mapped to white and values above are mapped to a yellow-to-red color map. This color map preserves the ordering of scalar data and red is an established signal color for critical values [268].

#### 7.5.2.1 WSS vs. Surface Pressure

Because both parameters represent scalar values, a color coding of both types of information may lead to visual clutter. Instead, we overlay the color-coded focus parameter with a contour plot of the context parameter within the lens (see Fig. 77a). The contour extraction is based on a user-defined range of isovalues. If multiple isolines have been extracted, we apply the same ordinal color map as for the focus visualization of the flow pressure. The spatial context inside and outside the lens is depicted as opaque surface rendering.

#### 7.5.2.2 WSS and Surface Pressure vs. Velocity

To provide focus information within the lens about the underlying flow, we display the streamline or pathline visualization of the velocity as described in Section 7.5.1.

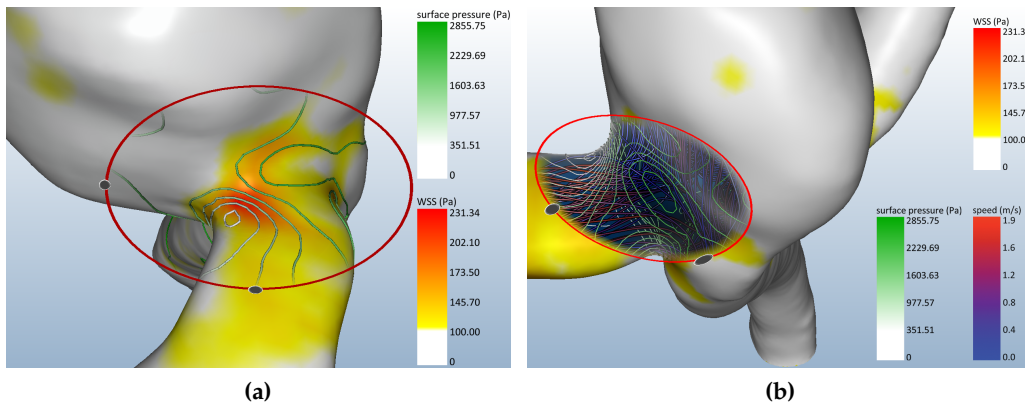


**Figure 77:** Application of the FLOWLENS in the near-wall scope. In (a) the WSS (context) is depicted as color-coded surface rendering. Within the FLOWLENS the pressure (focus) is enhanced as saturation-coded isolines (green). In (b) the surface pressure (context) is shown as color-coded surface rendering. Within the FLOWLENS the velocity (focus) is embedded as illustrative streamlines and the surface pressure is indicated by color-coded isolines. (Images adapted and reprinted from Gasteiger et al. [126] © IEEE 2011 with kind permission from IEEE.)

The surrounding vessel surface is depicted with the ghosted view rendering to reveal the embedded line visualization as well as to enhance the shape perception of the surface. Furthermore, we provide a contour plot of the current context parameter (WSS, OSI, or surface pressure) as attenuated information. The contour plot is adjusted by a user-defined threshold (see Fig. 77b).

### 7.5.3 *Aneurysm Scope*

The context parameter for the aneurysm scope is the velocity in the aneurysm including inflow and outflow. As described in Section 7.5.1, we depict the velocity with illustrative streamlines or pathlines. In contrast to the seeding strategy for the global flow, we use the mesh vertices of the ostium as the seeding location. Thus, the flow visualization is restricted to flow that runs in and out of the aneurysm through the ostium. This restriction is essential to evaluate the overall inflow and outflow conditions. Furthermore, the ostium extraction method we used [250] ensures a regular distribution of the mesh vertices to avoid fixed structures of the traced streamlines and pathlines. To adjust the number of lines, we provide a user-defined ratio value to show only a subset of the integral lines that were seeded at the ostium vertices. The vessel surface is conveyed by the ghosted view rendering of Gasteiger et al. [127].

#### 7.5.3.1 *Velocity vs. Vortex Structures*

To depict vortex structures as focus information, we employ the view-aligned probe plane of the lens combined with a color-coded LIC visualization of the resampled flow velocity. The coloring encodes the speed and is mapped to the blue-to-red color map as used for the streamlines and pathlines. Due to the dense representation of the LIC, a detailed view of the local vorticity is achieved. Furthermore, if the probe plane orientation is nearly coplanar to the central aneurysm axis of the aneurysm, the color coding conveys the inflow jet size, since the inflow speed is always higher than the outflow speed. The 3D extension of the jet, however, cannot be depicted due to the reduction to a 2D plane. Therefore, we employ the inflow jet surface depiction from Chapter 6 to overcome this limitation in the subsequent template for the velocity vs. inflow jet parameters. To convey the contextual inflow and outflow information, we extend the focus visualization by a thin and semi-transparent line rendering of the velocity (see Fig. 78a).

In addition to the dense LIC visualization, we utilize the vortex extraction approach that was already presented in the global scope. For a particular region in the contextual velocity visualization, the lens can be used to reveal 3D vortex structures (see Fig. 78b). This supports a better vortex identification and description of its 3D shape compared to the 2D LIC visualization. Both methods may also be used together to complement one another. First, the vortex structures are identified through the extraction approach and then investigated in more detail by means of the LIC visualization.

#### 7.5.3.2 *Velocity vs. In- and Outflow*

The inflow and outflow information as the focus parameters consists of the local speed as well as the inflow and outflow regions on the ostium. The speed is color-

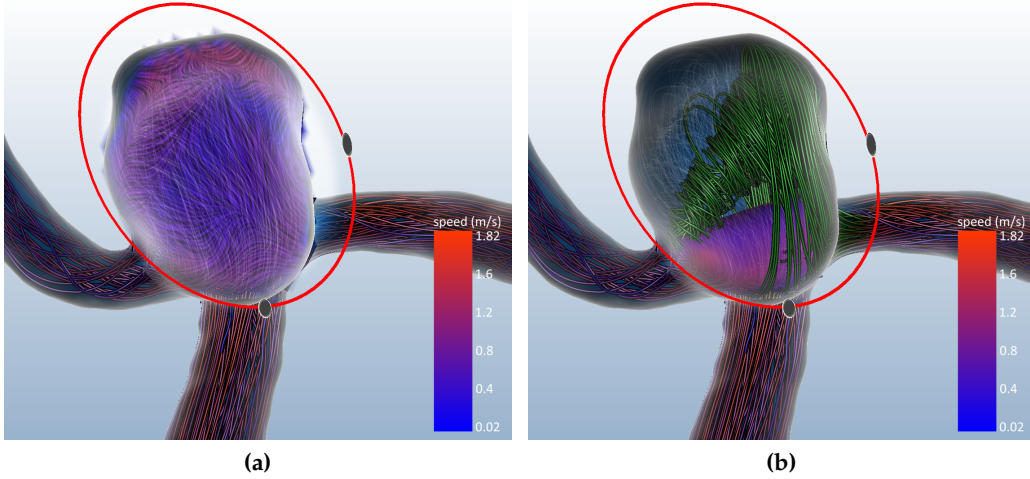


**Figure 78:** Application of the FLOWLENS in the aneurysm scope. In (a) the velocity (context) is depicted with illustrative streamlines. Within the FLOWLENS a dense representation of the vorticity (focus) is depicted by a color-coded LIC plane. In (b) the 3D shape of the vortex structure is enhanced within the FLOWLENS after flow filtering with the  $\lambda_2$ -criterion. (Image (a) reprinted from Gasteiger et al. [126] © IEEE 2011 with kind permission from IEEE.)

coded using blue-to-red speed encoding. To separate the inflow from the outflow region, we first compute the normalized volumetric flow rate  $Q'_i$  for each triangle  $i$  out of all  $k$  triangles of the ostium:

$$Q_i = A_i (\vec{v}_i \cdot \hat{n}_i) \quad (31)$$

$$Q'_i = \left( Q_i \sum_{j=1}^k Q_j \right) / |Q_{\max}|. \quad (32)$$

Here, we first compute the flow rate  $Q_i$  for the triangle  $i$  as defined in Equation 31 with  $A_i$  as the triangle area, and  $\vec{v}_i$  and  $\hat{n}_i$  as the flow vector and the normal of the triangle, respectively. In Equation 32, we perform the normalization where  $Q_{\max}$  represents the maximum triangle-wise volumetric flow rate. The normalization is necessary, since the volumetric flow rate is area-dependent. It ensures that the computed flow rate is always scaled between the negative and positive volume rate over all triangles, independently of the ostium mesh tessellation. Otherwise,  $Q'_i$  becomes smaller or larger in the case of a higher or smaller tessellation, respectively, which would require a later adaption of the color mapping.

Because  $Q_{\text{norm}}$  is a signed scalar value, the inflow (positive) and outflow (negative) region can be separated by finding the zero-crossing. We use a red isoline to depict the separation, as shown in Figure 79a. In order to enhance the separation, we overlay the inflow and outflow region with color-coded isolines. We use a binary color scheme with white for inflow and black for outflow lines to reduce a visual interference with the color-coded speed on the ostium mesh. Furthermore, we provide a depiction of the flow direction at the ostium based on short streamlines or pathlines seeded from the vertices of the ostium mesh. This reveals details about the flow behavior near the ostium. To minimize occlusions of the underly-

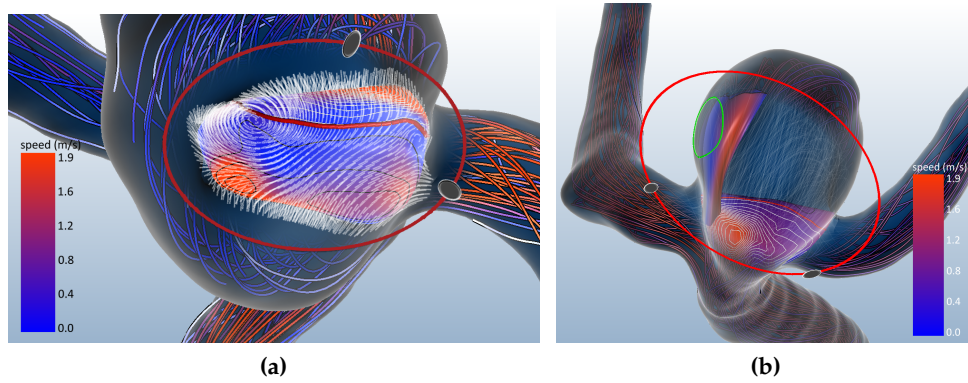


**Figure 79:** Application of the FLOWLens in the aneurysm scope. In (a) the in- and outflow at the ostium (focus) is separated by a red isoline within the FLOWLens. The flow at the ostium is indicated by short streamlines. In (b) the inflow jet (focus) is depicted with a color-coded stream surface within the FLOWLens. Additionally, the impingement zone is indicated as contour line (green).

ing focus visualization, the lines are semi-transparently rendered without color coding.

An example is given in Figure 79a, where near to the inflow-to-outflow separation line a vortex structure is shown.

#### 7.5.3.3 Velocity vs. Inflow Jet and Impingement Zone

The inflow jet is a three-dimensional flow structure, which also has to be conveyed by its visual representation. We extract and visualize this focus parameter with its impingement zone according to our approach as presented in the previous Chapter 6. In particular, we utilize the ostium mesh as the seeding structure for the extraction process and depict the inflow jet as a stream surface or as an inflow jet glyph within the lens. The impingement zone can be added as contour rendering on the aneurysm surface. Optionally, we provide context information in the FLOWLens that consists of the ostium mesh as an anatomic landmark as well as thin and semitransparent integral lines to convey the surrounding flow pattern. The ostium is color-coded in terms of the flow speed and overlaid with the inflow and outflow separation line as described in Section 7.5.3.2. The final focus-and-context visualization is shown in Figure 79b, where the inflow jet is depicted as a color-coded surface and its impingement zone as green contour rendering.

#### 7.5.4 Implementation

The FLOWLens approach is embedded in the prototyping environment MEVisLAB and implemented in C++, supported by OpenGL, GLSL and VTK. The visualization is accomplished by a multi-pass rendering consisting of an offscreen rendering and a final full screen render pass with a screen-aligned quad. We render the focus and context visualizations in two FBO offscreen textures using the aforementioned visualization techniques. The lens is rendered in two additional textures that contain the blending mask and the lens color (see Fig. 73). The blending mask encodes white as inside the lens shape, black as outside and a black-to-white gra-

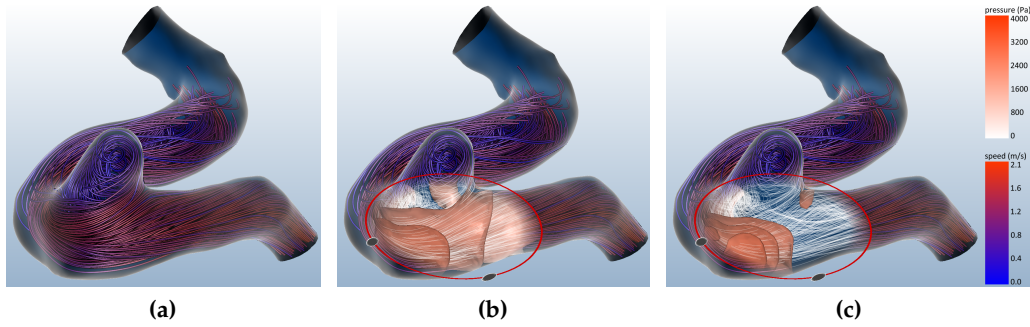


**Figure 80:** Application of the FLOWLENS in the global scope: (a) illuminated streamlines depict the velocity as context information, (b) depiction of flow pressure as isosurfaces within the lens where in (c) the isovalue has been changed.

dient as the transition zone. The lens color buffer consists of the lens appearance that includes the contour line and handles.

In the final composition, we linearly blend between the focus and context visualizations by utilizing the blending mask. Here, full white corresponds to an opaque rendering of the focus visualization and full black to the context visualization. Within the transition zone, both visualizations are smoothly blended. The lens appearance is rendered as an overlay onto the resulting visualization.

## 7.6 RESULTS

We applied our approach to seven flow datasets including five cerebral aneurysms and two pathological aorta cases. The hemodynamic information of the aneurysm datasets is obtained by CFD simulations and the velocity information for the aorta datasets is measured by 4D PC-MRI. Except for two aneurysm datasets, all datasets are time-dependent each covering a whole heart cycle. The unstructured flow grids for the CFD datasets are composed of 181,000 to 2,308,785 volume cells (tetrahedra and prisms) with a volume diagonal of 0.02 to 0.08 mm. The temporal resolution for the simulated datasets ranges from 180 to 200 time steps with 10 ms between each time step. The spatial resolution of the two measured datasets is  $132 \times 192 \times 15$  and  $132 \times 192 \times 25$  voxels, respectively, with an anisotropic voxel size of  $1.7 \times 1.7 \times 3.5$  mm. The temporal resolution ranges from 15 to 18 time steps with 50 ms between each time step.

On our prototype system, the pre-processing time of the datasets ranges from 20 to 120 sec on a mid-class desktop computer (Core 2 Duo 3.16GHz, 8GB RAM, Nvidia GeForce GTX 560 Ti with 2GB RAM), depending on the grid resolution of the datasets. The pre-processing includes dataset loading, streamline or pathline integration as well as vortex structure, inflow jet and impingement zone extraction. The density filtering of the resulting lines, the viewpoint changes, the adjustment of color schemes as well as the FLOWLENS interaction and blending are performed at interactive rates. The update rate of the LIC generation and time slicing, however, is not interactive for the unstructured datasets. In the following, we apply the FLOWLENS approach to some further datasets in addition to those previously shown.



See video no. 7  
on DVD



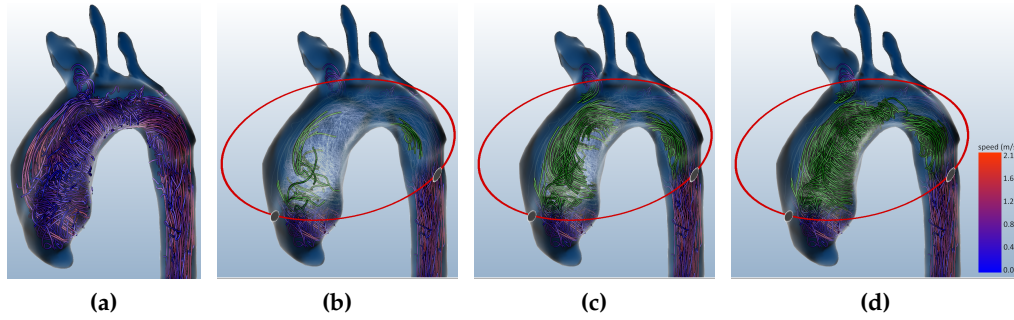


**Figure 81:** Application of the time slicing capability of the FLOWLENS to investigate a vortex structure development in the global scope of an aorta ectasia dataset shown in (a). The vortex structure is depicted with pathlines (green) and the lens shows their integration in (b) at the second, in (c) at the fourth and in (d) at the seventh time step.

In Figure 80, the lens is utilized for the global scope to investigate the pressure distribution in a saccular side-wall aneurysm. The velocity context information is depicted with illustrative streamlines color-coded according to the local speed (see Fig. 80a). To investigate the pressure distribution, the lens is placed over the parent vessel close to the aneurysm neck and shows the pressure by means of several isosurfaces (see Fig. 80b). The isosurfaces are based on several equally spaced isovalues over the whole pressure range. The user is also able to adapt the isosurface representation, e. g., by thresholding the pressure range to a certain interval with a subsequent selection of equally spaced isovalues (see Fig. 80c).

An example of the vortex structure depiction using the  $\lambda_2$ -criterion (see Sec. 7.5.1) and the time slicing capability of the FLOWLENS is shown in Figure 81 for an aorta ectasia dataset. After an unusual helical flow in the ascending aorta was observed in the global scope (see Fig. 81a), the lens is located over a focus region to reveal potential vortex structures. The lens shows the second (Fig. 81b), fourth (Fig. 81c) and seventh (Fig. 81d) time step of those pathlines (green) that depict the vortex structure evolution. The extracted vortical flow confirms observations in related clinical research reports [156]. These vortices may result from the altered vessel morphology and are also suspected to promote the corresponding vessel pathology further.

In Figure 82, a subsequent application of the near-wall and aneurysm scope is shown for an aneurysm with a bleb formation. As mentioned earlier, bleb formations may result from a former rupture or indicate an increased risk of rupture (see Sec. 2.3.1) [67]. The near-wall scope with color-coded OSI shows an elevated region above the aneurysm neck (see Fig. 82a). The FLOWLENS is utilized to investigate the underlying and nearby flow, in particular its correlation to the velocity and inflow jet.

For this purpose, illustrative streamlines are shown in the focus region that reveal a vortical flow behind the elevated OSI, presented as context information in the form of isolines (see Fig. 82b). Next to the vortical flow an increased flow speed can be observed and may represent the inflow jet. Thus, the lens switches to the aneurysm scope and embeds the inflow jet, which is visualized with the illustrative inflow jet glyph. Additionally, the impingement zone is depicted as green contour rendering within the lens. These visualizations show that the increased



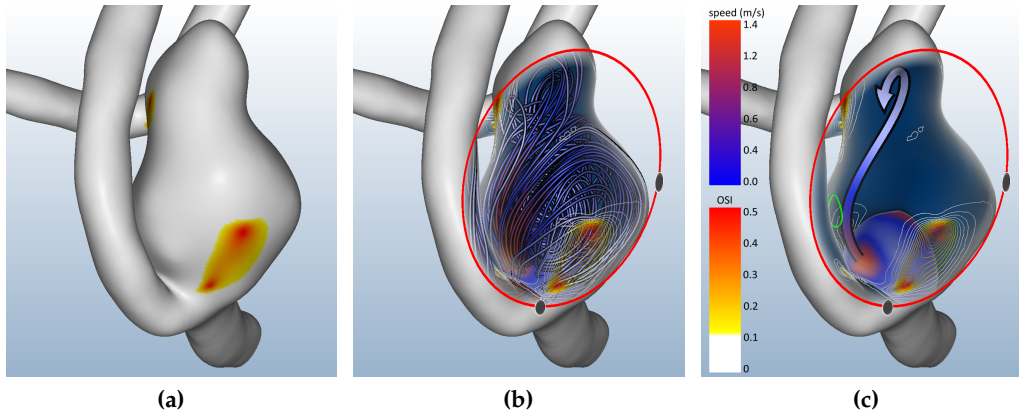


**Figure 82:** Application of the FLOWLENS to two scopes of a cerebral aneurysm with elevated OSI, shown in (a). First, the lens reveals in the near-wall scope a vortical flow behavior underneath the elevated OSI region (colored contours). Additionally, an increased flow speed next to that region is shown in (b). In (c) the lens has been switched to the aneurysm scope to depict the inflow jet and its impingement zone (green).

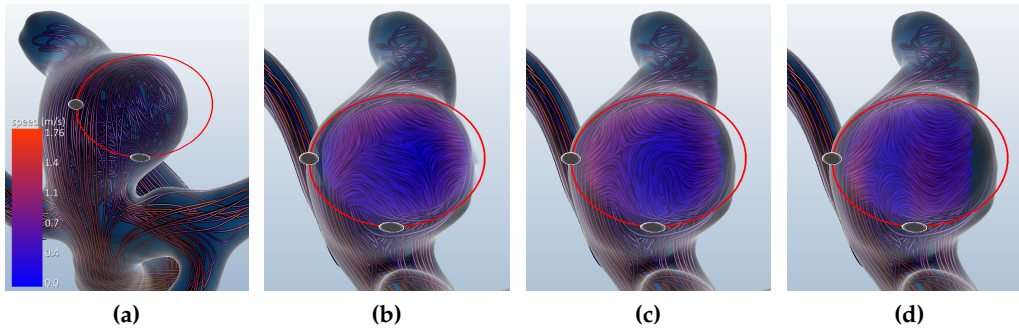


**Figure 83:** Application of the FLOWLENS to investigate the vortical flow behavior in a cerebral aneurysm more densely. For this purpose the probing and camera capabilities of the lens are utilized. In (a) the vortical flow behavior within the lens is shown. The center of camera rotation is changed to that region and a view-aligned probing plane with a color-coded LIC visualization is used to investigate the flow behavior more deeply in (b). The depth of the plane can be adjusted as shown in (c) and in (d).

OSI region does not correlate to the location of the inflow jet and its impingement zone but to the location of the vortical flow.

An example of the aneurysm scope is shown in Figure 83, where a dense vortical flow investigation is performed. The FLOWLENS is placed over a region where streamlines indicate a vortical flow (see Fig. 83a). First, the region is centered on the screen by means of the camera rotation displacement capability of the lens. Second, the view-aligned LIC representation is utilized to depict the vortical flow (see Fig. 83b). The LIC plane is sliced through the aneurysm sac and reveals multiple complex flow regions, which may indicate an increased risk of rupture (see Fig. 83c and Fig. 83d). The semitransparent streamlines as context information are omitted within the lens.

## 7.7 INFORMAL EVALUATION

We conducted an informal evaluation with two physicians and one biomedical researcher who are actively involved in the exploration of cerebral or cardiovascular blood flow. They were not involved in the FLOWLENS design. The aim of the evaluation was to gain a qualitative user feedback and to determine if the requirements in Section 7.3 were fulfilled. For this purpose, we designed an interview that was divided into three parts and conducted for each participant:

- A. The first part consisted of an introduction of the FLOWLENS where the domain expert had to evaluate the lens design and its transformation options, e. g., translation, scaling and rotation.
- B. In the second part, the three spatial scopes with the proposed visualization templates had to be evaluated. For each scope, the context parameter was shown at first and then individual focus parameters could be investigated within the lens. The participants had to evaluate the visualization of the individual parameters as well as the usability and usefulness of the FLOWLENS during the exploration.
- C. For the third part, the participants were asked to assess the time slicing capability of the flow lens and the transition zone between the focus and context information.

For each part, the participants could freely interact with our prototype system. Note that in the original work [126] on which the following evaluation is based on, some differences exist compared to the presented FLOWLENS approach. First, we presented only cerebral aneurysm datasets with simulated flow information to the participants. There were three datasets in total. Second, the vortex structure, inflow jet and impingement zone extraction approaches [125, 190] for the global and aneurysm scope were not incorporated because these approaches were developed later. We utilized the view-aligned LIC visualization for the vortical flow assessment and extracted the inflow jet manually. This extraction is based on a region with high inflow speed that is selected by a user-defined threshold. Subsequently, that region was filled with 3D arrow glyphs, which were aligned along the local velocity vectors. Based on this representation, the size of the impingement zone could be approximated due to the size and closeness of the arrow glyph bundle to the aneurysm wall.

**Part A:** All participants considered the FLOWLENS interaction as intuitive since it is similar to 2D tools in daily use, e. g., 2D measurement tools. Especially the rotation capability of the ellipsoidal lens shape was regarded as being useful to adapt the lens region to relevant anatomic structures. However, one physician stated an increased effort to adjust a specific ellipsoidal shape and prefers a circular shape with uniform scaling.

**Part B - Global Scope:** All domain experts stated an improved spatial perception of the streamlines and pathlines with depth-dependent halos in comparison to a standard illuminated line rendering. The improved perception was most clear if the camera had zoomed closer to the lines. Nevertheless, the biomedical expert preferred the purely illuminated line rendering for the investigation of the flow speed. He noticed that the halos occluded some parts of underlying lines, which

caused a decreased perception of the speed color-coding. All participants appreciated the adjustment of the number of lines and the blue-to-red color map. They considered them an intuitive way to conveying slow and fast flow. In this context, they emphasized the need for a color legend to establish an association between color values and numerical values.

After an overall investigation of the velocity, one physician employed the FLOWLENS for a specific and typical task. He placed the lens over a surface region at the ostium to investigate the local pressure distribution. Here the corresponding iso-surface rendering was initially not comprehensible but became clear after a short explanation. During the exploration, one physician preferred a low number of extracted isosurfaces and the exclusion of the thin and semi-transparent flow lines that were used as attenuated context information. The visual information was too complex and not necessary. The biomedical researcher regarded the pressure iso-surfaces as useful to convey the parabolic flow profile, especially the restriction of the pressure visualization to the lens content. He agreed that an integrated visualization of the streamlines and pressure was disturbing and should be provided only optionally.

All participants suggested more saturated colors to differentiate the pressure levels more stronger. Finally, the focal point displacement by the FLOWLENS was regarded as very useful. It simplifies the investigation of the focus and context parameter from different viewpoints by reducing the number of camera adjustments.

**Part B - Near-Wall Scope:** Two experts regarded the WSS and surface pressure as relevant parameters. One physician was not familiar with the OSI parameter and could not assess its relevance. The correlation of the surface parameters (WSS, OSI, pressure) to the underlying flow as the focus parameter was comprehensible. For example, one participant placed the FLOWLENS over a region of high WSS to investigate the speed of the underlying flow. However, the visualization of the surface parameters with isolines within the lens was regarded as disturbing since the flow was also depicted with lines.

**Part B - Aneurysm Scope:** The aneurysm scope was the most interesting spatial scope for the domain experts. Here the restriction of the integral lines to the inflow and outflow according to the ostium seeding strategy was rated as being useful because it limited the amount of lines to the relevant aneurysm section. Two participants rated the depiction of the vortex structures by the view-aligned LIC plane within the FLOWLENS as being intuitive and comprehensible, especially the view-aligned probing capability to sample the dataset. However, all three participants considered the visual information within the lens to be too complex due to the additional depiction of the ostium and the velocity information. This information should be provided optionally.

The overall separation of the inflow and outflow region at the ostium was rated as important for visually assessing the amount and location of both types of information. In terms of enhancing the separation by isolines, two participants suggested a more discrete distinction, e.g., a discrete color map or an inflow and outflow arrow glyph as well as a color legend for the isolines. Again, the domain experts suggested providing the short and semitransparent streamlines at the ostium as an optional feature. The domain experts rated the original inflow jet visualization positively because it conveyed the 3D extension of the hemodynamic parameters well. Additionally, the displacement of the camera focal point by the

FLOWLENS and the rotation of the ellipsoidal lens shape were rated as being useful to investigate the jet shape from different views.

**Part C:** All three experts regarded the time slicing capability in each scope and its restriction to the lens content as useful. It draws the attention to the focus region where temporal changes in the embedded focus parameter can be observed. However, one physician related the importance of this lens feature to the biomedical research domain only. It is less important in clinical practice where the impact of hemodynamic changes over the cardiac cycle on the risk of rupture is unknown. In most cases, a treatment procedure is always performed in the case of a detected aneurysm regardless of how much certain types of hemodynamic information change over time. Regarding the transition zone, the two physicians preferred a clear border around the FLOWLENS. They argued that a smooth transition zone blended the focus and context information together in this region, which may lead to misinterpretations.

## 7.8 CONCLUSION AND FUTURE WORK

We have presented a focus-and-context visualization approach to exploring multiple hemodynamic parameters in blood vessels with a focus on cerebral aneurysms. The qualitative analysis of these data involves the investigation of focus-and-context parameters in different spatial scopes. We identified relevant pairs of hemodynamic focus-and-context parameters and assigned them to different anatomic scopes: global, near-wall and aneurysm. For each scope, we proposed several visualization templates to depict the context and its focus parameter. The FLOWLENS was introduced to enable a flexible embedding and visual filtering of both parameters. For this purpose, the lens incorporated the visualization templates by compositing the visualizations by means of a picture-in-picture concept.

The placement of the lens occurs in 2D and provides several interaction possibilities, like a view-aligned sampling within the volumetric flow data. The FLOWLENS is capable of investigating simulated, measured as well as time-dependent flow datasets and can be extended with additional focus-and-context parameters as well as visualization templates. Moreover, although our work focused on the exploration of cerebral aneurysms, we have demonstrated that the FLOWLENS concept is also applicable to other vessel domains, e. g., aortic flow. At the time of writing this thesis, however, multivariate hemodynamic information for other vessel domains than cerebral aneurysms is hardly available. The domain expert feedback within the informal evaluation confirmed the general usefulness of the aggregation of hemodynamic focus-and-context pairs and their assignment to the presented spatial scopes. The participants regarded the FLOWLENS to be an intuitive exploration tool to support flexible visual filtering and investigations of hemodynamic correlations.

Based on the participants' feedback we conclude that some visualization templates provide too much visual information and should be embedded in the FLOWLENS only on demand, in particular the semitransparent integral lines. Another limitation of our approach relates to the number of focus-and-context parameters that are combined simultaneously with the lens. Since each parameter is visualized with a particular visualization method, a combination of several parameters in one final visualization increases the visual complexity. Thus, the selection of

appropriate visualization methods that can be combined and superimposed can be challenging. As a consequence, we recommend only the combination of two or three parameters. For the correlations between more parameters, especially in combination with a quantitative parameter selection, visual analysis methods should be considered.

For future work, the user feedback provides a valuable basis for a quantitative user study. The design of this user study will be based on the concept of Laidlaw et al. [199]. The FLOWLENS approach will be compared with a standard side-by-side view and a multiparameter visualization without a focus-and-context mechanism. For this comparison, the participants have to fulfill representative tasks that the domain experts normally have to accomplish. This might include the identification of surface regions with elevated near-wall velocity and WSS, the assessment of the inflow jet and its impingement zone, or counting the number of vortex structures. The three visualization approaches will be evaluated with respect to the participants' accuracy, response time and their personal preferences.

Furthermore, it would be worthwhile to investigate how effective seeding strategies for the integral lines can be incorporated during the visual exploration. In its current state, our approach uses uniformly distributed seed points in a certain vessel region as a fixed seed point strategy. However, it might be of interest to provide a flexible seeding to trace the flow in detail within the FLOWLENS. To cope with the high visual complexity of streamlines and pathlines, flow clustering techniques could be used to create expressive and more abstract flow representations. The FLOWLENS can then be used to reveal the expressive flow depiction in the lens region.





## DISCUSSION

---

### 8.1 INTRODUCTION

In the previous chapters, the important role of 4D hemodynamic information for the investigation, prognosis and treatment of CVDs was discussed. In the context of the medical and biomedical research domain, this kind of hemodynamic information is primarily obtained by means of 4D PC-MRI measuring and CFD simulations. Currently, no ground truth of the acquired and patient-specific hemodynamics exists. Furthermore, there exist no guidelines for the differentiation between healthy and pathological flow. This results from the high complexity and multifactorial influences of *in vivo* flow, as well as from limitations in the image data acquisition. The obtained information is volumetric and consists of scalar- and vector-valued data that are in most cases time-dependent and noisy. As a consequence, the data analysis is challenging, often observer-dependent, hardly reproducible and time-consuming.

This thesis focuses on contributions to support the qualitative analysis in the biomedical research domain, including an adaptive surface rendering, automatic extraction of qualitative hemodynamics and a flexible visual filtering to explore multivariate datasets. The contributions primarily rely on the following three implications:

- the embedded surface problem,
- the reproducibility of hemodynamic information extraction and
- the support in the visual exploration of multivariate datasets.

Further implications exist, such as reduction of data complexity with simplified and reliable visualizations, adapted interaction schemes and real-time capability. They offer interesting research areas for visualization scientists, who already proposed promising approaches and concepts with an outlook to further developments. Among other things, user- and anatomy-guided interactions, illustrative renderings, e. g., smart visibility and line rendering, (semi-)automatic flow feature extraction and visualization templates, seem to be appropriate ways to support biomedical engineers and physicians to efficiently perform their qualitative analysis.

Since the first feedback of the experts is promising, it is crucial to incorporate the state of the art and proposed techniques in the daily routine of the domain experts. On the one hand, this will enable a more thorough evaluation of the visual exploration techniques, which may lead to further improvements and developments. On the other hand, supportive exploration schemes are necessary to promote the impact of hemodynamic information on clinical decision making. As a matter of fact, the acquired flow information are not yet utilized in the clinical procedure for CVD diagnosis and treatment. This results mainly from the data acquisition *and* from the data processing side. Some physicians raise important questions about

the accuracy of the obtained hemodynamic information and the fact of inconsistent findings, especially for simulated blood flow [277]. There are several sources of uncertainty and approximations during the data acquisition pipeline, including primarily the spatiotemporal limitations of 4D PC-MRI, the error-prone image and geometry processing, the simplified CFD model assumptions and the errors that are introduced in the final visualization.

In terms of the data processing and analysis no standard procedures exist. Moreover, they require substantial time and personnel. Discussions and observations with domain experts have shown that the exploration with established tools, e. g., EnSight or ParaView, are cumbersome and time-consuming. Tailored approaches are necessary that motivate domain experts to analyze large datasets in reasonable time and effort. This would also support the urgent request from the domain experts to perform large-scale, multicenter and multi-population studies. These kinds of studies are necessary to identify clinically pertinent and consistent information. We are convinced that the presented and proposed visual exploration approaches in this thesis are a step in the right direction to support the visual exploration for such studies. Here, current and upcoming approaches can be categorized in three visualization paradigms, as proposed in recent work of Van Pelt and Vilanova [340]:

- **Exploratory paradigm.** This paradigm relies on techniques that support physicians in gaining new insights into pathological and healthy blood flow behaviors. This paradigm is mainly important for the clinical research domain where physicians currently only have few clear tasks and questions with respect to the flow behavior. Mostly, they focus on quantitative flow parameters, such as residence time, peak speed and regurgitant fractions. Qualitative flow parameters, such as the presence of vortices or the inflow jet behavior, are also important but require adapted visualizations and interaction schemes to simplify the exploration for the domain experts [222]. This *exploratory paradigm*, however, is also relevant for the biomedical research domain where new metrics can be identified to describe certain hemodynamic behavior. Techniques for this paradigm should incorporate global-to-local inspection, obtaining details on demand and intuitive interaction schemes, e. g., data aggregation and seeding. Therefore, the proposed adapted surface visualization approach from Chapter 5 and the FLOWLENS approach from Chapter 7 can be assigned to this paradigm.
- **Task-driven paradigm.** With an increased understanding of the hemodynamics certain indicators are revealed that correlate to the development and outcome of a CVD, for instance, the number and stability of vortices in cerebral aneurysms indicating their risk of rupture. Based on these indicators, domain experts are able to define tasks, which have to be conducted on large-scale, multicenter and multi-population datasets. This also includes tasks that focus on comparison purposes, e. g., flow complexity before and after a (virtual) treatment. Therefore, this *task-driven paradigm* is important for clinical trials where findings from the clinical and biomedical research domain are investigated on a larger and broader scale. Representative techniques should provide only essential visualizations and interaction options to achieve effective and efficient results. The results have to be statistically an-

alyzed to identify their degree of significance for a certain disease or healthy subject. The automatic detection and visualization of the inflow jet and its impingement zone proposed in Chapter 6 belong to this paradigm. Positive effects of this paradigm and associated visual exploration techniques would be the increased efficiency and reproducibility for conducting particular tasks as well as that a full exploration is no longer needed.

- **Education-driven paradigm.** This paradigm comprises techniques that support the construction of hemodynamic references in healthy and pathological cases, similar to atlases for the human physiology. Such references may not only be relevant for research but also for education and treatment discussions. A conceivable application scenario would be a training system for CVD treatment, designed for medical students. The system may provide adapted visual exploration techniques to steer the diagnosis and to evaluate treatment decisions. Similar training systems exist for other medical applications, such as spine and liver surgery [80, 238]. Techniques associated to this *education-driven paradigm* have to rely on approaches from the *task-driven paradigm*. This is based on the assumption that the education about specific hemodynamic information requires a reliable understanding of how this information should be analyzed.

The need for tailored visual exploration approaches and their application to large-scale studies is also based on observations that more and more clinical MRI scanners are equipped with 4D PC-MRI sequences and post-processing software. Recent reports about initial experiences of 4D PC-MRI in the clinical workflow to validate the clinical impact of measured flow confirm this observation [1]. Moreover, some vendors of CT and MRI scanners already offer workstations that integrate simplified CFD tools to approximate hemodynamics based on prior acquired patient-specific vessel anatomy and boundary conditions. In the following, we provide some recommendations for the development of visual exploration techniques and present some remaining challenges in the field of visual exploration of cardiovascular hemodynamics. In this context, we also recommend the aforementioned work of Van Pelt and Vilanova [340], who also discuss visual exploration aspects for an improved understanding of blood flow dynamics.

## 8.2 RECOMMENDATIONS FOR VISUAL EXPLORATION TECHNIQUES

The following recommendations are primarily based on the author's point of view and on conclusions from this thesis. They also incorporate feedback from domain experts and collaborators as well as results from discussions with colleagues, who are also actively working in the field of visual exploration of hemodynamics, in particular Mathias Neugebauer [245], Roy van Pelt [336] and Anja Hennemuth [151]. The recommendations are summarized in five groups that aim for an effective qualitative analysis. The recommendations are not only seen as suitable for single research or clinical trials but also for large-scale studies. Note that the resulting list is not exhaustive and should not be considered as *guidelines*. This would require more feedback from various domain experts and a quantitative performance analysis of the existent techniques. Nevertheless, the collected experiences over the last years merged with the discussions of other colleagues in this

field provide a reliable source to derive conclusions that can be used for further discussions and developments.

**SCENARIO-BASED DEVELOPMENTS** For the development of adapted visual exploration schemes, the specific needs and habits of the domain experts have to be considered. Therefore, it is worthwhile for visualization scientists to discuss the analysis process with the domain experts based on representative cases, e.g., healthy volunteers, aneurysms with bleb formations or aortic dissections. The discussion should be performed separately with domain experts in the biomedical research and in the clinical research domain because they have different points of view, time restrictions, tasks and capabilities, e.g., different flow visualization expertise and human-computer interaction skills. Ideally, the pool of experts should cover multicenter institutions to ensure a broader view of the analysis process.

The analysis itself can be accomplished with the approaches presented in this thesis or with available tools, such as EnSight or ParaView. During the analysis, the domain experts should comment on individual processing steps, such as the aims they want to achieve, their thoughts and the encountered challenges or restrictions. For the conduction of such discussions with subsequent developments we recommend the established *scenario-based design* concept proposed by Benyon et al. [22]. It describes scenarios that incorporate different aspects of a software system, such as its aims, the user group and conclusions for the development. This design concept consists of four steps and we describe them shortly with focus on the visual exploration of hemodynamics. For a more detailed description and its application to surgical training systems we refer to the contributions of Jeanette Mönch [237].

The design concept starts with the generation of *user stories*, which contain the observations and insights of the aforementioned discussion with the domain experts. Based on these user stories different *conceptual scenarios* are derived that contain requirements and design concepts for performing certain analysis steps, e.g., placing of seeding sources and investigation of the resulting integral lines. The prototyping and evaluation of the design concepts is accomplished by means of *concrete scenarios*, which are defined from the conceptual scenarios. They contain a more detailed description of each analysis step, including specific requirements and circumstances that may occur, e.g., enhancement of vortex regions out of all seeded integral lines. Finally, several concrete scenarios are formalized to *use cases* that contain all visualization and interaction steps, which are necessary for the whole analysis process. Given an appropriate number of domain experts such a scenario-based development ensures that the most relevant activities, capabilities and needs of the experts are considered.

**VISUAL FILTERING** The volumetric and dense flow datasets exhibit a high complexity that will result in visual clutter and occlusions when each hemodynamic information is visualized. As a consequence, different representations of the same flow field are recommended, which should be achieved by means of "smart" visual filtering approaches. With "smart", we mean different representations of the same flow field that convey different relevant flow structures and regions. Redundant and less important information should be omitted. What kinds of flow structures and regions are relevant should be derived from the aforementioned scenario-

based development process. Among other things, this information depends on the current vessel domain and on tasks the domain experts are interested in, e. g., vortex structures and regions with high flow speed or recirculation.

For each representation the level of detail should be adjusted by a simple threshold to provide information about both the local-to-global hemodynamics and the stability of the flow structure and region. We observed that domain experts were able to assess the visual filtering more properly when they were able to adjust the degree of filtering. Moreover, the overall filtering process should be accomplished (semi-)automatically with appropriate default parameter settings. Proper parameter settings can be identified by experimental evaluations with several domain experts and can be derived from the datasets.

For the filtering, we recommend the utilization of *flow feature extraction* methods for flow structures and *flow data aggregation* methods for decomposing the flow domain into semantic cluster regions. Depending on the type of flow structure and cluster region the aforementioned methods can be accomplished cell-based or integral line-based. We recommend cell-based data aggregation methods for flow clustering that relies on flow quantities, such as speed, direction and pressure. These methods are fast to compute and do not require any particle trace information.

Flow structure extraction and clustering that rely on derived flow properties, such as distances to anatomical structures or feature measurements by using the Jacobian matrix, should be accomplished by integral line-based methods. Integral lines convey particle traces and are able to structure the flow into different kinds of flow behavior. For integral line-based filtering, we recommend the presented and adapted *line predicates* concept by Salzbrunn et al. [287] as a flexible method to incorporate derived flow properties for flow feature detection and clustering. A line predicate can incorporate line-based measurements, e. g., length or curvature, and locally derived properties of the velocity field. This was demonstrated in Chapter 6 and in other works of hemodynamic flow filtering [33, 190].

Integral line-based methods depend on smooth and long line geometries that cover the flow domain. This requires robust and adaptive integration approaches, especially for measured flow data. Based on our experiments, we recommend an adaptive Runge-Kutta-4 method with a quadrilinear interpolation [190].

In the context of visual filtering, we recommend embedded focus-and-context techniques, such as the FLOWLENS from Chapter 7, to investigate correlations between different hemodynamic parameters. Focus and context parameters should be identified from discussions with domain experts and from reported patient studies. For a more quantitative filtering of multivariate hemodynamic parameters, *linking&brushing* has been proven as valuable filtering approach. As demonstrated in other medical applications [254, 374], brushing in the parameter space would efficiently reveal correlations between parameters and their spatial correlations in the physical space and vessel domain, respectively. This can be combined with the aforementioned focus-and-context approaches. For instance, the FLOWLENS is located over a region of high vortical flow, while the pressure and WSS values of this region are enhanced in the parameter space.

**DOMAIN-ADAPTED VISUALIZATIONS** The visual filtering should be accompanied with a simple and comprehensible visualization tailored to the capabilities

and habits of the domain experts. This should comprise perception-based color scales, illustrative depictions and visualization templates. Perception-based color scales ensure that changes of quantitative values are perceived as uniform color changes, i. e., perceptually linearized, and that the perceived orderings of the quantitative values are preserved [210]. Depending on the quantitative data type, color hues should be chosen that the domain experts are familiar with. For instance, in the collaboration with our clinicians we identified a blue-to-red color scale as appropriate to convey flow speed values. The clinicians associated blue with slow (venous) and red with fast (arterial) flow. However, this convention has not been widely accepted and may lead to misinterpretations for other domain experts because venous blood is not showing typically. In every case, a color legend is mandatory to ensure an association between color and data values.

The great potential of illustrative visualizations to create effective representations of complex information due to abstraction should be exploited, especially for the depiction of the extracted flow structures and clusters. Here, illustrative rendering styles, such as arrow glyphs, illustrative lines, surfaces and particles, are well accepted in the flow visualization community. Based on the feedback of our clinicians and collaborators, we also recommend the application of these illustrative visualization techniques for the biomedical and clinical usage. In combination with the aforementioned hierarchical clustering, the concept of *continuous abstraction* [335] seems to be promising that would provide a seamless transition between different levels of data abstraction of the flow field. At the highest level, only global flow features as overview are depicted, and more local features are revealed at lower levels where the domain experts want to explore the flow in more detail.

In the context of illustrative visualization techniques, we also recommend the application of smart visibility techniques, e. g., ghosted views, to reveal embedded flow structures and virtual treatment devices in the enclosing vessel surface. Techniques that change the spatial correlation between embedded and enclosing structures, e. g., exploded or cut-away views, have to be well designed to avoid misinterpretations and distractions. For example, an appropriate relation can be achieved by means of connecting lines as presented in the work of Van Pelt et al. [337] with exploded planar reformat.

Visualization templates integrate one or multiple techniques with default parameter settings to depict one or multiple hemodynamic parameters simultaneously. A template can also include appropriate default views on extracted flow structures from which the exploration can start. Here, automatic viewpoint selection approaches should be incorporated that consider the degree of feature occlusion and importance as well as viewpoint stability, as presented in Mühler et al. [242], for medical intervention planning. As a consequence, visualization templates would support the visual exploration procedure, because the domain experts are not occupied with adjusting the visualization but can focus on the exploration or task. Similar templates are already established in clinical workstations, e. g., bone structure removal in contrast-enhanced angiographic images and view selections to the three standard axes. Care has to be taken in terms of the selected visualization techniques for each template and hemodynamic parameter. Thus, we recommend a strong collaboration with the domain experts for the design process of the templates.



In our experience, the usage of animation to depict flow dynamics is appreciated by our domain experts. It naturally conveys the development of certain hemodynamic parameters over the cardiac cycle, e.g., the development of a vortical structure or inflow and outflow behavior. However, the animation should be restricted to certain parts of the flow domain or flow structure to avoid distractions and an inappropriate cognitive load. Similar to the (semi-)automatic visual filtering process, a manual slicing through different time points is required by the domain experts. As an alternative to animations, two other approaches are promising. First, based on the visualization template concept, interesting time frames during the cardiac cycle could be identified automatically and presented to the domain experts, e.g., systole and diastole detection or the occurrence of vortex structures. These selections can be used as starting point for further investigations. Second, variations over time can also be depicted with *fanning in time* visualizations that are known from illustrations and art [347]. These visualizations embed different states of changes, e.g., movement in still images by encoding the time steps with visual attributes, such as opacity or motion blurring. Van Pelt et al. [337] utilized this technique to convey the flow rates over time at a cross-section with opacity-modulated arrow trails.

**GUIDED INTERACTION** Most visualization methods are accompanied with user interactions, such as placement of probing planes or seeding sources for integral lines. We observed very different skills of the domain experts regarding the user interaction. While CFD experts and biomedical engineers are familiar with 3D interaction schemes, clinicians are not. This results from the daily work of the first two groups with professional 3D flow analysis tools, such as EnSight and ParaView (see Sec. 3.7). Clinicians are used to use tools on clinical workstations that involve mainly 2D interactions, e.g., measurements and zooming. Thus, the different habits should be considered when developing visual exploration approaches for these groups of domain experts.

As a remedy, guided interaction schemes are recommended that should reduce the degree of freedom to ease the interaction. Using domain knowledge and anatomical landmarks, such as centerlines or average flow direction, can assist in this process, and their usefulness has been demonstrated in several works [191, 248, 338]. Depending on the exploration task and anatomical case, a guided interaction may be the first part of a two step interaction. In the first step, it approximates the domain expert to the region of interest from which the expert can finalize the interaction afterwards.

**MANAGEMENT OF DATASETS** From a practical point of view and to enable large-scale, multicenter studies, a management of datasets is mandatory. Over the years we have collected different types of flow datasets from various clinical and academic centers, which include measured or simulated hemodynamics for different CVDs and vascular structures. For most datasets, additional or derived information are available, such as multimodal images, diagnosis reports, segmentations masks, vessel geometry and centerlines. It is obvious that the administration of these datasets becomes challenging and tedious if no systematic management is available.

We recommend a *flow database tool* that maintains all datasets with remote access by all participants of a collaboration, e.g., physicians, CFD and biomedical engineers as well as visualization scientists. The tool should provide capabilities to upload new and to modify existent datasets as well as to search particular information on some filter rules, viewers, and textual information with a subsequent download of these information. The design, evaluation and implementation may be based on the aforementioned *scenario-based design* concept [22].

Based on our experiences the different datasets and information should be grouped into *cases*. For example, each patient is assigned to one case with associated clinical and hemodynamic data, such as clinical image data and diagnosis reports, the extracted vessel geometry and the acquired hemodynamic information. Depending on the collaborator, however, different case information are relevant that have to be uploaded and modified. For instance, for a patient with a cerebral aneurysm a clinician would upload the image data and diagnosis reports with some morphological information about the aneurysm. A visualization scientist would complement that case with the segmentation mask and extracted vessel geometry. Subsequently, a CFD engineer provides the obtained hemodynamic information. To enable a systematic setup and modification of a case, the front end of the tool should provide different views and steered workflows, depending on the current collaborator. As a result, the degree of modification or "rights" are restricted to the scope of each collaborator, which avoids misleading or missing information for a case.

With respect to the searching capabilities different filter rules are necessary to identify appropriate cases for statistical studies. A possible scenario for a biomedical engineer could be the investigation of correlations between inflow jet and its impingement zone to the location of a cerebral aneurysm rupture. The inflow jet and impingement zone detection will be performed with the method proposed in Chapter 6. Thus, the filter rules would contain all saccular aneurysms with a clinical history of prior rupture and its location as well as the simulated flow data and the ostium surface. Such a flow database tool would also enable an efficient access to datasets for the evaluation of new visual exploration approaches. In daily practice and paper writing, considerable effort is often required to apply new methods to sufficient and appropriate datasets.

### 8.3 REMAINING CHALLENGES FOR VISUAL EXPLORATION

In this section, we present some remaining challenges for the visual exploration of spatial and volumetric cardiovascular hemodynamics that need to be resolved to increase their clinical acceptance and to derive clinically pertinent information. These challenges are partly in focus of the current research. A considerable amount of excellent work in all involved domains including medicine, 4D blood flow modeling and measuring as well as data analysis has already been achieved. However, it is somewhat sobering to reflect on where we are and what we should be heading for. At the time of writing this thesis, only a few reports about the influence of 4D PC-MRI on the clinical assessment in multiple cardiovascular pathologies exist [1]. Despite these preliminary works, we found no evidence that the analysis of volumetric hemodynamics is part of standard CVD diagnosis and treatment, especially for simulated flow information. Currently, only 1D or 2D hemodynamic

information that are obtained by 2D PC-MRI, Doppler US or catheter probes, are utilized in clinical practice. The following discussion identifies relevant challenges that have to be tackled by all involved experts and require an intensive collaboration with them. For complemented discussions on this topic, we refer to Van Pelt and Vilanova [340].

**UNCERTAINTY** As already mentioned in the introduction of this chapter, an important issue for incorporating hemodynamic information into clinical workflow is the existence of data uncertainty. Each stage in the workflow pipeline involves errors and inaccuracies due to approximations (see also Sec. 3.9): starting from the image data acquisition and data processing to the data visualization. In addition, due to the missing ground truth of hemodynamic information in healthy and pathological subjects, it is very hard to validate how accurate the quantitative and qualitative analysis is. Thus, the identification, quantification and visualization of uncertainty throughout the analysis pipeline is one of the biggest challenges. Note that this holds for the medical visualization in general, but that is more difficult with hemodynamic information, because the ground truth is unlikely to be obtained.

On the one hand, this requires more *in vitro* and *in vivo* validations of 4D PC-MRI and CFD with optical flow measurement methods on a large variety of vessel geometries as well as large-scale and multicenter patient studies. On the other hand, detailed investigations about the influence of CFD assumptions, such as volume grid size, blood rheology (Newtonian vs. non-Newtonian) and fluid-wall interactions on the resulting accuracy, are needed. The quantified results should be incorporated into the final hemodynamic visualization to convey its reliability.

Two promising approaches for the identification of the most likely flow trajectories in 4D PC-MRI datasets were recently proposed. In Schwenke et al. [298] the trajectories from a starting point were assessed according to a connectivity distribution that was computed by an anisotropic fast marching measurement, which incorporates the uncertainty of the measured velocity vectors. An alternative approach to incorporate the measurement uncertainty is proposed by Friman et al. [115], who utilize a sequential Monte Carlo sampling for investigating the probability distribution of flow trajectories. Following this approach, the statistical properties of PC-MRI images are first derived to describe the local uncertainty in the measured flow vectors. The local uncertainty is represented by random flow vectors at each voxel that are propagated to an uncertainty in particle traces by using the sequential Monte Carlo sampling. Finally, an uncertainty map is computed that encodes the number of occasions a probabilistic particle trace passes through a voxel.

An interesting idea to approximate a quasi ground truth for healthy and pathological hemodynamics was suggested by Van Pelt and Vilanova [340]. Based on a multitude of datasets and statistical analysis, a *statistical atlas* can be generated that describes common flow behaviors in both kinds of hemodynamics.

In the context of flow accuracy, it would also be worthwhile to combine 4D PC-MRI and CFD to exploit the advantages of both flow acquisition modalities. 4D PC-MRI offers the unique advantage to simultaneously capture the *in vivo* 4D flow behavior. CFD simulations offer a high spatiotemporal resolution and incorporate information about pressure that can be used to derive viscous shear stress,

such as WSS and OSI. Patient-specific inlet and outlet conditions for CFD models are already obtained from 4D PC-MRI, but a step further would be to adapt the CFD model at specific vessel locations, such as bendings and bifurcations by incorporating statistically measured flow information. However, for reliable shear stress information that are derived from measured flow, the time-varying anatomy of the vessel wall should be considered, in particular for large vessels like the aorta. This requires an efficient and reliable vessel segmentation approach over the cardiac cycle.

**COMPARATIVE VISUALIZATIONS** Little work has been carried out regarding comparative visualization of hemodynamics. A variety of comparable hemodynamic information is obtained where a qualitative analysis of differences is needed, e. g., measured vs. simulated flow information, the hemodynamics after a virtual treatment or between different CFD simulation setups and changes of hemodynamic parameters over time.

According to Verma and Pang [344] there exist three levels of flow comparison: The *image level* comparison is the simplest one and compares images as output of visualization algorithms, e. g., in a side-by-side view. However, the resulting images can be hard to interpret because what is being compared is not the data but the visual impressions of the data that are influenced by various factors, such as color scales and transfer functions. *Data level* comparisons instead use the raw data as starting point for the comparison that is based on some similarity metrics. An example could be the dot product between corresponding velocity vectors from a measured and simulated dataset that can be represented by a volume rendering. The *feature level* compares flow features extracted from the dataset, such as helical or vortical flow.

In the context of cardiovascular hemodynamics, the data and feature level comparison seem to be the most suitable approaches to identify similarities and differences. The greatest challenge of both levels consists of defining appropriate metrics (data level), a reliable and robust feature extraction (feature level) as well as how the comparison results should be conveyed. This applies especially for feature comparisons over time, because blood flow features can appear, disappear, merge, split and move. Similar to multiparameter visualizations, a variety of representations are available, such as side-by-side views, superimposing and glyphs, each with their own benefits and shortcomings. But also illustrative visualization approaches and interactive exploration schemes, as proposed in Chapter 6 and 7, are worthwhile to investigate.

**EVALUATIONS** As pointed out in the introduction of this chapter, various visual exploration techniques for cardiovascular hemodynamics exist. However, little work has been done for a quantitative evaluation of these techniques regarding their performance of tasks (see Chap. 5). More of these evaluations are necessary to improve the efficiency and acceptance rate of those techniques in the daily work of the domain experts. The challenge is to transfer the exploration goals of the experts into task-driven experiments, which can be measured, e. g., counting the number of vortices and rating their stability over time on a Likert scale. The aforementioned recommendation for a scenario-based development can help to

identify and formalize these tasks, as demonstrated in Laidlaw et al. [199] and Kuss et al. [198].

In addition to assess the visualization techniques, an interesting investigation would be how stereo displays, 3D pointing devices or combinations of both are able to improve the flow exploration and task performances. First results by Forsberg et al. [109] demonstrated a significantly faster performance of tasks by means of stereoscopic viewing for the investigations of integral line representations, but it does not generally improve accuracy. 3D pointing devices, such as the **SpaceMouse** (3Dconnexion Inc., Waltham, Massachusetts, USA) or the **PHANTOM** (Sensable, Wilmington, Massachusetts, USA), provide six degrees of freedom that enable a full 3D interaction. This 3D interaction characteristic can be seen in contrast to the recommended guided and simplified interaction before. The challenge would be to effectively combine the guided interaction schemes with the additional degrees of freedom to accomplish 3D interaction tasks, such as seeding and camera rotating, more easily. Moreover, stereo displays and 3D pointing devices can be combined into an integrated solution like the **zSpace** display (zSpace Inc., Sunnyvale, California, USA) to increase the effect of immersion during the flow exploration. To the best of our knowledge, no quantitative evaluations of these combinations for cardiovascular hemodynamics exist.

**WORKFLOW INTEGRATION** The investigation of volumetric hemodynamics requires several processing and analysis steps of the acquired datasets, especially for simulated datasets. Most of these steps are accomplished either in single or in existing workflow tools, such as **GIMIAS** or **OsiriX**. This also includes software solutions from vendors for MRI scanners, which already equipped their machines with preliminary tools for data processing and analysis (see Sec. 3.7). However, current visual exploration approaches that are provided by visualization scientists are not integrated in these software packages. Among other things, this requires time-consuming data conversion and visits to remotely located research facilities. As a consequence, the approved visual exploration methods that result from the aforementioned quantitative evaluations should be incorporated into existing workflow tools. This would support the collaboration and the reproducibility of analysis results in multicenter studies.

In the context of this workflow integration, a further challenge would be to provide real-time visualization for simulated hemodynamics based on unstructured grids. For the structured grids of measured flow datasets available GPU approaches exist, but little work has been done for unstructured datasets. This mainly involves fast grid cell identification and coherent GPU memory access to trace integral lines or particles. An efficient processing of unstructured grids is also of particular interest in terms of the aforementioned combination of measured and simulated flow information for compensating uncertainty.





### Part III

#### APPENDIX

And now these three remain: faith, hope and love.  
But the greatest of these is love.  
*(The Bible, Psalm 111, Verse 10)*



## BIBLIOGRAPHY

---

- [1] B. D. Allen, A. J. Barker, K. Parekh, L. C. Sommerville, S. Schnell, K. B. Jarvis, M. Carr, J. Carr, J. Collins, and M. Markl. Incorporating time-resolved three-dimensional phase contrast (4D flow) MRI in clinical workflow: initial experiences at a large tertiary care medical center. *Journal of Cardiovascular Magnetic Resonance*, 15(Suppl 1):P32, 2013. (Cited on pages 94, 213, and 218.)
- [2] P. Alliez, E. de Verdire, O. Devillers, and M. Isenburg. Isotropic surface remeshing. In *Shape Modeling International*, 2003, pages 49–58, 2003. (Cited on page 63.)
- [3] P. Alliez, G. Ucelli, C. Gotsman, and M. Attene. Recent advances in remeshing of surfaces. *Shape Analysis and Structuring*, pages 53–82, 2007. (Cited on pages 62 and 63.)
- [4] P. Angelelli and H. Hauser. Straightening tubular flow for side-by-side visualization. *IEEE Transactions on Visualization and Computer Graphics*, 17(12):2063–2070, 2011. (Cited on page 115.)
- [5] E. Angelini, Y. Jin, and A. Laine. State of the art of level set methods in segmentation and registration of medical imaging modalities. In J. Suri, D. Wilson, and S. Laxminarayan, editors, *Handbook of Biomedical Image Analysis*, Topics in Biomedical Engineering International Book Series, pages 47–101. Springer US, 2005. (Cited on page 56.)
- [6] S. Ansari, S. Schnell, T. Carroll, P. Vakil, M. Hurley, C. Wu, J. Carr, B. Bendok, H. Batjer, and M. Markl. Intracranial 4d flow MRI: Toward individualized assessment of arteriovenous malformation hemodynamics and treatment-induced changes. *American Journal of Neuroradiology*, 2013. (Cited on page 94.)
- [7] L. Antiga, B. Ene-Iordache, and A. Remuzzi. Computational geometry for patient-specific reconstruction and meshing of blood vessels from MR and CT angiography. *IEEE Transactions on Medical Imaging*, 22(5):674–684, 2003. (Cited on pages 61 and 92.)
- [8] L. Antiga, M. Piccinelli, L. Botti, B. Ene-Iordache, A. Remuzzi, and D. Steinman. An image-based modeling framework for patient-specific computational hemodynamics. *Medical & Biological Engineering & Computing*, 46(11):1097–1112, 2008. (Cited on pages 53, 56, 57, 62, 64, and 93.)
- [9] L. Antiga and D. A. Steinman. Robust and objective decomposition and mapping of bifurcating vessels. *IEEE Transactions on Medical Imaging*, 23(6):704–713, 2004. (Cited on page 93.)
- [10] S. Appanaboyina, F. Mut, R. Löhner, C. Putman, and J. Cebal. Simulation of intracranial aneurysm stenting: techniques and challenges. *Computer Methods in Applied Mechanics and Engineering*, 198(45):3567–3582, 2009. (Cited on pages 80, 81, and 82.)

- [11] A. Appel, F. J. Rohlf, and A. J. Stein. The haloed line effect for hidden line elimination. *SIGGRAPH Computer Graphics*, 13(2):151–157, Aug. 1979. (Cited on page [132](#).)
- [12] L. Augsburger, P. Reymond, E. Fonck, Z. Kulcsar, M. Farhat, M. Ohta, N. Stergiopoulos, and D. A. Rüfenacht. Methodologies to assess blood flow in cerebral aneurysms: current state of research and perspectives. *Journal of Neuro-radiology*, 36(5):270 – 277, 2009. (Cited on pages [53](#), [78](#), [81](#), and [192](#).)
- [13] R. Bade, J. Haase, and B. Preim. Comparison of fundamental mesh smoothing algorithms for medical surface models. In *Proceedings of Simulation und Visualisierung*, pages 289–304, 2006. (Cited on page [60](#).)
- [14] A. Baer, F. Adler, D. Lenz, and B. Preim. Perception-based evaluation of emphasis techniques used in 3D medical visualization. In *Vision, Modeling, and Visualization*, pages 295–304, 2009. (Cited on page [135](#).)
- [15] A. Baer, R. Gasteiger, D. W. Cunningham, and B. Preim. Perceptual evaluation of ghosted view techniques for the exploration of vascular structures and embedded flow. *Computer Graphics Forum*, 30(3):811–820, 2011. (Cited on pages [151](#), [152](#), [154](#), [156](#), and [158](#).)
- [16] A. Baer, C. Tietjen, R. Bade, and B. Preim. Hardware-accelerated stippling of surfaces derived from medical volume data. In *EG/IEEE EuroVis*, pages 235–242, 2007. (Cited on page [132](#).)
- [17] M. I. Baharoglu, C. M. Schirmer, D. A. Hoit, B.-L. Gao, and A. M. Malek. Aneurysm inflow-angle as a discriminant for rupture in sidewall cerebral aneurysms morphometric and computational fluid dynamic analysis. *Stroke*, 41(7):1423–1430, 2010. (Cited on pages [94](#), [161](#), and [163](#).)
- [18] A. Bair and D. House. Grid with a view: optimal texturing for perception of layered surface shape. *IEEE Transactions on Visualization and Computer Graphics*, 13(6):1656–1663, 2007. (Cited on page [134](#).)
- [19] R. Bammer, T. Hope, M. Aksoy, and M. Alley. Time-resolved 3D quantitative flow MRI of the major intracranial vessels: initial experience and comparative evaluation at 1.5 T and 3.0 T in combination with parallel imaging. *Magnetic Resonance in Medicine*, 57(1):127–140, 2007. (Cited on page [70](#).)
- [20] A. Barker, J. Bock, R. Lorenz, and M. Markl. 4D flow MR imaging. Technical report, Siemens Healthcare, 2010. (Cited on pages [43](#) and [91](#).)
- [21] D. Bartz, D. Cunningham, J. Fischer, and C. Wallraven. The role of perception for computer graphics. In *Eurographics State-of-the-Art Report 4*, pages 65–86, 2008. (Cited on page [134](#).)
- [22] D. Benyon, P. Turner, and S. Turner. *Designing interactive systems: people, activities, contexts, technologies*. Addison-Wesley Longman, 2005. (Cited on pages [214](#) and [218](#).)
- [23] P. Berg, D. Stucht, G. Janiga, O. Beuing, O. Speck, and D. Thévenin. Cerebral blood flow in a healthy circle of willis and two intracranial aneurysms:

- computational fluid dynamics versus 4D phase-contrast magnetic resonance imaging. *Journal of Biomechanical Engineering*, submitted, 2013. (Cited on page 76.)
- [24] E. A. Bier, M. C. Stone, K. Pier, W. Buxton, and T. D. DeRose. Toolglass and magic lenses: the see-through interface. In *ACM SIGGRAPH Computer Graphics and Interactive Techniques*, SIGGRAPH '93, pages 73–80, 1993. (Cited on pages 189 and 194.)
  - [25] J. Blaas, C. P. Botha, and F. H. Post. Interactive visualization of multi-field medical data using linked physical and feature-space views. In *EG/IEEE EuroVis*, pages 123–130, 2007. (Cited on page 188.)
  - [26] J. Bloomenthal. An implicit surface polygonizer. In *Graphics Gems IV*, pages 324–349. Academic Press, 1994. (Cited on page 58.)
  - [27] J. Bock, A. Frydrychowicz, A. Stalder, T. Bley, H. Burkhardt, J. Hennig, and M. Markl. 4D phase contrast MRI at 3 T: effect of standard and blood-pool contrast agents on SNR, PC-MRA, and blood flow visualization. *Magnetic Resonance in Medicine*, 63(2):330–338, 2009. (Cited on pages 50 and 51.)
  - [28] J. Bock, B. Kreher, J. Hennig, and M. Markl. Optimized pre-processing of time-resolved 2D and 3D phase contrast MRI data. In *Proceedings of the 15th Annual Meeting of ISMRM*, page 3138, 2007. (Cited on page 88.)
  - [29] H. Bogren, M. Buonocore, and R. Valente. Four-dimensional magnetic resonance velocity mapping of blood flow patterns in the aorta in patients with atherosclerotic coronary artery disease compared to age-matched normal subjects. *Journal of Magnetic Resonance Imaging*, 19(4):417–427, 2004. (Cited on page 68.)
  - [30] H. Bogunović, J. M. Pozo, M. C. Villa-Uriol, C. B. Majoie, R. van den Berg, H. A. G. van Andel, J. M. Macho, J. Blasco, L. San Román, and A. F. Frangi. Automated segmentation of cerebral vasculature with aneurysms in 3DRA and TOF-MRA using geodesic active regions: an evaluation study. *Medical Physics*, 38:210, 2011. (Cited on page 57.)
  - [31] R. Bordás, S. Seshadhri, G. Janiga, M. Skalej, and D. Thévenin. Experimental validation of numerical simulations on a cerebral aneurysm phantom model. *Interventional Medicine and Applied Science*, 4(4):193–205, 2012. (Cited on page 31.)
  - [32] S. Born, M. Markl, M. Gutberlet, and G. Scheuermann. Illustrative visualization of cardiac and aortic blood flow from 4D MRI data. In *IEEE Pacific Visualization*, 2013. (Cited on pages 114, 121, 122, and 165.)
  - [33] S. Born, M. Pfeifle, M. Markl, M. Gutberlet, and G. Scheuermann. Visual analysis of cardiac 4D MRI blood flow using line predicates. *IEEE Transactions on Visualization and Computer Graphics*, 19(6):900–912, 2013. (Cited on pages 111, 112, 121, 164, and 215.)

- [34] S. Born, M. Pfeifle, M. Markl, and G. Scheuermann. Visual 4D MRI blood flow analysis with line predicates. In *IEEE Pacific Visualization*, pages 105–112, 2012. (Cited on pages [111](#), [112](#), and [164](#).)
- [35] S. Born, A. Wiebel, J. Friedrich, G. Scheuermann, and D. Bartz. Illustrative stream surfaces. *IEEE Transactions on Visualization and Computer Graphics*, 16(6):1329–1338, 2010. (Cited on pages [105](#) and [132](#).)
- [36] M. Botsch and L. Kobbelt. A remeshing approach to multiresolution modeling. In *EG/ACM SIGGRAPH Symposium on Geometry processing*, SGP '04, pages 185–192, 2004. (Cited on page [63](#).)
- [37] M. Botsch and L. Kobbelt. Real-time shape editing using radial basis functions. *Computer Graphics Forum*, 24(3):611–621, 2005. (Cited on page [82](#).)
- [38] M. Botsch, L. Kobbelt, M. Pauly, P. Alliez, and B. Lévy. *Polygon mesh processing*. AK Peters Limited, 2010. (Cited on pages [62](#) and [63](#).)
- [39] M. Botsch and O. Sorkine. On linear variational surface deformation methods. *IEEE Transactions on Visualization and Computer Graphics*, 14(1):213–230, 2008. (Cited on page [62](#).)
- [40] N. Boukhelifa and D. J. Duke. Uncertainty visualization: why might it fail? In *Extended Abstracts on Human Factors in Computing Systems*, CHI EA '09, pages 4051–4056, 2009. (Cited on page [125](#).)
- [41] L. Boussel, V. Rayz, A. Martin, G. Acevedo-Bolton, M. T. Lawton, R. Higashida, W. S. Smith, W. L. Young, and D. Saloner. Phase-contrast magnetic resonance imaging measurements in intracranial aneurysms in vivo of flow patterns, velocity fields, and wall shear stress: Comparison with computational fluid dynamics. *Magnetic Resonance in Medicine*, 61(2):409–417, 2009. (Cited on page [75](#).)
- [42] L. Boussel, V. Rayz, C. McCulloch, A. Martin, G. Acevedo-Bolton, M. Lawton, R. Higashida, W. S. Smith, W. L. Young, and D. Saloner. Aneurysm growth occurs at region of low wall shear stress patient-specific correlation of hemodynamics and growth in a longitudinal study. *Stroke*, 39(11):2997–3002, 2008. (Cited on page [77](#).)
- [43] R. Brecheisen, B. Platel, B. M. ter Haar Romeny, and A. Vilanova. Illustrative uncertainty visualization of DTI fiber pathways. *The Visual Computer*, 29(4):297–309, 2013. (Cited on page [189](#).)
- [44] R. D. Brown, J. Huston, R. Hornung, T. Foroud, D. F. Kallmes, D. Kleindorfer, I. Meissner, D. Woo, L. Sauerbeck, and J. Broderick. Screening for brain aneurysm in the familial intracranial aneurysm study: frequency and predictors of lesion detection. *Neurosurgery: Pediatrics*, 108(6):1132–1138, 2008. (Cited on page [14](#).)
- [45] N. A. Buchmann, M. Yamamoto, M. Jermy, and T. David. Particle image velocimetry (PIV) and computational fluid dynamics (CFD) modelling of



- carotid artery haemodynamics under steady flow: a validation study. *Journal of Biomechanical Science and Engineering*, 5(4):421–436, 2010. (Cited on pages 73 and 74.)
- [46] M. J. Budoff. Computed tomography: overview. In M. J. Budoff and J. S. Shinbane, editors, *Cardiac CT Imaging*, pages 3–20. Springer London, 2010. (Cited on pages 21 and 22.)
- [47] K. Bürger, J. Schneider, P. Kondratieva, J. Krüger, and R. Westermann. Interactive visual exploration of unsteady 3d flows. In *EG/IEEE EuroVis*, pages 251–258, 2007. (Cited on page 100.)
- [48] R. Bürger and H. Hauser. Visualization of multi-Variateariate scientific data. In *EG/IEEE EuroVis*, pages 117–134, 2007. (Cited on page 188.)
- [49] M. Burns, M. Haidacher, W. Wein, I. Viola, and M. E. Gröller. Feature emphasis and contextual cutaways for multimodal medical visualization. In *EG/IEEE EuroVis*, pages 275–282, 2007. (Cited on page 133.)
- [50] S. Busking, C. P. Botha, and F. H. Post. Example-based interactive illustration of multi-field datasets. *Computers & Graphics*, 34(6):719–728, 2010. (Cited on page 188.)
- [51] J. Byrne, R. Beltechi, J. Yarnold, J. Birks, and M. Kamran. Early experience in the treatment of intracranial aneurysms by endovascular flow diversion: a multicentre prospective study. *PLoS One*, 5(9):e12492, 2010. (Cited on page 18.)
- [52] B. Cabral and L. C. Leedom. Imaging vector fields using line integral convolution. In *ACM SIGGRAPH Computer Graphics and Interactive Techniques*, SIGGRAPH '93, pages 263–270, 1993. (Cited on page 102.)
- [53] L. Cardamone and J. D. Humphrey. Arterial growth and remodelling is driven by hemodynamics. In *Modeling of Physiological Flows*, pages 187–203. Springer, 2012. (Cited on page 76.)
- [54] C. Carlhäll and A. Bolger. Passing strange flow in the failing ventricle. *Circulation: Heart Failure*, 3(2):326–331, 2010. (Cited on page 67.)
- [55] B. S. Carmo, Y. P. Ng, A. Prügel-Bennett, and G.-Z. Yang. A data clustering and streamline reduction method for 3D MR flow vector field simplification. In *Medical Image Computing and Computer-Assisted Intervention*, pages 451–458. Springer, 2004. (Cited on page 113.)
- [56] M. Cavazzuti, M. Atherton, M. Collins, and G. Barozzi. Beyond the virtual intracranial stenting challenge 2007: non-newtonian and flow pulsatility effects. *Journal of Biomechanics*, 43(13):2645–2647, 2010. (Cited on page 81.)
- [57] J. Cebal, S. Hendrickson, and C. Putman. Hemodynamics in a lethal basilar artery aneurysm just before its rupture. *American Journal of Neuroradiology*, 30(1):95–98, 2009. (Cited on page 79.)

- [58] J. Cebal, M. Hernandez, A. Frangi, C. Putman, R. Pergolizzi, and J. Burgess. Subject-specific modeling of intracranial aneurysms. In *Medical Imaging*, pages 319–327, 2004. (Cited on page 55.)
- [59] J. Cebal and H. Meng. Counterpoint: realizing the clinical utility of computational fluid dynamics—closing the gap. *American Journal of Neuroradiology*, 33(3):396–398, 2012. (Cited on page 42.)
- [60] J. Cebal, F. Mut, M. Raschi, E. Scrivano, R. Ceratto, P. Lylyk, and C. Putman. Aneurysm rupture following treatment with flow-diverting stents: computational hemodynamics analysis of treatment. *American Journal of Neuroradiology*, 32(1):27–33, 2011. (Cited on page 81.)
- [61] J. R. Cebal, M. A. Castro, S. Appanaboyina, C. M. Putmann, D. Millan, and A. F. Frangi. Efficient pipeline for image-based patient-specific analysis of cerebral aneurysm hemodynamics: technique and sensitivity. *IEEE Transaction on Medical Imaging*, 24(4):457–467, 2005. (Cited on pages 53 and 140.)
- [62] J. R. Cebal, M. A. Castro, J. E. Burgess, R. S. Pergolizzi, M. J. Sheridan, and C. M. Putman. Characterization of cerebral aneurysms for assessing risk of rupture by using patient-specific computational hemodynamics models. *American Journal of Neuroradiology*, 26(10):2550–2559, 2005. (Cited on pages 78 and 163.)
- [63] J. R. Cebal, F. Mut, J. Weir, and C. M. Putman. Association of hemodynamic characteristics and cerebral aneurysm rupture. *American Journal of Neuroradiology*, 32(2):264–270, 2011. (Cited on pages 35, 38, 44, 71, 78, 97, 161, 162, 163, 165, 174, 176, 190, and 192.)
- [64] J. R. Cebal, F. Mut, J. Weir, and C. M. Putman. Quantitative characterization of the hemodynamic environment in ruptured and unruptured brain aneurysms. *American Journal of Neuroradiology*, 32(1):145–151, 2011. (Cited on pages 13, 35, 36, 37, 79, 94, 161, 165, and 176.)
- [65] J. R. Cebal, R. Pergolizzi, and C. M. Putman. Computational fluid dynamics modeling of intracranial aneurysms: Qualitative comparison with cerebral angiography. *Academic Radiology*, 14(7):804–813, 2007. (Cited on page 166.)
- [66] J. R. Cebal, C. M. Putman, M. T. Alley, T. Hope, R. Bammer, and F. Calamante. Hemodynamics in normal cerebral arteries: qualitative comparison of 4D phase-contrast magnetic resonance and image-based computational fluid dynamics. *Journal of Engineering Mathematics*, 64(4):367–378, 2009. (Cited on pages 28 and 76.)
- [67] J. R. Cebal, M. Sheridan, and C. M. Putman. Hemodynamics and bleb formation in intracranial aneurysms. *American Journal of Neuroradiology*, 31(2):304–310, 2010. (Cited on pages 79, 135, 189, and 204.)
- [68] E. Cecchi, C. Giglioli, S. Valente, C. Lazzeri, G. F. Gensini, R. Abbate, and L. Mannini. Role of hemodynamic shear stress in cardiovascular disease. *Atherosclerosis*, 214(2):249–256, 2011. (Cited on page 77.)

- [69] P. Chai and R. Mohiaddin. How we perform cardiovascular magnetic resonance flow assessment using phase-contrast velocity mapping. *Journal of Cardiovascular Magnetic Resonance*, 7(4):705–716, 2005. (Cited on pages 45 and 46.)
- [70] M.-Y. Chan, Y. Wu, W.-H. Mak, W. Chen, and H. Qu. Perception-based transparency optimization for direct volume rendering. *IEEE Transactions on Visualization and Computer Graphics*, 15(6):1283–1290, 2009. (Cited on page 135.)
- [71] I. Chatziprodromou, V. D. Butty, V. B. Makhijani, D. Poulikakos, and Y. Ventikos. Pulsatile blood flow in anatomically accurate vessels with multiple aneurysms: a medical intervention planning application of computational hemodynamics. *Flow, Turbulence and Combustion*, 71(1):333–346, 2003. (Cited on page 162.)
- [72] Y. S. Chatzizisis, A. U. Coskun, M. Jonas, E. R. Edelman, C. L. Feldman, and P. H. Stone. Role of endothelial shear stress in the natural history of coronary atherosclerosis and vascular remodeling: molecular, cellular, and vascular behavior. *Journal of the American College of Cardiology*, 49(25):2379–2393, 2007. (Cited on pages 77 and 192.)
- [73] C.-h. Chen, W. Härdle, and A. Unwin. *Handbook of data visualization*. Springer, 2008. (Cited on page 187.)
- [74] C. Cheng, D. Tempel, R. van Haperen, A. van der Baan, F. Grosveld, M. Daemen, R. Krams, and R. de Crom. Atherosclerotic lesion size and vulnerability are determined by patterns of fluid shear stress. *Circulation*, 113(23):2744–2753, 2006. (Cited on page 69.)
- [75] A. Chien, S. Tateshima, M. Castro, J. Sayre, J. Cebal, and F. Viñuela. Patient-specific flow analysis of brain aneurysms at a single location: comparison of hemodynamic characteristics in small aneurysms. *Medical and Biological Engineering and Computing*, 46(11):1113–1120, 2008. (Cited on pages 38 and 97.)
- [76] P. Cignoni, R. Scopigno, and M. Tarini. A simple normal enhancement technique for interactive non-photorealistic renderings. *Computers & Graphics*, 29(1):125–133, 2005. (Cited on page 131.)
- [77] A. Cockburn, A. Karlson, and B. B. Bederson. A review of overview+detail, zooming, and focus+context interfaces. *ACM Computing Surveys*, 41(1):2:1–2:31, 2008. (Cited on pages 187 and 189.)
- [78] F. Cole, K. Sanik, D. DeCarlo, and et al. How well do line drawings depict shape? *ACM Transactions on Graphics*, 28(3):1–9, 2009. (Cited on pages 134 and 139.)
- [79] C. Conti, D. Rossinelli, and P. Koumoutsakos. GPU and APU computations of finite time lyapunov exponent fields. *Journal of Computational Physics*, 231(5):2229–2244, 2012. (Cited on page 121.)
- [80] J. Cordes, K. Hintz, J. Franke, C. Bochwitz, and B. Preim. Conceptual design and prototyping implementation of a case-based training system for spine

- surgery. In S. Hambach, A. Martens, and B. Urban, editors, *1st International e-Learning Baltics Science Conference*, pages 169–178, 2008. (Cited on page 213.)
- [81] A. Dardik, L. Chen, J. Frattini, H. Asada, F. Aziz, F. A. Kudo, and B. E. Sumpio. Differential effects of orbital and laminar shear stress on endothelial cells. *Journal of Vascular Surgery*, 41(5):869–880, 2005. (Cited on pages 42, 76, and 77.)
- [82] W. C. de Leeuw. *Presentation and Exploration of Flow Data*. PhD thesis, Delft University of Technology, 1997. (Cited on page 105.)
- [83] C. Deaton, E. S. Froelicher, L. H. Wu, C. Ho, K. Shishani, and T. Jaarsma. The global burden of cardiovascular disease. *European Journal of Cardiovascular Nursing*, 10(2 suppl):S5–S13, 2011. (Cited on page 3.)
- [84] D. DeCarlo, A. Finkelstein, S. Rusinkiewicz, and A. Santella. Suggestive contours for conveying shape. *ACM Transactions on Graphics*, 22(3):848–855, 2003. (Cited on pages 132, 139, and 159.)
- [85] H. Delingette and J. Montagnat. Shape and topology constraints on parametric active contours. *Computer Vision and Image Understanding*, 83(2):140–171, 2001. (Cited on page 56.)
- [86] J. Dequidt, C. Duriez, S. Cotin, and E. Kerrien. Towards interactive planning of coil embolization in brain aneurysms. *Medical Image Computing and Computer-Assisted Intervention*, pages 377–385, 2009. (Cited on page 80.)
- [87] T. Dey and W. Zhao. Approximate medial axis as a voronoi subcomplex. *Computer-Aided Design*, 36(2):195–202, 2004. (Cited on page 61.)
- [88] S. Dhar, M. Tremmel, J. Mocco, M. Kim, J. Yamamoto, A. Siddiqui, L. Hopkins, and H. Meng. Morphology parameters for intracranial aneurysm rupture risk assessment. *Neurosurgery*, 63(2):185–197, 2008. (Cited on page 13.)
- [89] C. Díaz and L. Altamirano Robles. Fast noncontinuous path phase-unwrapping algorithm based on gradients and mask. *Progress in Pattern Recognition, Image Analysis and Applications*, pages 116–123, 2004. (Cited on page 49.)
- [90] J. Diepstraten, D. Weiskopf, and T. Ertl. Transparency in interactive technical illustrations. *Computer Graphics Forum*, 21(3):317–325, 2002. (Cited on pages 133 and 137.)
- [91] J. Diepstraten, D. Weiskopf, and T. Ertl. Interactive cutaway illustrations. *Computer Graphics Forum*, 22(3):523–532, 2003. (Cited on page 133.)
- [92] H. Doleisch and H. Hauser. Smooth brushing for focus+ context visualization of simulation data in 3D. In *WSCG*, pages 147–154, 2002. (Cited on page 126.)
- [93] H. Doleisch and H. Hauser. Interactive visual exploration and analysis of multivariate simulation data. *Computing in Science Engineering*, 14(2):70–77, 2012. (Cited on page 126.)

- [94] M. Domin, S. Langner, N. Hosten, and L. Linsen. Direct glyph-based visualization of diffusion MR data using deformed spheres. In *Visualization in Medicine and Life Sciences, Mathematics and Visualization*, pages 185–204. 2008. (Cited on page 187.)
- [95] D. Dooley and M. F. Cohen. Automatic illustration of 3d geometric models: Surfaces. In *IEEE Visualization, Visualization'90*, pages 307–314, 1990. (Cited on page 132.)
- [96] J. B. Drexler, A. Hennemuth, S. Meier, R. Lorenz, J. Bock, A. Harloff, M. Markl, H. K. Hahn, et al. A tool for the interactive analysis and exploration of in-vivo haemodynamics from 4D PC MRI. *Journal of Cardiovascular Magnetic Resonance*, 14(Suppl 1):W70, 2012. (Cited on pages 91 and 94.)
- [97] P. Dyverfeldt, R. Gårdhagen, A. Sigfridsson, M. Karlsson, and T. Ebbers. On MRI turbulence quantification. *Journal of Magnetic Resonance Imaging*, 27(7):913–922, 2009. (Cited on page 94.)
- [98] T. Ebbers, L. Wigström, A. Bolger, J. Engvall, and M. Karlsson. Estimation of relative cardiovascular pressures using time-resolved three-dimensional phase contrast MRI. *Magnetic Resonance in Medicine*, 45(5):872–879, 2001. (Cited on page 94.)
- [99] J. Eriksson, C. Carlhall, P. Dyverfeldt, J. Engvall, A. Bolger, and T. Ebbers. Semi-automatic quantification of 4D left ventricular blood flow. *Journal of Cardiovascular Magnetic Resonance*, 12(9), 2010. (Cited on pages 46, 47, and 67.)
- [100] European Heart Network. European cardiovascular disease statistics, 2012. (last visited: 14 September 2013). (Cited on page 9.)
- [101] M. Everts, H. Bekker, J. B. Roerdink, T. Isenberg, et al. Illustrative line styles for flow visualization. In *Pacific Graphics*, pages 105–110, 2011. Short paper. (Cited on page 105.)
- [102] M. H. Everts, H. Bekker, J. B. Roerdink, and T. Isenberg. Depth-dependent halos: Illustrative rendering of dense line data. *IEEE Transactions on Visualization and Computer Graphics*, 15(6):1299–1306, 2009. (Cited on pages 140, 171, and 196.)
- [103] A. Fedorov and N. Chrisochoides. Tetrahedral mesh generation for non-rigid registration of brain MRI: analysis of the requirements and evaluation of solutions. In R. Garimella, editor, *Proceedings of the 17th International Meshing Roundtable*, pages 55–72. Springer, 2008. (Cited on page 87.)
- [104] A. Field. *Discovering statistics using SPSS*. Sage, 3rd edition, 2009. (Cited on pages 45 and 152.)
- [105] J. Fischer, D. Bartz, and W. Straßer. Illustrative display of hidden iso-surface structures. In *IEEE Visualization*, pages 663–670, 2005. (Cited on page 132.)

- [106] M. D. Ford, H. N. Nikolov, J. S. Milner, S. P. Lownie, E. M. DeMont, W. Kalata, F. Loth, D. W. Holdsworth, and D. A. Steinman. PIV-measured versus CFD-predicted flow dynamics in anatomically realistic cerebral aneurysm models. *Journal of Biomechanical Engineering*, 130(2):021015–021015–9, 2008. (Cited on page 73.)
- [107] M. D. Ford, G. R. Stuhne, H. N. Nikolov, D. F. Habets, S. P. Lownie, D. W. Holdsworth, and D. A. Steinman. Virtual angiography for visualization and validation of computational models of aneurysm hemodynamics. *IEEE Transactions on Medical Imaging*, 24(12):1586–1592, 2005. (Cited on page 73.)
- [108] T. R. Forget Jr, R. Benitez, E. Veznedaroglu, A. Sharan, W. Mitchell, M. Silva, and R. H. Rosenwasser. A review of size and location of ruptured intracranial aneurysms. *Neurosurgery*, 49(6):1322–1326, 2001. (Cited on page 78.)
- [109] A. Forsberg, J. Chen, and D. Laidlaw. Comparing 3D vector field visualization methods: a user study. *IEEE Transactions on Visualization and Computer Graphics*, 15(6):1219–1226, 2009. (Cited on page 221.)
- [110] M. Forsting and I. Wanke. *Intracranial vascular malformations and aneurysms: from diagnostic work-up to endovascular therapy*. Springer, 2008. (Cited on page 31.)
- [111] C. François, S. Srinivasan, M. Schiebler, S. Reeder, E. Niespodzany, B. Landgraf, O. Wieben, A. Frydrychowicz, et al. 4D cardiovascular magnetic resonance velocity mapping of alterations of right heart flow patterns and main pulmonary artery hemodynamics in tetralogy of fallot. *Journal of Cardiovascular Magnetic Resonance*, 14(1):16, 2012. (Cited on pages 28, 67, and 69.)
- [112] A. Frangi, A. Amini, and E. Bullitt. Vascular imaging. *IEEE Transactions on Medical Imaging*, 24(4):433 – 435, 2005. (Cited on page 19.)
- [113] A. Frangi, W. Niessen, K. Vincken, and M. Viergever. Multiscale vessel enhancement filtering. In W. Wells, A. Colchester, and S. Delp, editors, *Medical Image Computing and Computer-Assisted Intervention*, Lecture Notes in Computer Science, pages 130–137. Springer, 1998. (Cited on page 58.)
- [114] B. Freudenberg, M. Masuch, and T. Strothotte. Real-time halftoning: a primitive for non-photorealistic shading. In *EG Workshop on Rendering*, pages 227–232, 2002. (Cited on page 170.)
- [115] O. Friman, A. Hennemuth, A. Harloff, J. Bock, M. Markl, and H.-O. Peitgen. Probabilistic 4D blood flow tracking and uncertainty estimation. *Medical Image Analysis*, 15(5):720–728, 2011. (Cited on page 219.)
- [116] J. Frösen, R. Tulamo, A. Paetau, E. Laaksamo, M. Korja, A. Laakso, M. Niemelä, and J. Hernesniemi. Saccular intracranial aneurysm: pathology and mechanisms. *Acta Neuropathologica*, 123(6):773–786, 2012. (Cited on page 14.)
- [117] A. Frydrychowicz, M. Markl, D. Hirtler, A. Harloff, C. Schlensak, J. Geiger, B. Stiller, and R. Arnold. Aortic hemodynamics in patients with and without



- repair of aortic coarctation: in vivo analysis by 4D flow-sensitive magnetic resonance imaging. *Investigative Radiology*, 46(5):317–325, 2011. (Cited on page 68.)
- [118] A. Frydrychowicz, A. Stalder, M. Russe, J. Bock, S. Bauer, A. Harloff, A. Berger, M. Langer, J. Hennig, and M. Markl. Three-dimensional analysis of segmental wall shear stress in the aorta by flow-sensitive four-dimensional-MRI. *Journal of Magnetic Resonance Imaging*, 30(1):77–84, 2009. (Cited on page 67.)
- [119] A. Frydrychowicz, J. Winterer, M. Zaitsev, B. Jung, J. Hennig, M. Langer, and M. Markl. Visualization of iliac and proximal femoral artery hemodynamics using time-resolved 3D phase contrast MRI at 3 T. *Journal of Magnetic Resonance Imaging*, 25(5):1085–1092, 2007. (Cited on pages 71 and 72.)
- [120] G. W. Furnas. A fisheye follow-up: further reflections on focus+ context. In *Human Factors in Computing Systems*, SIGCHI, pages 999–1008, 2006. (Cited on page 188.)
- [121] G. P. Galdi, R. Rannacher, A. M. Robertson, and S. Turek. *Hemodynamical flows: modeling, analysis and simulation*. Birkhäuser, 2008. (Cited on page 64.)
- [122] M. Garbey and M. G. Davies. Remarks on solution verification and model validation of hemodynamic simulations. *Pumps and Pipes*, pages 45–54, 2011. (Cited on pages 94 and 95.)
- [123] H. Garcke, T. Preußer, M. Rumpf, A. C. Telea, U. Weikard, and J. J. V. Wijk. A phase field model for continuous clustering on vector fields. *IEEE Transactions on Visualization and Computer Graphics*, 7(3):230–241, 2001. (Cited on pages 107 and 164.)
- [124] R. Gasteiger, G. Janiga, D. Stucht, A. Hennemuth, O. Friman, O. Speck, M. Markl, and B. Preim. Vergleich zwischen 7 Tesla 4D PC-MRI Flussmessung und CFD-Simulation. In *Bildverarbeitung für die Medizin*, pages 304–308, 2011. (Cited on page 74.)
- [125] R. Gasteiger, D. J. Lehmann, R. van Pelt, G. Janiga, O. Beuing, A. Vilanova, H. Theisel, and B. Preim. Automatic detection and visualization of qualitative hemodynamic characteristics in cerebral aneurysms. *IEEE Transactions on Visualization and Computer Graphics*, 18(12):2178–2187, 2012. (Cited on pages 166, 167, 169, 171, 172, 173, 174, 175, 177, and 206.)
- [126] R. Gasteiger, M. Neugebauer, O. Beuing, and B. Preim. The FlowLens: a focus-and-context visualization approach for exploration of blood flow in cerebral aneurysms. *IEEE Transactions on Visualization and Computer Graphics*, 17(12):2183–2192, 2011. (Cited on pages 195, 197, 198, 199, 201, and 206.)
- [127] R. Gasteiger, M. Neugebauer, C. Kubisch, and B. Preim. Adapted surface visualization of cerebral aneurysms with embedded blood flow information. In *EG Workshop on Visual Computing for Biology and Medicine*, pages 25–32, 2010. (Cited on pages 129, 148, 170, 196, and 200.)

- [128] R. Gasteiger, C. Tietjen, A. Baer, and B. Preim. Curvature- and model-based surface hatching of anatomical structures derived from clinical volume datasets. In *SmartGraphics*, pages 255–262, 2008. (Cited on page 132.)
- [129] J. Geiger, M. Markl, L. Herzer, D. Hirtler, F. Loeffelbein, B. Stiller, M. Langer, and R. Arnold. Aortic flow patterns in patients with marfan syndrome assessed by flow-sensitive four-dimensional MRI. *Journal of Magnetic Resonance Imaging*, 35(3):594–600, 2012. (Cited on page 192.)
- [130] V. Gibbs, D. Cole, and A. Sassano. *Ultrasound physics and technology: how, why, and when*. Elsevier Health Sciences, 2009. (Cited on pages 25 and 30.)
- [131] S. Glasser, S. Oeltze, A. Hennemuth, C. Kubisch, A. Mahnken, S. Wilhelmsen, and B. Preim. Automatic transfer function specification for visual emphasis of coronary artery plaque. *Computer Graphics Forum*, 29(1):191–201, 2010. (Cited on page 133.)
- [132] A. S. Go, D. Mozaffarian, V. L. Roger, E. J. Benjamin, J. D. Berry, M. B. Turner, and et al. Heart disease and stroke statistics - 2013 update a report from the american heart association. *Circulation*, 127(1):e6–e245, 2013. (Cited on page 9.)
- [133] A. Gooch, B. Gooch, P. Shirley, and E. Cohen. A non-photorealistic lighting model for automatic technical illustration. In *Computer Graphics and Interactive Techniques*, pages 447–452, 1998. (Cited on pages 131 and 133.)
- [134] L. Goubergrits, J. Schaller, U. Kertzscher, N. Van Den Bruck, K. Poethkow, C. Petz, H.-C. Hege, and A. Spuler. Statistical wall shear stress maps of ruptured and unruptured middle cerebral artery aneurysms. *Journal of The Royal Society Interface*, 9(69):677–688, 2012. (Cited on page 117.)
- [135] N. Green, S. Chen, J. Messenger, B. Groves, and J. Carroll. Three-dimensional vascular angiography. *Current Problems in Cardiology*, 29(3):104–142, 2004. (Cited on pages 12, 19, 20, and 21.)
- [136] D. L. Gresh, B. E. Rogowitz, R. Winslow, D. Scollan, and C. Yung. Weave: A system for visually linking 3-D and statistical visualizations, applied to cardiac simulation and measurement data. In *IEEE Visualization*, pages 489–492, 2000. (Cited on pages 126 and 188.)
- [137] S. Grewenig, J. Weickert, and A. Bruhn. From box filtering to fast explicit diffusion. In *Pattern Recognition*, pages 533–542. Springer, 2010. (Cited on page 57.)
- [138] H. Griethe and H. Schumann. The visualization of uncertain data: methods and problems. In *Simulation and Visualization*, pages 143–156, 2006. (Cited on page 125.)
- [139] S. Grimm, S. Bruckner, A. Kanitsar, and E. Gröller. Flexible direct multi-volume rendering in dynamic scenes. In *Vision, Modeling, and Visualization*, pages 505–512, 2004. (Cited on page 183.)

- [140] G. Guglielmi, F. Viñuela, J. Dion, and G. Duckwiler. Electrothrombosis of saccular aneurysms via endovascular approach. *Journal of Neurosurgery*, 75(1):8–14, 1991. (Cited on page 17.)
- [141] T. Günther, K. Bürger, R. Westermann, and H. Theisel. A view-dependent and inter-frame coherent visualization of integral lines using screen contribution. In *Vision, Modeling, and Visualization*, pages 215–222, 2011. (Cited on page 124.)
- [142] H. Hahn and H. Peitgen. IWT-interactive watershed transform: a hierarchical method for efficient interactive and automated segmentation of multidimensional gray-scale images. In *SPIE Medical Imaging*, pages 643–653, 2003. (Cited on page 52.)
- [143] G. Haller. Lagrangian coherent structures from approximate velocity data. *Physics of Fluids*, 14(6):1851–1861, 2002. (Cited on page 113.)
- [144] A. Harloff, F. Albrecht, J. Spreer, A. Stalder, J. Bock, A. Frydrychowicz, J. Schöllhorn, A. Hetzel, M. Schumacher, J. Hennig, et al. 3D blood flow characteristics in the carotid artery bifurcation assessed by flow-sensitive 4D MRI at 3T. *Magnetic Resonance in Medicine*, 61(1):65–74, 2009. (Cited on pages 69 and 70.)
- [145] A. Harloff, J. Simon, S. Brendecke, D. Assefa, T. Helbing, A. Frydrychowicz, J. Weber, M. Olschewski, C. Strecker, J. Hennig, et al. Complex plaques in the proximal descending aorta an underestimated embolic source of stroke. *Stroke*, 41(6):1145–1150, 2010. (Cited on page 68.)
- [146] R. H. Hashemi, W. G. Bradley, and C. J. Lisanti. *MRI: the basics*. Wolters Kluwer Health, 2012. (Cited on page 22.)
- [147] M. Hassouna and A. Farag. Robust centerline extraction framework using level sets. In *IEEE Computer Vision and Pattern Recognition*, pages 458–465, 2005. (Cited on page 61.)
- [148] H. Hauser, R. S. Laramée, and H. Doleisch. State-of-the-art report in flow visualization. Technical report, VRVis Research Center, 2002. (Cited on page 102.)
- [149] E. Heiberg, T. Ebbers, L. Wigström, and M. Karlsson. Three-dimensional flow characterization using vector pattern matching. *IEEE Transactions on Visualization and Computer Graphics*, 9(3):313–319, 2003. (Cited on page 164.)
- [150] F. Helderma, G. Mauritz, K. Andringa, A. Vonk-Noordegraaf, and J. Marcus. Early onset of retrograde flow in the main pulmonary artery is a characteristic of pulmonary arterial hypertension. *Journal of Magnetic Resonance Imaging*, 33(6):1362–1368, 2011. (Cited on page 69.)
- [151] A. Hennemuth. *Computer-assisted diagnosis and therapy planning in coronary artery disease based on cardiac CT and MRI*. PhD thesis, University Bremen, 2012. (Cited on page 213.)

- [152] A. Hennemuth, O. Friman, C. Schumann, J. Bock, J. Drexl, M. Markl, and H.-O. Peitgen. Fast interactive exploration of 4D MRI flow data. In *SPIE Medical Imaging*, pages 79640E–1–79640E–11, 2011. (Cited on pages 29, 50, 52, 91, 120, and 123.)
- [153] M. Hlawatsch, P. Leube, W. Nowak, and D. Weiskopf. Flow radar glyphs—static visualization of unsteady flow with uncertainty. *IEEE Transactions on Visualization and Computer Graphics*, 17(12):1949–1958, 2011. (Cited on page 125.)
- [154] Y. Hoi, S. H. Woodward, M. Kim, D. B. Taulbee, and H. Meng. Validation of CFD simulations of cerebral aneurysms with implication of geometric variations. *Journal of Biomechanical Engineering*, 128(6):844–851, 2006. (Cited on page 59.)
- [155] Q. Hong, Q. Li, and J. Tian. Implicit reconstruction of vasculatures using bivariate piecewise algebraic splines. *IEEE Transactions on Medical Imaging*, 31(3):543–553, 2012. (Cited on page 95.)
- [156] M. Hope, T. Hope, A. Meadows, K. Ordovas, T. Urbania, M. Alley, and C. Higgins. Bicuspid aortic valve: four-dimensional MR evaluation of ascending aortic systolic flow patterns. *Radiology*, 255(1):53–61, 2010. (Cited on pages 67 and 204.)
- [157] M. Hope, A. Meadows, T. Hope, K. Ordovas, D. Saloner, G. Reddy, M. Alley, and C. Higgins. Clinical evaluation of aortic coarctation with 4D flow MR imaging. *Journal of Magnetic Resonance Imaging*, 31(3):711–718, 2010. (Cited on pages 68 and 69.)
- [158] M. Hope, J. Wrenn, M. Sigovan, E. Foster, E. Tseng, and D. Saloner. Imaging biomarkers of aortic disease: increased growth rates with eccentric systolic flow. *Journal of the American College of Cardiology*, 60(4):356–357, 2012. (Cited on pages 35 and 67.)
- [159] T. Hope, M. Hope, D. Purcell, C. von Morze, D. Vigneron, M. Alley, and W. Dillon. Evaluation of intracranial stenoses and aneurysms with accelerated 4D flow. *Journal of Magnetic Resonance Imaging*, 28(1):41–46, 2010. (Cited on page 71.)
- [160] D. House, A. Bair, and C. Ware. On the optimization of visualizations of complex phenomena. In *IEEE Visualization*, pages 87–94, 2005. (Cited on page 133.)
- [161] M. Hummel, C. Garth, B. Hamann, H. Hagen, and K. I. Joy. Iris: Illustrative rendering for integral surfaces. *IEEE Transactions on Visualization and Computer Graphics*, 16(6):1319–1328, 2010. (Cited on pages 104, 105, 132, 160, and 170.)
- [162] E. Insko and J. Carpenter. Magnetic resonance angiography. *Seminars in Vascular Surgery*, 17(2):83–101, 2004. (Cited on page 24.)

- [163] V. Interrante, H. Fuchs, and S. M. Pizer. Conveying the 3D shape of smoothly curving transparent surfaces via texture. *IEEE Transactions on Visualization and Computer Graphics*, 3(2):98–117, 1997. (Cited on pages [131](#) and [133](#).)
- [164] V. Interrante, S. Kim, and H. Hagh-Shenas. Conveying 3D shape with texture: recent advances and experimental findings. In *SPIE Electronic Imaging*, pages 197–206, 2002. (Cited on page [132](#).)
- [165] T. Isenberg, B. Freudenberg, N. Halper, S. Schlechtweg, and T. Strothotte. A developer’s guide to silhouette algorithms for polygonal models. *IEEE Computer Graphics and Applications*, 23(4):28–37, 2003. (Cited on pages [132](#) and [139](#).)
- [166] T. Ishibashi, Y. Murayama, M. Urashima, T. Saguchi, M. Ebara, H. Arakawa, K. Irie, H. Takao, and T. Abe. Unruptured intracranial aneurysms: incidence of rupture and risk factors. *Stroke*, 40(1):313–316, 2009. (Cited on page [13](#).)
- [167] H. Isoda, Y. Ohkura, T. Kosugi, M. Hirano, M. Alley, R. Bammer, N. Pelc, H. Namba, and H. Sakahara. Comparison of hemodynamics of intracranial aneurysms between MR fluid dynamics using 3D cine phase-contrast MRI and MR-based computational fluid dynamics. *Neuroradiology*, 52(10):913–920, 2010. (Cited on page [76](#).)
- [168] G. Janiga, O. Beuing, S. Seshadhri, M. Neugebauer, R. Gasteiger, B. Preim, G. Rose, M. Skalej, and D. Thévenin. Virtual stenting using real patient data. In *Modelling Fluid Flow*, Fluid Flow Technologies, pages 978–963, 2009. (Cited on page [82](#).)
- [169] G. Janiga, C. Rössl, M. Skalej, and D. Thévenin. Realistic virtual intracranial stenting and computational fluid dynamics for treatment analysis. *Journal of Biomechanics*, 46(1):7 – 12, 2013. (Cited on pages [64](#) and [82](#).)
- [170] J. Jeong and F. Hussain. On the identification of a vortex. *Journal of Fluid Mechanics*, 285(69):69–94, 1995. (Cited on pages [112](#) and [164](#).)
- [171] J. Jiang and C. Strother. Interactive decomposition and mapping of sacular cerebral aneurysms using harmonic functions: its first application with patient-specific computational fluid dynamics (CFD) simulations. *IEEE Transactions on Medical Imaging*, 32(2):153–164, 2013. (Cited on pages [62](#) and [158](#).)
- [172] B. Jobard and W. Lefer. Creating evenly-spaced streamlines of arbitrary density. In *Visualization in Scientific Computing*, volume 97, pages 43–55, 1997. (Cited on pages [104](#) and [124](#).)
- [173] B. Jobard, N. Ray, and D. Sokolov. Visualizing 2D flows with animated arrow plots. *CoRR*, abs/1205.5204:1–12, 2012. (Cited on page [102](#).)
- [174] T. Judd, F. Durand, and E. H. Adelson. Apparent ridges for line drawing. *ACM Transactions on Graphics*, 26(3):19–26, 2007. (Cited on page [132](#).)
- [175] S. Juvela. Prevalence of and risk factors for intracranial aneurysms. *The Lancet Neurology*, 10(7):595–597, 2011. (Cited on page [12](#).)

- [176] W. A. Kalender. *Computed tomography: fundamentals, system technology, image quality, applications*. Publicis, 3rd edition, 2011. (Cited on page 21.)
- [177] D. Kalkofen, E. Mendez, and D. Schmalstieg. Interactive focus and context visualization for augmented reality. In *IEEE and ACM International Symposium on Mixed and Augmented Reality*, pages 1–10, 2007. (Cited on page 189.)
- [178] D. Kallmes. Point: CFD - computational fluid dynamics or confounding factor dissemination. *American Journal of Neuroradiology*, 33(3):395–396, 2012. (Cited on page 42.)
- [179] M. Kaplan. Hybrid quantitative invisibility. In *ACM Non-Photorealistic Animation and Rendering*, pages 51–52, 2007. (Cited on page 132.)
- [180] C. Karmonik, J. Bismuth, M. Davies, and A. Lumsden. Computational fluid dynamics as a tool for visualizing hemodynamic flow patterns. *Methodist DeBakey Cardiovascular Journal*, 5(3):26–33, 2009. (Cited on pages 42, 44, 45, and 72.)
- [181] P. Kilner, G. Yang, A. Wilkes, R. Mohiaddin, D. Firmin, and M. Yacoub. Asymmetric redirection of flow through the heart. *Nature*, 404(6779):759–761, 2000. (Cited on page 67.)
- [182] M. Kim, D. B. Taulbee, M. Tremmel, and H. Meng. Comparison of two stents in modifying cerebral aneurysm hemodynamics. *Annals of Biomedical Engineering*, 36(5):726–741, 2008. (Cited on page 81.)
- [183] S. Kim, H. Hagh-Shenas, and V. Interrante. Conveying shape with texture: experimental investigations of texture’s effects on shape categorization judgments. *IEEE Transactions on Visualization and Computer Graphics*, 10(4):471–483, 2004. (Cited on pages 132 and 134.)
- [184] G. Kindlmann. Superquadric tensor glyphs. In *EG/IEEE Symposium on Visualization*, pages 147–154, 2004. (Cited on page 187.)
- [185] G. Kindlmann and C.-F. Westin. Diffusion tensor visualization with glyph packing. *IEEE Transactions on Visualization and Computer Graphics*, 12(5):1329–1336, 2006. (Cited on page 188.)
- [186] G. Kindlmann, R. Whitaker, T. Tasdizen, and T. Moller. Curvature-based transfer functions for direct volume rendering: methods and applications. In *IEEE Visualization*, pages 513–520, 2003. (Cited on page 131.)
- [187] R. M. Kirby, H. Marmanis, and D. H. Laidlaw. Visualizing multivalued data from 2D incompressible flows using concepts from painting. In *IEEE Visualization*, pages 333–540, 1999. (Cited on page 102.)
- [188] C. Kleinstreuer. *Biofluid dynamics: principles and selected applications*. CRC, 2006. (Cited on pages 36, 38, 64, and 65.)
- [189] J. J. Koendrink, A. J. van Doorn, and A. M. L. Kappers. Surface perception in pictures. *Perception & Psychophysics*, 52(5):487–496, 1992. (Cited on pages 134 and 153.)



- [190] B. Köhler, R. Gasteiger, U. Preim, H. Theisel, M. Gutberlet, and B. Preim. Semi-automatic vortex extraction in 4D PC-MRI cardiac blood flow data using line predicates. *IEEE Transactions on Visualization and Computer Graphics*, 2013. to appear. (Cited on pages 197, 198, 206, and 215.)
- [191] B. Köhler, M. Neugebauer, R. Gasteiger, G. Janiga, O. Speck, and B. Preim. Surface-based seeding for blood flow exploration. In *Bildverarbeitung für die Medizin*, pages 81–86, 2012. (Cited on pages 118 and 217.)
- [192] R. Kosara, H. Hauser, and D. L. Gresh. An interaction view on information visualization. In *EG State-of-the-Art Report*, pages 123–137, 2003. (Cited on page 188.)
- [193] R. Kosara, S. Miksch, H. Hauser, J. Schrammel, V. Giller, and M. Tschechli. Useful properties of semantic depth of field for better f+c visualization. In *EG/IEEE Symposium on Visualization*, pages 205–210, 2002. (Cited on page 189.)
- [194] H. Krishnan, J. Guhring, C. Garth, A. Greiser, M. A. Gulsun, and K. I. Joy. Analysis of time-dependent flow-sensitive PC-MRI data. *IEEE Transactions on Visualization and Computer Graphics*, 18(6):966–977, 2012. (Cited on pages 113, 114, 120, 121, 122, 140, and 164.)
- [195] J. Krüger, J. Schneider, and R. Westermann. Clearview: an interactive context preserving hotspot visualization technique. *IEEE Transactions on Visualization and Computer Graphics*, 12(5):941–948, 2006. (Cited on page 189.)
- [196] J. P. Ku, C. J. Elkins, and C. A. Taylor. Comparison of CFD and MRI flow and velocities in an in vitro large artery bypass graft model. *Annals of Biomedical Engineering*, 33(3):257–269, 2005. (Cited on pages 73 and 74.)
- [197] A. Kuhn, D. J. Lehmann, R. Gaststeiger, M. Neugebauer, B. Preim, and H. Theisel. A clustering-based visualization technique to emphasize meaningful regions of vector fields. In *Vision, Modeling, and Visualization*, pages 191–198, 2011. (Cited on pages 107, 108, 120, and 164.)
- [198] A. Kuß, M. Gensel, B. Meyer, V. J. Dercksen, and S. Prohaska. Effective techniques to visualize filament-surface relationships. *Computer Graphics Forum*, 29(3):1003–1012, 2010. (Cited on pages 134 and 221.)
- [199] D. H. Laidlaw, R. M. Kirby, C. D. Jackson, J. S. Davidson, T. S. Miller, M. da Silva, W. H. Warren, and M. J. Tarr. Comparing 2D vector field visualization methods: a user study. *IEEE Transactions on Visualization and Computer Graphics*, 11(1):59–70, 2005. (Cited on pages 125, 160, 209, and 221.)
- [200] R. Lall, C. Eddleman, B. Bendok, and H. Batjer. Unruptured intracranial aneurysms and the assessment of rupture risk based on anatomical and morphological factors: sifting through the sands of data. *Neurosurgical Focus*, 26(5):E2, 2009. (Cited on page 14.)
- [201] J. Lankhaar, M. Hofman, J. Marcus, J. Zwanenburg, T. Faes, and A. Vonk-Noordegraaf. Correction of phase offset errors in main pulmonary artery

- flow quantification. *Journal of Magnetic Resonance Imaging*, 22(1):73–79, 2005. (Cited on pages 29, 48, and 49.)
- [202] R. Laramée, H. Hauser, L. Zhao, and F. Post. Topology-based flow visualization, the state of the art. In H. Hauser, H. Hagen, and H. Theisel, editors, *Topology-based Methods in Visualization*, Mathematics and Visualization, pages 1–19. Springer, 2007. (Cited on pages 99, 101, and 106.)
- [203] R. S. Laramée, H. Hauser, H. Doleisch, B. Vrolijk, F. H. Post, and D. Weiskopf. The state of the art in flow visualization: dense and texture-based techniques. *Computer Graphics Forum*, 23(2):203–222, 2004. (Cited on pages 101 and 103.)
- [204] I. Larrabide, M. Kim, L. Augsburger, M. C. Villa-Uriol, D. Rüfenacht, and A. F. Frangi. Fast virtual deployment of self-expandable stents: method and in vitro evaluation for intracranial aneurysmal stenting. *Medical Image Analysis*, 16(3):721–730, 2012. (Cited on pages 80 and 93.)
- [205] I. Larrabide, M.-C. Villa-Uriol, R. Cárdenes, V. Barbarito, L. Carotenuto, A. J. Geers, H. G. Morales, J. M. Pozo, M. D. Mazzeo, H. Bogunović, et al. Angiolab - a software tool for morphological analysis and endovascular treatment planning of intracranial aneurysms. *Computer Methods and Programs in Biomedicine*, 108(2):806–819, 2012. (Cited on page 92.)
- [206] K. Lawonn, R. Gasteiger, and B. Preim. Adaptive surface visualization of vessels with embedded blood flow based on the suggestive contour measure. In *Vision, Modeling, and Visualization*, pages 113–120, 2013. (Cited on pages 159, 160, and 264.)
- [207] K. Lawonn, T. Mönch, and B. Preim. Streamlines for illustrative real-time rendering. *Computer Graphics Forum*, 32(3pt3):321–330, 2013. (Cited on pages 132 and 139.)
- [208] D. Lee and T. Carroll. Magnetic resonance imaging. In J. J. Goldberger and J. Ng, editors, *Practical Signal and Image Processing in Clinical Cardiology*, pages 251–273. Springer London, 2010. (Cited on page 22.)
- [209] D. Lesage, E. D. Angelini, I. Bloch, and G. Funka-Lea. A review of 3d vessel lumen segmentation techniques: models, features and extraction schemes. *Medical Image Analysis*, 13(6):819–845, 2009. (Cited on pages 54 and 57.)
- [210] H. Levkowitz. *Color theory and modeling for computer graphics, visualization, and multimedia applications*. Kluwer Academic Pub, 1997. (Cited on pages 116, 151, 187, 190, and 216.)
- [211] L. Li and H.-W. Shen. Image-based streamline generation and rendering. *IEEE Transactions on Visualization and Computer Graphics*, 13(3):630–640, 2007. (Cited on pages 104, 123, and 124.)
- [212] W. Li, L. Ritter, M. Agrawala, B. Curless, and D. Salesin. Interactive cutaway illustrations of complex 3D models. *ACM Transactions on Graphics*, 26(3):31–1–31–12, 2007. (Cited on pages 133 and 135.)

- [213] N. Liu and M.-Y. Pang. A survey of shadow rendering algorithms: projection shadows and shadow volumes. In *Workshop on Computer Science and Engineering*, volume 1, pages 488–492, 2009. (Cited on page 133.)
- [214] W. Lorensen and H. Cline. Marching cubes: a high resolution 3D surface construction algorithm. *SIGGRAPH Computer Graphics*, 21(4):163–169, 1987. (Cited on pages 52 and 58.)
- [215] J. Lotz, C. Meier, A. Leppert, and M. Galanski. Cardiovascular flow measurement with phase-contrast MR imaging: basic facts and implementation. *Radiographics*, 22(3):651–671, 2002. (Cited on pages 25, 26, 28, and 29.)
- [216] V. Luboz, X. Wu, K. Krissian, C.-F. Westin, R. Kikinis, S. Cotin, and S. Dawson. A segmentation and reconstruction technique for 3D vascular structures. In *Medical Image Computing and Computer-Assisted Intervention*, pages 43–50. Springer, 2005. (Cited on page 59.)
- [217] T. Luft, C. Colditz, and O. Deussen. Image enhancement by unsharp masking the depth buffer. *ACM Transactions on Graphics*, 25(3):1206–1213, 2006. (Cited on pages 133, 141, and 143.)
- [218] B. Ma, R. Harbaugh, and M. Raghavan. Three-dimensional geometrical characterization of cerebral aneurysms. *Annals of Biomedical Engineering*, 32(2):264–273, 2004. (Cited on pages 14 and 15.)
- [219] O. Mallo, R. Peikert, C. Sigg, and F. Sadlo. Illuminated lines revisited. In *IEEE Visualization*, pages 19–26, 2005. (Cited on page 104.)
- [220] M. Markl, M. Draney, M. Hope, J. Levin, F. Chan, M. Alley, N. Pelc, and R. Herfkens. Time-resolved 3-dimensional velocity mapping in the thoracic aorta: visualization of 3-directional blood flow patterns in healthy volunteers and patients. *Journal of Computer Assisted Tomography*, 28(4):459–468, 2004. (Cited on pages 67 and 68.)
- [221] M. Markl, A. Frydrychowicz, S. Kozerke, M. Hope, and O. Wieben. 4D flow MRI. *Journal of Magnetic Resonance Imaging*, 36(5):1015–1036, 2012. (Cited on pages 25, 28, 29, 30, 41, 44, 67, 68, 72, 182, and 190.)
- [222] M. Markl, P. Kilner, and T. Ebbers. Comprehensive 4D velocity mapping of the heart and great vessels by cardiovascular magnetic resonance. *Journal of Cardiovascular Magnetic Resonance*, 13(1):1–22, 2011. (Cited on pages 28, 38, 46, 47, 67, 91, 94, 135, 163, and 212.)
- [223] M. Markl, F. Wegent, T. Zech, S. Bauer, C. Strecker, M. Schumacher, C. Weiller, J. Hennig, and A. Harloff. In-vivo wall shear stress distribution in the carotid artery: effect of bifurcation geometry, internal carotid artery stenosis and recanalization therapy. *Circulation: Cardiovascular Imaging*, 3(6):647–655, 2010. (Cited on page 69.)
- [224] J. Martinez Esturo, M. Schulze, C. Rössl, and H. Theisel. Global selection of stream surfaces. *Computer Graphics Forum*, 32(2pt1):113–122, 2013. (Cited on pages 104, 123, and 125.)

- [225] O. Mattausch, T. Theußl, H. Hauser, and E. Gröller. Strategies for interactive exploration of 3D flow using evenly-spaced illuminated streamlines. In *ACM Spring Conference on Computer Graphics*, pages 230–241, 2003. (Cited on pages 104, 105, 123, and 189.)
- [226] N. Max, R. Crawfis, and D. Williams. Visualizing wind velocities by advecting cloud textures. In *IEEE Visualization*, pages 179–184, 1992. (Cited on page 102.)
- [227] M. R. Mayberg, H. H. Batjer, R. Dacey, M. Diringer, E. C. Haley, R. C. Heros, L. L. Sternau, J. Torner, H. Adams, and W. Feinberg. Guidelines for the management of aneurysmal subarachnoid hemorrhage: a statement for health-care professionals from a special writing group of the stroke council, american heart association. *Stroke*, 25(11):2315–2328, 1994. (Cited on page 13.)
- [228] M. McGuire and J. F. Hughes. Hardware-determined feature edges. In *ACM Non-Photorealistic Animation and Rendering*, pages 35–47, 2004. (Cited on page 140.)
- [229] T. McInemey and D. Terzopoulos. Topology adaptive deformable surfaces for medical image volume segmentation. *IEEE Transactions on Medical Imaging*, 18(10):840–850, 1999. (Cited on pages 55 and 56.)
- [230] T. McLoughlin, R. S. Laramée, R. Peikert, F. H. Post, and M. Chen. Over two decades of integration-based, geometric flow visualization. *Computer Graphics Forum*, 29(6):1807–1829, 2010. (Cited on pages 99, 100, 101, and 105.)
- [231] S. Meckel, A. Stalder, F. Santini, E. Radü, D. Rüfenacht, M. Markl, and S. Wetzel. In vivo visualization and analysis of 3-D hemodynamics in cerebral aneurysms with flow-sensitized 4-D MR imaging at 3 T. *Neuroradiology*, 50(6):473–484, 2008. (Cited on page 70.)
- [232] S. Mendis, P. Puska, and B. Norrving. Global atlas on cardiovascular disease prevention and control, 2011. WHO report. (Cited on pages 9 and 10.)
- [233] H. Meng, V. Tutino, J. Xiang, and A. Siddiqui. High WSS or low WSS? Complex interactions of hemodynamics with intracranial aneurysm initiation, growth, and rupture: toward a unifying hypothesis. *American Journal of Neuroradiology*, 2013. (preprint). (Cited on pages 77 and 94.)
- [234] E. Metaxa, M. Tremmel, J. Xiang, J. Kolega, M. Mandelbaum, A. Siddiqui, J. Mocco, and H. Meng. High wall shear stress and positive wall shear stress gradient trigger the initiation of intracranial aneurysms. In *Summer Bioengineering Conference*, pages 17–21, 2009. (Cited on page 77.)
- [235] C. Metz, M. Schaap, A. van der Giessen, T. van Walsum, and W. Niessen. Semi-automatic coronary artery centerline extraction in computed tomography angiography data. In *IEEE Biomedical Imaging: From Nano to Macro*, pages 856–859, 2007. (Cited on page 55.)
- [236] R. Millán, L. Dempere-Marco, J. Pozo, J. Cebal, and A. Frangi. Morphological characterization of intracranial aneurysms using 3-D moment invariants. *IEEE Transactions on Medical Imaging*, 26(9):1270–1282, 2007. (Cited on page 92.)

- [237] J. Mönch. *Szenariobasierte Konzeption, Entwicklung und Evaluierung chirurgischer Trainingssysteme*. PhD thesis, Otto-von-Guericke University of Magdeburg, 2011. (Cited on page [214](#).)
- [238] J. Mönch, K. Mühler, C. Hansen, K.-J. Oldhafer, G. Stavrou, C. Hillert, C. Logge, and B. Preim. The liversurgerytrainer: training of computer-based planning in liver resection surgery. *International Journal of Computer Assisted Radiology and Surgery*, 8(5):809–818, 2013. (Cited on page [213](#).)
- [239] T. Mönch, R. Gasteiger, G. Janiga, H. Theisel, and B. Preim. Context-aware mesh smoothing for biomedical applications. *Computers & Graphics*, 35(4):755–767, 2011. (Cited on page [60](#).)
- [240] J. E. Moore, C. Xu, S. Glagov, C. K. Zarins, and D. N. Ku. Fluid wall shear stress measurements in a model of the human abdominal aorta: oscillatory behavior and relationship to atherosclerosis. *Atherosclerosis*, 110(2):225–240, 1994. (Cited on page [37](#).)
- [241] H. Morales, I. Larrabide, A. Geers, L. San Roman, J. Blasco, J. Macho, and A. Frangi. A virtual coiling technique for image-based aneurysm models by dynamic path planning. *IEEE Transactions on Medical Imaging*, 32(1):119–129, 2013. (Cited on pages [80](#) and [93](#).)
- [242] K. Mühler, M. Neugebauer, C. Tietjen, and B. Preim. Viewpoint selection for intervention planning. In *EG/IEEE EuroVis*, pages 267–274, 2007. (Cited on page [216](#).)
- [243] F. Mut and J. Cebral. Effects of flow-diverting device oversizing on hemodynamics alteration in cerebral aneurysms. *American Journal of Neuroradiology*, 33(10):2010–2016, 2012. (Cited on page [81](#).)
- [244] National Heart Lung and Blood Institute. Division of cardiovascular diseases strategic plan, September 2008. (last visited: 14 September 2013). (Cited on page [42](#).)
- [245] M. Neugebauer. *Computergestützte Exploration von zerebralen Aneurysmen - geometrische Verarbeitung und interaktive Visualisierung*. PhD thesis, Otto-von-Guericke University of Magdeburg, 2014. (to appear). (Cited on pages [116](#) and [213](#).)
- [246] M. Neugebauer, V. Diehl, M. Skalej, and B. Preim. Geometric reconstruction of the ostium of cerebral aneurysms. In *Vision, Modeling, and Visualization*, pages 307–314, 2010. (Cited on pages [61](#) and [196](#).)
- [247] M. Neugebauer, R. Gasteiger, O. Beuing, and et al. Map displays for the analysis of scalar data on cerebral aneurysm surfaces. *Computer Graphics Forum*, 28(3):895–902, 2009. (Cited on pages [116](#), [117](#), and [129](#).)
- [248] M. Neugebauer, G. Janiga, O. Beuing, M. Skalej, and B. Preim. Anatomy-guided exploration of blood flow in cerebral aneurysms. *Computer Graphics Forum*, 30(3):1041–1050, 2011. (Cited on pages [117](#), [118](#), [122](#), [123](#), [164](#), [188](#), [194](#), and [217](#).)



- [249] M. Neugebauer, K. Lawonn, P. Berg, G. Janiga, O. Beuing, and B. Preim. Amnvis - a system for qualitative exploration of near-wall hemodynamics in cerebral aneurysms. *Computer Graphics Forum*, 32(3pt3):251–260, 2013. (Cited on pages 118, 119, and 123.)
- [250] M. Neugebauer and B. Preim. Generation of a smooth ostium surface for aneurysm surface models. In *Bildverarbeitung für die Medizin*, pages 399–403, 2011. (Cited on pages 61 and 200.)
- [251] P. Neumann, T. Isenberg, and S. Carpendale. NPR lenses: interactive tools for non-photorealistic line drawings. In *Smart Graphics*, pages 10–22, 2007. (Cited on page 189.)
- [252] M. Nienhaus and J. Döllner. Blueprints:illustrating architecture and technical parts using hardware-accelerated non-photorealistic rendering. In *Graphics Interface*, pages 49–56, 2004. (Cited on page 132.)
- [253] A. M. Nixon, M. Gunel, and B. E. Sumpio. The critical role of hemodynamics in the development of cerebral vascular disease. *Neurosurgery*, 112(6):1240–1253, 2010. (Cited on page 3.)
- [254] S. Oeltze. *Visual exploration and analysis of perfusion data*. PhD thesis, Otto-von-Guericke University of Magdeburg, 2010. (Cited on pages 187, 188, and 215.)
- [255] S. Oeltze, H. Doleisch, H. Hauser, P. Muigg, and B. Preim. Interactive visual analysis of perfusion data. *IEEE Transactions on Visualization and Computer Graphics*, 13(6):1392–1399, 2007. (Cited on page 188.)
- [256] S. Oeltze, A. Hennemuth, S. Glaßer, C. Kühnel, and B. Preim. Glyph-based visualization of myocardial perfusion data and enhancement with contractility and viability information. In *EG Workshop on Visual Computing for Biology and Medicine*, pages 11–20, 2008. (Cited on page 187.)
- [257] Y. Ohtake, A. Belyaev, M. Alexa, G. Turk, and H. Seidel. Multi-level partition of unity implicits. In *ACM SIGGRAPH Courses*, pages 463–470, 2005. (Cited on page 58.)
- [258] R. Orth, M. Wallace, and M. Kuo. C-arm cone-beam CT: general principles and technical considerations for use in interventional radiology. *Journal of Vascular and Interventional Radiology*, 19(6):814–820, 2008. (Cited on page 19.)
- [259] S. Osher and R. P. Fedkiw. Level set methods: an overview and some recent results. *Journal of Computational physics*, 169(2):463–502, 2001. (Cited on page 56.)
- [260] M. Otto. *Uncertain vector field visualization*. PhD thesis, Otto-von-Guericke University of Magdeburg. (to appear). (Cited on page 125.)
- [261] A. Perez-Garcia, V. Ayala-Ramirez, R. E. Sanchez-Yanez, and J.-G. Avina-Cervantes. Monte carlo evaluation of the hausdorff distance for shape matching. In *Progress in Pattern Recognition, Image Analysis and Applications*, pages 686–695, 2006. (Cited on page 175.)



- [262] M. Piotin, R. Blanc, L. Spelle, C. Mounayer, R. Piantino, P. Schmidt, and J. Moret. Stent-assisted coiling of intracranial aneurysms. *Stroke*, 41(1):110–115, 2010. (Cited on page 18.)
- [263] A. Pobitzer, A. Lez, K. Matkovic, and H. Hauser. A statistics-based dimension reduction of the space of path line attributes for interactive visual flow analysis. In *IEEE PacificVis*, pages 113–120, 2012. (Cited on page 126.)
- [264] A. Pobitzer, R. Peikert, R. Fuchs, B. Schindler, A. Kuhn, H. Theisel, K. Matković, and H. Hauser. The state of the art in topology-based visualization of unsteady flow. *Computer Graphics Forum*, 30(6):1789–1811, 2011. (Cited on page 106.)
- [265] N. Plevaya, M. Kalani, G. Steinberg, and V. Tse. The transition from hunterian ligation to intracranial aneurysm clips: a historical perspective. *Neurosurgical Focus*, 20(6):1–7, 2006. (Cited on page 16.)
- [266] F. H. Post, B. Vrolijk, H. Hauser, R. S. Laramée, and H. Doleisch. The state of the art in flow visualisation: feature extraction and tracking. *Computer Graphics Forum*, 22(4):775–792, 2003. (Cited on pages 101 and 105.)
- [267] E. Praun, H. Hoppe, M. Webb, and A. Finkelstein. Real-time hatching. In *ACM SIGGRAPH*, pages 581–586, 2001. (Cited on page 132.)
- [268] B. Preim and D. Bartz. *Visualization in medicine: theory, algorithms, and applications*. Morgan Kaufmann, 2007. (Cited on page 199.)
- [269] B. Preim and C. Tietjen. Illustrative rendering for intervention planning: methods, applications, experiences. In *Workshop on Eurographics (Tutorial)*, pages 108–123, 2006. (Cited on pages 130, 131, and 132.)
- [270] F. Quek and C. Kirbas. Vessel extraction in medical images by wave-propagation and traceback. *IEEE Transactions on Medical Imaging*, 20(2):117–131, 2001. (Cited on page 55.)
- [271] A. P. Randles, M. Bächer, H. Pfister, and E. Kaxiras. A lattice boltzmann simulation of hemodynamics in a patient-specific aortic coarctation model. In O. Camara, T. Mansi, M. Pop, K. Rhode, M. Sermesant, and A. Young, editors, *Statistical Atlases and Computational Models of the Heart. Imaging and Modelling Challenges*, volume 7746 of *Lecture Notes in Computer Science*, pages 17–25. Springer, 2013. (Cited on page 66.)
- [272] V. Rayz, L. Boussel, L. Ge, J. Leach, A. Martin, M. Lawton, C. McCulloch, and D. Saloner. Flow residence time and regions of intraluminal thrombus deposition in intracranial aneurysms. *Annals of Biomedical Engineering*, 38(10):3058–3069, 2010. (Cited on page 192.)
- [273] J. Reininghaus, N. Kotava, D. Guenther, J. Kasten, H. Hagen, and I. Hotz. A scale space based persistence measure for critical points in 2D scalar fields. *IEEE Transactions on Visualization and Computer Graphics*, 17(12):2045–2052, 2011. (Cited on page 182.)

- [274] G. Reiter, U. Reiter, G. Kovacs, B. Kainz, K. Schmidt, R. Maier, H. Olschewski, and R. Rienmueller. Magnetic resonance–derived 3-dimensional blood flow patterns in the main pulmonary artery as a marker of pulmonary hypertension and a measure of elevated mean pulmonary arterial pressure. *Circulation: Cardiovascular Imaging*, 1(1):23–30, 2008. (Cited on page 69.)
- [275] P. Rheingans and D. Ebert. Volume illustration: nonphotorealistic rendering of volume models. *IEEE Transactions on Visualization and Computer Graphics*, 7(3):253–264, 2001. (Cited on page 134.)
- [276] F. Ritter, C. Hansen, V. Dicken, O. Konrad, B. Preim, and H.-O. Peitgen. Real-time illustration of vascular structures. *IEEE Transactions on Visualization and Computer Graphics*, 12(5):877–884, 2006. (Cited on pages 134 and 155.)
- [277] A. Robertson and P. Watton. Computational fluid dynamics in aneurysm research: critical reflections, future directions. *American Journal of Neuroradiology*, 33(6):992–995, 2012. (Cited on page 212.)
- [278] S. Roes, S. Hammer, R. van der Geest, N. Marsan, J. Bax, H. Lamb, J. Reiber, A. de Roos, and J. Westenberg. Flow assessment through four heart valves simultaneously using 3-dimensional 3-directional velocity-encoded magnetic resonance imaging with retrospective valve tracking in healthy volunteers and patients with valvular regurgitation. *Investigative Radiology*, 44(10):669–675, 2009. (Cited on page 67.)
- [279] T. Ropinski, S. Oeltze, and B. Preim. Survey of glyph-based visualization techniques for spatial multivariate medical data. *Computers & Graphics*, 35(2):392–401, 2011. (Cited on pages 187 and 188.)
- [280] T. Ropinski, M. Specht, J. Meyer-Spradow, K. Hinrichs, and B. Preim. Surface glyphs for visualizing multimodal volume data. In *Vision, Modeling, and Visualization*, pages 3–12, 2007. (Cited on page 187.)
- [281] C. Rössl and H. Theisel. Streamline embedding for 3D vector field exploration. *Transactions on Visualization and Computer Graphics*, 18(3):407–420, 2012. (Cited on page 107.)
- [282] S. Rusinkiewicz, M. Burns, and D. DeCarlo. Exaggerated shading for depicting shape and detail. *ACM Transactions on Graphics*, 25(3):1199–1205, 2006. (Cited on page 132.)
- [283] I. A. Sadarjoen and F. H. Post. Detection, quantification, and tracking of vortices using streamline geometry. *Computers & Graphics*, 24(3):333 – 341, 2000. (Cited on page 106.)
- [284] O. Sahni, K. Jansen, M. Shephard, C. Taylor, and M. Beall. Adaptive boundary layer meshing for viscous flow simulations. *Engineering with Computers*, 24(3):267–285, 2008. (Cited on page 64.)
- [285] O. Sahni, J. Müller, K. Jansen, M. Shephard, and C. Taylor. Efficient anisotropic adaptive discretization of the cardiovascular system. *Computer Methods in Applied Mechanics and Engineering*, 195(41):5634–5655, 2006. (Cited on page 64.)

- [286] M. P. Salisbury, S. E. Anderson, R. Barzel, and D. H. Salesin. Interactive pen-and-ink illustration. In *ACM SIGGRAPH Computer Graphics and Interactive Techniques*, pages 101–108, 1994. (Cited on pages 131 and 139.)
- [287] T. Salzbrunn, C. Garth, G. Scheuermann, and J. Meyer. Pathline predicates and unsteady flow structures. *The Visual Computer*, 24(12):1039–1051, 2008. (Cited on pages 107, 121, 164, and 215.)
- [288] T. Salzbrunn, H. Jänicke, T. Wischgoll, and G. Scheuermann. The state of the art in flow visualization: partition-based techniques. In *Simulation and Visualization*, pages 75–92, 2008. (Cited on pages 99, 101, 106, and 108.)
- [289] T. Salzbrunn and G. Scheuermann. Streamline Predicates. *IEEE Transactions on Visualization and Computer Graphics*, 12(6):1601–1612, 2006. (Cited on pages 107, 121, and 164.)
- [290] G. Scheuermann, H. Kruger, M. Menzel, and A. P. Rockwood. Visualizing nonlinear vector field topology. *IEEE Transactions on Visualization and Computer Graphics*, 4(2):109–116, 1998. (Cited on page 107.)
- [291] M. Schirski, C. Bischof, and T. Kuhlen. Interactive particle tracing on tetrahedral grids using the GPU. In *Vision, Modeling, and Visualization*, pages 153–160, 2006. (Cited on page 100.)
- [292] C. Schlick. A customizable reflectance model for everyday rendering. In *EG Workshop on Rendering*, pages 73–83, 1993. (Cited on page 138.)
- [293] R. Schmidt, K. Singh, and R. Balakrishnan. Sketching and composing widgets for 3D manipulation. *Computer Graphics Forum*, 27(2):301–310, 2008. (Cited on page 194.)
- [294] P. Schneider and D. Eberly. *Geometric tools for computer graphics*. Morgan Kaufmann, 2003. (Cited on page 59.)
- [295] J. Schöberl. NETGEN: an advancing front 2D/3D-mesh generator based on abstract rules. *Computing and Visualization in Science*, 1(1):41–52, 1997. (Cited on pages 63 and 86.)
- [296] C. Schumann, M. Neugebauer, R. Bade, B. Preim, and H.-O. Peitgen. Implicit vessel surface reconstruction for visualization and CFD simulation. *International Journal of Computer Assisted Radiology and Surgery*, 2(5):275–286, 2008. (Cited on pages 58, 59, 85, and 95.)
- [297] C. Schumann, S. Oeltze, R. Bade, and B. Preim. Model-free surface visualization of vascular trees. In *EG/IEEE EuroVis*, pages 283–290, 2007. (Cited on page 58.)
- [298] M. Schwenke, A. Hennemuth, B. Fischer, and O. Friman. Blood flow computation in phase-contrast MRI by minimal paths in anisotropic media. In *Medical Image Computing and Computer-Assisted Intervention*, pages 436–443. Springer, 2011. (Cited on page 219.)
- [299] J. A. Sethian. Fast marching methods. *SIAM Review*, 41(2):199–235, 1999. (Cited on page 56.)

- [300] D. Sforza, C. Putman, E. Scrivano, P. Lylyk, and J. Cebal. Blood-flow characteristics in a terminal basilar tip aneurysm prior to its fatal rupture. *American Journal of Neuroradiology*, 31(6):1127–1131, 2010. (Cited on pages 79 and 186.)
- [301] D. M. Sforza, C. M. Putman, and J. R. Cebal. Hemodynamics of cerebral aneurysms. *Annual Review of Fluid Mechanics*, 41:91–107, 2009. (Cited on pages 13, 65, 77, 78, 190, and 192.)
- [302] S. C. Shadden, J. O. Dabiri, and J. E. Marsden. Lagrangian analysis of fluid transport in empirical vortex ring flows. *Physics of Fluids*, 18(4):047105–1–047105–11, 2006. (Cited on pages 113 and 182.)
- [303] H. Si. On refinement of constrained delaunay tetrahedralizations. In P. P. Pá˘bay, editor, *Meshing Roundtable*, pages 509–528. Springer, 2006. (Cited on page 87.)
- [304] V. Soltészová. *Perception-Augmenting Illumination*. PhD thesis, 2012. (Cited on page 132.)
- [305] T. Sørensen, P. Beerbaum, H. Körperich, and E. Pedersen. Three-dimensional, isotropic MRI: a unified approach to quantification and visualization in congenital heart disease. *Journal of Cardiovascular Imaging*, 21(2):283–292, 2005. (Cited on pages 44 and 45.)
- [306] J. Soulis, O. Lampri, D. Fytanidis, and G. Giannoglou. Relative residence time and oscillatory shear index of non-newtonian flow models in aorta. In *IEEE Biomedical Engineering*, pages 1–4, 2011. (Cited on page 37.)
- [307] B. Spencer, R. S. Laramee, G. Chen, and E. Zhang. Evenly spaced streamlines for surfaces: an image-based approach. *Computer Graphics Forum*, 28(6):1618–1631, 2009. (Cited on page 104.)
- [308] M. Srichai, R. Lim, S. Wong, and V. Lee. Cardiovascular applications of phase-contrast MRI. *American Journal of Roentgenology*, 192(3):662–675, 2009. (Cited on page 25.)
- [309] A. F. Stalder, A. Frydrychowicz, A. Harloff, Q. Yang, J. Bock, J. Hennig, K. C. Li, and M. Markl. Vortex core detection and visualization using 4D flow-sensitive MRI. In *Magnetic Resonance in Medicine*, page 3708, 2010. (Cited on pages 112, 115, and 165.)
- [310] Z. Stankovic, Z. Csatari, P. Deibert, W. Euringer, P. Blanke, W. Kreisel, Z. Zadeh, F. Kallfass, M. Langer, and M. Markl. Normal and altered three-dimensional portal venous hemodynamics in patients with liver cirrhosis. *Radiology*, 262(3):862–873, 2012. (Cited on page 71.)
- [311] D. Steinman, J. Milner, C. Norley, S. Lownie, and D. Holdsworth. Image-based computational simulation of flow dynamics in a giant intracranial aneurysm. *American Journal of Neuroradiology*, 24(4):559–566, 2003. (Cited on pages 53 and 163.)
- [312] D. Sujudi and R. Haimes. Identification of swirling flow in 3D vector fields. Technical report, Department of Aeronautics and Astronautics, MIT, 1995. (Cited on pages 112, 113, and 164.)

- [313] V. Surazhsky and C. Gotsman. Explicit surface remeshing. In *EG/ACM SIGGRAPH Symposium on Geometry processing*, pages 20–30, 2003. (Cited on page 63.)
- [314] J. S. Suri, K. Liu, L. Reden, and S. Laxminarayan. A review on MR vascular image processing algorithms: acquisition and prefiltering: part i. *IEEE Transactions on Information Technology in Biomedicine*, 6(4):324–337, 2002. (Cited on page 24.)
- [315] N. A. Svakhine, D. S. Ebert, and W. M. Andrews. Illustration-inspired depth enhanced volumetric medical visualization. *IEEE Transactions on Visualization and Computer Graphics*, 15(1):77–86, 2009. (Cited on page 134.)
- [316] N. A. Svakhine, Y. Jang, D. S. Ebert, and K. P. Gaither. Illustration and photography inspired visualization of flows and volumes. In *IEEE Visualization*, pages 87–95, 2005. (Cited on pages 101 and 133.)
- [317] J. Tao, J. Ma, C. Wang, and C.-K. Shene. A unified approach to streamline selection and viewpoint selection for 3D flow visualization. *IEEE Transactions on Visualization and Computer Graphics*, 19(3):393–406, 2013. (Cited on page 125.)
- [318] S. Tateshima, A. Chien, J. Sayre, J. R. Cebral, and F. Viñuela. The effect of aneurysm geometry on the intra-aneurysmal flow condition. *Neuroradiology*, 52(12):1135–1141, 2010. (Cited on pages 53, 54, and 59.)
- [319] S. Tateshima, K. Tanishita, Y. Hakata, S.-y. Tanoue, and F. Viñuela. Alteration of intraaneurysmal hemodynamics by placement of a self-expandable stent. *Journal of Neurosurgery*, 111(1):22–27, 2009. (Cited on page 81.)
- [320] G. Taubin. A signal processing approach to fair surface design. In *ACM SIGGRAPH Computer Graphics and Interactive Techniques*, pages 351–358, 1995. (Cited on pages 57 and 60.)
- [321] C. Taylor and D. Steinman. Image-based modeling of blood flow and vessel wall dynamics: applications, methods and future directions. *Annals of Biomedical Engineering*, 38(3):1188–1203, 2010. (Cited on pages 53, 57, 66, and 73.)
- [322] C. A. Taylor, M. T. Draney, J. P. Ku, D. Parker, B. N. Steele, K. Wang, and C. K. Zarins. Predictive medicine: computational techniques in therapeutic decision-making. *Computer Aided Surgery*, 4(5):231–247, 1999. (Cited on page 73.)
- [323] C. A. Taylor and J. Humphrey. Open problems in computational vascular biomechanics: hemodynamics and arterial wall mechanics. *Computer Methods in Applied Mechanics and Engineering*, 198(45):3514–3523, 2009. (Cited on pages 76, 77, and 95.)
- [324] R. Taylor. Visualizing multiple fields on the same surface. *IEEE Computer Graphics and Applications*, 22(3):6–10, 2002. (Cited on pages 187 and 188.)



- [325] C. Teitzel, R. Grosso, and T. Ertl. Efficient and reliable integration methods for particle tracing in unsteady flows on discrete meshes. In *Visualization in Scientific Computing*, pages 31–41, 1997. (Cited on pages 104 and 140.)
- [326] A. Telea and J. J. Van Wijk. Simplified representation of vector fields. In *IEEE Visualization*, pages 35–507, 1999. (Cited on pages 107, 113, and 164.)
- [327] M. Termeer. *Comprehensive visualization of cardiac MRI data*. PhD thesis, Vienna University of Technology, 2009. (Cited on page 187.)
- [328] H. Theisel, T. Weinkauff, H.-C. Hege, and H.-P. Seidel. Saddle connectors - an approach to visualizing the topological skeleton of complex 3D vector fields. In *IEEE Visualization*, pages 225–232, 2003. (Cited on pages 107, 108, and 120.)
- [329] C. Tietjen, T. Isenberg, and B. Preim. Combining silhouettes, surface, and volume rendering for surgery education and planning. In *EG/IEEE EuroVis*, pages 303–310, 2005. (Cited on page 135.)
- [330] C. Tietjen, C. Kubisch, S. Hiller, and B. Preim. Gpu-basierte smart visibility techniken für die planung von tumor-operationen. In *Bildverarbeitung für die Medizin*, pages 272–276. Springer, 2009. (Cited on page 133.)
- [331] C. Tietjen, R. Pfisterer, A. Baer, R. Gasteiger, and B. Preim. Hardware-accelerated illustrative medical surface visualization with extended shading maps. In *SmartGraphics*, pages 166–177, 2008. (Cited on pages 130 and 134.)
- [332] L. A. Treinish. Multi-resolution visualization techniques for nested weather models. In *IEEE Visualization*, pages 513–516, 2000. (Cited on page 188.)
- [333] C. Tropea, A. L. Yarin, and J. F. Foss. *Handbook of experimental fluid mechanics*. Springer, 2007. (Cited on pages 31 and 32.)
- [334] R. Unterhinninghofen, S. Ley, J. Ley-Zaporozhan, H. von Tengg-Kobligk, M. Bock, H. Kauczor, G. Szabó, and R. Dillmann. Concepts for visualization of multidirectional phase-contrast MRI of the heart and large thoracic vessels. *Academic Radiology*, 15(3):361–369, 2008. (Cited on pages 44 and 45.)
- [335] M. Van der Zwan, W. Lueks, H. Bekker, and T. Isenberg. Illustrative molecular visualization with continuous abstraction. *Computer Graphics Forum*, 30(3):683–690, 2011. (Cited on page 216.)
- [336] R. F. P. van Pelt. *Real-time illustrative visualization of cardiovascular hemodynamics*. PhD thesis, Technical University of Eindhoven, 2012. (Cited on pages 26, 110, 120, 140, and 213.)
- [337] R. F. P. van Pelt, J. O. Bescós, M. Breeuwer, R. E. Clough, and M. E. Gröller. Exploration of 4D MRI blood-flow using stylistic visualization. *IEEE Transactions on Visualization and Computer Graphics*, 16(6):1339–1347, 2010. (Cited on pages 51, 52, 110, 111, 123, 194, 216, and 217.)



- [338] R. F. P. van Pelt, J. O. Bescós, M. Breeuwer, R. E. Clough, M. E. Groller, B. ter Haar Romenij, and A. Vilanova. Interactive virtual probing of 4D MRI blood-flow. *IEEE Transactions on Visualization and Computer Graphics*, 17(12):2153–2162, 2011. (Cited on pages 110, 111, 123, 164, 170, 182, and 217.)
- [339] R. F. P. van Pelt, S. S. A. M. Jacobs, B. M. ter Haar Romeny, and A. Vilanova. Visualization of 4D blood-flow fields by spatiotemporal hierarchical clustering. *Computer Graphics Forum*, 31(3pt2):1065–1074, 2012. (Cited on pages 113, 114, 122, and 165.)
- [340] R. F. P. van Pelt and A. Vilanova i Bartroli. Understanding blood-flow dynamics: challenges in visualization. *Computer*, 2013. (to appear). (Cited on pages 126, 212, 213, and 219.)
- [341] W. van Rooij, M. Sprengers, A. de Gast, J. Peluso, and M. Sluzewski. 3D rotational angiography: the new gold standard in the detection of additional intracranial aneurysms. *American Journal of Neuroradiology*, 29(5):976–979, 2008. (Cited on pages 20 and 21.)
- [342] J. J. van Wijk. Spot noise texture synthesis for data visualization. *SIGGRAPH Computer Graphics*, 25(4):309–318, 1991. (Cited on page 102.)
- [343] S. Venkataraman. 4D visualization of cardiac flow, September 2010. NVIDIA GPU Technology Conference. (Cited on page 120.)
- [344] V. Verma and A. Pang. Comparative flow visualization. *IEEE Transactions on Visualization and Computer Graphics*, 10(6):609–624, 2004. (Cited on pages 125 and 220.)
- [345] J. Viega, M. J. Conway, G. Williams, and R. Pausch. 3D magic lenses. In *ACM User Interface Software and Technology*, pages 51–58, 1996. (Cited on pages 189 and 194.)
- [346] R. Vindlacheruvu, A. Mendelow, and P. Mitchell. Risk–benefit analysis of the treatment of unruptured intracranial aneurysms. *Journal of Neurology, Neurosurgery & Psychiatry*, 76(2):234–239, 2005. (Cited on page 15.)
- [347] I. Viola and E. Gröller. Smart visibility in visualization. In *Computational Aesthetics*, pages 209–216, 2005. (Cited on pages 101, 133, 189, and 217.)
- [348] I. Viola, A. Kanitsar, and M. E. Gröller. Importance-driven feature enhancement in volume visualization. *IEEE Transactions on Visualization and Computer Graphics*, 11(4):408–418, 2005. (Cited on page 189.)
- [349] M. H. Vlak, A. Algra, R. Brandenburg, and G. J. Rinkel. Prevalence of unruptured intracranial aneurysms, with emphasis on sex, age, comorbidity, country, and time period: a systematic review and meta-analysis. *The Lancet Neurology*, 10(7):626–636, 2011. (Cited on page 12.)
- [350] P. Walker, G. Cranney, M. Scheidegger, G. Waseleski, G. Pohost, and A. Yoganathan. Semiautomated method for noise reduction and background phase error correction in MR phase velocity data. *Journal of Magnetic Resonance Imaging*, 3(3):521–530, 1993. (Cited on page 50.)

- [351] C. Wallraven, M. Breidt, D. W. Cunningham, and H. H. Bühlhoff. Evaluating the perceptual realism of animated facial expressions. *ACM Transactions on Applied Perception*, 4(4):1–20, 2008. (Cited on page 135.)
- [352] L. Wang, Y. Zhao, K. Mueller, and A. E. Kaufman. The magic volume lens: an interactive focus+context technique for volume rendering. In *IEEE Visualization*, pages 367–374, 2005. (Cited on page 189.)
- [353] L. R. Wanger, J. Ferwerda, and D. P. Greenberg. Perceiving spatial relationships in computer-generated images. *IEEE Computer Graphics and Applications*, 12(3):44–58, 1992. (Cited on page 133.)
- [354] M. Ward, G. Grinstein, and D. Keim. *Interactive data visualization: foundations, techniques, and applications*. AK Peters, Ltd., 2010. (Cited on page 187.)
- [355] Y. Wei, S. Cotin, J. Allard, L. Fang, C. Pan, and S. Ma. Interactive blood-coil simulation in real-time during aneurysm embolization. *Computers & Graphics*, 35(2):422–430, 2011. (Cited on page 80.)
- [356] C. Weigle and D. C. Banks. A comparison of the perceptual benefits of linear perspective and physically-based illumination for display of dense 3d streamtubes. *IEEE Transactions on Visualization and Computer Graphics*, 14(6):1723–1730, 2008. (Cited on pages 134 and 155.)
- [357] T. Weinkauff and D. Günther. Separatrix persistence: Extraction of salient edges on surfaces using topological methods. *Computer Graphics Forum*, 28(5):1519–1528, 2009. (Cited on page 182.)
- [358] T. Weinkauff, J. Sahner, H. Theisel, and H.-C. Hege. Cores of swirling particle motion in unsteady flows. *IEEE Transactions on Visualization and Computer Graphics*, 13(6):1759–1766, 2007. (Cited on page 164.)
- [359] D. Weiskopf. *GPU-based interactive visualization techniques*. Springer, 2007. (Cited on page 103.)
- [360] D. Weiskopf, T. Schafhitzel, and T. Ertl. Texture-based visualization of unsteady 3d flow by real-time advection and volumetric illumination. *IEEE Transactions on Visualization and Computer Graphics*, 13(3):569–582, 2007. (Cited on page 103.)
- [361] M. Wermer, I. van der Schaaf, A. Algra, and G. Rinkel. Risk of rupture of unruptured intracranial aneurysms in relation to patient and aneurysm characteristics: an updated meta-analysis. *Stroke*, 38(4):1404–1410, 2007. (Cited on pages 13 and 14.)
- [362] S. Wetzel, S. Meckel, A. Frydrychowicz, L. Bonati, E. Radue, K. Scheffler, J. Hennig, and M. Markl. In vivo assessment and visualization of intracranial arterial hemodynamics with flow-sensitized 4D MR imaging at 3T. *American Journal of Neuroradiology*, 28(3):433–438, 2007. (Cited on page 70.)
- [363] P. White and J. Wardlaw. Unruptured intracranial aneurysms. *Journal of Neuroradiology*, 30(5):336–350, 2003. (Cited on page 78.)

- [364] D. Wiebers. Unruptured intracranial aneurysms: natural history, clinical outcome, and risks of surgical and endovascular treatment. *The Lancet*, 362(9378):103–110, 2003. (Cited on page 13.)
- [365] C. M. Wittenbrink, A. T. Pang, and S. K. Lodha. Glyphs for visualizing uncertainty in vector fields. *IEEE Transactions on Visualization and Computer Graphics*, 2(3):266–279, 1996. (Cited on page 125.)
- [366] G. Wong, M. Kwan, R. Ng, S. Yu, and W. Poon. Flow diverters for treatment of intracranial aneurysms: current status and ongoing clinical trials. *Journal of Clinical Neuroscience*, 18(6):737–740, 2011. (Cited on page 18.)
- [367] G. Wong, H. Tan, M. Kwan, R. Ng, S. Yu, X. Zhu, and W. Poon. Evolution of intracranial aneurysm treatment: from hunterian ligation to the flow diverter. *Surgical Practice*, 15(1):16–20, 2011. (Cited on pages 16 and 17.)
- [368] J. Wu, Q. Hu, and X. Ma. Comparative study of surface modeling methods for vascular structures. *Computerized Medical Imaging and Graphics*, 37(1):4 – 14, 2013. (Cited on pages 58 and 95.)
- [369] J. Wu, M. Wei, Y. Li, X. Ma, F. Jia, and Q. Hu. Scale-adaptive surface modeling of vascular structures. *BioMechanical Engineering OnLine*, 9(1):75–91, 2010. (Cited on pages 58, 59, 63, and 95.)
- [370] J. Xiang, S. Natarajan, M. Tremmel, D. Ma, J. Mocco, L. Hopkins, A. Siddiqui, E. Levy, and H. Meng. Hemodynamic–morphologic discriminants for intracranial aneurysm rupture. *Stroke*, 42(1):144–152, 2010. (Cited on pages 13, 78, and 79.)
- [371] X. Xie, Y. He, F. Tian, H.-S. Seah, X. Gu, and H. Qin. An effective illustrative visualization framework based on photic extremum lines (pels). *IEEE Transactions on Visualization and Computer Graphics*, 13(6):1328–1335, 2007. (Cited on page 132.)
- [372] J. Yi and J. Ra. A locally adaptive region growing algorithm for vascular segmentation. *International Journal of Imaging Systems and Technology*, 13(4):208–214, 2003. (Cited on page 55.)
- [373] H. Younis, M. Kaazempur-Mofrad, R. Chan, A. Isasi, D. Hinton, A. Chau, L. Kim, and R. Kamm. Hemodynamics and wall mechanics in human carotid bifurcation and its consequences for atherogenesis: investigation of inter-individual variation. *Biomechanics and Modeling in Mechanobiology*, 3(1):17–32, 2004. (Cited on page 77.)
- [374] S. Zachow, P. Muigg, T. Hildebrandt, H. Doleisch, and H.-C. Hege. Visual exploration of nasal airflow. *IEEE Transactions on Visualization and Computer Graphics*, 15(6):1407–1414, 2009. (Cited on pages 126, 131, 188, and 215.)



## ABBREVIATIONS

---

3D-RA	Rotational Angiography
BAV	Bicuspid Aortic Valve
CAA	Central Aneurysm Axis
CE-MRA	Contrast-Enhanced Magnetic Resonance Angiography
CFD	Computational Fluid Dynamics
CHF	Congestive Heart Failure
CoW	Circle of Willi
CPU	Central Processing Unit
CVD	Cardiovascular Disease
CT	Computer Tomography
CTA	Computed Tomography Angiography
DSA	Digital Subtraction Angiography
EIA	External Iliac Artery
F+C	Focus-and-Context
FBO	Frame Buffer Object
FSI	Fluid-Structure Interaction
FTLE	Finite Time Lyapunov Exponent
HU	Hounsfield Unit
ICA	Internal Carotid Artery
ITK	Insight Segmentation and Registration Toolkit
GDC	Guglielmi Detachable Coil
GLSL	OpenGL Shading Language
GPU	Graphics Processing Unit
GUI	Graphical User Interface
LBS	Lattice Boltzmann Simulation
LIC	Line Integral Convolutions
LDV	Laser Doppler Velocimetry

MC	Marching Cube
MHz	Megahertz
MIP	Maximum Intensity Projection
MPUI	Multi-Level Partition of Unity Implicits
MPR	Multi-Planar Reformations
MRI	Magnetic Resonance Imaging
MWSS	Maximum Wall Shear Stress
NO	Nitric Oxide
OSI	Oscillatory Shear Index
PAH	Pulmonary Arterial Hypertension
PDE	Partial Differential Equation
PIV	Particle Image Velocimetry
PC-MRA	Time-Averaged Phase Contrast Magnetic Resonance Angiography
PC-MRI	Phase Contrast Magnetic Resonance Imaging
PTV	Particle Tracking Velocimetry
Re	Reynolds number
RF	Radio Frequency
ROI	Region of Interest
SAH	Subarachnoid Hemorrhage
SNR	Signal-to-Noise Ratio
T	Tesla
TMIP	Temporal Maximum Intensity Projection Image
TMOP	Temporal Mean Orientation Projection
TOF-MRA	Time-of-Flight Angiographic Imaging
ToT	Turnover Time
US	Ultrasound
VSD	Ventricular Septal Defect
VTK	Visualization Toolkit
WHO	World Health Organization
WSS	Wall Shear Stress



## PUBLICATIONS

---

### Journal papers

1. B. Köhler, **R. Gasteiger**, U. Preim, H. Theisel, M. Gutberlet and B. Preim. "Semi-Automatic Vortex Extraction in 4D PC-MRI Cardiac Blood Flow Data using Line Predicates", in *Journal of IEEE Transactions on Visualization and Computer Graphics (TVCG)*, 19(12):2773-2782, 2013.
2. G. Janiga, P. Berg, O. Beuing, M. Neugebauer, **R. Gasteiger**, B. Preim, G. Rose, M. Skalej and D. Thévenin. "Recommendations for Accurate Numerical Blood Flow Simulations of Stented Intracranial Aneurysms", in *Journal of Biomedical Engineering (JBME)*, 58(3):303-314, 2013.
3. **R. Gasteiger**, D.J. Lehmann, R.F.P. van Pelt, G. Janiga, O. Beuing, A. Vilanova, H. Theisel and B. Preim. "Automatic Detection and Visualization of Qualitative Hemodynamic Characteristics in Cerebral Aneurysms", in *Journal of IEEE Transactions on Visualization and Computer Graphics (TVCG)*, 18(12):2178-2187, 2012.
4. **R. Gasteiger**, M. Neugebauer, O. Beuing and B. Preim. "The FLOWLENS: A Focus-and-Context Visualization Approach for Exploration of Blood Flow in Cerebral Aneurysms", in *Journal of IEEE Transactions on Visualization and Computer Graphics (TVCG)*, 17(12):2183-2192, 2011.
5. A. Baer, **R. Gasteiger**, D. Cunningham and B. Preim. "Perceptual Evaluation of Ghosted View Techniques for the Exploration of Vascular Structures and Embedded Flow", in *EG Computer Graphics Forum (CGF)*, 30(3):811-820, 2011.
6. T. Mönch, **R. Gasteiger**, G. Janiga, H. Theisel and B. Preim. "Context-Aware Mesh Smoothing for Biomedical Applications", in *Journal of Computers & Graphics (CG)*, 35(4):755-767, 2011.
7. M. Neugebauer, **R. Gasteiger**, O. Beuing, V. Diehl, M. Skalej and B. Preim. "Map Displays for the Analysis of Scalar Data on Cerebral Aneurysm Surfaces", in *EG Computer Graphics Forum (CGF)*, 28(3):895-902, 2009.

### Conference papers

1. K. Lawonn, **R. Gasteiger** and B. Preim. "Adaptive Surface Visualization of Vessels with Embedded Blood Flow Based on the Suggestive Contour Measure", in *Proceedings of Vision, Modeling, Visualization (VMV)*, pages 113-120, 2013.
2. K. Lawonn, **R. Gasteiger** and B. Preim. "Qualitative Evaluation of Feature Lines on Anatomical Surfaces", in *Proceedings of Bildverarbeitung für die Medizin (BVM)*, pages 187-192, 2013.
3. B. Köhler, M. Neugebauer, **R. Gasteiger**, G. Janiga, O. Speck and B. Preim. "Surface-Based Seeding for Blood Flow Exploration", in *Proceedings of Bildverarbeitung für die Medizin (BVM)*, pages 81-86, 2012.
4. F. Klink, **R. Gasteiger**, H. Paukisch and U. Vorwerk. "Workflow zur generativen Herstellung von Felsenbeinfaksimilemodellen für die Optimierung von Cochlea-Implantat Operationen", in *Proceedings of Entwerfen, Entwickeln, Erleben (Kongress: Gemeinsames Kolloquium Konstruktionstechnik)*, pages 475-482, 2012.
5. M. Neugebauer, **R. Gasteiger**, U. Vorwerk, J. Dornheim and B. Preim. "Workflow für die Segmentierung von Felsenbeindatensätzen zur Erzeugung künstlicher Felsenbein-Präparate", in *Proceedings of Computer- und Roboterassistierte Chirurgie (CURAC)*, 2012.
6. **R. Gasteiger**, G. Janiga, D. Stucht, A. Hennemuth, O. Friman, O. Speck, M. Markl and B. Preim. "Vergleich zwischen 7 Tesla 4D PC-MRI Flussmessung und CFD-Simulation", in *Proceedings of Bildverarbeitung für die Medizin (BVM)*, pages 304-308, 2011.
7. D. Stucht, **R. Gasteiger**, S. Serowy, M. Markl, B. Preim and O. Speck. "Bildbasierte Korrektur von Phasensprüngen in 4D PC-MRI Flussdaten", in *Proceedings of Bildverarbeitung für die Medizin (BVM)*, pages 424-428, 2011.
8. **R. Gasteiger**, M. Neugebauer, C. Kubisch and B. Preim. "Adapted Surface Visualization of Cerebral Aneurysms with Embedded Blood Flow Information", in *Proceedings of EG Workshop on Visual Computing for Biology and Medicine (VCBM)*, pages 25-32, 2010.
9. **R. Gasteiger**, M. Neugebauer, V. Diehl, O. Beuing and B. Preim. "Entwurf einer angepassten Visualisierung von zerebralen Aneurysmen mit innenliegenden Blutflussinformationen", in *Proceedings of Computer- und Roboterassistierte Chirurgie (CURAC)*, pages 61-66, 2012.
10. M. Neugebauer, **R. Gasteiger**, V. Diehl, O. Beuing and B. Preim. "Automatic Generation of Context Visualizations for Cerebral Aneurysms from MRA Datasets", in *Proceedings of Computer Assisted Radiology and Surgery (CARS)*, pages 112-113, 2009.

11. C. Tietjen, R. Pfisterer, A. Baer, **R. Gasteiger** and B. Preim. "Hardware-Accelerated Illustrative Medical Surface Visualization with Extended Shading Maps", in *Proceedings of SmartGraphics*, pages 166-177, 2008.
12. **R. Gasteiger**, C. Tietjen, A. Baer and B. Preim. "Curvature- and Model-Based Surface Hatching of Anatomical Structures Derived from Clinical Volume Datasets", in *Proceedings of SmartGraphics*, pages 255-262, 2008.
13. C. Tietjen, **R. Gasteiger**, A. Baer and B. Preim. "Curvature- and Model-Based Surface Hatching of Patient-Specific Muscle Surfaces", in *Proceedings of Bildverarbeitung für die Medizin (BVM)*, pages 117-121, 2008.
14. **R. Gasteiger**, F. Ritter, B. Preim and T. Preusser. "Visualisierung von Simulationsparametern thermischer Tumorablationsverfahren", in *Proceedings of Simulation und Visualisierung (SimVis)*, pages 325-340, 2007.

### Book chapter

- A. Vilanova, B. Preim, R.F.P. van Pelt, **R. Gasteiger**, M. Neugebauer and T. Wischgoll. "Visual Exploration of Simulated and Measured Blood Flow", in *Scientific Visualization: Uncertainty, Multifield, Biomedical and Scalable Visualization*, Springer Verlag, 2013, to appear.



## CURRICULUM VITAE

---

### Personal Details

Name: **Rocco Gasteiger**  
Address: Bahnhofstraße 47  
39104 Magdeburg  
Mobile: +49 160 12 35 10 9  
Email: rocco.gasteiger@ovgu.de  
Date of birth: 07 October 1978  
Place of birth: Grimma  
Civil status: Single, no children  
Nationality: German



### School and Vocational Education

08/1997 – 07/2000 Company Klaus-Peter Benedix, *degree*: graduated roofer  
09/1992 – 07/1997 Sophiengymnasium Colditz, *degree*: "Abitur"

### Civilian Service

09/2000 – 07/2001 Municipal administration, Großbardau

### Academic Education

since 10/2007 Otto-von-Guericke University Magdeburg, Department of Simulation and Graphics, Visualization group, research assistant  
– *Teaching*: Visualization, Illustrative Visualization, Computer-assisted Diagnostic and Therapy  
– *Thesis topic*: "Visual Exploration of Cardiovascular Hemodynamics"  
05/2011 – 07/2011 Technical University Eindhoven, Department of BioMedical Engineering, the Netherlands, research stay  
– *Supervisors*: Prof. Dr. Anna Vilanova and Dr. Roy van Pelt  
– *Topic*: "Extraction of Qualitative Hemodynamic Parameters"

- 10/2001 – 09/2007 Otto-von-Guericke University Magdeburg, Department of Simulation and Graphics, Visualization Group, Computational Visualistics studies
- *Application subject:* Medicine
  - *Degree:* Dipl.-Ing. of Computational Visualistics (grade: 1.7)
  - *Thesis topic:* "Krümmungs- und modellbasierte Schraffierung auf patientenspezifischen, anatomischen Oberflächen" (grade: 1.3)
- 10/2005 – 03/2006 Fraunhofer MEVIS, Bremen, internship
- *Research topic:* "Visualisierung von Simulationsparametern in der Radiofrequenzablation"
  - *Supervisor:* Dr. Felix Ritter
- 11/2003 – 02/2004 MelTec GmbH, Magdeburg, software internship
- *Research topic:* "Verwaltung und Analyse von statistischen Daten"
  - *Supervisor:* Dr. Peter Karcher

### Research Awards

- 2013 2nd place of the Dirk Bartz Medical Prize (group prize)
- 3rd place of the Best Paper Award for the contribution presented in Lawonn et al. [206] (VMV 2013)
- 2012 Winner of the Karl-Heinz Höhne Award (*MedVis-Award*)

### Additional Research Activities

- 04/2006 – 07/2006 Otto-von-Guericke University Magdeburg, Department of Simulation and Graphics, Visualization Group in cooperation with ICCAS, Leipzig, student research assistant
- *Topic:* software development for surface curvature estimation
- 05/2005 – 07/2005 Otto-von-Guericke University Magdeburg, Department of Simulation and Graphics, Visualization Group in cooperation with ICCAS, Leipzig, student research assistant
- *Topic:* software development for RhinoVision, an image processing software for the paranasal sinuses
- 11/2004 – 02/2005 Otto-von-Guericke University Magdeburg, Media Center, student research assistant



– *Topics:* video editing, camera operator

### Further Educations

10/2010 – 01/2011	Otto-von-Guericke University Magdeburg, language center, certificate for UNICert III/A, "English in Engineering" (grade: 2.0)
04/2010 – 07/2010	Otto-von-Guericke University Magdeburg, language center, certificate of participation in UNICert III, "English in Engineering"
07/2009	Otto-von-Guericke University Magdeburg in cooperation with Hanover Medical School, certificate of participation for "Presentation techniques in scientific context"

### Expertise

Development	C++, Qt, VTK, OpenGL, GLSL, CUDA
Project Management	SVN and Wiki management, Doxygen, CMake
Typesetting	L <sup>A</sup> T <sub>E</sub> X, MS Word
Applications	Visual Studio, MeVisLab, MeshLab, NetGen, Adobe Creative Suite, ParaView, Sculptris, 3D Studio Max, MS Office

### Additional Skills

Languages	English (fluent in speech and writing) Russian (basic knowledge)
Driving Licence	A and B

<b>Personal Interests</b>	Christian faith, reading, sport, programming
---------------------------	--

Magdeburg, 07 February 2014



## COLOPHON

This document was typeset using the typographical look-and-feel `classicthesis` developed by André Miede. The style was inspired by Robert Bringhurst's seminal book on typography "*The Elements of Typographic Style*". `classicthesis` is available for both  $\text{\LaTeX}$  and  $\text{\LyX}$ :

<http://code.google.com/p/classicthesis/>

Happy users of `classicthesis` usually send a real postcard to the author, a collection of postcards received so far is featured here:

<http://postcards.miede.de/>

*Final Version* as of March 10, 2014 (`classicthesis` version 2.0).